NUREG/CR–4219
ORNL/TM–9593/V12&N1
Vol. 12, No. 1

Heavy-Section Steel Technology Program

Semiannual Progress Report for October 1994 – March 1995

Prepared by
W. E. Pennell

Oak Ridge National Laboratory

Prepared for
U.S. Nuclear Regulatory Commission

AVAILABILITY NOTICE

Availability of Reference Materials Cited in NRC Publications

Most documents cited in NRC publications will be available from one of the following sources:

1. The NRC Public Document Room, 2120 L Street, NW., Lower Level, Washington, DC 20555-0001

2. The Superintendent of Documents, U.S. Government Printing Office, P. O. Box 37082, Washington, DC 20402-9328

3. The National Technical Information Service, Springfield, VA 22161-0002

Although the listing that follows represents the majority of documents cited in NRC publications, it is not intended to be exhaustive.

Referenced documents available for inspection and copying for a fee from the NRC Public Document Room include NRC correspondence and internal NRC memoranda; NRC bulletins, circulars, information notices, inspection and investigation notices; licensee event reports; vendor reports and correspondence; Commission papers; and applicant and licensee documents and correspondence.

The following documents in the NUREG series are available for purchase from the Government Printing Office: formal NRC staff and contractor reports, NRC-sponsored conference proceedings, international agreement reports, grantee reports, and NRC booklets and brochures. Also available are regulatory guides, NRC regulations in the *Code of Federal Regulations*, and *Nuclear Regulatory Commission Issuances*.

Documents available from the National Technical Information Service include NUREG-series reports and technical reports prepared by other Federal agencies and reports prepared by the Atomic Energy Commission, forerunner agency to the Nuclear Regulatory Commission.

Documents available from public and special technical libraries include all open literature items, such as books, journal articles, and transactions. *Federal Register* notices, Federal and State legislation, and congressional reports can usually be obtained from these libraries.

Documents such as theses, dissertations, foreign reports and translations, and non-NRC conference proceedings are available for purchase from the organization sponsoring the publication cited.

Single copies of NRC draft reports are available free, to the extent of supply, upon written request to the Office of Administration, Distribution and Mail Services Section, U.S. Nuclear Regulatory Commission, Washington, DC 20555-0001.

Copies of industry codes and standards used in a substantive manner in the NRC regulatory process are maintained at the NRC Library, Two White Flint North, 11545 Rockville Pike, Rockville, MD 20852-2738, for use by the public. Codes and standards are usually copyrighted and may be purchased from the originating organization or, if they are American National Standards, from the American National Standards Institute, 1430 Broadway, New York, NY 10018-3308.

DISCLAIMER NOTICE

NUREG/CR–4219
ORNL/TM–9593/V12&N1
Vol. 12, No. 1

Heavy-Section Steel Technology Program

Semiannual Progress Report for October 1994 – March 1995

Manuscript Completed: April 1996
Date Published: July 1996

Prepared by
W. E. Pennell

Oak Ridge National Laboratory
Managed by Martin Marietta Energy Systems, Inc.

Oak Ridge National Laboratory
Oak Ridge, TN 37831–6285

S. N. Malik, NRC Project Manager

Prepared for
Division of Engineering Technology
Office of Nuclear Regulatory Research
U.S. Nuclear Regulatory Commission
Washington, DC 20555–0001
NRC Job Code B0119

Abstract

The Heavy-Section Steel Technology (HSST) Program is conducted for the Nuclear Regulatory Commission (NRC) by Oak Ridge National Laboratory (ORNL). The program focus is on the development and validation of technology for the assessment of fracture-prevention margins in commercial nuclear reactor pressure vessels. The HSST Program is organized in seven tasks: (1) program management, (2) constraint effects analytical development and validation, (3) evaluation of cladding effects, (4) ductile-to-cleavage fracture-mode conversion, (5) fracture analysis methods development and applications, (6) material property data and test methods, and (7) integration of results.

The program tasks have been structured to place emphasis on the resolution of fracture issues with near-term licensing significance. Resources to execute the research tasks are drawn from ORNL with subcontract support from universities and other research laboratories. Close contact is maintained with the sister Heavy-Section Steel Irradiation Program at ORNL and with related research programs both in the United States and abroad. This report provides an overview of principal developments in each of the seven program tasks from October 1994–March 1995.

Contents

List of Figures

List of Tables

Preface

The Heavy-Section Steel Technology (HSST) Program, which is sponsored by the Nuclear Regulatory Commission, is an engineering research activity devoted to extending and developing the technology for assessing the margin of safety against fracture of the thick-walled steel pressure vessels used in light-water-cooled nuclear power reactors. The program is being carried out in close cooperation with the nuclear power industry. This report covers HSST work performed in October 1994–March 1995. The work performed by the Oak Ridge National Laboratory (ORNL) and by subcontractors is managed by the Engineering Technology Division (ETD) of ORNL. Major tasks at ORNL are carried out by the ETD and the Metals and Ceramics Division. The following is a list of previous progress reports on this program:

ORNL-4176
ORNL-4315
ORNL-4377
ORNL-4463
ORNL-4512
ORNL-4590
ORNL-4653
ORNL-4681
ORNL-4764
ORNL-4816
ORNL-4855
ORNL-4918
ORNL-4971
ORNL/TM-4655 (Vol. II)
ORNL/TM-4729 (Vol. II)
ORNL/TM-4805 (Vol. II)
ORNL/TM-4914 (Vol. II)
ORNL/TM-5021 (Vol. II)
ORNL/TM-5170
ORNL/NUREG/TM-3
ORNL/NUREG/TM-28
ORNL/NUREG/TM-49
ORNL/NUREG/TM-64
ORNL/NUREG/TM-94
ORNL/NUREG/TM-120
ORNL/NUREG/TM-147
ORNL/NUREG/TM-166
ORNL/NUREG/TM-194
ORNL/NUREG/TM-209
ORNL/NUREG/TM-239
NUREG/CR-0476 (ORNL/NUREG/TM-275)
NUREG/CR-0656 (ORNL/NUREG/TM-298)
NUREG/CR-0818 (ORNL/NUREG/TM-324)
NUREG/CR-0980 (ORNL/NUREG/TM-347)
NUREG/CR-1197 (ORNL/NUREG/TM-370)
NUREG/CR-1305 (ORNL/NUREG/TM-380)
NUREG/CR-1477 (ORNL/NUREG/TM-393)
NUREG/CR-1627 (ORNL/NUREG/TM-401)
NUREG/CR-1806 (ORNL/NUREG/TM-419)
NUREG/CR-1941 (ORNL/NUREG/TM-437)
NUREG/CR-2141, Vol. 1 (ORNL/TM-7822)
NUREG/CR-2141, Vol. 2 (ORNL/TM-7955)
NUREG/CR-2141, Vol. 3 (ORNL/TM-8145)
NUREG/CR-2141, Vol. 4 (ORNL/TM-8252)
NUREG/CR-2751, Vol. 1 (ORNL/TM-8369/V1)
NUREG/CR-2751, Vol. 2 (ORNL/TM-8369/V2)
NUREG/CR-2751, Vol. 3 (ORNL/TM-8369/V3)
NUREG/CR-2751, Vol. 4 (ORNL/TM-8369/V4)
NUREG/CR-3334, Vol. 1 (ORNL/TM-8787/V1)
NUREG/CR-3334, Vol. 2 (ORNL/TM-8787/V2)
NUREG/CR-3334, Vol. 3 (ORNL/TM-8787/V3)
NUREG/CR-3744, Vol. 1 (ORNL/TM-9154/V1)
NUREG/CR-3744, Vol. 2 (ORNL/TM-9154/V2)
NUREG/CR-4219, Vol. 1 (ORNL/TM-9593/V1)
NUREG/CR-4219, Vol. 2 (ORNL/TM-9593/V2)
NUREG/CR-4219, Vol. 3, No. 1 (ORNL/TM-9593/V3&N1)
NUREG/CR-4219, Vol. 3, No. 2 (ORNL/TM-9593/V3&N2)
NUREG/CR-4219, Vol. 4, No. 1 (ORNL/TM-9593/V4&N1)
NUREG/CR-4219, Vol. 4, No. 2 (ORNL/TM-9593/V4&N2)
NUREG/CR-4219, Vol. 5, No. 1 (ORNL/TM-9593/V5&N1)
NUREG/CR-4219, Vol. 5, No. 2 (ORNL/TM-9593/V5&N2)
NUREG/CR-4219, Vol. 6, No. 1 (ORNL/TM-9593/V6&N1)
NUREG/CR-4219, Vol. 6, No. 2 (ORNL/TM-9593/V6&N2)
NUREG/CR-4219, Vol. 7, No. 1 (ORNL/TM-9593/V7&N1)
NUREG/CR-4219, Vol. 7, No. 2 (ORNL/TM-9593/V7&N2)
NUREG/CR-4219, Vol. 8, No. 1 (ORNL/TM-9593/V8&N1)
NUREG/CR-4219, Vol. 8, No. 2 (ORNL/TM-9593/V8&N2)
NUREG/CR-4219, Vol. 9, No. 1 (ORNL/TM-9593/V9&N1)
NUREG/CR-4219, Vol. 9, No. 2 (ORNL/TM-9593/V9&N2)
NUREG/CR-4219, Vol. 10, No. 1 (ORNL/TM-9593/V10&N1)
NUREG/CR-4219, Vol. 10, No. 2 (ORNL/TM-9593/V10&N2)
NUREG/CR-4219, Vol. 11, No. 1 (ORNL/TM-9593/V11&N1)
NUREG/CR-4219, Vol. 11, No. 2 (ORNL/TM-9593/V11&N2)

Executive Summary

W. E. Pennell

The Heavy-Section Steel Technology (HSST) Program is conducted for the Nuclear Regulatory Commission (NRC) by Oak Ridge National Laboratory (ORNL). The program focus is on the development, validation, and application of technology for the assessment of fracture-prevention margins in commercial nuclear reactor pressure vessels (RPVs). The scope of the project includes development and experimental validation of analysis methods, development of testing techniques and the generation of materials property data, integration of analysis methods and materials data into a comprehensive RPV integrity assessment methodology, technology transfer through participation in national and international codes and standards activities, and support to NRC in the area of RPV integrity assessment. Program activities are structured to provide support to NRC for the resolution of specific RPV licensing issues. Licensing issues directly influenced by this technology include the definition of RPV pressure-temperature (P-T) curves and low-temperature overpressure protection relief valve set points, evaluation of RPV integrity under pressurized-thermal-shock (PTS) transient loading, safety evaluations of RPVs containing material with low-upper-shelf (LUS) Charpy energy, and data transfer from small-scale surveillance specimens for application in RPV structural integrity assessments.

1 Program Management

An NRC letter transmitting a revised Statement of Work for the HSST Program for the FY 1995 through FY 1998 performance period (ending December 31, 1998) was received at ORNL on February 15, 1995. Preparation of the HSST Program 189 was completed, and a preliminary version was forwarded to the NRC HSST Project Manager for review. Negotiations relating to the scope and schedule for work defined in the preliminary 189 were completed. NRC directed the HSST Program to provide background calculations to support the NRC evaluation of information provided by Consumers Power Company for the Palisades Plant.

The HSST Program Manager (PM) gave a number of presentations at technical society meetings and at meetings sponsored by the NRC: a meeting on Constraint Issues in Shallow Crack Behavior sponsored by the Pressure Vessel Research Council, the 22nd Water Reactor Safety Meeting, and the NRC-sponsored Workshop on Constraint Effects in Fracture. The HSST PM briefed members of the NRC research and regulatory staffs on recent findings from the HSST Program investigation of shallow-flaw fracture toughness. An overview of the HSST Program scope, objectives, and current status, together with results from recent research conducted in the program, was presented to L. C. Shao and M. E. Mayfield of NRC in February and to E. S. Beckjord and D. Morrison in March. International interactions took place during this reporting period with personnel from the United Kingdom, Germany, Italy, and the Netherlands.

A meeting was held with Dr. Paul Harrup, Chief Inspector, United Kingdom Nuclear Installation Inspectorate (NII), to discuss results from the HSST biaxial fracture-toughness testing. Large-scale biaxial tests of RPV material are under consideration in the United Kingdom as part of a safety evaluation of RPVs for the MAGNOX reactors. The suggestion was made that the proposed MAGNOX test specimen be analyzed to determine the K_J-ln(R) trajectory for the full range of potential K_{Jc} values. An evaluation of the K_J-ln(R) trajectories can contribute to the overall evaluation of the acceptability of the biaxial test specimen design. An international fracture technology research team visited ORNL for an information interchange in November. The team included representatives from AEA Technology United Kingdom; Gessellschaft fur Anlagen und Reaktorsicherheit, Germany; the Joint Research Center, Netherlands; and the University of Pisa, Italy.

Active participation was maintained in the American Society of Mechanical Engineers (ASME) Sect. XI Working Group on Operating Plant Criteria (WGOPC), the Task Group on Application of NDE (TGANDE) to Plant Operating Criteria, and the Operability Task Group (OTG). HSST Program research results communicated to these groups included test data obtained from material taken from the longitudinal weld of the pressure vessel from a canceled nuclear plant, stress-intensity-factor influence coefficients (SIFICs) for finite-length surface flaws, interim conclusions from an investigation of the influence of metallurgical factors on fracture toughness, effects of biaxial loading on the shallow-flaw fracture toughness of RPV steel, and an estimate the lower-bound shallow-flaw fracture-toughness curve for RPV steel, with biaxial effects adjustments.

During the current reporting period, HSST Program personnel published four NUREG/CR reports, produced four letter reports, and gave five presentations at program

reviews and technical society and NRC-sponsored national and international meetings.

2 Constraint Effects Analytical Development and Validation

The focus of this task is on the development and validation of dual-parameter stress-based correlations to reflect the effect of crack-tip constraint on the fracture toughness of pressure vessel steels. Crack-tip constraint conditions of particular concern in RPV structural integrity evaluations are those associated with shallow flaws and biaxial loading.

Work continued on the development of a material with relevant properties that simulate "prototypical" irradiated RPV base metal properties. This material is required for the fabrication of test specimens that will be used to investigate constraint effects on fracture toughness. Work performed during the last reporting period had shown that not all of the desired characteristics of irradiated material could be attained by heat treatment. Analyses of the cruciform beam specimens, performed using several different stress-strain curve representations, showed the most important parameters to be the yield stress and the postyield strain hardening. The work was subcontracted to a commercial vendor, Lenape Forge, who selected the heat-treating procedure to give a specified room temperature yield strength. Dimensions of the plate segment used were $254 \times 122 \times 23$ cm thick ($100 \times 48 \times 9$-1/8 in.). The vendor normalized the material at 1650°F for 12 h, followed by a water quench and air temper at 825°F for 5 h. A test block was removed from one corner of the plate, and two tensile coupons were machined from this material and tested at room temperature. Tensile properties obtained from these tests were acceptable, and the plate was shipped back to ORNL. A cut-up plan was prepared to yield 40 blanks for machining intermediate-size cruciform specimens. Sufficient additional material remains for fabrication of four additional large-scale specimens.

Investigation of the effect of constraint on failure ductility was continued using specialized tensile fracture ductility specimens. Prior work by researchers at U.S. Steel has shown that (1) ductility measured for plane-strain specimens could be correlated with fracture toughness, K_{Ic}, and (2) the temperature dependence of K_{Ic} and plane-strain failure ductility were similar. The HSST Program is extending this concept to determine if the effect of constraint on the strain field developed in the crack-tip region is a dominant factor in the determination of fracture toughness. A matrix of plane-strain tensile specimens, similar to the specimens used by the U.S. Steel researchers, was designed and fabricated. The specimen had a thin test section integral to two thick end sections. Five of these specimens were tested to failure. The specimens failed by progressive cracking that initiated near the center of the plane-strain section. Axial strain gages "sensed" crack initiation at an axial strain level close to 4%. A detailed elastic-plastic finite-element analysis of the plane-strain tensile specimen showed that because of a gradient in transverse strain across the specimen, true plane-strain conditions were not obtained. A notched-bar specimen design was developed having symmetrical straight-sided transverse slots with a tip radius equal to one-half the slot width. This specimen design produced uniform through-thickness strains across ~90% of the specimen width. A series of 10 of the notched-bar specimens was tested to investigate the effect of notch-tip radius on fracture toughness. All of the specimens were tested at –50°F. Extension of the notch section of the test specimen was measured using clip gages. The total energy density at failure was determined by integrating the area under the load-displacement curve and dividing by the volume of the test ligament. With the exception of the specimens with the smallest tip radius, all of the results gave a near-constant energy density at failure, with a mean value of 169.8 MJ/m^3 (24,623 $in.\text{-}lb/in.^3$). This finding suggests that fracture energy density is a material property, independent of crack-tip radius.

Fractographic analyses of fracture surfaces from the cruciform tests were performed by the University of Maryland under an HSST Program subcontract. These analyses were conducted to determine the location of the cleavage initiation site(s) relative to the fatigue precrack flaw, the amount of ductile tearing preceding cleavage initiation, and the size of the plastic zone. The fracture surface of specimen BB-5 revealed that 0.2 mm of plastic deformation occurred before the cleavage fracture took place. The cleavage initiation site was located very close to the fatigue crack front. Results from specimens tested under different biaxial loading ratios showed that less ductile tearing occurs before cleavage as the level of loading biaxiality increases. Information from this investigation will provide the data required for the validation of crack-tip constraint-effects models and dual-parameter fracture-toughness correlations.

Biaxial loading is present in all loading conditions of concern in RPV integrity evaluations. Results from the development phase of the shallow-flaw biaxial-loading-effects program revealed that biaxial loading had the effect of increasing crack-tip constraint and decreasing the lower-bound fracture toughness of RPV steel. An investigation of the effectiveness of existing dual-parameter fracture-toughness correlations in predicting this result was completed. The J-Q dual-parameter correlation of O'Dowd and Shih and the D-A constraint correction technique of Dodds and Anderson were both evaluated. These constraint

correlation/correction methods are similar in that both are stress based. Fracture is assumed to occur when crack-tip opening mode stresses reach critical values. A higher applied stress-intensity factor (SIF) is required to generate the critical stresses when the crack-tip constraint is relaxed. Application of the D-A correction to the ORNL shallow- and deep-flaw single-edge-notched-beam (SENB) test data was successful. The D-A correction did not, however, predict the observed effects of biaxial loading on fracture toughness. Finite-element analysis showed that out-of-plane far-field stresses had very little effect on in-plane stresses in the crack-tip region. This finding explained the lack of sensitivity of the D-A correlation to out-of-plane biaxial loading effects. The same finite-element analyses showed the width of the crack-tip plastic zone in the direction of crack propagation to be strongly influenced by out-of-plane stresses. The crack-tip-opening displacement (CTOD), which is an established measure of fracture toughness, is directly related to the width of the plastic zone. These facts were used to develop a strain-based dual-parameter fracture-toughness correlation with a function of the plastic zone width as the second parameter. The strain-based dual-parameter fracture-toughness correlation appears to work well when applied to data from the biaxial shallow-flaw fracture-toughness tests.

A series of six development tests on cruciform specimens containing finite-length surface flaws was completed. The objective for these tests was to validate the test specimen design and test procedures required for planned tests of clad cruciform specimens. Characterization tests were performed to develop a reference stress-strain curve for the test specimen material. Finite-element analyses were performed to define the distribution of the applied SIF as a function of angular location around the flaw front. The maximum SIF was found to occur at the deepest point of the flaw under uniaxial loading and at an angle of ~15° from the free surface for 1:1 biaxial loading. Fracture initiation site data were obtained from the test specimen fracture surfaces and found to correspond with the location of the maximum calculated SIFs. The tests confirmed the acceptability of the test specimen design and the test procedure.

3 Evaluation of Cladding Effects

Stainless-steel cladding can act to inhibit the initiation and propagation of cracks from finite-length surface flaws. This property is not reflected in existing RPV structural integrity analysis methods. Objectives for this task are to (1) experimentally determine the influence cladding on crack initiation from finite-length surface flaws in a prototypical RPV biaxial stress field and (2) develop and validate the technology required for incorporation of those effects into RPV structural-integrity assessment methods.

An assessment of the potential significance of incorporating a more refined treatment of cladding effects into RPV structural integrity assessments was completed during this reporting period. The assessment was undertaken to provide the basis for defining the scope and direction of the "cladding effects" research program. The assessment took the form of (1) a review of the treatment of cladding effects in current RPV integrity assessment procedures, (2) an evaluation of the available cladding-effects experimental data to determine if a basis existed for revising the RPV integrity assessment procedures, and (3) an assessment of the potential impact of revising the treatment of cladding effects in those procedures.

The review of the treatment of cladding effects in current RPV integrity assessment procedures focused on the evaluation of PTS loading using the approach defined in NRC Regulatory Guide (RG) 1.154. An important feature of the analysis model in RG 1.154 that may be impacted by cladding issues is the requirement that initial flaws of depth <20% of wall thickness must be assumed to be infinitely long for the purpose of calculating SIFs (K_I). This requirement was imposed in response to results from ORNL thermal-shock experiments on unclad cylinders. Those results indicated that, in the absence of cladding, a semicircular surface flaw subjected to sufficiently severe thermal-shock loading would propagate in surface length to become a very long flaw. Subsequent thermal-shock experiments, performed at ORNL with a large test cylinder, studied the effects of cladding on the crack initiation and propagation behavior of both surface and subclad flaws. The presence of cladding was found to reduce the potential for propagation of both through-clad and subclad flaws. A case exists, therefore, for reevaluation of the shallow-flaw geometry specification contained in RG 1.154.

Recent HSST Program analytical studies considered the effects of cladding on the extension of shallow finite-length cracks in the inner surface of an RPV. The studies demonstrated a close association between the properties of the cladding overlay material, the severity of the thermal-shock loading, and the critical flaw shapes and depths predicted for RPVs subjected to postulated PTS transients. Both ductile tearing and cleavage fracture initiation modes were considered in the studies. Tearing-toughness data for irradiated cladding were obtained from a previously completed ORNL testing program. The analyses showed that the cladding toughness is sufficiently high to prevent tearing. The cleavage fracture initiation study employed three-dimensional (3-D) finite-element analyses to investigate the behavior of an almost semicircular, finite-length flaw under PTS transient loading conditions. The study was structured to determine the effects of using semicircular surface flaws as initial flaws, as opposed to two-dimensional (2-D) flaws,

in a PTS analysis of a clad RPV. Results from this study indicate that semicircular flaws must be deeper than 2-D flaws to produce crack initiation. The predicted impact of using finite-length surface flaws in place of 2-D flaws in an RPV PTS analysis was to reduce the conditional probability of failure between a factor of ≈3 for the more severe thermal transient to a factor of ≈20 for the less severe thermal transient.

Conclusions derived from the evaluations just outlined were that the inclusion of a more refined treatment of cladding effects in RPV integrity assessment procedures was both justified and potentially very significant. An HSST workscope was developed to provide (1) a quantitative description of cladding effects on the fracture behavior of shallow finite-length surface flaws in RPVs and (2) a basis for improved treatment of surface-flaw geometries in fracture assessment procedures applied to PTS and P-T limit transients. Testing and analysis of clad specimens containing finite-length shallow surface cracks will be performed as part of the workscope. The ORNL-developed clad cruciform specimen, which can be loaded either uniaxially or biaxially, will be used in the testing program together with full-scale uniaxial clad-beam specimens. A preliminary test matrix incorporating 28 intermediate- and large-scale cruciform test specimens was defined.

Full-scale clad beam specimens were fabricated from a shell segment of an RPV from a canceled nuclear plant. Test were conducted on specimens containing through-thickness shallow flaws ~11 mm deep. The tips of these flaws were located near the edge of the cladding heat-affected zone in the RPV shell-course longitudinal weld material. Fracture-toughness values ranging from 225 to 393 MPa$\sqrt{m}$ were observed in two tests conducted at –25°C (–13°F). The lower toughness value is compatible with a lower bound to the ORNL shallow-flaw fracture-toughness data from A 533 B plate material. Crack-tip constraint in this test was investigated by means of an elastic-plastic finite-element analysis of the test specimen using a model with a highly refined representation of the crack-tip region. Results from this analysis were interpreted in terms of the J-Q methodology of O'Dowd and Shih and the J-A_{cr} correlation of Dodds and Anderson. The value of Q was determined to be –0.36, indicating a moderate departure from plane-strain constraint conditions. Application of the J-A_{cr} correlation showed the fracture-toughness value obtained from the latest full-scale clad beam test to be compatible with data obtained previously from tests performed on intermediate-scale SENB specimens fabricated from A 533 B RPV steel. Drop-weight tests were performed on plate material from the RPV shell segment to determine the nil-ductility-transition (NDT) temperature for this material. This information is required to set the test temperature for the next set of full-scale clad beam tests in which the crack tip will be located in plate material. NDT for the material was determined to be –34.4°C (–30°F).

The initial phase of an analytical study of clad modeling effects on predictions of cleavage fracture initiation from shallow surface flaws in an RPV subjected to PTS transient loading was completed. Deterministic analyses were performed using the Fracture Analysis of Vessels, Oak Ridge (FAVOR) code. A range of length/depth aspect ratios was considered for the finite-length surface flaws. The severity of the stylized PTS transients used in this study was characterized by the coolant temperature (T_f) at completion of the transient event. A range of RPV internal pressures was investigated. The finite yield strength and the high cleavage fracture toughness of the cladding material were included in the model. It was found that the critical-flaw geometry for crack initiation from a flaw of a given depth was transient-severity dependent. For the most severe transients (lowest T_f values), results for the infinite-length flaws gave the minimum values for critical-flaw depth. With increasing T_f, a crossover point was reached, beyond which the curve for semicircular flaws (aspect ratio = 2) gave the minimum values for critical-flaw depth. The value of T_f corresponding to this crossover point was found to increase with increasing internal pressure.

The HSST Program is participating in an international program for the analysis of results from large-scale fracture-toughness tests. The international program is designated project FALSIRE. In the current reporting period the British spinning cylinder experiment SC-4 was analyzed. In this experiment 40- and 60-mm-long axial semicircular flaws were located in the inner surface of a cylinder fabricated from A 508 class 3 pressure vessel steel. The cylinder inside radius, wall thickness, and length, were 500, 200, and 1300 mm, respectively. Simulated pressure stresses were introduced by centrifugal force in the spinning cylinder. Thermal stresses were introduced by spraying the inner surface of the hot cylinder with cold water. Thermocouples, strain gauges, and alternating-current-potential-drop (ACPD) measured test specimen temperatures, strains, and crack growth throughout the test. The analysis of this experiment was performed by the University of Maryland under an HSST Program subcontract. The analysis predictions of hoop strains on the outer surface of the test specimen were significantly higher than the measured values. The reason for this discrepancy remains uncertain at this time. The analysis predicted tearing initiation at a location on the crack front close to where tearing initiation was observed in the test. Tearing initiation occurred much later in the test than was predicted by the analysis. The SIF required for tearing initiation was, therefore, significantly higher than the predicted value. This

discrepancy is believed to be caused by a reduction in crack-tip constraint and an associated increase in the material fracture toughness.

4 Ductile-to-Cleavage Fracture-Mode Conversion

This task investigates the effect of prior ductile tearing on cleavage-fracture-initiation toughness. Ductile tearing prior to cleavage fracture initiation is frequently observed in tests performed at temperatures corresponding with the lower transition region of the fracture-toughness curve. Evidence exists that ductile tearing may act to increase crack-tip constraint and thereby influence fracture toughness.

Work continued on the characterization of precleavage tearing behavior and development of a fracture-mode-conversion model. The process of precleavage ductile tearing and mode conversion to cleavage is being investigated metallurgically. Material selected for this investigation was weld material taken from the RPV from a canceled nuclear plant. Fracture-toughness tests on this material were performed at the National Institute for Standards and Technology under an HSST Program subcontract. Fracture surfaces from some of these tests showed significant stable tearing prior to final cleavage fracture. Material for the metallurgical investigation was taken from broken Charpy specimens from the circumferential weld of the RPV. Sections were taken to reveal the microstructure. Inclusions present on the face parallel to the fracture surface were examined using a scanning electron microscope (SEM), and quantitative image analysis was used to characterize their size distribution and spacing. The lack of uniformity in particle spacing was apparent in the micrographs. These data suggest that significant errors may be introduced in tearing models that assume a random distribution of particle size, shape, and location.

A fracture prediction model, which includes the effects of precleavage ductile tearing, is being developed for application at transition-region temperatures. In this reporting period an extensive review of published research results on this topic was completed. The void formation and growth model for ductile crack extension emerged from this review as one of the most successful approaches to calculating crack extension resulting from ductile tearing. Application of the void formation and growth model requires that the void volume fraction in the material at the onset of tearing be determined and that a characteristic length be defined. The fractographic investigations outlined above will provide information on the void volume fraction. The characteristic length is related to the spacing between void nucleation centers. Predictions of ductile tearing behavior have been shown to be strongly influenced by the value assumed for the characteristic length. This influence dictates that the crack-tip region of analytical models used for the analysis of ductile tearing must employ extremely small elements. Analysis performed with such a model is computationally intensive and not well suited for direct application in RPV structural integrity assessments. The HSST Program is, therefore, investigating the use of a simpler model in which void growth and coalescence are confined to a narrow material layer that is centered about the macroscopic fracture plane. This development is being conducted by Professor R. Dodds at the University of Illinois with support from an HSST Program subcontract. Professor Dodds' model uses a simplified form of the Gurson material model to predict void growth and element failure. The model is implemented in the WARP-3D computer program. During this report period enhancement and verification of computer software to model ductile crack growth using the G-T model were completed. The WARP-3D software for 3-D nonlinear analyses of fracture mechanics specimens and structural components was installed on an IBM RISC-6000 workstation at ORNL.

5 Fracture Analysis Methods Development and Application

Development of the FAVOR computer program continued. FAVOR is an advanced program for the analysis of RPV failure rates under PTS transient loading. The program is being developed in a manner that will make an executable version of FAVOR available to users without making the source deck available to them. This feature makes configuration control of the program possible.

Support was provided to NRC in preparing a planned revision to RG 1.154. The proposed revision to RG 1.154 permits two analysis methods. One method generates a best-estimate frequency of failure, while the other generates a complete probabilistic risk assessment (PRA). The technology required for the PRA analysis is being developed jointly by the HSST Program at ORNL and NRC-funded programs at the Idaho National Engineering Laboratory and at Sandia National Laboratory. During this report period work was initiated on development of the specialized FAVOR module that will generate data to be used as input into a PRA uncertainty analysis.

A reevaluation of the PTS screening criteria specified in Title 10, Part 50, Sect. 61 of the Code of Federal Regulations (10 CFR 50.61) was completed. This reevaluation was undertaken in support of the RG 1.154 revision. The PTS screening criteria were developed before RG 1.154 existed. The objective for the reevaluation was to

determine how the combination of (1) application of the RG 1.154 analysis methods and (2) use of current input data would influence the selection of screening values of RT_{NDT}. The FAVOR computer program was used to perform the required analysis. As a first step in the reevaluation, the original analyses performed to define the PTS screening criteria were regenerated. This step confirmed consistency in the analytical methods. Modifications defined in items (1) and (2) were then incorporated into the analysis. Screening values of RT_{NDT} obtained from this analysis were very similar to those currently defined in 10 CFR 50.61.

Analyses were performed to investigate the equivalency of the margins specified in the acceptance criteria of ASME Sect. III Appendix G (cleavage fracture) and the draft RG 1.161 (LUS ductile tearing). Results from these analyses were used by NRC to resolve issues raised by the Advisory Committee for Reactor Safeguards relating to the RG 1.161.

6 Material Property Data and Test Methods

This task provides support to the other fracture technology development tasks and performs evaluations of specific RPV materials issues. In this report period exploratory heat treatments were performed to provide Task 2 with RPV material with the yield strength and transition temperature properties characteristic of irradiated RPV steels. Test blocks were quenched from an austenizing temperature of 900°C (1650°F) and tempered at 510°C (950°F). Tensile tests were performed on the material in both the quench-only and the quenched-and-tempered condition. The average yield stress on the material was 1203 MPa (175 ksi) and 972 MPa (141 ksi) in the quench-only and the quenched-and-tempered conditions, respectively. These yield stress values are higher than required for the Task 2 application. Task 3 is performing tests on clad specimens fabricated from shell segments from the RPV from a canceled nuclear plant. Drop-weight tests were performed to determine the NDT for this material. The drop-weight NDT was determined to be –34.4°C (–30°F).

An initial investigation of metallurgical features that could be important to the modeling of tearing-cleavage conversion behavior was completed, and a draft letter report was prepared. This investigation was performed in support of the tearing-cleavage conversion research being conducted in Task 4. The material selected for investigation was weld metal from the RPV from a canceled nuclear plant. Large-scale fracture-toughness specimens with cracks located in this material had exhibited significant ductile crack extension prior to failure by cleavage fracture. The examinations were conducted using a SEM, equipped with a Robinson backscattered electron detector and an image analysis system. Data obtained from these examinations showed the average particle diameter, mean free path, and particle elongation ratios to all have non-Gaussian distributions. An important conclusion from this work was that significant errors could be introduced if tearing-cleavage conversion models are based on an assumed random distribution of particle parameters.

An investigation of the ductile tearing characteristics of seven heats of modified A 302 grade B steel and one early vintage heat of A 533 grade B steel was completed. Both baseline material characterization data and fracture-mechanics-based J-R curve data were generated for these materials. The Charpy V-notch (CVN) upper-shelf energies (USEs) were found to correlate with values of J after 1.5 mm (0.06 in.) of stable crack growth. A letter report documenting results from this investigation was completed.

A review of RPV material fracture-toughness issues that could influence the safety factors applied to low-temperature overpressurization (LTOP) transients was completed, and a letter report was produced. The review considered (1) the relevance of crack pop-in data, (2) the role of cladding as a cleavage crack initiation source, (3) the potential influence of warm prestress (WPS), and (4) new information on the margin between dynamic and static transition temperature curves. Pop-in crack initiation data were found to fit in with the full-cleavage-instability K_{Jc} data, but the pop-in data were at the low end of the K_{Jc} data scatter band. The cladding process was found to have no adverse effect on the transition temperature performance of the underlying base metal. WPS was found to have the potential to increase the in-service fracture toughness of RPV steel such that K_I instability at lower-shelf temperatures could be elevated by a factor of 2 or more. There is, however, no experimental demonstration that the WPS benefits can be retained in materials that are exposed to damage mechanisms such as strain aging or neutron damage. Static to dynamic margins were evaluated using statistical methods to evaluate data scatter in transition temperature tests. The objective of this evaluation was to assess the accuracy of the temperature spread between the lower-bound K_{Ic} and K_{Ia} curves that appear in the ASME Code, Sect. XI, Appendix A. The evaluation, which considered newly developed crack-arrest data, indicated that the temperature offset between the K_{Ic} and K_{Ia} curves is in the 23 to 30°C range, a 10°C difference from the offset used in the ASME Code.

A letter report was completed documenting a plan to investigate the difference between J-R curves developed isothermally vs those developed nonisothermally. The need for the data to be obtained from the planned tests was identified when discrepancies were observed between predicted valued of ductile crack extension and the extent of ductile tearing observed in an HSST Program intermediate pressure vessel test (PTSE-2A).

Dynamic fracture-toughness tests are being performed by the Carderock Division, Naval Surface Warfare Center (CDNSWC) under an HSST Program subcontract. Data from these tests will be used to assess the stability of arrested cracks in a dynamic crack-arrest analysis. In the current reporting period a section of HSST Plate 14 was identified for shipment to CDNSWC, a specimen fabrication plan for the characterization specimens and the dynamic fracture toughness test specimens was completed, specimen grips were procured, Charpy impact specimens were tested, and the reference temperature was obtained as 7°F. Machining of the 1T compact specimens was completed.

7 Integration of Results into a State-of-the-Art Methodology

The primary objective for this task is to extract and interpret fracture technology advances generated in the HSST Program research tasks, in the Heavy-Section Steel Irradiation Program, and other fracture technology research programs and to assemble them into a validated state-of-the-art methodology for assessing the structural integrity of irradiation-embrittled RPVs containing flaws. In addition, this task is responsible for the rapid transfer of fracture technology advances to national consensus codes and standards. Task 7 also provides special technical assistance to NRC for the evaluation and resolution of RPV structural integrity issues.

Research in this task during the current reporting period has focused on development of a methodology for estimating full-constraint K_{Ic} values from small-specimen fracture-toughness data. Transition-range fracture-toughness data from small specimens is characterized by (1) loss of triaxial constraint near the crack tip with a consequent elevation of median fracture toughness (size effect) and (2) significant scatter. Successful application of fracture-toughness data from small specimens to the structural integrity evaluation of large components requires development of methods that account for both of these effects. A three-parameter Weibull fit has been used to represent the statistical variability, and associated size effects, of small-specimen cleavage fracture-toughness data in the transition temperature range. A draft test method, based on Weibull statistical methods, has been developed by the American Society of Testing and Materials (ASTM) Task Group E08.08.03 for evaluating fracture-toughness data for ferritic steels in the transition temperature region. In its present form the draft ASTM test method deals with the data scatter and statistical size-effect issues but does not deal with the constraint-induced size-effect issue. Development carried out in this task combined the validity criterion of ASTM Standard E399 with the Weibull size-effect equation to produce a practical method for calculating K_{Ic} values using small-specimen transition-range data sets. This development has been proposed as an addition to the draft ASTM standard.

Heavy-Section Steel Technology Program Semiannual Progress Report for October 1994–March 1995

1 Program Management*

W. E. Pennell

The Heavy-Section Steel Technology (HSST) Program is conducted for the Nuclear Regulatory Commission (NRC) by Oak Ridge National Laboratory (ORNL). The program focus is on development and validation of technology for the assessment of fracture-prevention margins in commercial nuclear reactor pressure vessels (RPVs).

RPV structural integrity issues of current concern to the NRC are defined in the FY 1994 Statement of Work (SOW) for the HSST Program. Six technical issues are identified in the SOW: (1) crack-tip constraint effects on fracture toughness of RPV materials, (2) effects of stainless steel cladding on the initiation and propagation of shallow surface cracks, (3) ductile-to-cleavage fracture-mode conversion, (4) fracture analysis methods development, (5) materials property data and test methods development, and (6) integration of results from the research programs into a state-of-the-art methodology for RPV structural integrity assessments. The HSST Program is structured to provide the research results required for resolution of these issues. Management direction and control of the program are implemented using a seven-element Level 1 work breakdown structure (WBS) and a linked cost-schedule performance monitoring system. The current HSST Program Level 1 WBS is shown in Fig. 1.1. Each element of the Level 1 WBS represents a separate research or management task with a designated task leader. Within each of the Level 1 WBS elements, a Level 2 WBS defines research subtasks, and a Level 3 WBS defines the individual milestones within a subtask.

Staffing for the research tasks is drawn from the Engineering Technology, Metals and Ceramics, and Computing Applications Divisions at ORNL. Subcontracts with consultants, universities, and other research laboratories are used to gain access to special expertise and capabilities required for certain research tasks. A summary of resources applied to the HSST research tasks during this report period is given in Fig. 1.2.

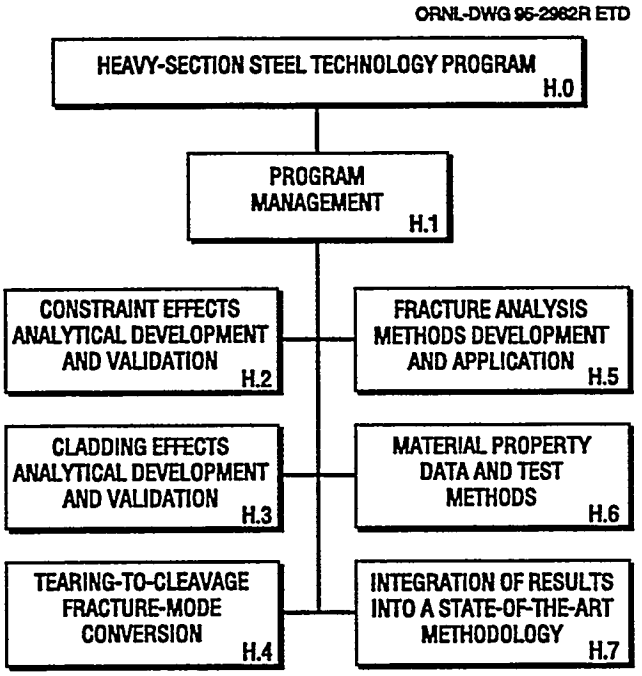

Figure 1.1 Level 1 breakdown structure for HSST Program

An NRC letter transmitting a revised SOW for the HSST Program for the FY1995 through FY 1998 performance period (ending December 31, 1998) was received at ORNL on February 15, 1995. Preparation of the HSST Program 189 was completed, and a preliminary version of the 189 was forwarded to the NRC HSST Project Manager for review. Negotiations relating to the scope and schedule for work defined in the preliminary 189 were completed. Principal results from those negotiations were (1) the definition of adjustments to the Task 5 (Fracture Analysis Methods Development and Application) milestone schedule and (2) a decision to delete all elements of work relating to dynamic crack reinitiation from an arrested cleavage crack.

The HSST Program Manager (PM) gave a number of presentations at technical society meetings and at meetings sponsored by the NRC. A meeting on Constraint Issues in Shallow Crack Behavior was sponsored by the Pressure Vessel Research Council (PVRC) and held at the United

*This report is written in metric units. Conversions from English units for all SI quantities are listed at the end of the report.

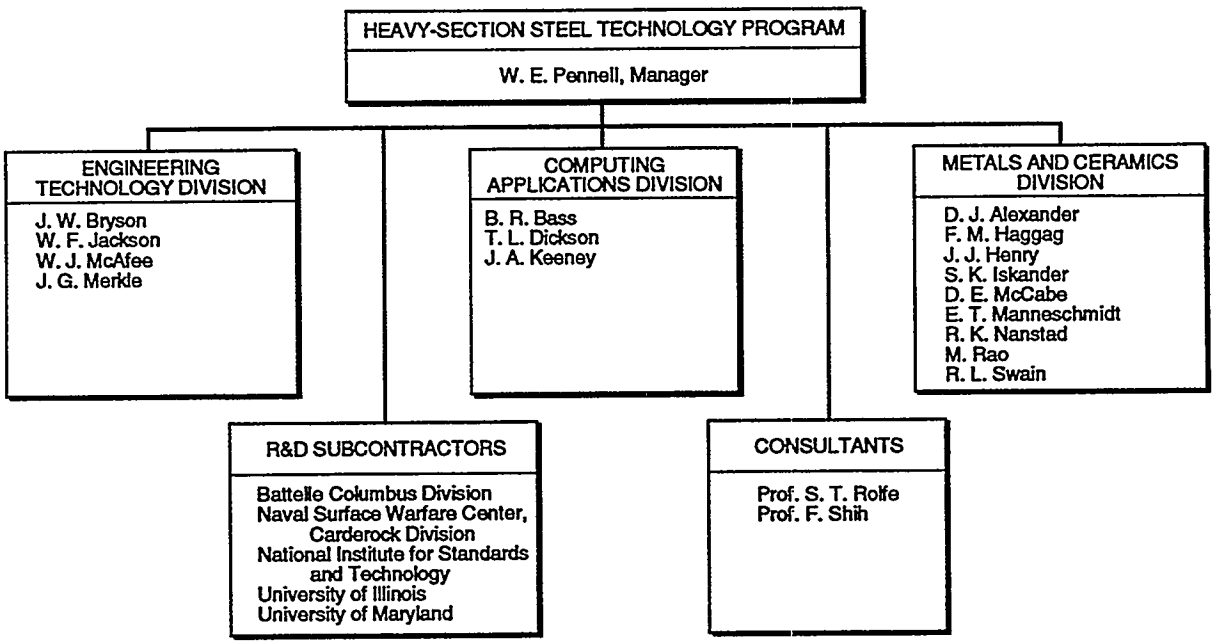

Figure 1.2 Resources applied to HSST Program R&D tasks

Engineering Center in New York, on October 12, 1994. The PVRC meeting provided a forum for the interchange of information on shallow-flaw fracture technology developments from ongoing programs in both the United States and Europe. The meeting was chaired by Dr. J. Barsom. Presentations were given by Dr. Steve Garwood of The Welding Institute (U.K.), J. Smith of the University of Kansas, Dr. S. Bhandari of FRAMATOME (France), Professor F. Shih of Brown University, and the HSST PM. The HSST Program presentation covered (1) normalization of shallow-flaw fracture-toughness data, (2) test observations of biaxial effects on shallow-flaw fracture toughness, and (3) development and validation of dual-parameter fracture-toughness corrections and correlations, with special emphasis on the performance of stress- and strain-based methodologies. The HSST portion of a joint HSST/ Heavy-Section Steel Irradiation paper, entitled "Reactor Vessel Structural Integrity Research," was presented at the 22nd Water Reactor Safety Meeting at the Bethesda Mariott Hotel in Bethesda, Maryland, on October 24, 1994. An NRC-sponsored Workshop on Constraint Effects in Fracture—No. 3 was held at the NRC offices at Two White Flint Building, Rockville, Maryland, on March 28–29, 1995. A presentation entitled "Development of a Strain-Based Dual-Parameter Fracture Toughness Correlation" was given at this meeting. Feedback from the meeting participants provided useful information that will be factored into the future presentation and development of the K_{Jc}-ln(R) dual-parameter fracture-toughness correlation.

The HSST PM met with members of the NRC research and regulatory staffs at the NRC White Flint, Rockville offices on October 25, 1994. The purpose of the meeting was to brief the NRC staff on recent findings from the HSST Program investigation of shallow-flaw fracture toughness. L. C. Shao and M. E. Mayfield visited ORNL on February 16, 1995, for a review of NRC programs. The HSST PM presented an overview of the HSST Program scope, objectives, and current status, together with results from recent research conducted in the program. Of particular interest to the reviewers were data from the ongoing investigation of shallow-flaw and biaxial-loading effects on the fracture toughness of RPV steels, and the dual-parameter constraint-effects correlation derived from those data. These research results are directly relevant to an ongoing NRC evaluation of the adequacy of the pressurized-thermal-shock (PTS) screening criteria incorporated into Title 50, Part 50, Sect. 61, of the Code of Federal Regulations. NRC personnel requested that the HSST Program initiate a high-priority effort to provide NRC with an assessment of the impact of this newly developed technology on the adequacy of the PTS screening criteria. NRC directed the HSST Program to provide background calculations to support the NRC evaluation of information provided by Consumers Power Company for the Palisades Plant. Adjustments were made to the subtasks in Task 5 to accommodate this request. E. S. Beckjord and D. Morrison visited ORNL on March 30, 1995, for a review of NRC programs. The HSST PM gave a brief presentation of the current HSST Program scope and objectives and reviewed ongoing fracture-toughness constraint-effects research activities during a tour of the testing laboratories.

International interactions took place during this reporting period with personnel from the United Kingdom, Germany, Italy, and the Netherlands. Dr. Paul Harrup, Chief Inspector, United Kingdom Nuclear Installation Inspectorate requested a meeting with the HSST PM for discussions on biaxial testing. The meeting took place on October 24, 1994, in conjunction with the Water Reactor Safety Meeting. Dr. Harrup explained that large-scale biaxial tests of RPV material were under consideration in the United Kingdom in support of an evaluation of the safety of the RPVs for the MAGNOX reactors. Dr. Harrup had been briefed on the preliminary results from the HSST biaxial testing program and, in particular, the HSST Program finding that the effects of biaxial loading could be obscured if the test specimen experienced a nonprototypic loss of contained-plasticity prior to fracture. The HSST Program preliminary results were reviewed with Dr. Harrup. The feature of the K_J-ln(R) trajectory corresponding with loss of contained yielding was discussed. The suggestion was made that the proposed MAGNOX test specimen be analyzed to determine the K_J-ln(R) trajectory for the full range of potential K_{Jc} values. An evaluation of the K_J-ln(R) trajectories can contribute to the overall evaluation of the acceptability of the biaxial test specimen design.

Several requests were received from foreign research organizations for members of their research teams to visit ORNL for discussions on the ongoing HSST Program research into shallow flaw and biaxial loading effects on crack-tip constraint and fracture toughness. The requests were combined into a single visit on November 11, 1994. The makeup of the visiting research team was as follows:

Visitor	Organization	Country
Dr. A. Sherry	AEA Technology	United Kingdom
Dr. J. Sievers	Gessellschaft fur Anlagen und Reaktorsicherheit	Germany
Dr. A. McAllister	Joint Research Center	Netherlands
Dr. M. Beghini	University of Pisa	Italy

The HSST PM is an active voting member of the American Society of Mechanical Engineers (ASME) Sect. XI Working Group on Operating Plant Criteria (WGOPC), the Task Group on Application of NDE (TGANDE) to Plant Operating Criteria, and the Operability Task Group (OTG). At the December 1994 meeting of the WGOPC, HSST PM informed the WG members that material taken from the longitudinal weld of the pressure vessel from a canceled nuclear plant had a yield stress in the range 96 ksi $\geq \sigma_y \geq$ 82 ksi. Article G-2000 of ASME Sect. XI states that the reference K_{IR} curve may be used for materials having a yield strength not exceeding 90 ksi if (1) K_{ID} data from at least three heats of material, including the weld metal and heat-affected zone, are not less than K_{IR} and (2) the effects of radiation on the K_{IR} curve are determined for the material. Radiation effects are estimated using the procedure of Article A-4400 of ASME Sect. XI [which incorporates American Society of Testing and Materials (ASTM) E 185] and result in a calculated shift in the reference temperature for nil-ductility transition (RT_{NDT}) for the K_{IR} curve and a determination of the yield stress of the radiated material. It appears that radiation to the end-of-license-period neutron fluence would increase the yield stress of the weld metal from this reactor vessel to a value significantly above 90 ksi. The question therefore arises, "Is an RT_{NDT} adjustment a sufficient adjustment to account for all of the effects of radiation on the K_{IR} curve for a radiated material with a yield stress well in excess of 90 ksi?" The question was referred to the ASME Sect. XI Subgroup on Evaluation Standards.

The WGOPC has initiated work on a proposal to update the stress-intensity factor (SIF) calculation procedure of Appendix G of Sect. XI of the code. The proposed Appendix G update will include the stress-intensity-factor influence coefficients (SIFICs) for finite-length surface flaws developed by the HSST Program. Inclusion of the HSST SIFICs will permit the RPV P-T curve to be defined using a cooldown profile tailored to deal with the "tight-window" areas of the P-T operating envelope. The HSST PM presented a review of the shallow-flaw fracture-toughness data base to the WGOPC. Interim conclusions from the work were presented: (1) the metallurgical factors investigated did not result in data points below the ASME K_{Ic} curve, (2) 1:1 biaxial loading could reduce the shallow-flaw fracture toughness of RPV steel to ~60% of the value obtained from uniaxial single-edge-notch-bend (SENB) tests, and (3) the lower-bound shallow-flaw fracture-toughness curve, with biaxial-effects adjustments, could be marginally lower than the ASME K_{Ic} curve.

The objective for the OTG is to prepare a draft of a proposed code case on the operability of nuclear plants in which (1) nonconforming pipe support conditions have been discovered during operation or (2) an event, not included in the design basis loading, has occurred. These conditions can cause increased loads to be applied to the nozzles of components that interface with the nonconforming piping, including vessel nozzles. The proposed code case is intended to address only conditions that are not covered by existing Sect. XI rules and criteria (e.g., it would *not* apply to the evaluation of flaws). At the December 12, 1994, meeting all remaining issues relating

to the proposed Operability Code Case were resolved with the exception of an NRC objection to the inclusion of a defined period (24 months) for application of the operability criteria. The proposed code case was forwarded to the WGOPC for further action. The TGANDE is exploring means whereby the demonstrated improvement in ultrasonic flaw detection and sizing capabilities can be used to support a case for reducing the postulated flaw size (¼t) which must be used in calculations leading to a definition of the P-T curve for an RPV.

During the current reporting period, HSST Program personnel published three NUREG/CR reports,[1–3] produced six letter reports,[4–9] and gave five presentations at program reviews, technical society meetings, and NRC-sponsored national and international meetings.[10–14]

References

1. J. A. Keeney, B. R. Bass, and W. J. McAfee, Martin Marietta Energy Systems, Inc., Oak Ridge Natl. Lab., "Preliminary Assessment of the Fracture Behavior of Weld Material in Full-Thickness Clad Beams," USNRC Report NUREG/CR-6228 (ORNL/TM-12735), October 1994.*

2. G. R. Irwin and X. Zhang, University of Maryland for Martin Marietta Energy Systems, Inc., Oak Ridge Natl. Lab., "Cleavage Behaviors in Nuclear Vessel Steels," USNRC Report NUREG/CR-6262 (ORNL/Sub/79-7778/11), November 1994.*

3. W. J. McAfee, B. R. Bass, J. W. Bryson, and W. E. Pennell, Martin Marietta Energy Systems, Inc., Oak Ridge Natl. Lab., "Biaxial Loading Effects on Fracture Toughness of Reactor Pressure Vessel Steel," USNRC Report NUREG/CR-6273 (ORNL/TM-12866), March 1995.*

4. D. E. McCabe, Martin Marietta Energy Systems, Inc., Oak Ridge Natl. Lab., "Assessment of Metallurgical Effects that Impact Pressure Vessel Safe Margin Issues," ORNL/NRC/LTR-94-26, October 1994.†

5. J. A. Keeney, Martin Marietta Energy Systems, Inc., Oak Ridge Natl. Lab., "Cleavage Fracture Analyses of the French Clad Beam Experiments-DSR3 and DD2," ORNL/NRC/LTR-94/24, October 1994.†

6. D. E. McCabe, R. K. Nanstad, R. L. Swain, and E. T. Manneschmidt, Martin Marietta Energy Systems, Inc., Oak Ridge Natl. Lab., "Presentation of Preliminary J-R Curve Fracture Toughness Data on Modified A302B Steel," ORNL/NRC/LTR-94/29, October 1994.†

7. J. G. Merkle and T. L. Dickson, Martin Marietta Energy Systems, Inc., Oak Ridge Natl. Lab., "Technical Bases, Comparative Calculations, and Uncertainty Appraisals for Current RPV Code and Regulatory Stress-Intensity-Factor Estimates," ORNL/NRC/LTR-94/32, November 1994.†

8. J. A. Keeney, Martin Marietta Energy Systems, Inc., Oak Ridge Natl. Lab., "Analysis of Multiple Cracks in the NESC-1 Spinning Cylinder Experiment," ORNL/NRC/LTR-94/35, December 1994.†

9. D. E. McCabe, Martin Marietta Energy Systems, Inc., Oak Ridge Natl. Lab., "Experimental Plan for Effects of Thermal Gradients on Fracture Toughness," ORNLNRC/LTR-94/43, December 1994.†

10. W. E. Pennell, "Shallow-Flaw and Biaxial Loading Effects on the Fracture Toughness of Reactor Pressure Vessel Material," presented at the Pressure Vessel Research Council Meeting, New York, October 1994.

11. W. E. Pennell, "Reactor Pressure Vessel Structural Integrity Research," presented at the 22nd Water Reactor Safety Meeting, Bethesda, Md., October 1994.

12. W. E. Pennell, "Biaxial Loading Effects on Fracture Toughness of Reactor Pressure Vessel Material," presented at the FALSIRE II Workshop, Atlanta, November 1994.

13. W. E. Pennell, "Development of a Strain-Based Dual-Parameter Fracture Toughness Correlation," presented at the NRC Workshop on Constraint Effects in Fracture, Rockville, Md., March 1995.

14. W. E. Pennell, "HSST Program Review," presented to L. C. Shao and M. E. Mayfield of the NRC at ORNL, February 1995.

*Available for purchase from the National Technical Information Service, Springfield, VA 22161.
†Available in NRC PDR for inspection and copying for a fee.

2 Constraint Effects Analytical Development and Validation

W. J. McAfee

The purpose of this task is to investigate and quantify the effects of constraint on the cleavage initiation toughness of RPV steels in the lower transition temperature region. The work comprises complementary analytical and experimental efforts. Task 2 is divided into two subtasks: 2.1 Biaxial Loading Effects Validation Testing, (i) Verification Phase Testing and (ii) Analytical Support, and 2.2 Constraint Effects Correlation. Progress during this reporting period for each subtask is discussed below. Additionally, a final summary is provided for a subtask, 2.3 Finite-Length Flaw Behavior, which was active in prior reporting periods.

2.1 Biaxial Loading Effects Validation Testing

2.1.1 Development of Heat-Treating Specification for Surrogate Irradiated Base Material (W. J. McAfee and W. E. Pennell)

Transfer of constraint methodologies and data bases developed under Task 2 to the evaluation of RPV behavior requires demonstration of the developed methodologies for materials whose relevant properties simulate "prototypical" irradiated RPV base metal properties. A desirable goal for the base metal is a temperature at the 68-J Charpy V-notch (CVN) impact energy level ($T_{68\text{-}J}$) greater than 50°C (≈120°F) and a room temperature yield strength, YS_{RT}, in the range of 620 to 690 MPa (90 to 100 ksi). These values are typical for radiation-sensitive RPV steel irradiated to a fluence of 1.5×10^{19} neutrons/cm^2 (>1 MeV). It was concluded from heat-treating work performed during the last reporting period that not all of the above desired parameters could necessarily be attained with heat treating alone. From analyses performed for the cruciform beam specimens using several different stress-strain curve representations, it was determined that the most important parameters were the yield stress and subsequent stress-strain curve shape, that is, the strain-hardening characteristics. Explicit control of the transition temperature was eliminated as a goal. However, from the previous heat-treating work, it was expected that, when the yield stress was increased, the transition temperature would shift toward a higher temperature. It was thus expected that the actual properties (yield stress and transition temperature) would be close to the target values above. The approach chosen was then to select a commercial vendor who would, based on its expertise, select the heat-treating procedure to yield the desired room temperature yield strength.

The job for heat treating Plate 14 was placed with Lenape Forge in West Chester, Pennsylvania. The plate segment used was 254 × 122 × 23 cm thick (100 × 48 × 9-1/8 in.). The 122-cm dimension is in the rolling direction for the parent plate. To achieve essentially a two-dimensional (2-D) heat transfer during the quenching operation, Lenape Forge machined the four edges of the plate smooth and welded a 23-cm square thermal buffer around the outer edge of the plate. To assist Lenape Forge in selecting a heat-treating procedure, the HSST Program provided the complete material certification records on Plate 14 and the results of the prior heat-treating work, that is, the yield strength response to the heat-treating procedures investigated at ORNL. Based primarily on the carbon content, Lenape Forge selected a procedure of normalizing at 1650°F for 12 h, water quenching, and air tempering at 825°F for 5 h. A test block, ~150 by 250 mm square (3 by 5 in.) was removed from one corner of the plate, and two tensile coupons were machined and tested at room temperature by Lenape Forge to verify the results. These tensile results are shown in Table 2.1.

Table 2.1 Summary of tensile properties of commercially heat-treated Plate 14

Property	Test A	Test B
Yield strength (0.2%) off-set, MPa (ksi)	614 (89)	614 (89)
Ultimate strength, MPa (ksi)	765 (111)	772 (112)
Total elongation, %	20	18
Reduction in area, %	63	61

These tensile properties were acceptable, and the plate was shipped back to ORNL. A cut-up plan was prepared to yield 40 of the 240 × 240 × 114 mm (9-1/4 × 9-1/4 × 4-1/2 in.) blanks for machining intermediate-size cruciform specimens and for characterization material. Current matrices require 32 cruciform specimens. Sufficient additional material remains to supply four large-scale specimens that can be machined with the longitudinal beam arms as an integral part of the specimen. Cut-up of the plate and fabrication of 24 intermediate-size beam specimens for the load ratio verification matrix will begin in April. Characterization will also be initiated to determine the nil-ductility transition (NDT) temperature, the temperature at the 68-J CVN impact energy level ($T_{68\text{-}J}$) and the tensile properties at test temperatures of NDT – 30°C, NDT, and NDT + 20°C.

2.1.2 Tests of Tensile Constraint Specimens (W. J. McAfee, W. E. Pennell, and J. W. Bryson)

During the previous reporting period, an effort was initiated to investigate the effect of constraint on failure ductility through use of specialized tensile fracture ductility specimens. The motivation for this activity is based primarily on results by Clausing[1] and Barsom[2] in which it was shown that a relationship exists between failure ductility and fracture toughness. Clausing[1] performed a series of experiments in which he measured the effect of constraint on failure ductility for seven different structural steels. He performed tests at room temperature in which he compared the failure ductility determined from conventional round bar tensile specimens to that from a plane-strain, tensile specimen. He observed that the measured true fracture strain for the round bar specimens was essentially the same for all seven steels that had yield strengths ranging from 270 MPa (39.1 ksi) to 1710 MPa (248 ksi). The failure ductility measured in the plane-strain specimens, that is, the plane-strain ductility, however, was highly dependent on yield strength. The ratio of plane-strain ductility to round bar ductility ranged from 72% for the lowest to 17% for the highest yield strength steels. The ductility measured for the plane-strain specimens correlated directly with that determined for slow-bend CVN specimens of the same steels tested at room temperature. It was concluded that the decrease in CVN toughness with increasing yield strength was a direct consequence of the decrease in plane-strain failure ductility with increasing yield. Barsom[2] extended the work of Clausing to a direct comparison of plane-strain ductility with fracture toughness, K_{Ic}. Fracture toughness was determined for four steels with room temperature yield strengths ranging from 614 MPa (89 ksi) to 1696 MPa (246 ksi). Tests of three-point beam bend specimens were used to determine fracture toughness for these steels over the temperature range from approximately –196°C (–320°F) to –46°C (–50°F). Failure ductility was measured using the same plane-strain specimen configuration as was used by Clausing. It was found that the temperature dependence of K_{Ic} and plane-strain failure ductility were similar. A preliminary relationship was developed whereby fracture toughness, K_{Ic}, was a function of the square root of the yield strength and the square of the plane-strain ductility. This work demonstrated that the strain field developed in the crack-tip region may be a dominant factor in the determination of fracture toughness.

A matrix of plane-strain tensile specimens was designed and fabricated from the Combustion Engineering (CE) plate material for testing. This material was used to take advantage of the data base of uniaxial and biaxial fracture toughness results on this material and to further assist in the interpretation of the load-ratio behavior observed in the biaxial loading development tests. The plane-strain specimen design initially used for the ORNL testing followed the same design as that developed by Clausing and Barsom. The specimen had a thin, short [2-mm-thick by 6.35-mm-long by 25.4-mm-wide (0.080- by 0.25- by 1.0-in.)] test section integral to two thick end sections (see Fig. 2.1). It was thought that the end sections, being much stiffer than the test section, would provide sufficient constraint to yield plane-strain conditions over most of the test section. Two typical specimens of this design are shown in Fig. 2.2. Five

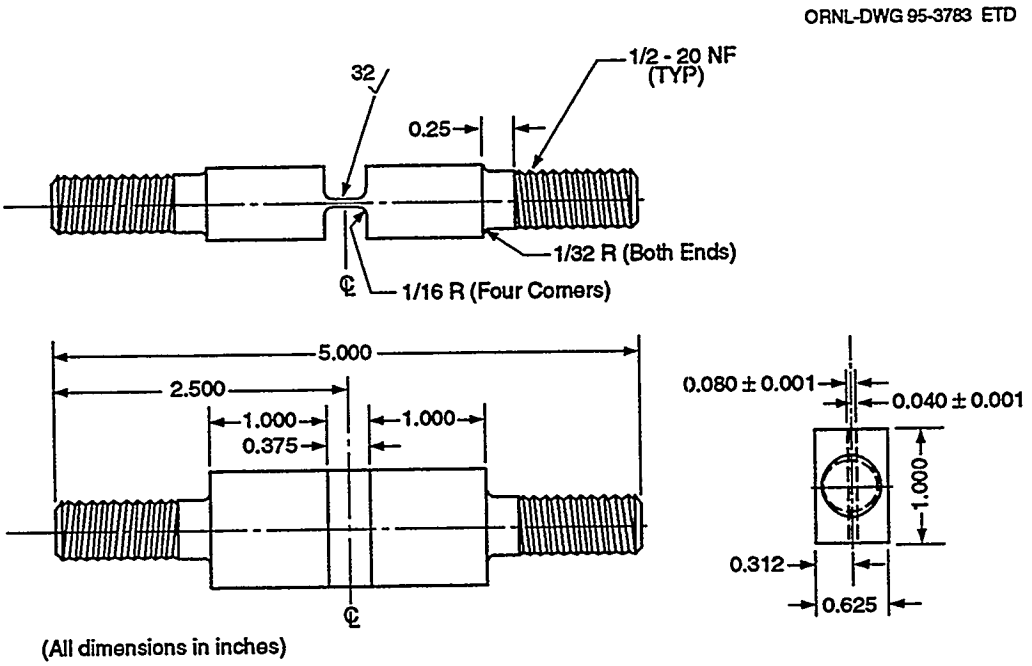

Figure 2.1 Details of initial plane-strain tensile specimen design

ORNL-PHOTO 8261-94

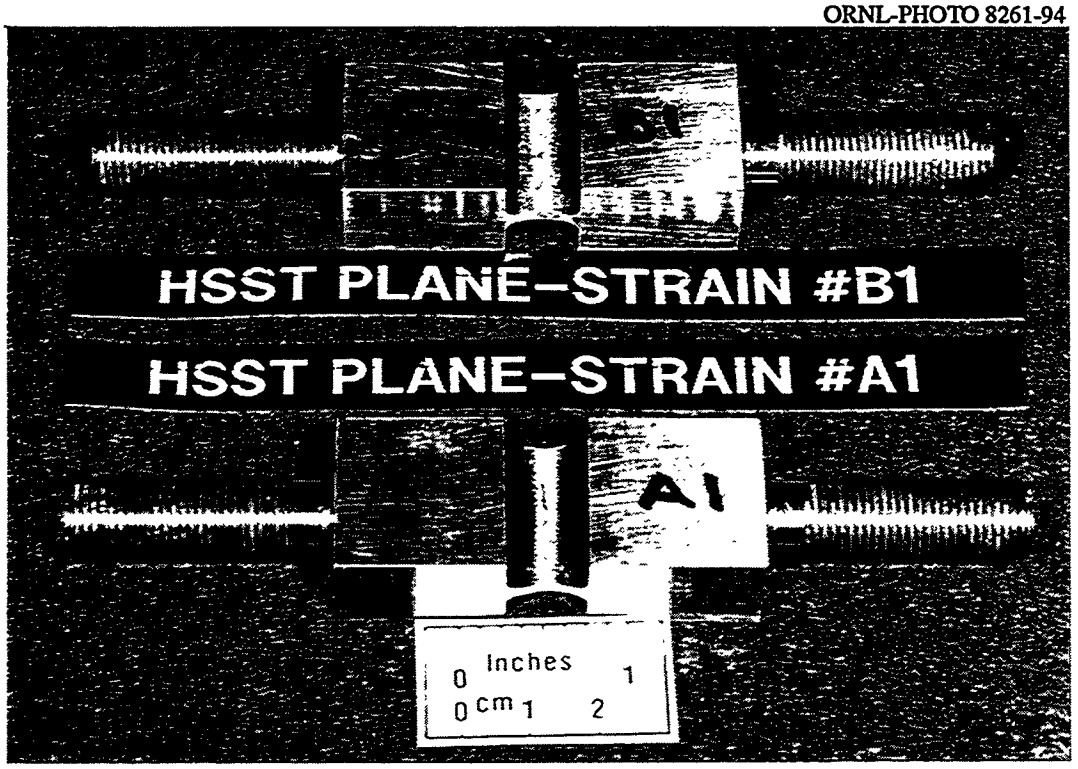

Figure 2.2 Photograph of initial plane-strain tensile specimens showing characteristic failure

of these specimens were fabricated and tested to failure. On the first four specimens, extensiometers were used to measure the axial strain and the thickness reduction strain (henceforth thickness strain) on the test section. Two of these specimens were tested at room temperature and two at –46°C (–50°F). The measured thickness strain was essentially equal to the axial strain providing verification that the test section was under plane-strain conditions (axial strain = thickness strain, transverse strain = 0) at least at the geometric center. This is shown for plane-strain specimen B2 in Fig. 2.3, where, for comparison purposes, a decrease in thickness is plotted as a positive strain. The stress-strain behavior of these specimens was different from that previously obtained using standard round bar tensile specimens (see Fig. 2.4). The upper-lower yield region behavior is not evident in these specimens; there is a smooth transition from the elastic to the plastic regime. Second, the plane-strain specimens exhibited greater strain hardening, reaching a higher ultimate stress but a lower failure strain (~80% of that for the round bar specimen). Third, the specimens failed by progressive cracking that initiated near the center of the plane-strain section. For the room temperature tests, crack initiation was followed by slow ductile crack growth. For the –46°C tests, crack initiation was followed by rapid crack growth from the center region to near the edges of the specimen. The tests were discontinued when a minimum 20% rapid load drop was recorded. The characteristic failure can be seen for the specimens shown in Fig. 2.2.

It was concluded that the extensiometers were insensitive to detection of crack initiation, particularly for through-thickness measurements, and, for these tests performed at –46°C, in-test visual inspection of the specimen surfaces could not be performed to detect crack initiation. Thus, the strain at crack initiation could not be determined accurately from the set-up used. For specimen No. 5 in this series, high-elongation, foil-type strain gages were mounted on the gage length surfaces to measure axial and transverse strain. Two gages were mounted at the center of front and back faces of the test section, oriented in the axial direction for the specimen. Two additional gages were mounted on the front and back faces on the test section transverse centerline (transverse being the direction perpendicular to load application) approximately 1/8 in. off the axial centerline. This specimen was tested at room temperature. The axial strain gages "sensed" crack initiation at an axial strain level near 4% by indicating a relaxation in strain as load continued to increase. This effect is shown in Fig. 2.5, where the reversed direction in strain indicates formation of a transverse through-crack across the axial centerline of the specimen. Comparable behavior was exhibited by the transverse gages except that the load at which strain relaxation commenced was higher than for the axial gages, indicating that crack formation initiated near the center of the test section and grew along a transverse plane in both directions past the transverse gages. Thus, the center axial gages "sensed" the crack before the transverse gages. The magnitude of the transverse strains was approximately –0.8% as compared to

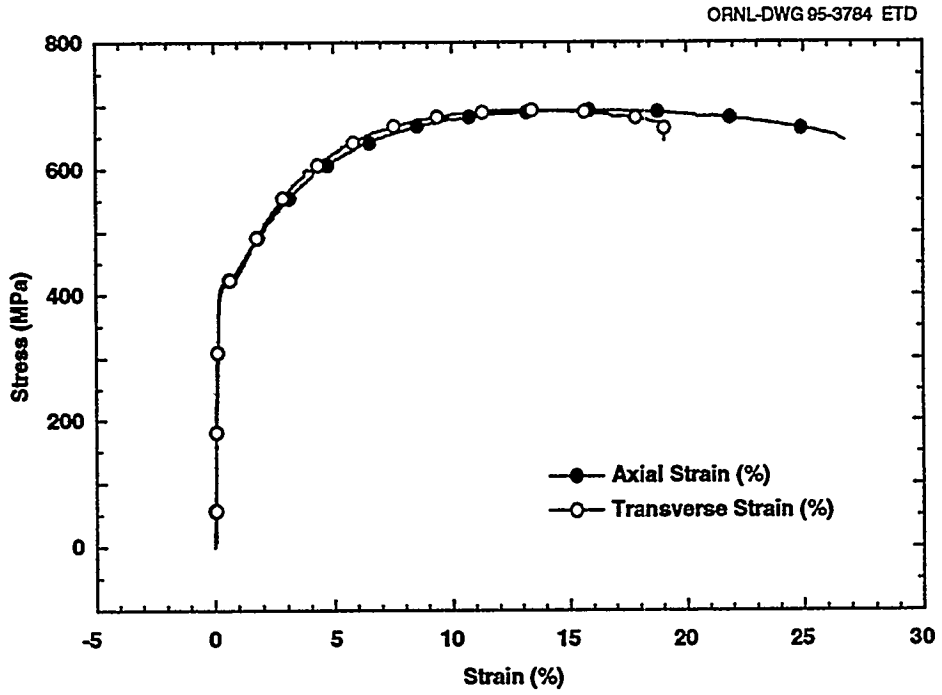

Figure 2.3 Comparison of axial and through-thickness stress-strain behavior for plane-strain specimen B2, CE plate material in as-received condition, –46°C (–50°F)

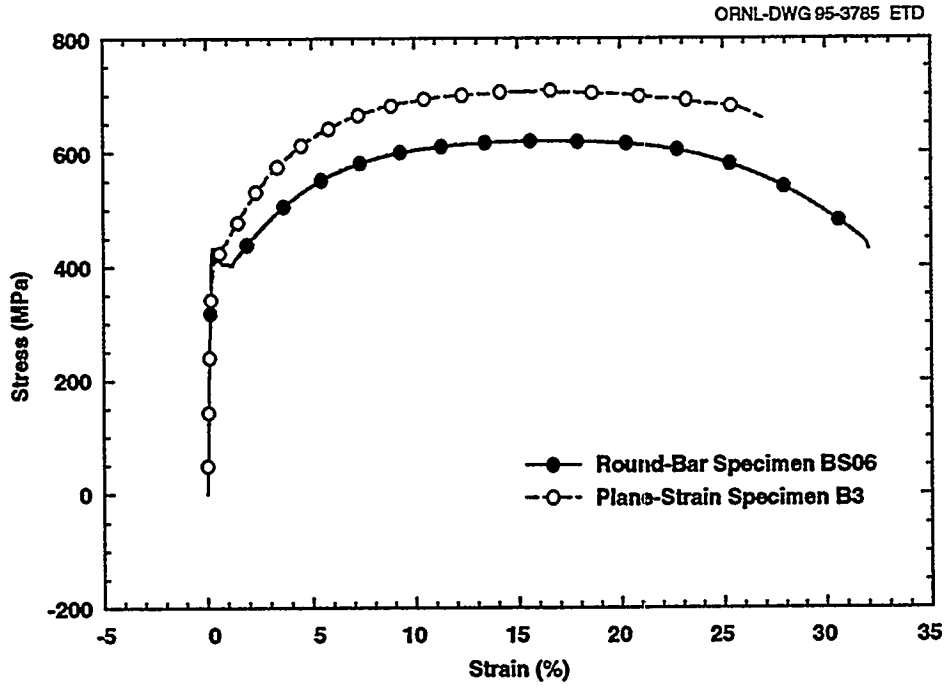

Figure 2.4 Comparison of stress–axial strain curve from standard round bar specimen with typical curve from plane-strain specimen, CE plate material in as-received condition, –46°C (–50°F)

≈4% axial strain. An axial extensiometer was used as the control for monitoring specimen behavior. Thus, the test was continued to load drop, which was well beyond the point of crack initiation. Posttest thickness measurements of the crack surface did not provide an accurate measure of failure ductility because additional distortion of the test section was induced by continued plastic straining beyond the point of crack initiation.

A determination of failure ductility for the five specimens tested was performed as follows. The procedure used in

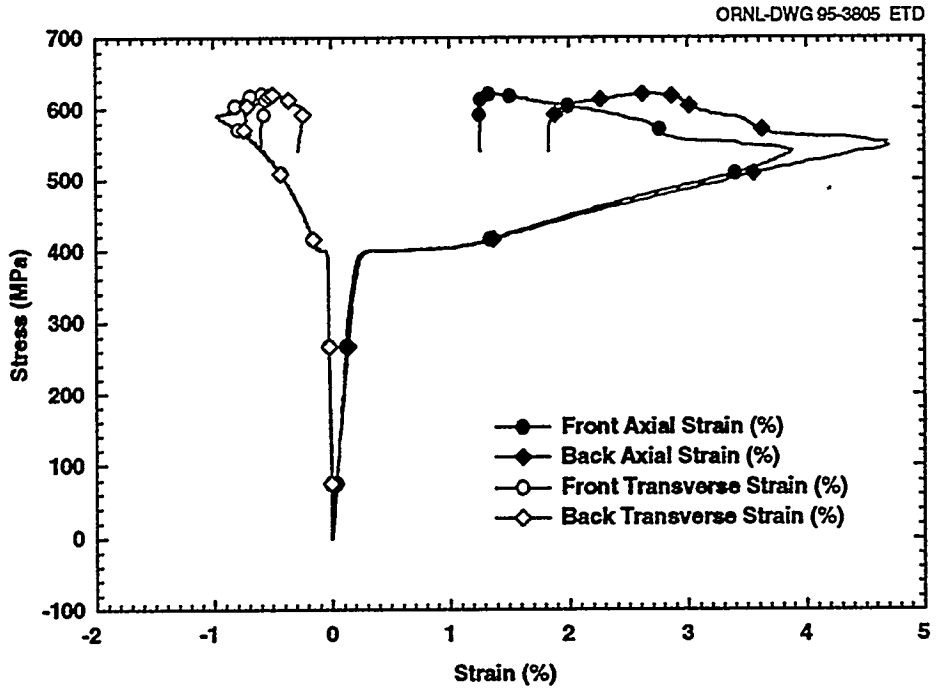

Figure 2.5 Comparison of axial and transverse strains measured using surface-mounted strain gages for test of plane-strain Specimen A3, CE plate material in as-received condition, 23°C (73°F)

performing the plane-strain tests was to continue the test until a rapid drop of load was observed. This load drop was caused by rapid propagation of the initial crack in the transverse direction toward the edges of the test section. It was determined that the point of rapid load drop did not correspond to the point of crack initiation but was more a point of plastic instability. Continuation of the tests beyond the point of crack initiation, because of continued transverse straining, introduced additional distortion in the area of initial crack development. The failure ductility values determined are then more representative of final failure than of crack initiation and should be considered as upper bounds to failure ductility.

Measurements of the test section thickness were made for each specimen. The procedures as set forth in ASTM E8 for determining final thickness[3] could not be used directly because the ligament remaining at each edge of the specimen prevented putting the initial fracture area back together. In addition, the fracture surfaces were characterized by formation of a shear lip along the intersection of the fracture surface with each free surface of the specimen. Generally, these shear lips were of the same orientation at each surface; that is, the specimen failed on a through-thickness diagonal rather than classic cup-cone behavior usually evidenced by round bar tensile specimens. Thickness measurements were then made near the center of the specimen as close to the fracture edge as practicable. A micrometer with conical, radiused measuring tips [0.3175 mm (0.0125 in.)] was used to achieve near point contact with the surface. Several measurements were taken over the center region of the specimen to locate the minimum thickness. The measured thicknesses are given in Table 2.2. Failure ductility was calculated from

$$\varepsilon_f = \ln\left(\frac{t_o}{t_f}\right),$$

where

ε_f = failure ductility,
t_o = initial thickness,
t_f = final thickness.

The average failure ductility at room temperature was 0.621 compared to 0.634 for –46°C (–50°F). When related to the material yield strength, which varies from approximately 393 MPa (57 ksi) at room temperature to approximately 427 MPa (62 ksi) at –46°C, this low dependence of ductility on temperature is consistent with the data of Clausing.[1] His data indicated that failure ductility did not begin to decrease with an increase in yield strength for values of yield strength less than ~586 MPa (85 ksi). The engineering strains at load-drop as measured by the axial extensiometer and as calculated using thickness reduction are also shown in Table 2.1 for comparison.

Table 2.3 shows a comparison of failure ductilities from round bar tensile specimens with those determined from

Table 2.2 Failure ductility determined from plane-strain tensile tests

Specimen	Test temperature (°F)	Final thickness (in.)	$\ln\left(\frac{t_o}{t_f}\right)$	Thickness strain[a] (in./in.)	Axial strain (in./in.)
A1	RT	0.04105	0.667	–0.487	0.297[b]
B1	RT	0.04605	0.552	–0.424	0.313[b]
B2	–50	0.04250	0.633	–0.469	0.267[b]
B3	–50	0.04245	0.634	–0.469	0.269[b]
A3	RT	0.04200	0.644	–0.475	0.285[c]

[a]Determined from final thickness measurements.
[b]Determined using clip gage with 0.25-in. span.
[c]Determined from cross-head displacement.

Table 2.3 Comparison of failure ductility for round bar and plane-strain tensile tests

Test temperature (°F)	Reduction in area	Failure ductility		Ductility ratio of plane-strain/round bar[c]
		Round bar[a]	Plane-strain[b]	
RT	0.691	1.1740	0.621	0.53
–50	0.661	1.0818	0.634	0.59

[a]Round bar: $\varepsilon_f = \ln\left(\frac{1}{1-RA}\right)$.

[b]Plane-strain: $\varepsilon_f = \ln\left(\frac{t_o}{t_f}\right)$.

[c]Ratio = (plane-strain/round bar) ductility.

these plane-strain tests. The round bar ductility was determined from the measured average reduction in area for six specimens tested at each temperature. For all data at both test temperatures, the ratio of plane-strain to round bar ductility is 0.56, indicating a 44% reduction in failure ductility caused by plane-strain conditions.

The failure of these specimens was characterized by development of an initial crack near the axial centerline on the gage section followed by stable crack propagation across the gage section in a plane perpendicular to the loading direction. This did not seem to be consistent with plane-strain conditions being established over most of the gage section, in which case one would expect that crack initiation would lead to rapid crack growth. A detailed elastic-plastic finite-element analysis of the plane-strain tensile specimen was thus performed to determine what the strain conditions were in the test section. The analysis showed that because of a gradient in transverse strain across the specimen, true plane-strain conditions were not obtained or at best would be obtained over a very small area at the center of the specimen. Additional analyses were performed in which the specimen width was increased with other specimen dimensions remaining the same. These analyses showed that a specimen width near 5 cm (2 in.) would be required to establish uniform plane-strain conditions over a large enough area to be able to make reliable failure ductility measurements.

Because the primary purpose of this effort was to evaluate the effect of constraint on failure, an alternate specimen design was developed that provided greater control over constraint conditions. A tensile-type specimen with a notch will have uniform plane-strain conditions at the notch tip for conditions where the notch-tip length is much greater than the notch-tip radius. This type specimen can be obtained conceptually by simply shrinking the gage length of the plane-strain specimen described above until the gage length effectively becomes a notch. Several alternative designs were assessed through use of detailed finite-element analyses. The primary criterion for acceptability was that a near-uniform axial strain field be developed across the entire cross section of the specimen for load levels up to almost the ultimate strength of the material and that plane-strain conditions be established over essentially all the specimen width. It was determined that a specimen

geometry having symmetrical straight-sided flaws with a single ligament and with a flaw-tip radius equal to half the flaw width yielded uniform through-thickness strains across ~90% of the specimen width if the notch-tip radius was in the range of one-half the ligament thickness. This is illustrated in Fig. 2.6, where comparisons are shown between the normal stress and normal strain components developed across a typical specimen ligament with the above dimensions. Note that the strain components at different levels through the thickness of the ligament remain essentially equal up to load levels well beyond material yield, whereas the stress components indicate constant

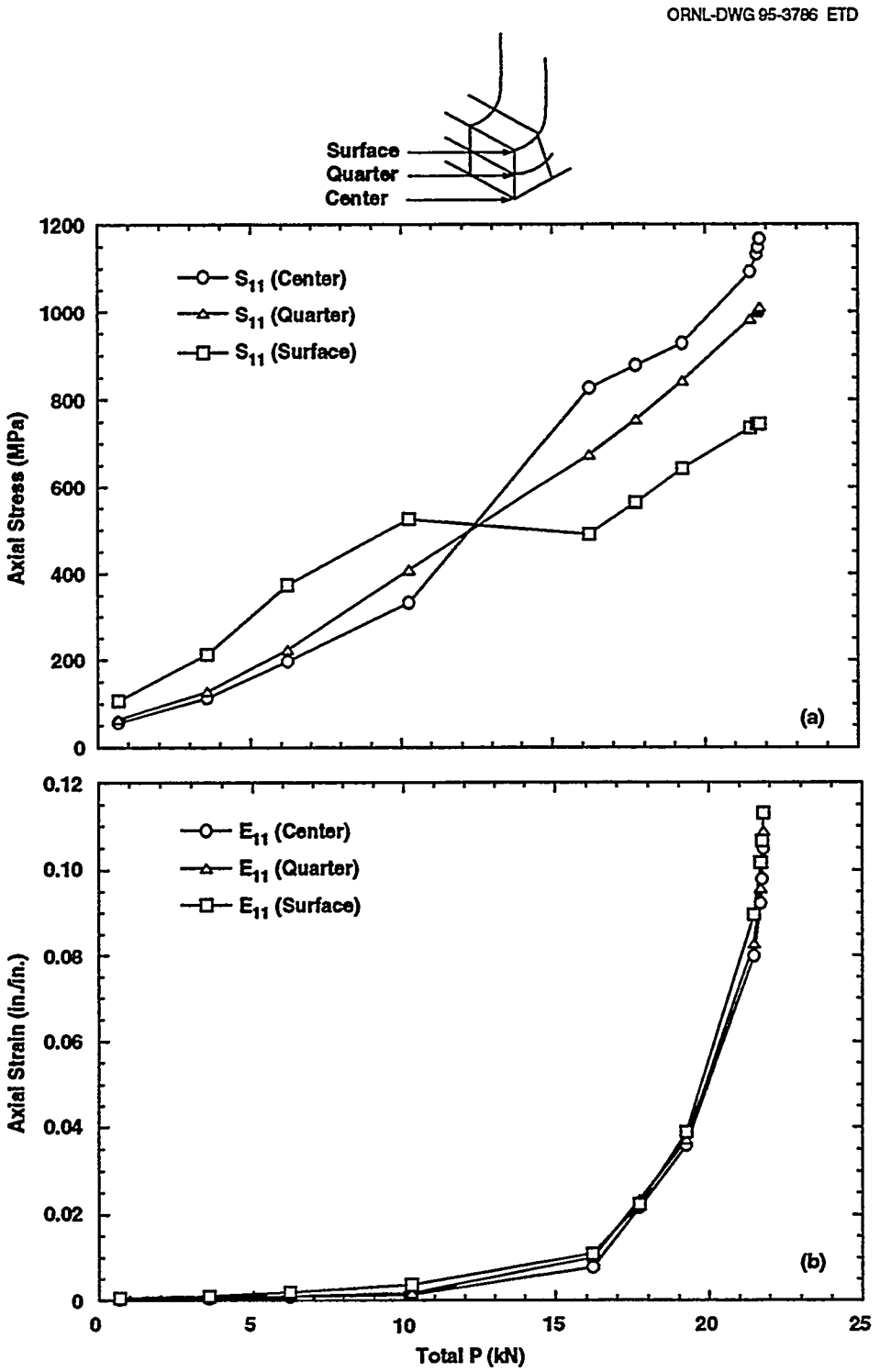

Figure 2.6 Elastic-plastic finite-element analyses showing that specimen with single central ligament with notch-tip radius one-half of ligament thickness resulted in uniform strain distribution across ligament thickness at all load levels

redistribution of stress across the ligament. For cases where the notch-tip radius was less than one-half the ligament thickness, the stresses tended to develop a high peak value at the surface (root of the notch) with a sharp gradient through the ligament thickness. If the radius of the notch tip is of the same general size as the remaining ligament, the sides of the notch remain plane and failure ductility [e.g., crack-tip-opening displacement (CTOD)] may be determined directly from crack-mouth-opening displacement (CMOD) measurements for the notch. Because of the features of this specimen, it has been called a CTOD specimen.

Details of the final specimen design are shown in Fig. 2.7. Note that, because of the thin ligament (weak in bending) for these specimens, a strongback was required to protect the specimen integrity. The strongback was installed after the tensile bar had been final machined but before the notch was machined. This method prevented inadvertent bending,

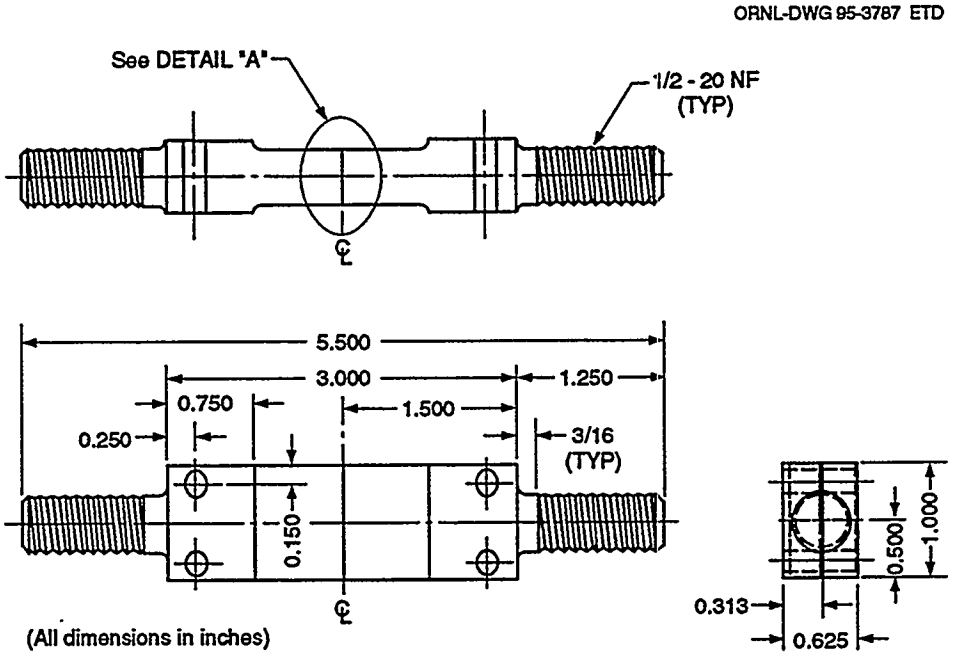

NOTES:
1. All radii must blend without undercuts or steps.
2. Threads must be turned concentric to centerline within 0.001 in. TIR.

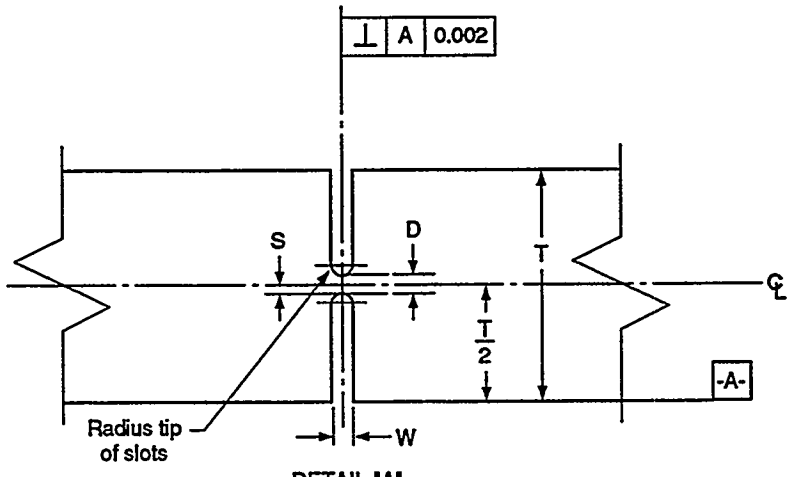

Figure 2.7 Details of CTOD specimen as designed: (*a*) side view and (*b*) top view

breaking, or other distortion of the ligament in subsequent handling (Fig. 2.8). The strongback was removed after the specimen had been mounted in the test machine, all instrumentation installed, and a slight preload applied to maintain geometry. A matrix of ten specimens was defined to investigate the effect of notch-tip radius on fracture toughness. Two specimens were machined with a flat ligament (i.e., no notch-tip radius), both to investigate a specimen design that is somewhat easier to machine and to provide information on a notch-tip radius of infinity. Finite-element analyses of this latter specimen indicated that uniform strain conditions were not achieved across the ligament cross section as was for the notch-tip radius specimens. For this specimen, there was a high peak strain (and stress) at the surface, which makes interpretation of crack initiation conditions difficult. Material from the CE plate was used for all specimens. The matrix of specimens is shown in Table 2.4.

All ten of the specimens were tested at –46°C (–50°F). Measurements of CTOD were made by mounting a clip gage across the notch mouth on each side of the specimen (two clip gages). As discussed previously, the stiffness of the body of the specimen with respect to the test ligament permits use of the CMOD measurement as the notch CTOD. Note that clip gages with a 25.4-mm span were used. In the data reduction, the elastic strain developed in the body of the specimen was subtracted from the measured CMOD, yielding the final CTOD. A summary of the results for the CTOD is shown in Table 2.3. The CTOD values are the average of the front and back surface clip gages at the point of specimen failure. The fracture energy density (E_f) was calculated from

$$E_f = \frac{\int P d\delta}{W(2R)^2}$$

ORNL-PHOTO 641-96

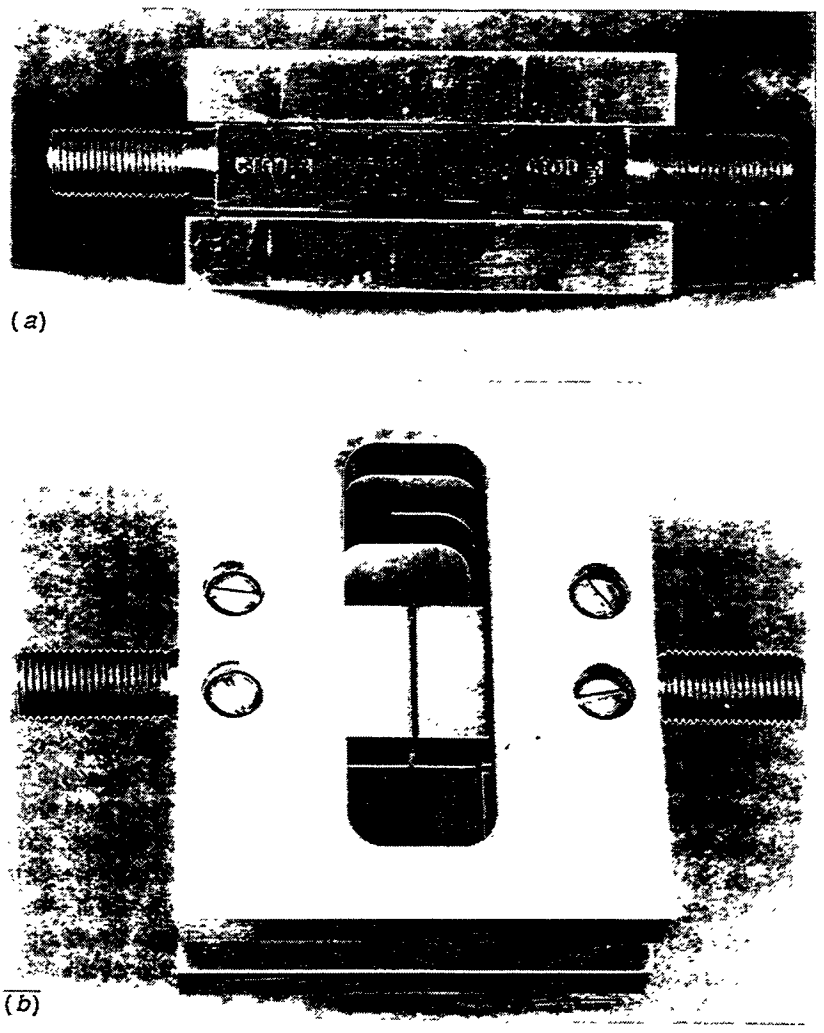

(a)

(b)

Figure 2.8 Typical CTOD specimen in final configuration showing machined slot and strongback used to prevent bending during handling: (*a*) side view and (*b*) top view

Table 2.4 Summary of CTOD specimen results

Specimen	Radius-R [mm (in.)]	$2R = L_t$ [mm (in.)][a]	CTOD [mm (in.)]	Fracture energy density [MJ/m^3 (in.-lb/in.^{3})]
04	0.127 (0.005)	0.254 (0.010)	0.000028 (0.00110)	101.1 (14,663)
05	0.127 (0.005)	0.254 (0.010)	0.000262 (0.00094)	37.4 (5,418)
06	0.254 (0.010)	0.508 (0.020)	0.000104 (0.00409)	150.0 (21,749)
07	0.254 (0.010)	0.508 (0.020)	0.000090 (0.00352)	155.5 (22,552)
01	0.508 (0.020)	1.016 (0.040)	0.000195 (0.00766)	165.9 (24,056)
02	0.508 (0.020)	1.016 (0.040)	0.000221 (0.00869)	195.4 (28,345)
03	0.508 (0.020)	1.016 (0.040)	0.000196 (0.00773)	163.6 (23,732)
08	1.270 (0.050)	2.540 (0.100)	0.000568 (0.02247)	188.2 (27,301)
09	NA	1.016 (0.040)	0.000352 (0.01387)	244.0 (35,385)
10	NA	1.016 (0.040)	0.000279 (0.01098)	182.5 (26,469)

[a] L_t = ligament thickness

where

E_f = fracture energy density,
$\int P d\delta$ = area under load–CTOD curve,
W = width of specimen ligament (nominally 1 in.),
R = notch-tip radius (2R is ligament length and thickness).

For specimens CTOD01 through CTOD08, this is an approximation because the cross section of the ligament is not uniform. However, for purposes of these preliminary comparisons, it is deemed sufficiently accurate. Specimens CTOD04 and CTOD05, which had a notch-tip radius of 0.127 mm (0.005 in.) did not appear to yield reliable results. Posttest examination would lead to the conclusion that there were minor imperfections in the machined notch. Additionally, the magnitude of the CTOD values measured were at the low end of the sensitivity range for the clip gages used. Thus, the results for CTOD04 and CTOD05 should be viewed with some caution. Specimen CTOD03 was machined with the ligament slightly off the specimen longitudinal centerline; the ligament did not lie on the plane of symmetry for the specimen. During testing, this specimen was subjected to slight bending, as would be expected, although the test results were consistent with other specimens of the same notch-tip radius. The CTOD results for all specimens are shown in Fig. 2.9 where $(CTOD)^{0.5}$ has been plotted as a function of $(\text{notch-tip radius})^{0.5}$. Note that the notch-tip radius is simply one-half the ligament thickness. Effectively, all the data lie on a straight line having a slope of 0.02388 (dimensionless). Because fracture toughness is proportional to $(CTOD)^{0.5}$, Fig. 2.9 may be interpreted as a graphical relationship between notch-tip radius and fracture toughness. This presentation of the data is consistent with the premise developed by Wilshaw et al.[4] that fracture toughness is linearly related to notch-tip radius over a range of radius sizes. Wilshaw additionally observed that there is a radius size below which there is no additional reduction in toughness. Obviously, the radius sizes for these tests did not reach such a lower limit. The total energy density at failure was calculated by simply integrating the area under the load-CTOD curve and dividing by the volume of the test ligament. The thickness of the ligament was taken as the minimum, as-machined dimension; the volume of the radius between the ligament and specimen body was ignored. These results are shown in Fig. 2.10 and include the data for specimens with uniform ligament thickness. With the exception of the specimens with the smallest tip radius, all of the results represent a near-constant energy density at failure with a mean value of 169.8 MJ/m^3 (24,623 in.-lb/in.^{3}). The preliminary conclusion is that directly measured fracture energy is a material property independent of crack-tip radius. This may permit estimation of fracture toughness directly from this type specimen. More data and analyses are needed, and additional tests are planned. Attention will be directed at specimens with smaller tip radii and at limited specimens tested at different temperatures to determine if the fracture energy follows the conventional fracture-toughness transition curve.

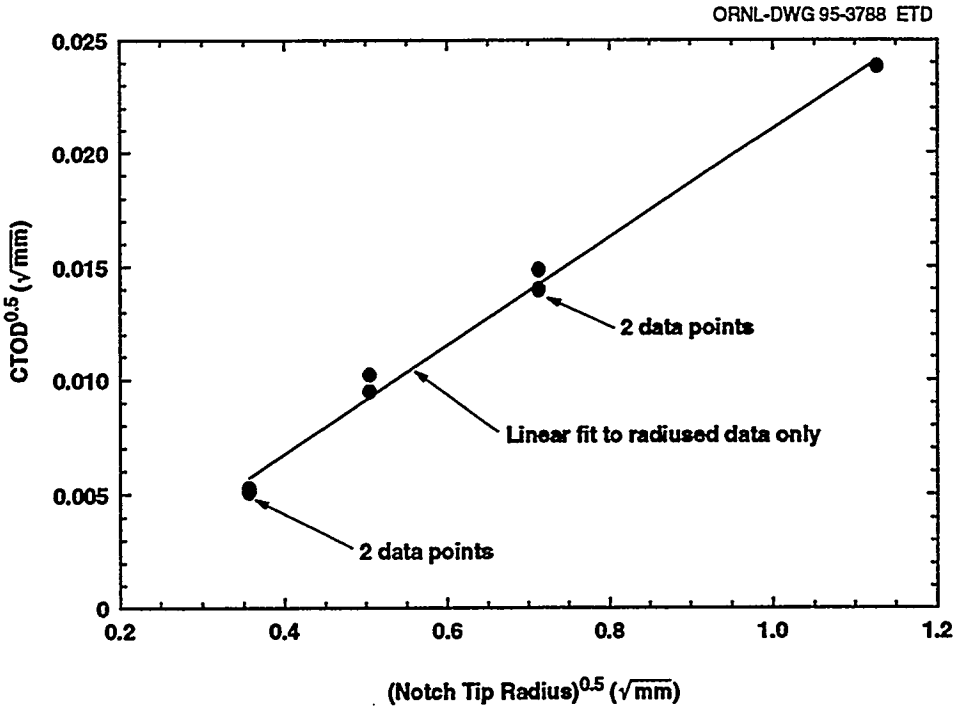

Figure 2.9 CTOD as function of notch-tip radius as measured on ten CTOD fracture energy specimens

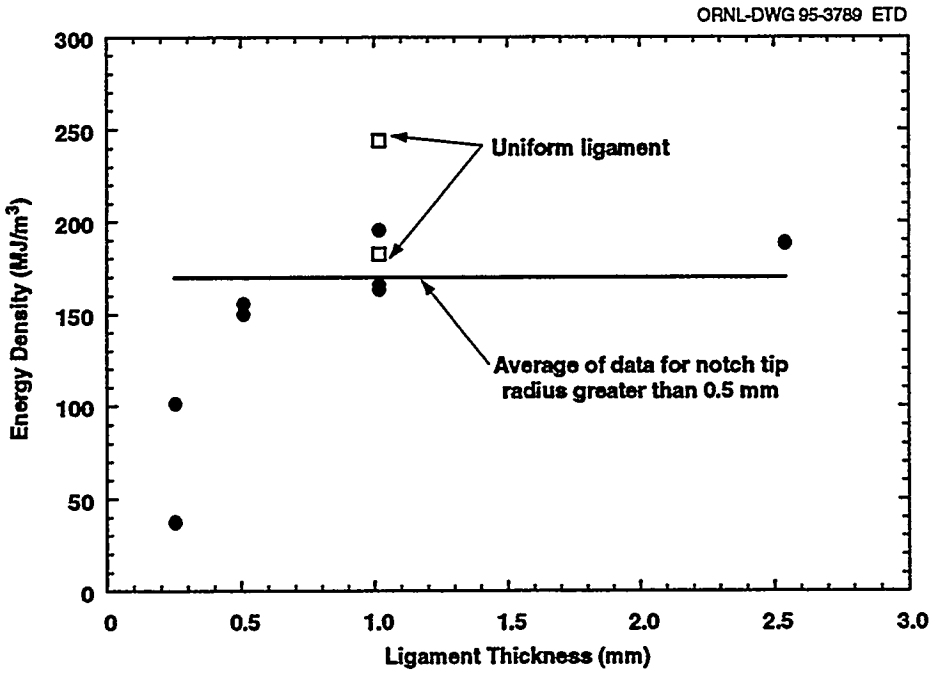

Figure 2.10 Fracture energy density as function of notch-tip radius as measured on ten CTOD fracture energy specimens

2.1.3 Metallographic Examination of Cruciform Specimen Fracture Surfaces

(W. J. McAfee, B. R. Bass, and J. W. Bryson, ORNL; W. L. Fourney and X. J. Zhang, University of Maryland)

Fractographic analysis of the fracture surfaces from the cruciform tests provide additional information relative to the effect of biaxial loading on fracture toughness. The types of information that are of value include location of the cleavage initiation site(s) relative to the fatigue precrack flaw, the amount of ductile tearing preceding cleavage initiation, and, if possible, the size of the plastic zone developed. This information will provide additional input for an interpretation of the test results and for the development and validation of analytical models. Four fracture surfaces were selected from the tests performed in the development phase. These specimens were BB-5, -7, -10, and -11 and represent the full range of biaxial load ratios and fracture behavior. The fractographic examinations are being performed by the Mechanical Engineering Department at the University of Maryland.

Optical examination of the fracture surface for specimen BB-10 revealed two main cleavage initiation sites. The remaining specimens displayed only one initiation site each. The fracture surface of specimen BB-5 revealed that a substantial amount of plastic deformation, represented by a stretch and ductile zone of 0.2 mm, occurred before the cleavage fracture took place. The main cleavage initiation region was located ~2.1 mm from the centerline of the specimen and was very close to the fatigue crack front. The width of the fatigue precrack for this specimen was about 2.6 mm. Distinct cleavage propagation lines were observed radiating from the initiation site. The distance between the initiation site and the edge of the ductile fracture zone was ~0.12 mm. Enlargement of the initiation area revealed that the initiation site was close to a small particle clump that may have contributed to triggering initiation although the toughness value obtained was consistent with the other specimen in this series tested under 0.6:1 biaxial loading.

Measurements of the length of ductile crack extension, Δa, prior to cleavage initiation for each specimen are shown in Table 2.5. The results shown are consistent in that a higher degree of constraint results in less ductile tearing prior to cleavage. Also, the measured fracture toughness correlates directly with the measured ductile tearing. This finding tends to substantiate the use of a dual-parameter stress-strain-based fracture methodology.

The fracture surfaces will next be examined using scanning electron microscopy (SEM) to perform detailed analysis of the fracture zones. Each surface will be sectioned to remove a sample small enough to fit into the SEM. Sectioning will be performed along lines ~15 mm (0.6 in.) each side of the identified initiation site. Examination of these small coupons using the SEM will permit better definition of the fracture processes present in the initiation site region. The exposed cross sections will also provide surfaces from which definition of plastic zone development may be possible. The exact procedures for this investigation have not been determined as yet.

Table 2.5 Summary of results from fracture surface examinations

Specimen	Load ratio	K_{Jc} (ksi $\sqrt{in.}$)	Ductile crack extension, Δa (μm)
BB-11	0:1	191	160–260
BB-5	0.6:1	175	100–160
BB-7	1:1	215	120–200
BB-10	1:1	109	10–40

2.2 Analyses and Evaluation of Constraint Models

(W. J. McAfee, B. R. Bass, W. E. Pennell, and J. W. Bryson)

During this reporting period, a NUREG report[5] was published summarizing the tests and analysis results for the development phase of the biaxial beam test program, providing an assessment of the capability of existing dual-parameter constraint methodologies in interpreting the results observed, and providing a preliminary alternative dual-parameter model that overcomes shortcomings apparent in the existing models. The interested reader is referred to that report for full details of these results. The following is a brief summary of the findings and conclusions relative to the evaluation of dual-parameter methodologies.

The tests in the HSST development phase, biaxial loading effects on fracture toughness in the transition temperature region, were carried out using cruciform specimens fabricated from a single heat of A 533 B pressure vessel steel. Tests were performed for conditions of uniaxial loading (transverse-to-longitudinal load ratio of 0:1) and for biaxial 0.6:1 and 1:1 loading ratios. The resulting fracture-toughness data are shown in Fig. 2.11 as a function of the biaxiality loading ratio. The plot indicates a pronounced reduction in the lower-bound shallow-crack fracture toughness as the biaxiality ratio is varied from 0:1 to 1:1. As the biaxiality ratio approaches 1:1, the lower bound to the

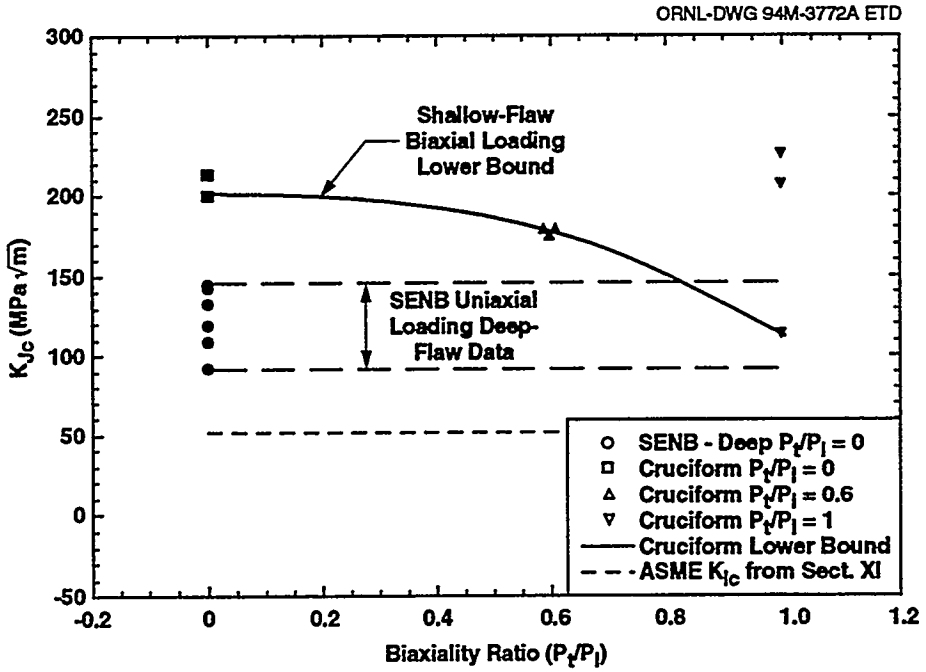

Figure 2.11 Reduction in lower-bound toughness values as function of biaxiality ratio for single heat of A 533 B pressure vessel steel

shallow-crack toughness approaches that derived from SENB uniaxial deep-crack data[6] for A 533 B pressure vessel steel. The limited biaxial-toughness data base, depicted in Fig. 2.11, provides evidence of a significant biaxial loading effect on cleavage fracture toughness in the transition temperature region for RPV steels.

2.2.1 Evaluation of Stress-Based Methodologies

Two stress-based dual-parameter methodologies that are being investigated within the HSST Program are the J-Q methodology of O'Dowd and Shih,[7–9] combined with the RKR fracture criteria,[10] and the Dodds-Anderson (D-A) constraint correction technique.[11–13] These two fracture methodologies share the common feature of utilizing the effects of crack-tip constraint on in-plane stresses at the crack tip to infer the effect of constraint on fracture toughness. In Ref. 14, both the J-Q methodology and the D-A constraint scaling model were applied to shallow- and deep-crack SENB specimen results[6] and to uniaxially and biaxially loaded cruciform specimens. Analysis results from these applications indicated that both methodologies could be used successfully to interpret experimental data from the shallow- and deep-crack uniaxially loaded SENB specimen tests. Figures 2.12 and 2.13 summarize an application of the D-A constraint correction model to fracture-toughness data from the HSST shallow-crack SENB program. In Fig. 2.12, the shallow- and deep-crack toughness data are plotted as a function of crack depth for a normalized temperature range of –10 to –25°C. As expected in a low-constraint geometry, Fig. 2.12 shows both an increase in the mean fracture-toughness value and in data scatter from the shallow-crack specimens when compared with the deep-crack specimens. The corresponding toughness data, following application of the D-A correction model, are shown in Fig. 2.13. The regression analysis shown in Fig. 2.13 implies that the corrected toughness data are essentially independent of crack depth.

When the J-Q and D-A constraint methodologies were applied to the uniaxially and biaxially loaded cruciform specimens, the results were considerably more difficult to interpret than those of the SENB specimens. The uniaxially loaded cruciform specimen analyzed in Ref. 14 failed at a sufficiently high load that the far-field bending stress began to impinge on the near-tip stress fields, a factor that rendered the J-Q results inconclusive. A modified D-A scaling procedure employed in Ref. 14 resulted in a J_{FB}/J_0 ratio (J_{FB} = J finite body; J_0 = J infinite body) for biaxial 0.6:1 loading that was ~25% greater than that for uniaxial loading. This result implies a greater constraint loss with concomitant increased toughness for biaxial 0.6:1 loading than for uniaxial loading, which is inconsistent with toughness results determined from the experimental data. However, these results from the D-A approach were obtained using an engineering model developed by Dodds et al.[13] that approximates the scaling factors (J_{FB}/J_0) of the original D-A model. In the original formulation,[12] toughness data are adjusted to small-scale yielding (SSY) values based on ratios of areas (or volumes) within principal stress contours around the crack tip. The

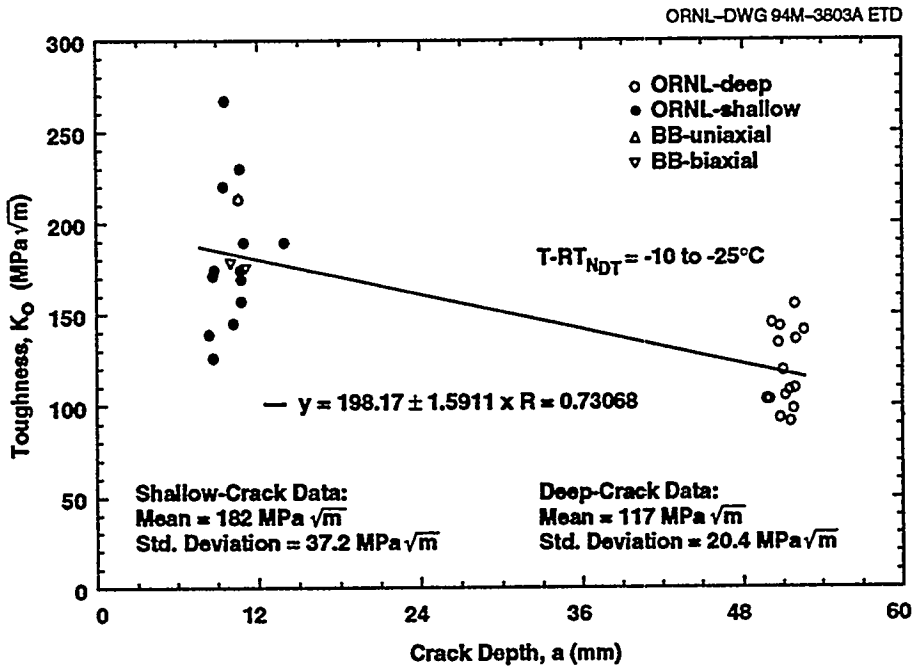

Figure 2.12 Mean value and scatter in toughness data that increase for shallow-flaw specimens as compared to deep-flaw specimens for same material and test conditions

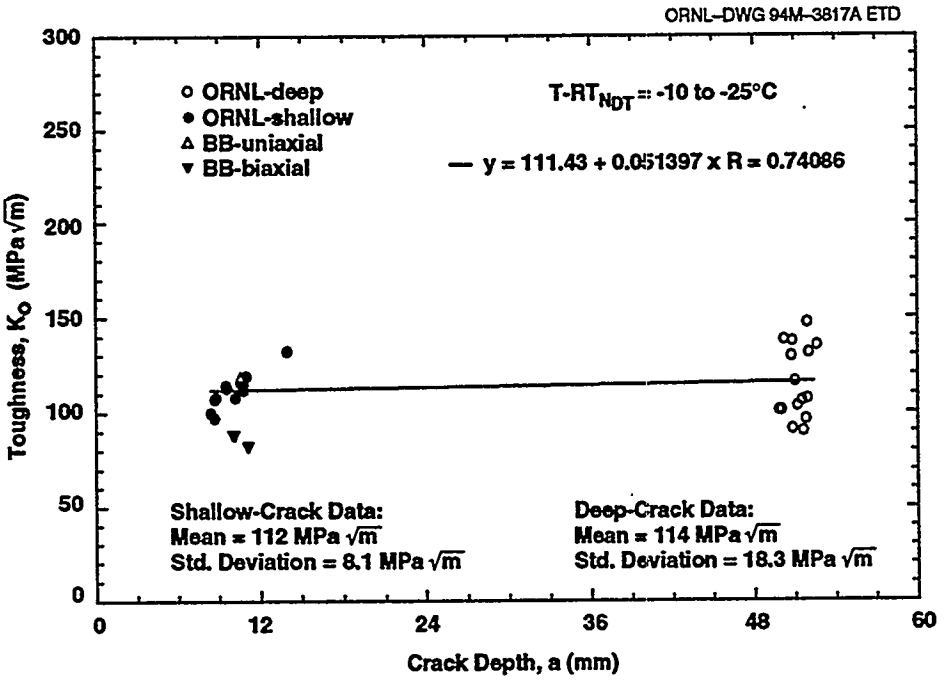

Figure 2.13 D-A constraint adjustment procedure applied to SENB data that predicts no change in toughness with flaw crack

engineering model applied to the cruciform specimens approximates these ratios using the stress distribution in the crack plane directly ahead of the crack tip that draws upon a J-Q description of the crack-tip fields. Thus, the engineering model assumes that the stressed areas are similarly shaped, allowing the comparison of distances ahead of the crack rather than areas (or volumes). In Ref. 14, the possibility was raised that the engineering model may not be suitable for the cruciform specimen that possesses 3-D stress fields that vary through the thickness of the test section.

In an effort to resolve these uncertainties, additional 3-D finite-element analyses were performed to further assess the details of the D-A scaling procedure and to evaluate the stress and strain fields developed in the region of the crack tip for cases of uniaxial and biaxial loading. As reported in Ref. 5, the D-A methodology predicts a small biaxial effect on constraint. Using the D-A methodology, the predicted failure J for biaxial loading is essentially equal to the measured value for uniaxial loading. The D-A methodology does not predict the possibility for the low toughness value observed in the 1:1 biaxial test (see Fig. 2.11). The conclusion reached was that the D-A and J-Q methodologies applied to the in-plane stress fields at the crack tip do not adequately describe the effect of biaxial loading on fracture toughness.

To better understand these results, additional analyses were performed on the cruciform specimen to clarify the relationship between biaxial loading ratio and development of the stress fields and plastic zone in the near crack-tip region. For comparison purposes, the stress components were determined at a nodal location (N-5006) at a distance r = 2.54 mm (0.1 in.) from the crack tip. Analysis results indicated that the point located at r = 2.54 mm (0.1 in.) experienced yielding at different load levels, depending on the out-of-plane loading ratio.

Relevant stress components (Cartesian normal stresses, hydrostatic stress, and Mises effective stress) are shown in Figs. 2.14–2.16 to provide a better understanding of plastic zone development in the cruciform specimen. The Cartesian normal stress components (s_{11}, s_{22}, s_{33}) represent good approximations to the magnitude of the principal stress values (the shear stress components are small). Applications of increasing ratios for out-of-plane to in-plane loading are accompanied by substantial elevations of the hydrostatic stress and the out-of-plane normal stress (s_{11}). In contrast, the in-plane normal stress components (s_{22}, s_{33}) do not change a great deal as a function of load ratio, except at the highest load levels.

Development of the plastic zone can be correlated with the applied biaxial loading ratio and resultant out-of-plane normal stress component (s_{11}). For the uniaxial (0:1) loading case (Fig. 2.14), the out-of-plane component is well below the two in-plane components, and the onset of yielding occurs at a relatively low applied load. When the out-of-plane load is increased to a 0.6:1 ratio (Fig. 2.15), the out-of-plane component roughly tracks the lower in-plane component up to 580 kN (130 kip) and then begins to increase at a substantially higher rate. The effect of the 0.6:1 load ratio is to delay the onset of yielding to a much higher load [~756 kN (170 kip)] than was observed in the 0:1 load case.

For the 1:1 load case (Fig. 2.16), the out-of-plane component (s_{11}) turns up and essentially tracks the opening-mode (maximum) stress component (s_{33}) beyond the 667-kN (150-kip) load level. Also, the normal stress components (s_{11}, s_{33}) and the hydrostatic stress are observed to

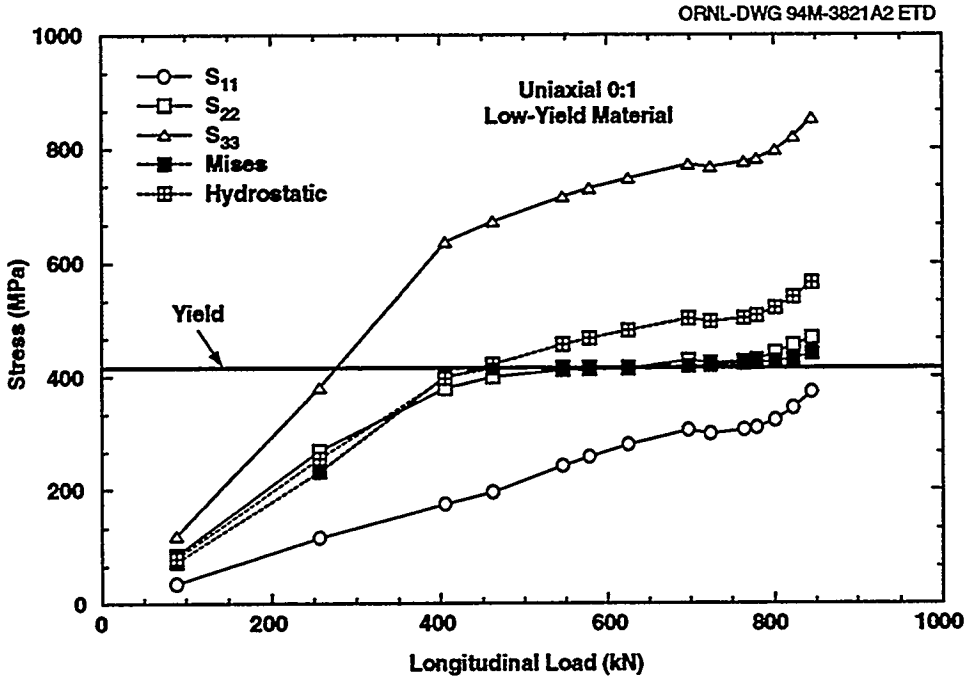

Figure 2.14 Stress components at material point 2.54 mm ahead of crack tip for uniaxial (0:1) loading

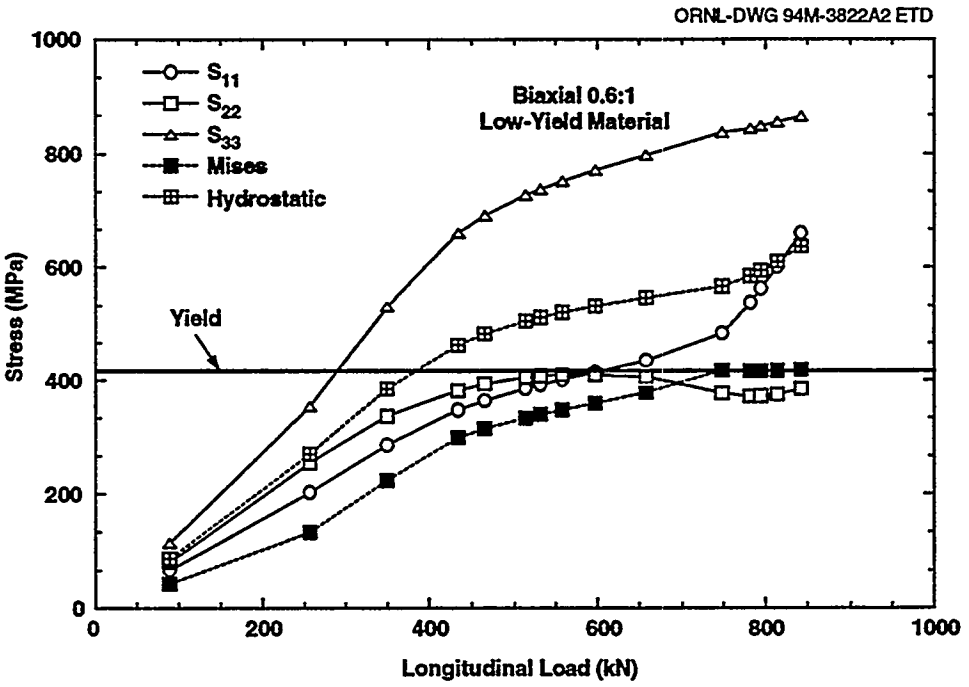

Figure 2.15 Stress components at material point 2.54 mm ahead of crack tip for uniaxial (0.6:1) loading

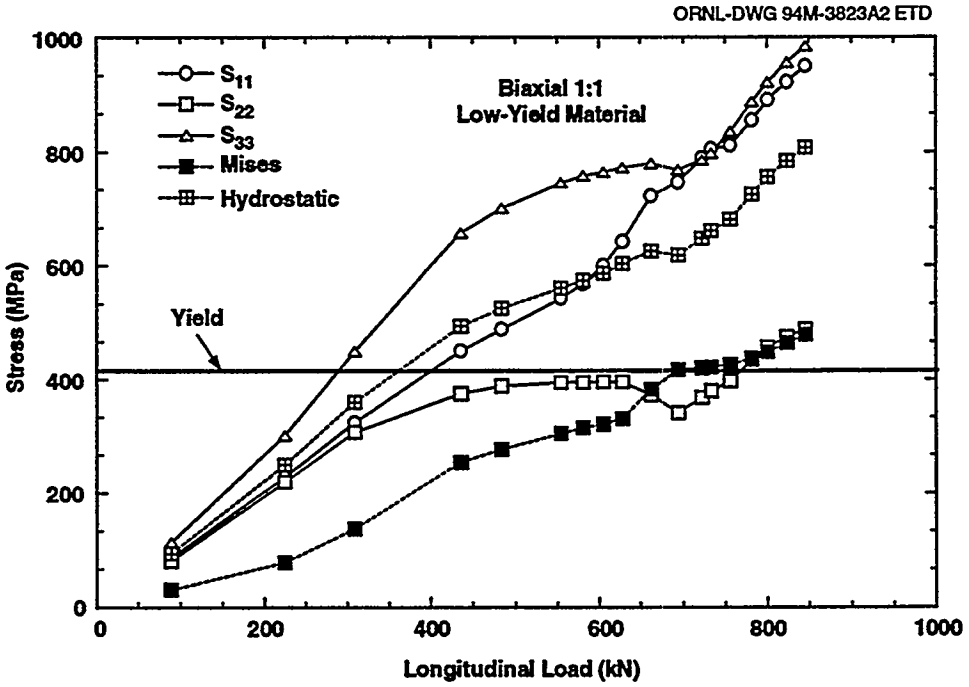

Figure 2.16 Stress components at material point 2.54 mm ahead of crack tip for uniaxial (1:1) loading

increase at a greater rate beyond 667 kN (150 kip). [In this load range, observe that the hydrostatic and the out-of-plane stresses for the 1:1 load case are substantially elevated above those of the 0.6:1 case (see Fig. 2.15).] Near the 667-kN (150-kip) level, the plastic zone width progresses abruptly through N-5006, and the node exhibits significant strain hardening. An increase in differences between principal stress components is reflected in the increasing Mises effective stress.

Figures 2.14–2.16 illustrate that increasing the out-of-plane to in-plane biaxial loading ratio from 0:1 to 1:1 results in a dramatic increase of the out-of-plane normal

stress component, while the two in-plane components remain relatively unchanged (except at the highest loads). Thus, far-field biaxial stresses have little effect on in-plane stresses in the cruciform specimen. This effect is further illustrated in Fig. 2.17, which depicts the variation of stress components at N-5006 with far-field biaxial stress ratio. The conclusion reached is that conventional stress-based cleavage fracture methodologies formulated in terms of in-plane stress components cannot detect the biaxial toughness effect clearly demonstrated in the ORNL data base.

2.2.2 Evaluation of Stress-Strain-Based Methodologies

As just discussed, while out-of-plane biaxial loading has no significant effect on in-plane stresses ahead of the crack tip, it does influence development of the crack-tip plastic zone in the direction of crack propagation, indicating that a strain-based fracture-toughness correlation is appropriate for RPV steels in the transition temperature region. Fractographic data obtained from examinations of broken halves of uniaxially and biaxially loaded cruciform specimens[14] were found to be consistent with a strain-based fracture-toughness correlation. Using analysis results, it was shown that cleavage initiation sites were located in the region of the crack-tip process zone where strain was increasing, whereas the stress peak had passed that location and was decreasing with increasing applied load. The expectation is that a cleavage initiation event will be governed by a criterion that exhibits a rising near-tip field at the initiation site under increasing applied load.

Previous investigations of strain-based methodologies in the transition region include those of Clausing,[15] Barsom,[16] Merkle,[17] Weiss,[18] Pennell,[19] and Tetelman and McEvily (T-M).[20] Clausing[15] related the decrease in toughness associated with increased strength of structural steels to a decrease in plane-strain ductility. Barsom[16] and Merkle[17] developed expressions for K_{Ic} based on plane-strain ductility, both of which compared well with measured toughness data in the transition temperature region.

Weiss[18] developed an analytical relation for fracture toughness based on the material fracture strain that Pennell[19] adapted to provide an estimate of biaxial loading effects on cleavage fracture toughness for RPV steels. Pennell[19] predicted the ratio of toughness values (K_b/K_u) corresponding to equibiaxial and uniaxial loading conditions, respectively, to be 0.47 compared to the lower-bound K_b/K_u ratio of 0.57 obtained from measured data in this work. The good agreement between analytical prediction and measured data is further support for the validity of a strain-based fracture-toughness correlation.

According to the T-M criterion,[20] plastically induced fracture initiates in a ligament immediately adjacent to the blunted crack tip when the ligament strain reaches the

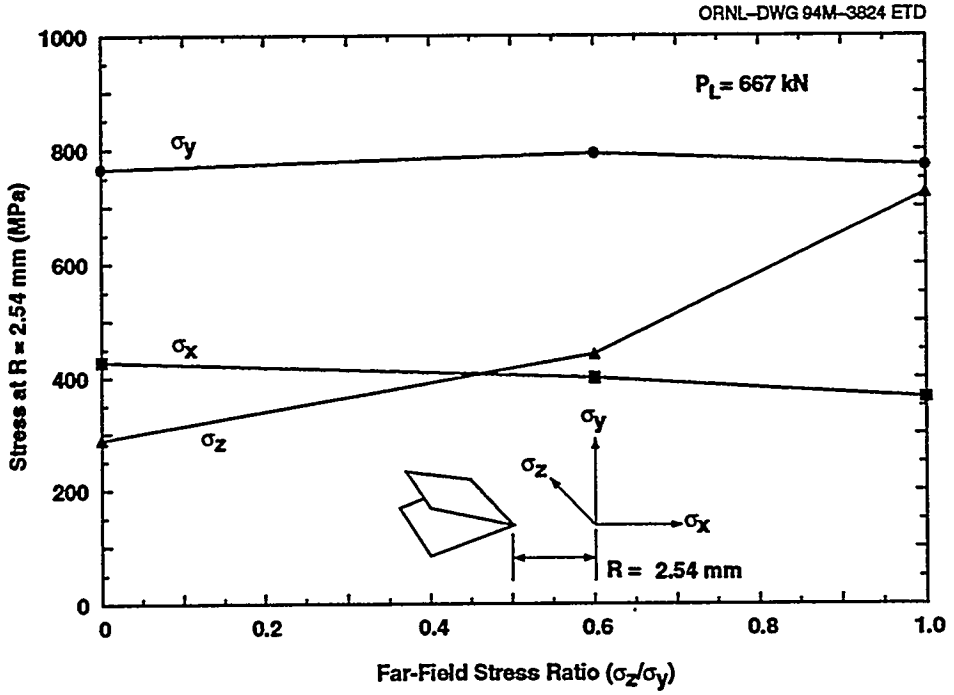

Figure 2.17 **Analyses results that show far-field stress biaxiality exerting little influence on in-plane stresses near the crack tip**

fracture strain (e_f) of the material. Pennell[21] has interpreted the T-M fracture criterion as a limiting condition for absorption of energy by the crack-tip material as a result of inelastic deformation. In addition, it was suggested that the effects of constraint on fracture toughness can be quantified by analyzing the response of the crack-tip material to increasing load and determining the radius of the blunted crack tip corresponding to the crack-tip ligament strain at fracture (e_f). Direct application of the latter strain-based approach would require a finite-strain elastic-plastic finite-element analysis to determine the crack-tip radius as a function of the ligament strain. To circumvent this computationally intensive approach, Pennell[21] proposes an alternative methodology that utilizes R, the plastic zone width in the plane of the crack, as a correlation parameter for fracture toughness. An important feature of this methodology is that the parameter R can be calculated accurately in a small-strain analysis.

An analytical basis for the approach utilizing plastic zone width R as a correlation parameter is found in the T-M development.[20] The T-M formulation relates R and crack-tip displacement as a function of applied stress, crack depth, and crack-tip radius for the case of plane-stress tensile loading and contained yielding. For the latter conditions, the T-M formulation leads to a proportional relationship between R and the crack-opening displacement. An analytical relation for the case of plane-strain tensile loading is not provided, although some approximations are discussed in Ref. 20.

Development of an HSST strain-based methodology is focusing on correlations of the cruciform test results with simple functions of the plastic zone width R. The investigation of biaxial loading effects on ligament conditions [at location r = 2.54 mm (0.1 in.)] described previously provides the variation of R with applied load shown in Fig. 2.18; the biaxial load ratio is taken as a parameter in this figure. The analyses revealed that increasing the load ratio from 0:1 to 0.6:1 effectively delays the onset of yielding to a much higher applied load. Further increase of the ratio to 1:1 leads to relatively abrupt uncontained yielding at an intermediate load level [at ~667 kN (150 kip)], followed by behavior essentially like that of the uniaxial case for load levels beyond those shown in Fig. 2.18. Thus, a material point ahead of the crack tip experiences yielding at different load levels, depending on the out-of-plane loading. As observed by Pennell,[21] the abrupt development of uncontained yielding in the 1:1 case may explain why some researchers, using small test specimens in which uncontained yielding was unavoidable, have reported no effects of biaxial loading on fracture toughness.

The ORNL/HSST strain-based constraint effects model, incorporating R as a second parameter, was utilized to predict the effect of biaxial loading on fracture toughness. This approach is illustrated in Fig. 2.19, where the biaxial fracture-toughness data from Fig. 2.11 are plotted as a function of the natural logarithm of the plastic zone width [ln(R)]. The data conform essentially to a straight-line relationship when plotted as a function of ln(R). The range

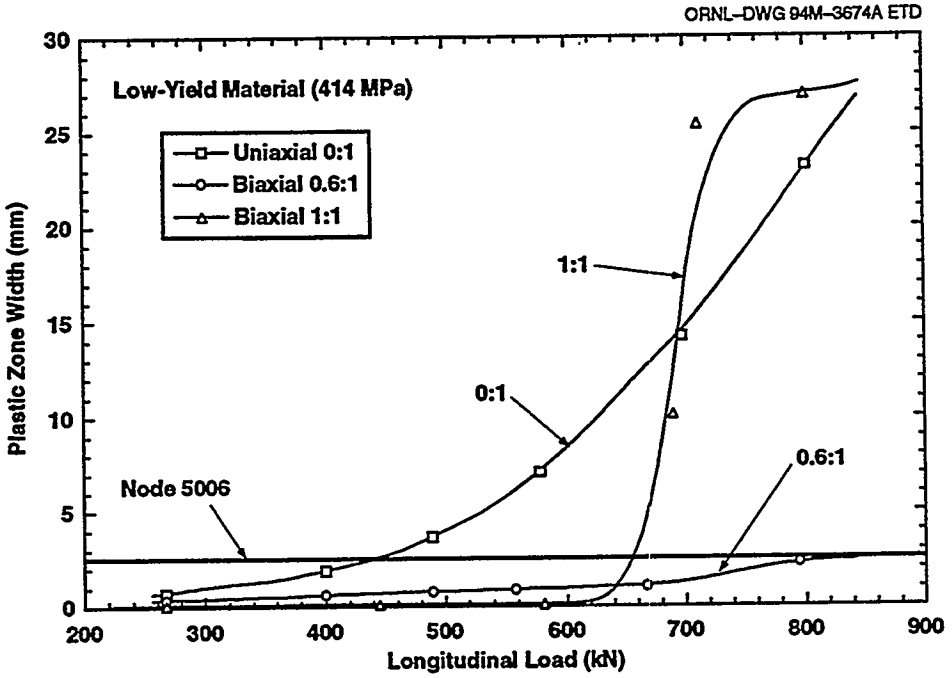

Figure 2.18 Material point (Node 5006) 2.54 mm ahead of crack tip that experiences yielding at different load levels, depending on out-of-plane loading ratio

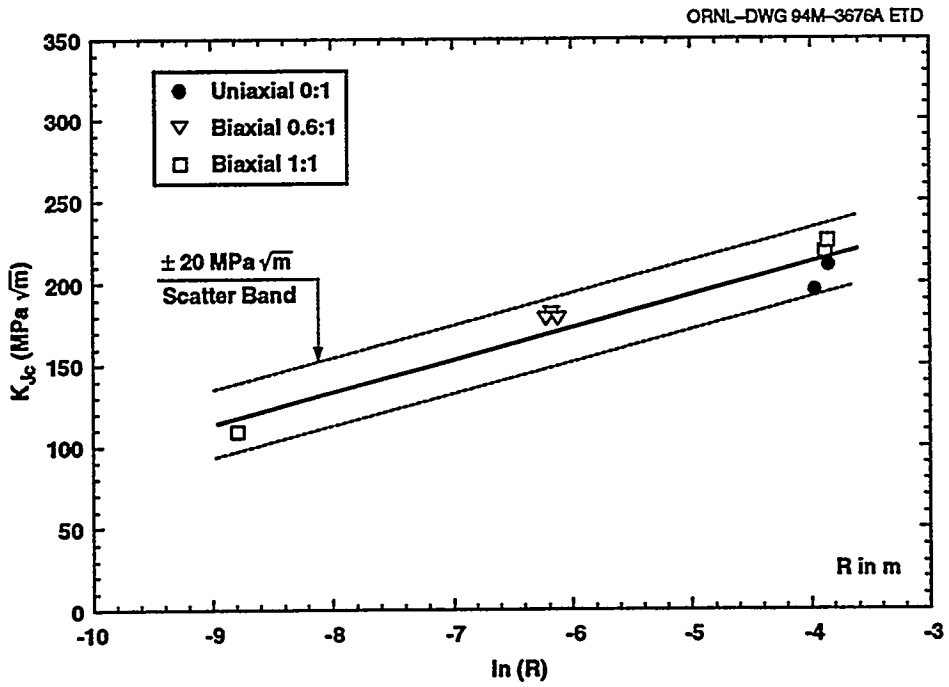

Figure 2.19 Shallow-flaw fracture-toughness locus, K_J-ln(R), defined by results from cruciform specimen tests

±20 MPa of similar fracture-toughness loci would be required to span the full range of normalized temperatures that could be encountered in an RPV transient analysis.

In Fig. 2.20, K_J vs ln(R) loading trajectories for the three cruciform analyses are superposed on the fracture-toughness locus of Fig. 2.19. These trajectories have three distinct phases that are characterized by the growth rate for R. The range of fracture-toughness values possible at T – NDT = –10°C, for a given loading condition, is predicted by the intersection of the K_J vs ln(R) loading trajectory with this fracture-toughness locus. In Fig. 2.20, unique K_{Jc} values are predicted for the uniaxial and biaxial 0.6:1 loading cases. The intersection of the K_J vs ln(R) trajectory for biaxial 1:1 loading with the toughness locus predicts both low and high K_{Jc} values for this loading condition. In fact, these low and high toughness values were realized in two tests of the biaxial 1:1 loading case; these toughness data are given in Fig. 2.11. Uncontained yielding that developed in two of the biaxial 1:1 tests gave high toughness values that were similar to those of the uniaxial loading tests.

Implicit in the previous correlation of biaxial toughness data with the parameter R is an apparent influence of crack-tip strains on determination of cleavage fracture toughness in the transition region. Specifically, strains in the plastic zone adjacent to the blunted crack tip are observed to increase as the root radius of the blunted crack decreases. Furthermore, the root radius of the blunted crack can be related directly to the width R of the plastic zone under certain conditions (see Ref. 19). Thus, correlation of fracture toughness with the width R may be caused by the effect of biaxial loading in restricting the growth of the root radius of the blunted crack. Consequences of this effect may be such that strains in the near-tip region increase to the plane-strain fracture ductility of the material. Confirmation of this fracture model for the cruciform specimen under uniaxial and biaxial loading requires computationally intensive finite-strain inelastic analyses of the crack-tip region that are not yet completed. Some evidence for these arguments is provided by normalized curves for cleavage fracture toughness (K_{Jc}) and crack-tip opening displacement (CTOD) of the cruciform specimens vs ln(R), which are found to have similar trends (see Fig. 2.21). These results lend support to the argument that the strain-based K_J vs ln(R) approach has potential as a dual-parameter correlation model capable of representing fracture behavior of RPV steels in the transition region, including effects of biaxial out-of-plane loading on fracture toughness.

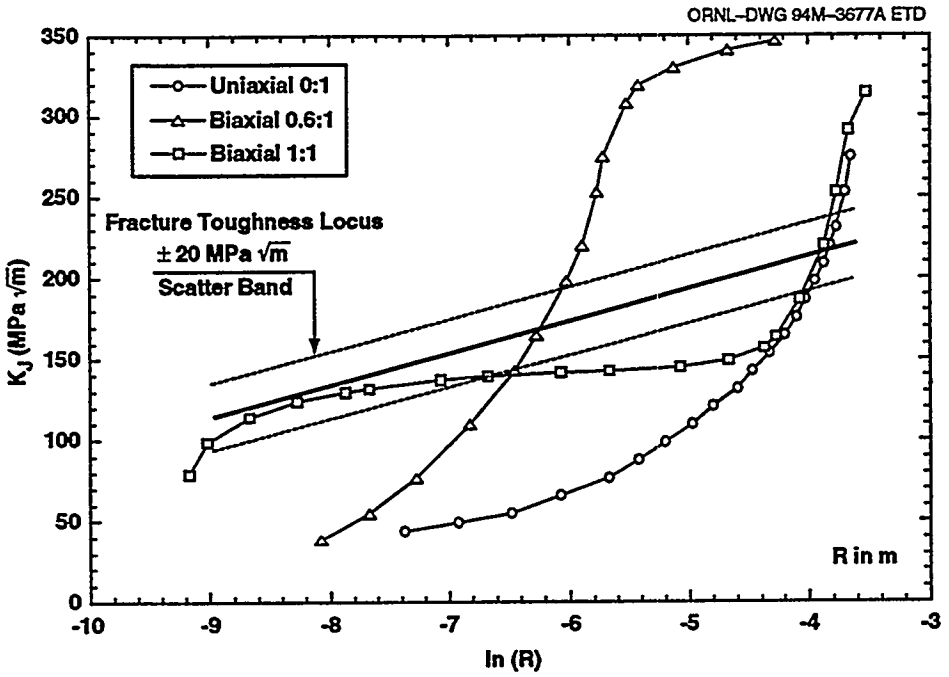

Figure 2.20 K_J-ln(R) trajectories for biaxial loading with three distinct phases characterized by plastic zone width (R) growth rate. Intersection of trajectory for 1:1 loading with fracture-toughness locus predicts both low and high K_{Jc} values for this loading condition

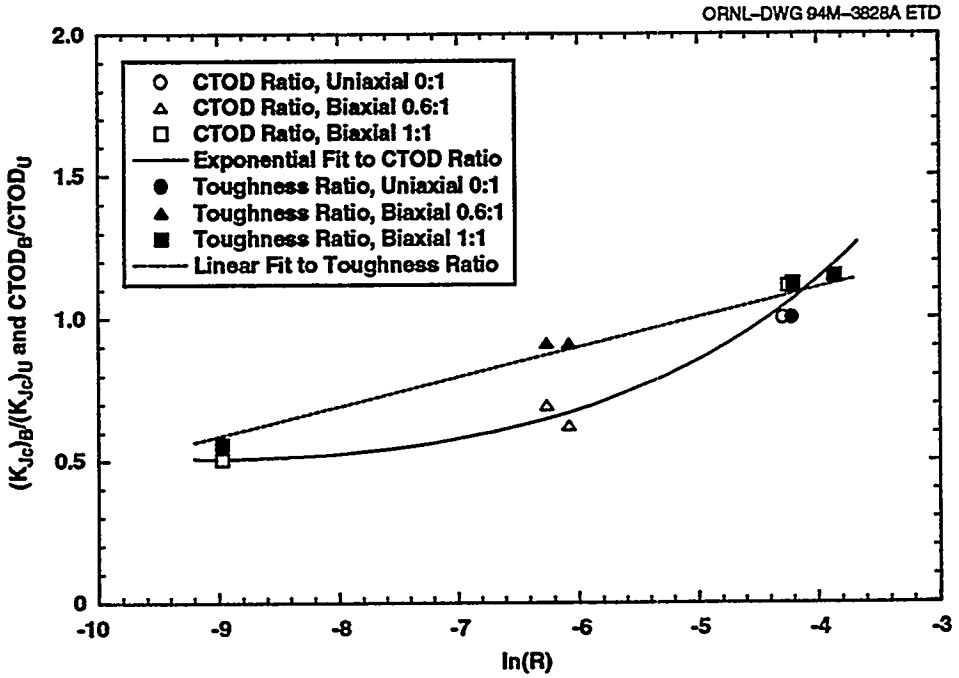

Figure 2.21 Similar trends of normalized K_{Jc} and CTOD curves suggesting that biaxial loading acts to inhibit crack-tip blunting and thereby decrease fracture toughness by increasing strains adjacent to the crack tip

2.3 Test and Analysis of Unclad Finite-Length Flaw Cruciform Specimens

(W. J. McAfee and J. W. Bryson)

The overall objective of these tests is to investigate the influence of finite-length flaw profiles, out-of-plane loading, and material condition on the effective fracture toughness of RPV plate material. The biaxial, finite-length flaw test specimen design has been described in detail previously.[22] A series of six specimens was fabricated and tested to demonstrate the viability of the design and to develop fabrication and test procedures required for implementation of a large matrix of clad cruciform beam tests. Reduction of the data from these finite-length flaw tests has been completed. To calculate toughness values, finite-element analyses of the finite-length flaw specimen under 0:1 and 1:1 loading were performed. Characterization tests were performed to develop a reference stress-strain curve for the material in the as-received condition at the nominal test temperature. This curve is shown in Fig. 2.22. The finite-element results were used to develop tabular values of toughness, K_J, as a function of angular location around the flaw front and load. These results are shown graphically in Figs. 2.23 and 2.24 for the uniaxial (0:1) and biaxial (1:1) load cases, respectively. On each fracture surface, the initiation site was located, and its angular position from the specimen free surface was measured (see Figs. 2.25–2.28). The failure load and initiation site position were then used to interpolate from the prepared tables to determine toughness. The results are summarized in Table 2.6. Specimen CF5 appeared to have possibly two initiation sites, one near 84°, considered the primary site, and another near 48° below the surface. Toughness values were determined for both these locations. For the uniaxial load case, K_J is essentially uniform over the central portion of the flaw front (i.e., that portion centered about 90°), so that this angular difference made little difference in the values of toughness determined. The toughness results thus determined are shown plotted on Figs. 2.23 and 2.24. It is observed that the initiation sites are consistent with the development of K values around the flaw front. That is, for the uniaxial case, as the plastic zone develops in front of the flaw with increasing load, K has it maximum values over the central portion of the flaw front (i.e., at the deepest point). Both uniaxial specimens failed in this region. For the biaxial case, however, K tends to become maximum near 15° below the free surface. The two biaxially loaded specimens failed between 14° and 22° below the surface.

In reducing the data, it was observed that the ratio of transverse to longitudinal measured beam arm strains was in the range of 0.9:1 for both of the biaxial tests. The pressure ratio, which has normally been used to calculate longitudinal load from total load, was 1.0 for both tests. Since alignment is carefully checked before each test, this situation could occur if there were a change in boundary support conditions caused by deformation of the specimen. Due to the short length of the beam arms [25.4 cm (10 in.], a small change in contact location can introduce a measurable change in effective beam arm length. The toughness values

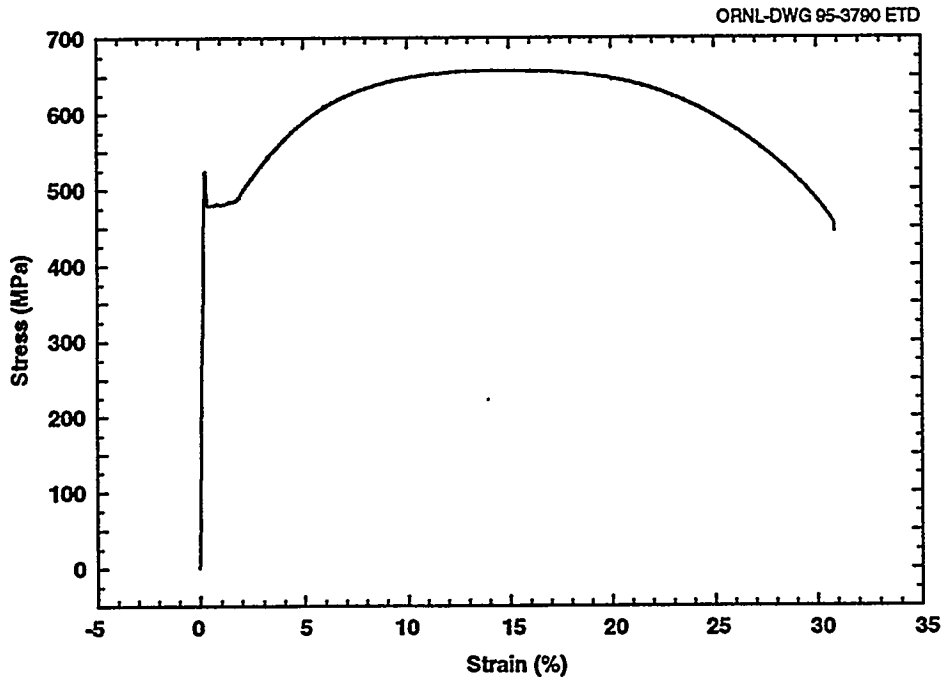

Figure 2.22 Reference stress-strain curve used in final analyses of finite-length flaw specimens

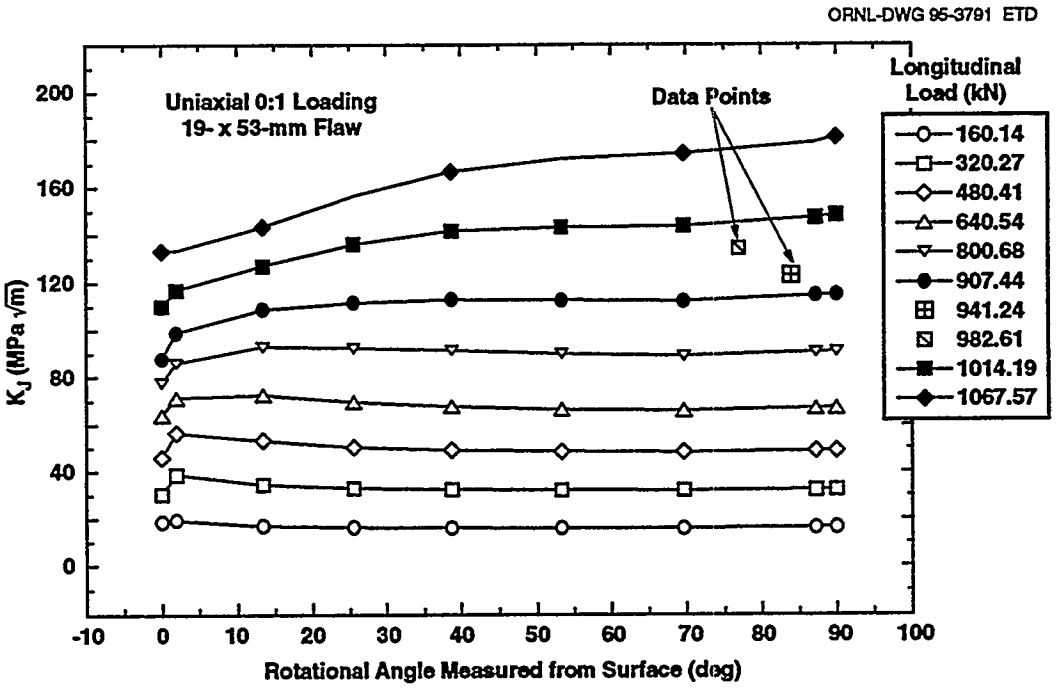

Figure 2.23 Analysis results for finite-length flaw specimen under uniaxial (0:1) load

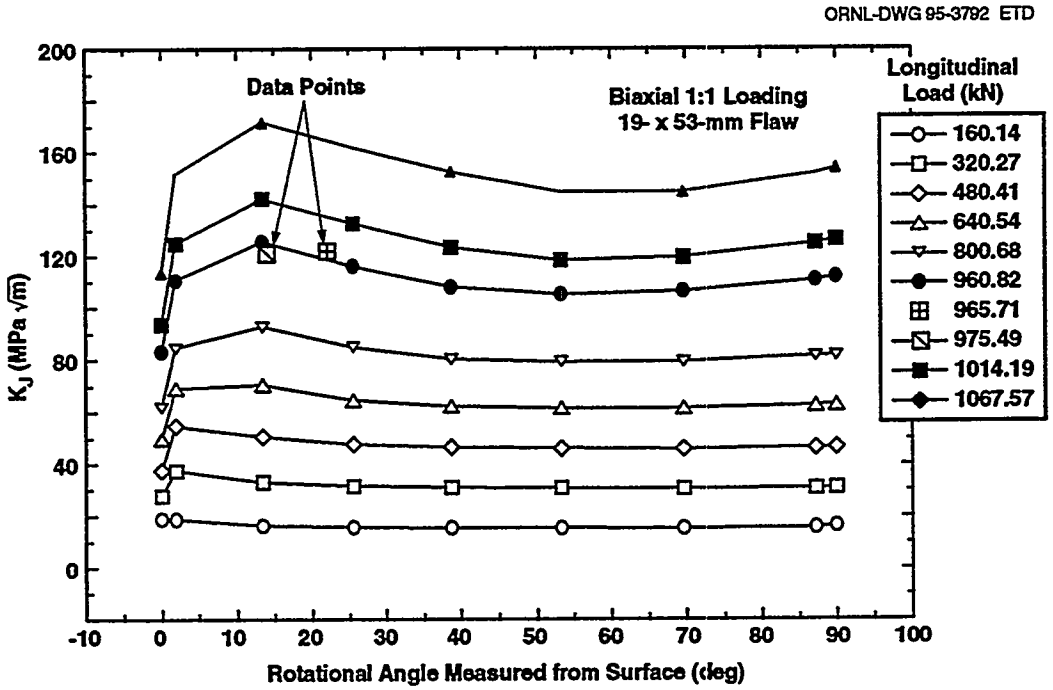

Figure 2.24 Analysis results for finite-length flaw specimen under uniaxial (1:1) load

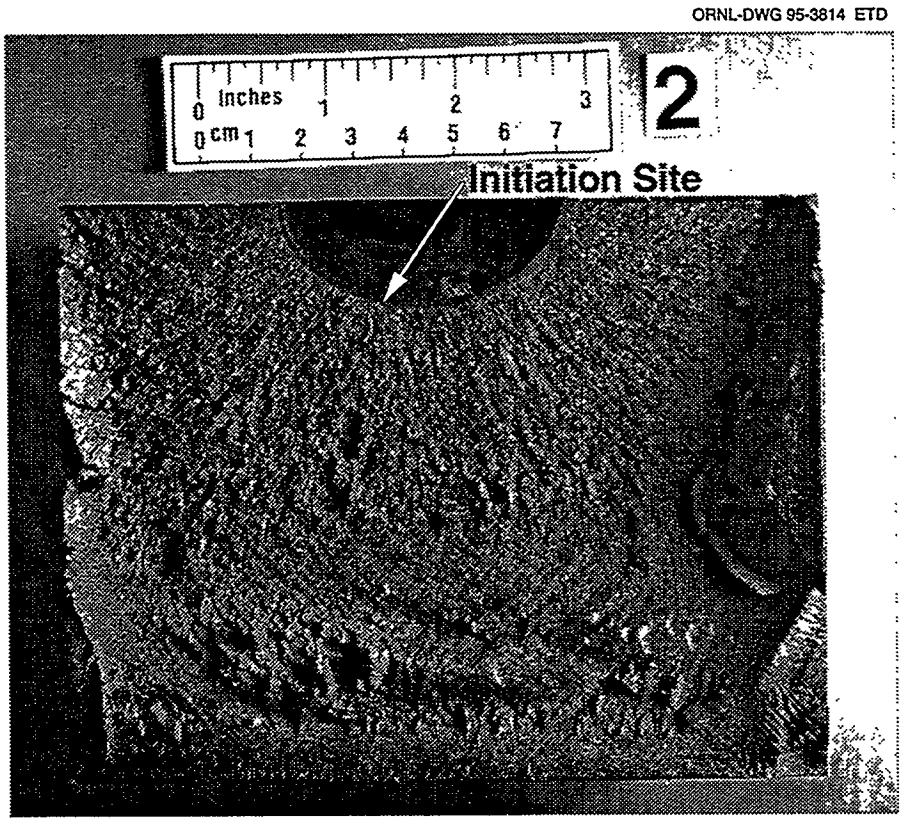

Figure 2.25 Fracture surface for finite-length flaw specimen CF-2 showing location of cleavage initiation site

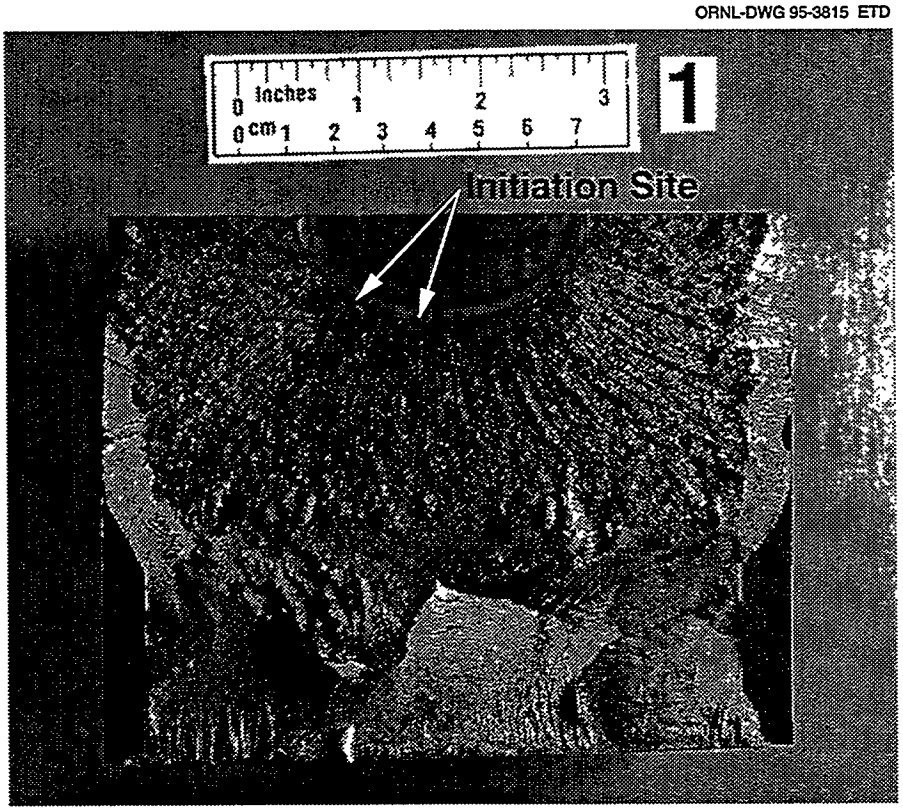

Figure 2.26 Fracture surface for finite-length flaw specimen CF-5 showing location of cleavage initiation site(s)

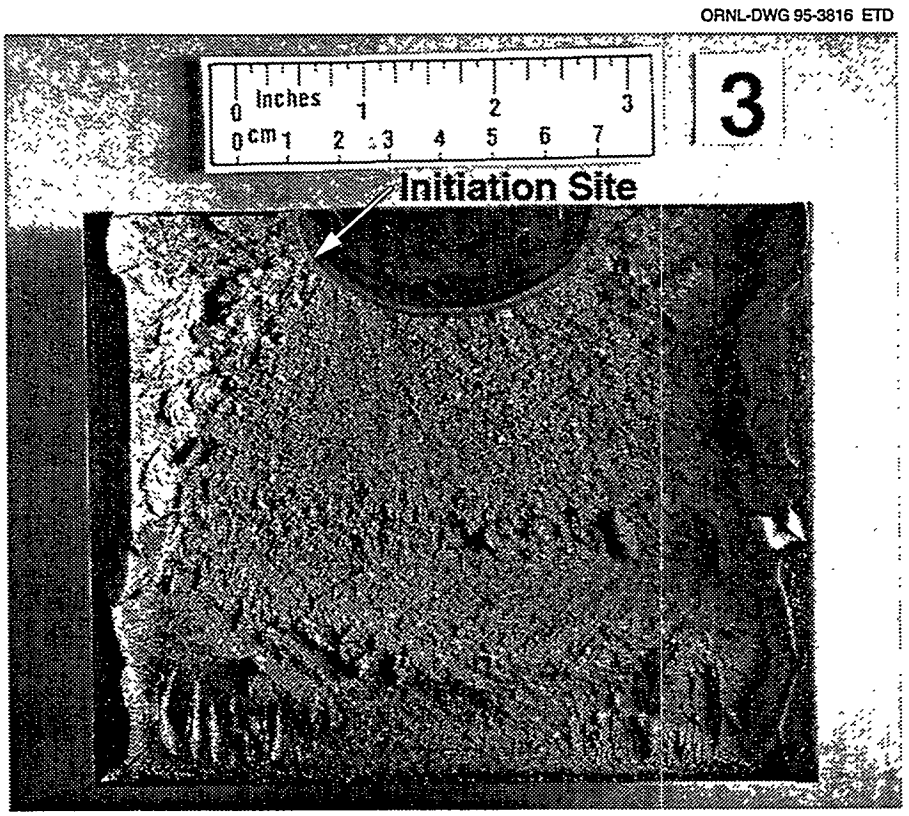

Figure 2.27 Fracture surface for finite-length flaw specimen CF-3 showing location of cleavage initiation site

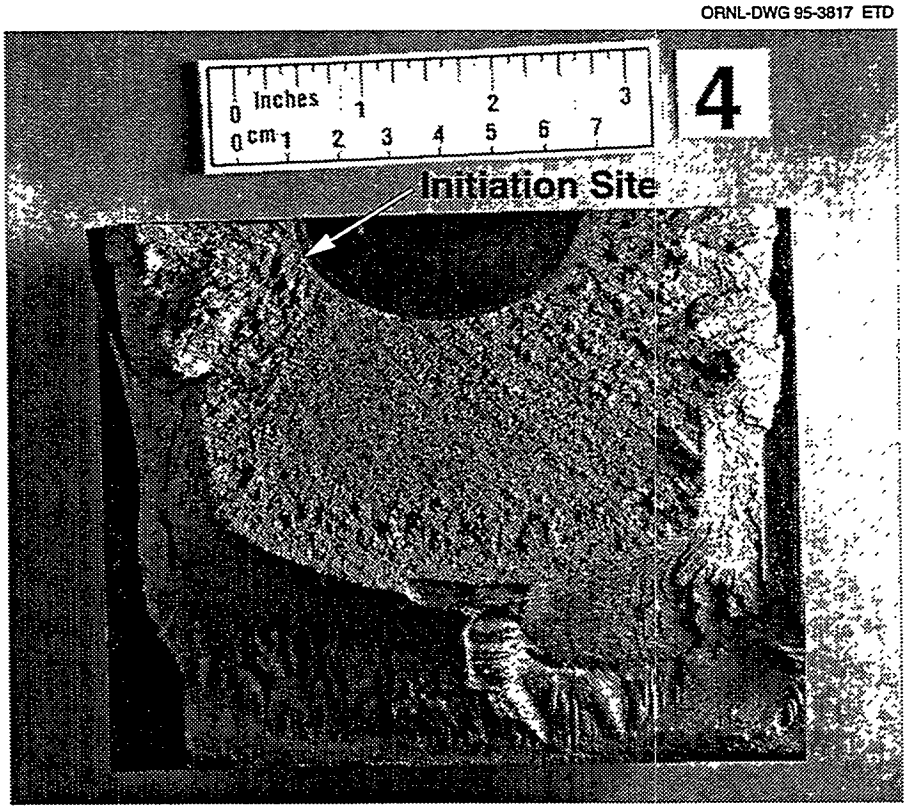

Figure 2.28 Fracture surface for finite-length flaw specimen CF-6 showing location of cleavage initiation site

Table 2.6 Summary of toughness values for finite-length flaw specimens

Specimen	Biaxiality	Failure load [kN (kip)]	Initiation site angle[a] (deg)	Toughness K_{Jc} [MPa$\sqrt{m}$ (ksi$\sqrt{in.}$)]
CF-2	0:1	941.2 (211.60)	77	121.6 (110.7)
CF-5[b]	0:1	982.6 (220.9)	84	135.8 (123.6)
CF-5[c]	0:1	982.6 (220.9)	48	138.0 (125.6)
CF-3	1:1	965.7 (217.1)	22	120.4 (109.6)
CF-6	1:1	975.5 (219.3)	14	129.6 (117.9)
CF-3M[d]	0.9:1	1012.4 (227.6)[d]	22	127.8 (116.3)
CF-6M[d]	0.9:1	1039.1 (233.6)[d]	14	134.7 (122.6)

[a]Angle measured from surface.
[b]Primary initiation site.
[c]Secondary initiation site.
[d]Recalculated for load redistribution.

for the biaxially loaded specimens were reevaluated based on biaxiality ratios determined from the measured beam arm strains. New analyses were performed using a nominal biaxiality ratio of 0.9:1, which was representative of the beam arm strain ratio for specimens CF-3 and -6. A table of toughness values as a function of load and angle around the flaw front was constructed as was described previously. Toughness for each test was then interpolated from this table. These results are shown in Fig. 2.29 and also in Table 2.6 as specimens CF-3M and -6M. These revised toughness values represent increases of ~6% for CF-3 and 4% for CF-6.

A biaxial loading effect was observed in these tests by the location of the cleavage initiation site. The fracture-toughness values obtained were statistically inconclusive so far as determining the effect of out-of-plane loading. The small number of tests certainly contributed to this. The data did, however, demonstrate a shallow-flaw effect when compared to the toughness values from a series of 1T compact tension specimens using this same material (HSST as-received Plate 14), same nominal flaw location within the plate, and same flaw orientation (see Fig. 2.30). Finally, the fabrication and test procedure development is currently being applied to a matrix of clad, finite-length flaw specimens being tested under HSST Task H3.

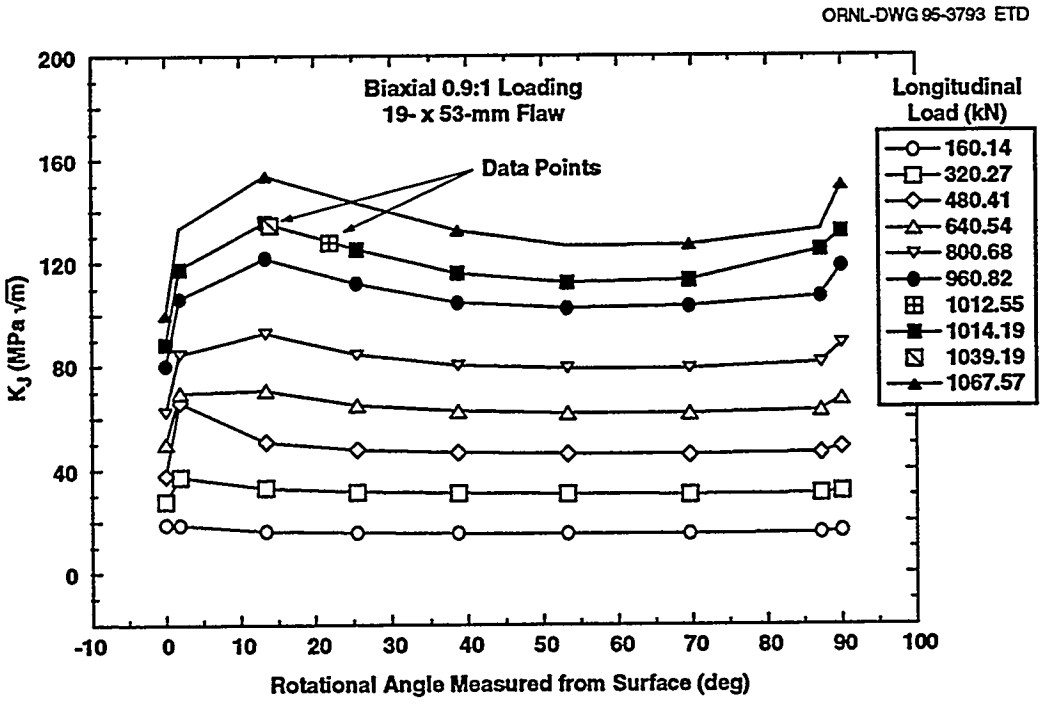

Figure 2.29 Analysis results for finite-length flaw specimen under uniaxial (0.9:1) load

Constraint

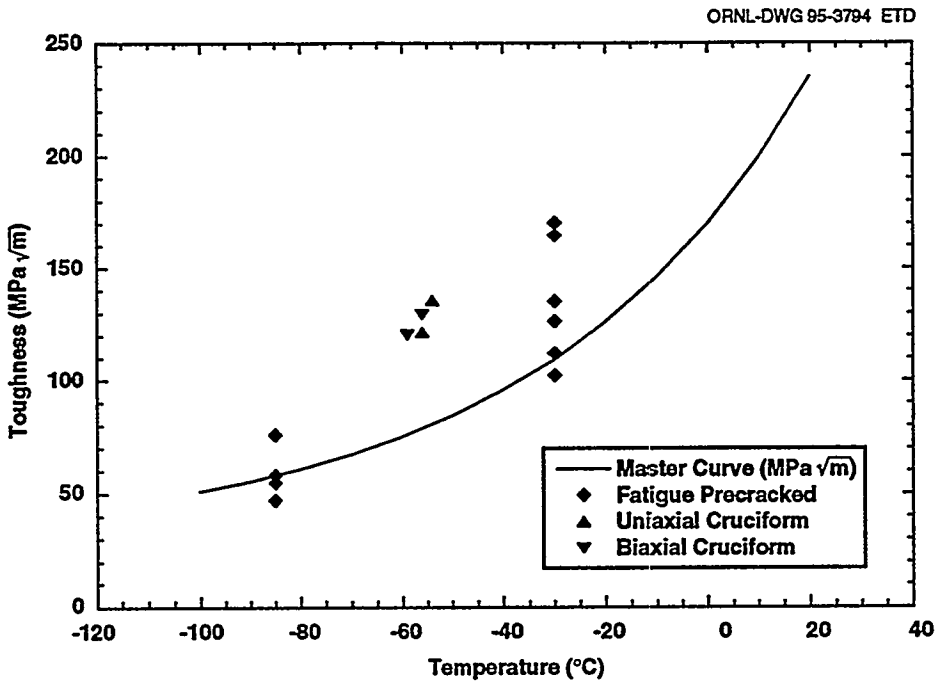

Figure 2.30 Finite-length flaw biaxial data showing shallow-flaw effect when compared to data developed using 1T compact tension specimens of same material

References

1. D. P. Clausing, "Effect of Plastic Strain on Ductility and Toughness," *Int. J. Fract. Mech.* 6(1), 71–85 (March 1970).*

2. J. M. Barsom, "Relationship Between Plane-Strain Ductility and K_{Ic} for Various Steels," *J. Eng. Ind., Trans. ASME*, 93, B (4), 1209–15, November 1971.*

3. ASTM E 8-91, "Standard Test Methods of Tension Testing of Metallic Materials," *Annual Book of ASTM Standards*, Vol. 03.01 (American Society for Testing and Materials, Philadelphia, Pa., 1992).

4. T. R. Wilshaw, C. A. Rau, and A. S. Tetelman, "A General Model to Predict the Elastic-Plastic Stress Distribution and Fracture Strength of Notched Bars in Plane Strain Bending," *Eng. Fract. Mech.*, 1, 191–211 (1968).*

5. W. J. McAfee, B. R. Bass, W. E. Pennell, and J. W. Bryson, Martin Marietta Energy Systems, Inc., Oak Ridge Natl. Lab., "Biaxial Loading Effects on Fracture Toughness of Reactor Pressure Vessel Steel," USNRC Report NUREG/CR-6273 (ORNL/TM-12866), March 1995. †

6. T. H. Theiss and D. K. M. Shum, Martin Marietta Energy Systems, Inc., Oak Ridge Natl. Lab., "Experimental and Analytical Investigation of the Shallow-Flaw Effect in Reactor Pressure Vessels," USNRC Report NUREG/CR-5886 (ORNL/TM-12115), July 1992.†

7. N. P. O'Dowd and C. F. Shih, "Family of Crack-Tip Fields Characterized by a Triaxiality Parameter: Part I—Structure of Fields," *J. Mech. Phys. Solids* 39, 989–1015 (1991).*

8. N. P. O'Dowd and C. F. Shih, "Family of Crack-Tip Fields Characterized by a Triaxiality Parameter: Part II—Fracture Applications," *J. Mech. Phys. Solids* 40, 939–63 (1992).*

9. N. P. O'Dowd and C. F. Shih, Naval Surface Warfare Center, "Two Parameter Fracture Mechanics: Theory and Applications," USNRC Report NUREG/CR-5958 (CDNSWC/SME-CR-16-92), February 1993.

10. R. O. Ritchie, J. F. Knott, and J. R. Rice, "On the Relationship Between Critical Tensile Stress and Fracture Toughness in Mild Steel," *J. Mech. Phys. Solids* 21, 395–410 (1973).*

11. R. H. Dodds, T. L. Anderson, and M. T. Kirk, "A Framework to Correlate a/W Ratio Effects on Elastic-Plastic Fracture Toughness (J_c)," *Int. J. Fract. Mech.* 48, 1–22 (1991).*

12. T. L. Anderson and R. H. Dodds, "Specimen Size Requirements for Fracture Toughness Testing in the Ductile-Brittle Transition Region," *J. Test. Eval.* 19, 123–34 (1991).*

13. R. H. Dodds, C. F. Shih, and T. L. Anderson, "Continuum and Micromechanics Treatment of Constraint in Fracture," University of Illinois, UILU/ENG-92-2014, November 1992.

14. B. R. Bass, J. W. Bryson, T. J. Theiss, and M. C. Rao, Martin Marietta Energy Systems, Inc., Oak Ridge Natl. Lab., "Biaxial Loading and Shallow Flaw Effects on Crack-Tip Constraint and Fracture Toughness," USNRC Report NUREG/CR-6132 (ORNL/TM-12498), January 1994.†

15. D. P. Clausing, "Effect of Plastic-Strain State on Ductility and Toughness," *Int. J. Fract. Mech.* 6(1) (March 1970).*

16. J. M. Barsom, "Relationship Between Plane-Strain Ductility and K_{Ic} for Various Steels," Paper 71-PVP-13, *J. Eng. Ind.* 93, 1209–15 (November 1971).*

17. J. G. Merkle, Union Carbide Corp., Nucl. Div., Oak Ridge Natl. Lab., "An Elastic-Plastic Thick-Walled Hollow Cylinder Analogy for Analyzing the Strains in the Plastic Zone Just Ahead of a Notch Tip," ORNL/TM-4071, January 1973.†

18. V. Weiss, "Material Ductility and Fracture Toughness of Metals," *Proceedings of the International Conference on Mechanical Behavior of Materials, Kyoto, Japan, August 15–20, 1971* (The Society of Materials Science, Japan, 1971).

19. W. E. Pennell, "Heavy-Section Steel Technology Program: Recent Developments in Crack Initiation and Arrest Research," *Nucl. Eng. Des.* 142 (2&3), 255–66 (1993).*

20. A. S. Tetleman and A. J. McEvily, Jr., *Fracture of Structural Materials*, John Wiley & Sons, Inc., New York, 1967.

21. W. E. Pennell, "Reactor Pressure Vessel Structural Integrity Research," *Nucl. Eng. Des.* 157, 159–75 (1995).*

22. W. E. Pennell et al., Martin Marietta Energy Systems, Inc., Oak Ridge Natl. Lab., "Heavy Section Steel Technology Semiannual Progress Report for April 1993–October 1993," USNRC Report NUREG/CR-4219 (ORNL/TM-9593, V10&N2), May 1995.†

*Available in public technical libraries.

†Available for purchase from the National Technical Information Service, Springfield, VA 22161.

3 Evaluation of Cladding Effects

B. R. Bass

3.1 Introduction

During this reporting period, work continued on developing a quantitative description of the effects of cladding on the fracture behavior of shallow surface cracks in RPVs and a methodology for including cladding effects in current RPV integrity assessment procedures.

3.2 Assessment of Clad Modeling Effects on Cleavage Initiation in Embrittled RPVs (B. R. Bass and T. L. Dickson)

The HSST Program is investigating the effects of the cladding overlay on the propensity for cleavage initiation of shallow flaws on the inner surface of cladded RPVs. Shallow flaws having depths on the order of the combined thickness of the clad and heat-affected zone (HAZ) dominate the frequency distribution of flaws[1–2] assumed in probabilistic fracture-mechanics (PFM) assessments of RPVs. Consequently, the initiation probabilities associated with these flaws under PTS loading conditions can strongly influence the predicted failure probabilities for RPVs. Behavior of these shallow flaws during a PTS transient clearly would be influenced by the material/fracture properties and mechanical interactions associated with the elements (i.e., cladding, HAZ, and near-surface base material) that compose the cladding overlay structure. Thus, coordinated experimental and analytical studies are being conducted within the HSST Program to provide a quantitative description of effects of the cladding overlay on fracture behavior of shallow surface flaws.

This section describes the initial phase of an analytical study of clad modeling effects on predictions of cleavage fracture initiation in an RPV subjected to PTS transient loading conditions. These analyses were carried out in support of an HSST clad cruciform beam testing program that is intended to provide unique shallow-flaw biaxial toughness data from the clad overlay region of prototypic RPV material. First, some prior experimental and analytical work that addresses cladding issues, as well as a brief description of the HSST clad cruciform beam testing program, are reviewed. Then, deterministic analyses performed with the FAVOR fracture analysis code are used to predict envelopes of minimum (critical) flaw sizes (depths and lengths) required to achieve cleavage initiation for the prescribed PTS transients. These envelopes, defined in terms of flaw sizes and loading conditions, will be validated with results from the scheduled HSST clad cruciform beam testing program.

3.2.1 Cladding Issues and Prior Research

The principal function of the cladding overlay in an RPV is to minimize the volume of corrosion products entering the primary system coolant. Potential benefits or liabilities of the cladding that relate to the structural integrity of the vessel are not considered in safety assessment procedures applied to RPVs. The fracture-mechanics model[3] referred to in the RG 1.154 for evaluating the integrity of RPVs under PTS loading conditions includes cladding as a discrete region only to the extent that thermal and stress effects are considered in the context of a linear-elastic fracture-mechanics (LEFM) model. Specifically, consideration of the clad region is limited to incorporating the relatively lower (compared to base metal) thermal conductivity and the higher coefficient of thermal expansion. The cladding and HAZ are assumed to have the same fracture toughness as that of the base metal. Also, all flaws are considered to be surface flaws; that is, the flaws extend through the cladding to the inner surface of the vessel. These simplifying assumptions generally have been regarded as a conservative approach to treatment of the clad region in RPV safety assessments.

Another important feature of the RG 1.154 analysis model that may be influenced by cladding issues is the assumption that initial flaws of depth <20% of wall thickness are infinitely long (i.e., 2-D) for the purpose of calculating SIFs (K_J). This assumption regarding 2-D initial flaws was based in part on results of analyses and assessments of ORNL unclad thermal-shock experiments.[4–6] These results indicated that, in the absence of cladding, a semicircular surface flaw subjected to sufficiently severe thermal-shock loading will propagate in surface length to become a very long flaw. Furthermore, lateral extension of the surface flaw is predicted to occur before the time in the transient when a 2-D flaw of the same depth would initiate and propagate radially. Thus, calculations were not performed for short, shallow through-clad surface flaws in the Integrated Pressurized Thermal Shock (IPTS) studies[7–9] that contributed to the development of RG 1.154.

Evaluation

Much attention has been focused on efforts to better understand the influence of the cladding overlay on RPV integrity under postulated accident and operating conditions. Several experimental and analytical studies have examined potentially beneficial effects of the cladding overlay when considered as a structural element of an RPV. In an early HSST analytical study, Robinson et al.[10] investigated the influence of selected variables on the tendency of preexisting flaws in an RPV to initiate during a loss-of-coolant accident. Based on a comparison of RPV models with and without cladding, they noted a marked ameliorating effect of cladding on the tendency for flaw initiation and suggested that cladding effects should be included in RPV assessments. Subsequently, experiments were performed at ORNL on a thermally shocked cylinder to investigate the influence of cladding properties on flaw behavior.

Thermal-shock experiments[11–12] performed at ORNL with a large test cylinder studied the effects of cladding on behavior of both surface and subclad flaws. Four experiments (TSE-8 through -11) were conducted with cladding and flaws located on the inner surface of the cylinder. The thermal shock was achieved by first heating the cylinder to 93°C and then shocking the inner surface with liquid nitrogen at –160°C. Substantial subsurface and radial propagation of several flaws was observed during two of the clad cylinder experiments (i.e., TSE-8 and -11). In these experiments, there was no breaching of the cladding by subclad flaws or extension of flaws on the surface. The contour of the arrested flaw that extended from an initially semielliptical subclad flaw in experiment TSE-8 is depicted in Fig. 3.1. The TSE-9 experiment provided a direct comparison of results with the previously performed TSE-7 test,[4] which had essentially the same flaw geometry (i.e., a 0.75-in.-deep semicircular surface flaw) and loading conditions, but no clad layer. In TSE-7, three initiation-arrest events terminated with a final crack depth of 2.3 in. By comparison, only a single event occurred in TSE-9, and the extension was only 0.25 in. The presence of cladding reduced the potential for propagation of both through-clad surface and subclad flaws.

More recent HSST studies by Keeney-Walker et al.[13,14] and Shum et al.[15] considered the effects of cladding on the extension of shallow finite-length cracks in the inner surface of an RPV. Refined treatments of surface-flaw initial geometries were used to quantify the degree of conservatism associated with the assumption of 2-D initial flaws in the fracture-mechanics model of RG 1.154. These studies reflect a close association between the properties of the cladding overlay structure, the severity of the thermal-shock loading, and the critical flaw shapes and depths predicted for RPVs subjected to postulated PTS transients.

Shallow through-clad surface cracks subjected to transient PTS loading conditions (from the Rancho Seco transient) were analyzed by Keeney-Walker et al.[13] using finite-element techniques and elastic-plastic constitutive models. The clad yield stress used in Ref. 13 (~138 MPa) is at the low end of data for cladding. Because ductile tearing is considered the relevant fracture mode for stainless-steel RPV cladding, the J_R methodology was employed to determine the propensity for initiation of tearing in the cladding. Tearing toughness data for irradiated cladding were obtained from an ORNL testing program described by Haggag et al.[16] In Fig. 3.2 (from Ref. 16), tearing initiation toughness (J_{Ic}) of irradiated stainless steel cladding is seen to be similar to that of irradiated low-upper-shelf (LUS) weld material. However, results from Ref. 13 indicated that the cladding toughness given in Fig. 3.2 is sufficiently high that ductile tearing is unlikely to occur for the crack geometries, material properties, and PTS loading conditions assumed in that study.

Shum et al.[15] employed 3-D finite-element techniques to investigate the behavior of an almost semicircular, finite-length flaw under PTS transient loading conditions. For the case in which the cladding shares the toughness of the base material, the study indicates that the almost semicircular flaw would propagate unrestrained in the axial direction, followed by propagation into the vessel wall. When the cladding is made tougher than the base material, analysis results imply that the almost semicircular flaw would not initiate during the PTS transient for the conditions assumed in that study.

Keeney-Walker et al.[14] conducted an analytical study to determine the effects of using semicircular surface flaws as initial flaws, as opposed to 2-D flaws in a PTS analysis of a cladded RPV. Based on results described in Ref. 13, it was assumed that no extension of flaws would occur in the clad layer. The mean K_{Ic} curve used in these analyses was taken from the IPTS studies[7–9] and is defined by assuming that the ASME lower-bound curve[17] represents the mean minus two standard deviations (-2σ). The results from 3-D thermoelastic (TE) finite-element analyses and from IPTS/OCA-P analyses[18] are plotted in Fig. 3.3 (taken from Ref. 14). The deterministic results in Fig. 3.3 indicate that deeper semicircular flaws are required for crack initiation as compared to 2-D flaws, except for the least severe transient. A filter was constructed from the results in Fig. 3.3 to exclude some flaw sizes as potential initiators in PFM analyses of various PTS transients. The impact of including the finite-length surface flaw was to reduce the conditional probability of failure between a factor of ~3 for the more severe thermal transient to a factor of ~20 for the less severe thermal transient.

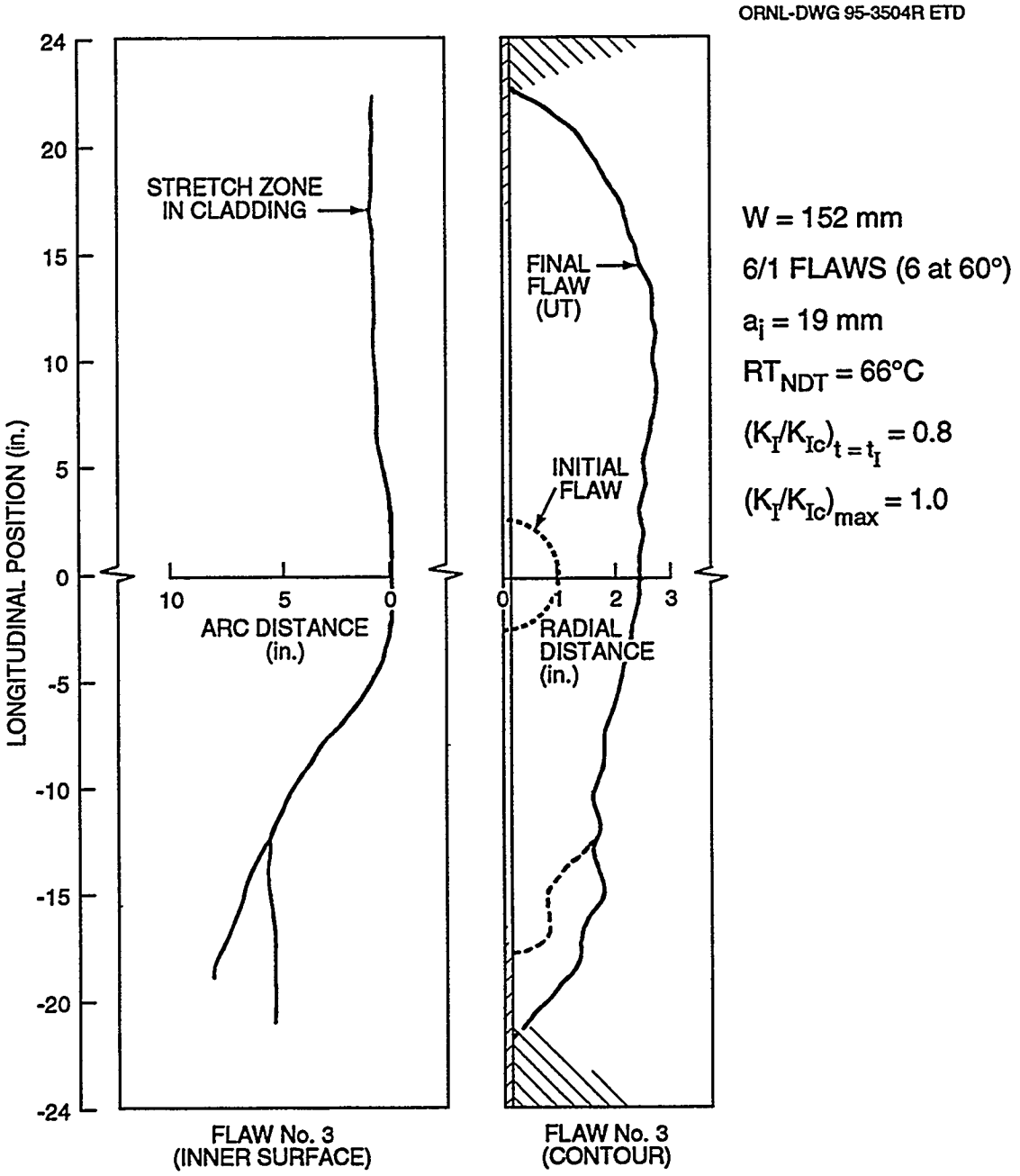

Figure 3.1 In TSE-8, one of six 6/1 subclad flaws shown propagated, extended in length (subclad) and depth, with no penetration of cladding

Some studies have indicated that an apparent increase in toughness of the cladding overlay may be the result of high toughness in the HAZ. McCabe[19–20] interpreted results from testing of unirradiated and irradiated clad bend bars to imply that fracture behavior of through-clad surface flaws was controlled by the fracture-toughness properties of the HAZ. In these tests, the HAZ was tougher than the base metal both before and after irradiation, although the HAZ exhibited an irradiation-induced toughness shift similar to that of base metal. If the fracture toughness of the HAZ remains greater than that of the base metal, then current design and analysis procedures will tend to be conservative. However, if the HAZ toughness is low, any beneficial effects of the cladding overlay must come from the ductile tearing resistance of the clad layer itself.

Some additional insight into fracture toughness of the near-HAZ region of unirradiated RPV material is provided by data from an HSST clad beam testing program.[21] The program is utilizing full-thickness clad beam specimens (225- by 225-mm cross section) to quantify fracture toughness for shallow cracks in materials for which metallurgical conditions are prototypic of those found in RPVs. The

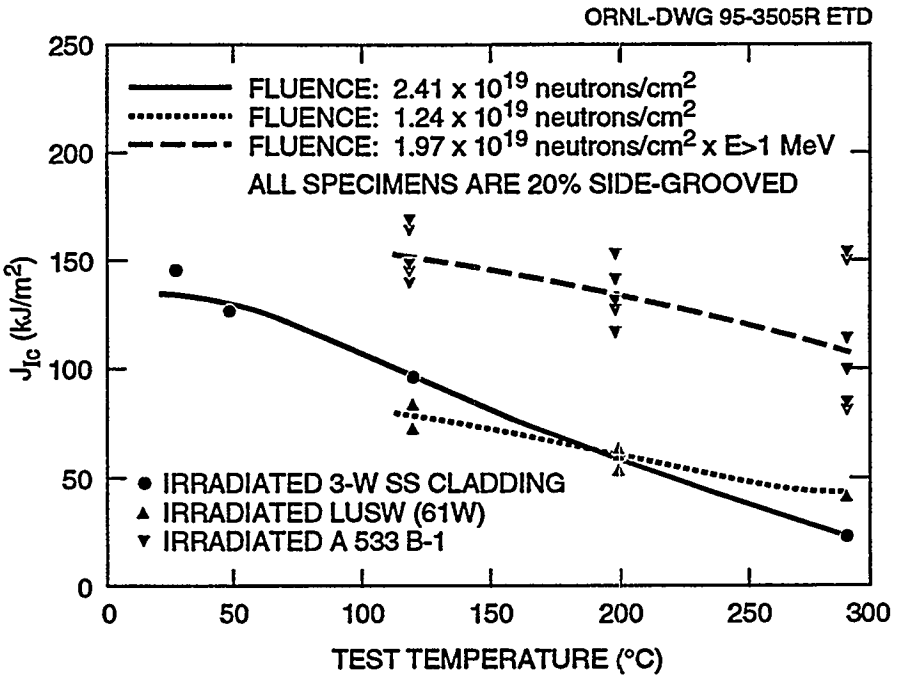

Figure 3.2 Ductile tearing initiation-toughness curves (J_{Ic}) for A 533 B low-upper-shelf weld material and cladding in irradiated condition (from Ref. 19)

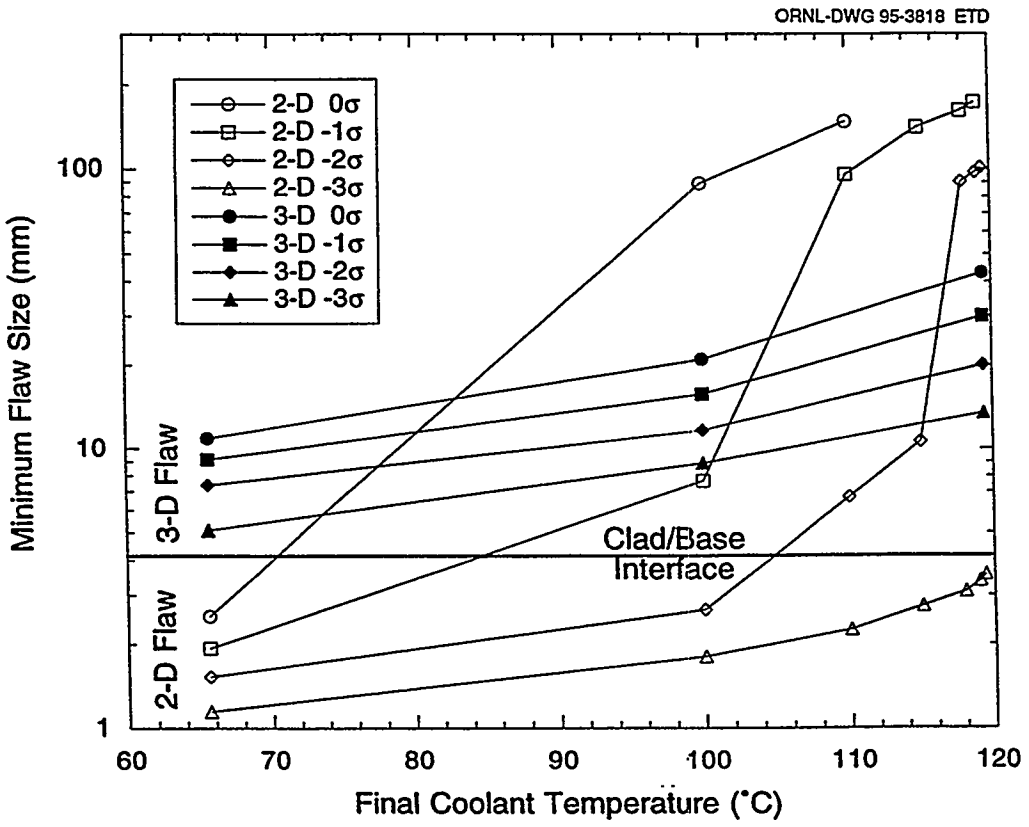

Figure 3.3 Comparison of predictions for minimum flaw depth that will initiate in cleavage by OCA-P and 3-D finite element analyses

beam specimens are fabricated from a standard nuclear unit power plant shell (SNUPPS) segment (removed from a canceled nuclear plant) that includes weld, plate, and clad material. Test were conducted on specimens containing through-thickness shallow flaws (~11 mm deep) that were located near the edge of the cladding HAZ in fabrication weld material. A large variation in fracture toughness (i.e., ranging from 225 to 393 MPa$\sqrt{m}$) was observed in two of the tests conducted at –25°C. The lower toughness value represents a lower bound to additional ORNL shallow-flaw toughness data from A 533 B plate material[22] tested at the same temperature referenced to the nil-ductility temperature (see Fig. 3.4). The single low-toughness value obtained from the clad beam tests appears inconsistent with an interpretation of the HAZ as a high-toughness region (such as that described in Refs. 19–20). However, the clad beam data provide an extremely limited sampling of toughness properties in the HAZ and near-HAZ regions.

A factor that has potential for influencing crack initiation in the near-HAZ region is locally intensified strain-aging embrittlement (LISAE), currently being studied by Dawes.[23] Localized strain aging of material occurs at the tips of preexisting cracks located adjacent to areas where further welding operations are carried out (e.g., cracks in areas influenced by the cladding process). The transient temperature distribution of the welding process causes high opening-mode tensile stresses to be generated at the crack tip. These stresses occur at a time when local temperatures are sufficiently high for thermally activated carbon and nitrogen atoms to be available for diffusion to dislocations and to effectively lock them. An effect of this diffusion process is to restrict further plastic deformation of the crack-tip material. It follows that the transition-range fracture toughness of material at the crack tip is reduced by restricting its ability to yield and to blunt. Thus, LISAE could affect the fracture toughness associated with preexisting subclad cracks.

3.2.2 Cladding Assessment Program

Currently, there is no clear consensus on how to treat the cladding overlay in assessments of shallow-flaw behavior in RPVs. A joint Electric Power Research Institute (EPRI)/ NRC Experts' Workshop Meeting[24] described several areas of investigation that should be addressed to clarify these cladding issues:

- measurement of the material and fracture-toughness properties of cladding and quantifying long-term aging effects on cladding properties;
- assessment of the mechanical effects of cladding on crack initiation and extension in the base material;
- estimation of the residual stresses produced during the history-dependent loading of the cladding (i.e., during the cladding applications, the stress-relieving process, the preservice hydrotest, and startup/shutdown cycles);

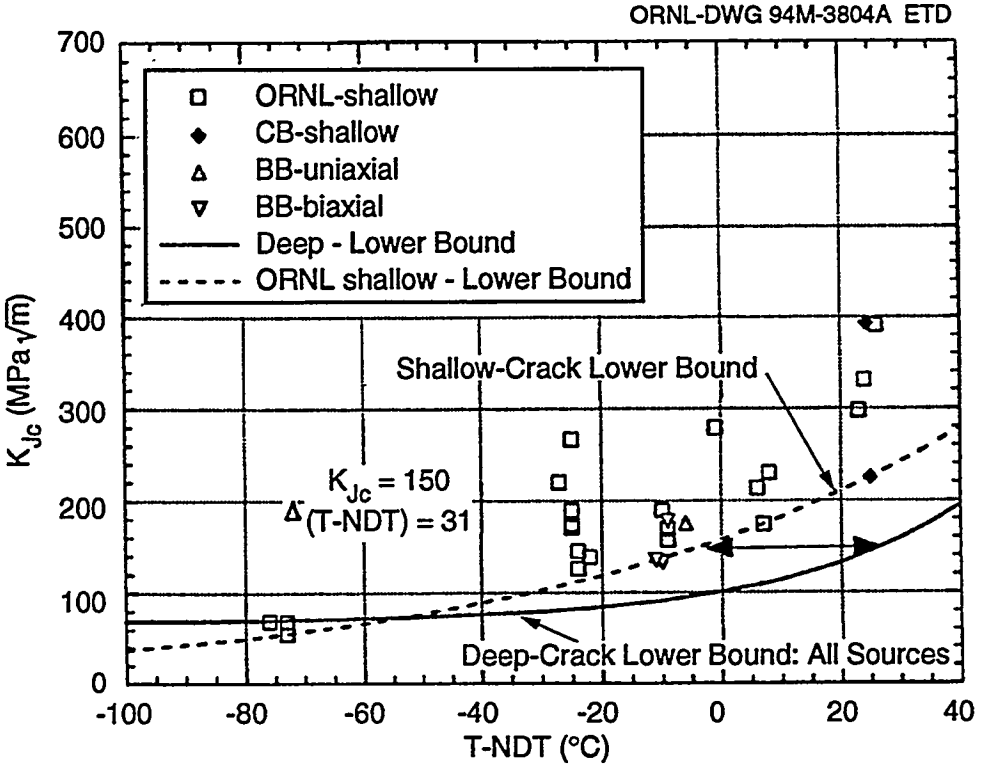

Figure 3.4 HSST shallow-crack fracture-toughness results as function of normalized temperature T – NDT

- effects of differences in thermal expansion coefficients between the cladding and base metal in analyses of overcooling accidents.

Reference 24 asserted that at least some of the simplifications employed in RPV clad modeling (and described previously) are overly conservative, primarily because of a lack of appropriate data regarding material and toughness properties and service flaw distribution. Enhancements in RPV analysis models were also recommended to remove uncertainties concerning whether other cladding assumptions are conservative or nonconservative.

Research plans have been formulated within the HSST Program that focus on several of the issues raised in Ref. 24. An HSST workscope was developed to provide (1) a quantitative description of cladding effects on the fracture behavior of shallow finite-length surface flaws in RPVs and (2) a basis for improved treatment of surface-flaw geometries in fracture assessment procedures applied to PTS and pressure-temperature (P-T) limit transients. Testing and analysis of clad specimens containing finite-length shallow surface cracks will be performed as part of the workscope. Ductile deformation and failure processes are known to be sensitive to the biaxial stress fields (i.e., axial/circumferential in a cylindrical vessel) that are imposed on an RPV wall by pressure and thermal loading conditions. Consequently, an ORNL-developed clad cruciform specimen[25–27] that can be loaded either uniaxially or biaxially was proposed for the testing program. This approach ensures that effects of PTS biaxial stress fields on shallow through-clad surface flaws are simulated in the test specimen in a controlled and cost-effective manner.

Clad cruciform specimens will be fabricated from clad-weld-plate material taken from the SNUPPS reactor vessel shell section located at ORNL. The weld-overlay cladding from the SNUPPS segment will be retained in the test section of the cruciform specimen. These test sections will be fabricated from the SNUPPS clad-weld material in the "as-received" condition to take advantage of the relatively high yield-stress properties of the weld material.[21] A preliminary test matrix incorporating 28 intermediate- and large-scale cruciform test specimens has been defined for the testing program.

3.2.3 Reactor Vessel PTS Analyses

This section describes the initial phase of an analytical study of clad modeling effects on predictions of cleavage fracture initiation in an RPV subjected to PTS loading conditions.

3.2.3.1 RPV Model and Loading Conditions

The model of the vessel had an internal radius (R_i) of 2.18 m (86 in.), wall thickness (w) of 0.216 m (8.5 in.), and cladding thickness of 5.1 mm (0.2 in.). The thermophysical and elastic properties used in these PTS analyses are given in Table 3.1. The assumed level of embrittlement was the current PTS screening criterion for axially oriented welds;[28] that is, $RT_{NDTs} + 2\sigma = 132°C$ (270°F).

Table 3.1 Thermophysical and elastic properties of base material and cladding

Property	Base material	Clad material
Thermal conductivity	42 W/m-°C (24 Btu/h-ft-°F)	17.5 W/m-°C (10 Btu/h-ft-°F)
Specific heat	502 J/kg-°K (0.12 Btu/lb-°F)	502 J/kg-°K (0.12 Btu/lb-°F)
Density	7.84 g/cm^3 (489 lb/ft^3)	7.84 g/cm^3 (489 lb/ft^3)
Elastic modulus	193,000 MPa (28,000 ksi)	186,150 MPa (27,000 ksi)
Thermal expansion coefficient	14.1×10^{-6}/°C (7.85×10^{-6}/°F)	17.8×10^{-6}/°C (9.90×10^{-6}/°F)
Poisson's ratio	0.3	0.3

Loading of the vessel was provided by stylized thermal transients of varying severity, analogous to the PTS benchmark transients utilized in the NRC/EPRI-cosponsored PTS benchmarking exercise.[29] The thermal transient is characterized by an exponentially decaying coolant temperature given by

$$T(t) = T_f + (T_i - T_f) \exp(-\beta * t) \qquad (3.1)$$

where

$T(t)$ = the coolant temperature at time t,
T_i = the coolant temperature at time t = 0,
T_f = the final coolant temperature,
β = the exponential decay constant (min^{-1}).

In these analyses, values of T_f ranged from 66°C (150°F) to 121°C (250°F), while β was held constant at 0.15 min^{-1} in all cases. The initial temperature was 288°C (550°F), and the internal pressure was assigned values of 0, 6.9, and 13.8 MPa (0, 1, and 2 ksi). Figure 3.5 depicts the coolant temperature as a function of transient time as determined from Eq. (3.1) for three different values of the final coolant temperature.

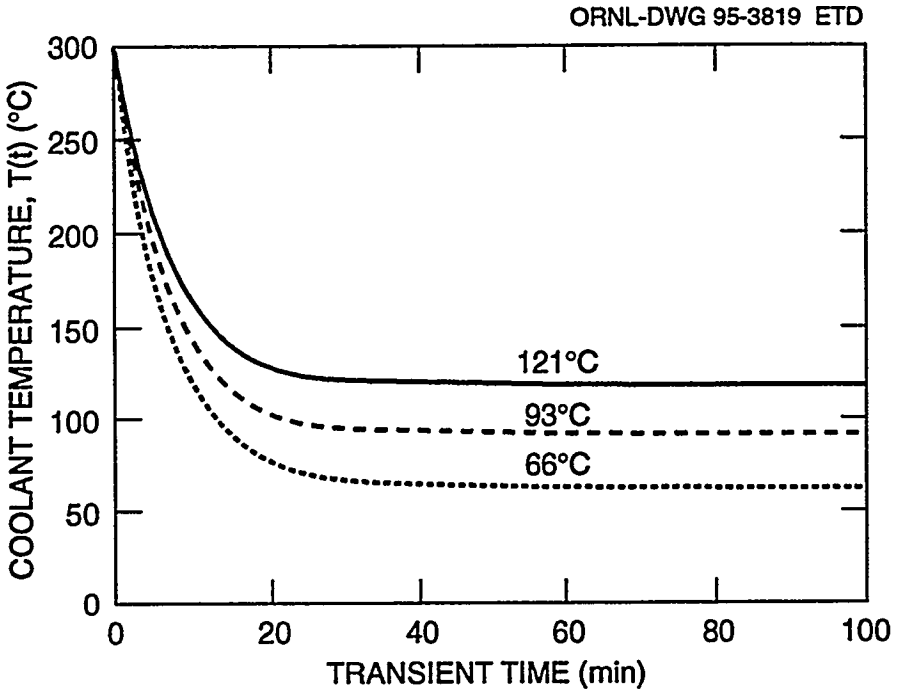

Figure 3.5 Coolant temperature as function of time for thermal transients described by Eq. (3.1)

For these calculations, the clad stress-free temperature was taken to be the initial (or operating) temperature of 288°C. Effects of varying the clad stress-free temperature on the models described herein will be examined in a later study.

3.2.3.2 Deterministic Analyses

The deterministic fracture minimization option of the FAVOR program[30] was used to generate critical flaw sizes for a matrix of stylized thermal transients and selected values of constant internal pressure. Specifically, FAVOR was used to compute the minimum flaw depth for cleavage initiation for a specified embrittlement, flaw geometry, and transient loading condition. All of these deterministic analyses utilized the ASME K_{Ic} curve. Critical flaw sizes were calculated for axially oriented flaws with aspect ratios (total flaw length-to-depth) of 2, 6, 10, and infinity (or 2-D). Assessments of specific refinements in modeling the cladding overlay were carried out using the RPV models given in Table 3.2. The material model designated as EPFM in Table 3.2 incorporates an approximation for effects of clad plasticity that does not allow the stress in the clad thickness to exceed 379 MPa (55 ksi). In Models II and IV, cleavage initiation is not allowed to occur at the discrete angular location on the crack front that resides in the clad region.

The base case of Model I in Table 3.2 is the model that was used in the IPTS studies referenced by RG 1.154. The elements of Model I include the ASME fracture-toughness correlation, the LEFM model, and cladding toughness

Table 3.2 RPV models and toughness correlations used in deterministic critical flaw analyses

Model No.	Material model	Clad model
I	LEFM	Base metal toughness[a]
II	LEFM	No initiation allowed
III	EPFM[b]	Base metal toughness[a]
IV	EPFM[b]	No initiation allowed

[a] In all cases, the base metal fracture toughness is given by the ASME toughness correlation.
[b] Cladding plasticity is modeled by restricting stress in clad region to not exceed 379 MPa (55 ksi).

equal to that of base metal. In Figs. 3.6–3.8, analysis results are given for Model I expressed in terms of critical flaw depth (a_{cr}) vs final coolant temperature (T_f) for three values of constant internal pressure, that is, 0, 6.9, and 13.8 MPa (0, 1, and 2 ksi), respectively. [The Figs. 3.6–3.8, as well as the other figures in this section, are presented with two scales for plots of critical crack depth: (1) a scale having maximum crack depth of 100 mm and (2) an expanded scale to elucidate differences in critical flaw depths predicted for lower values of T_f.] Over the lower range of T_f values, results for the 2-D flaws exhibit the minimum values for critical flaw depth. With increasing T_f, a crossover point is reached, beyond which the curve for semicircular flaws (aspect ratio = 2) provides the minimum values for critical flaw depth. This result is similar to that observed in the analyses of Ref. 15 and summarized in Fig. 3.3. The value of T_f corresponding to this crossover

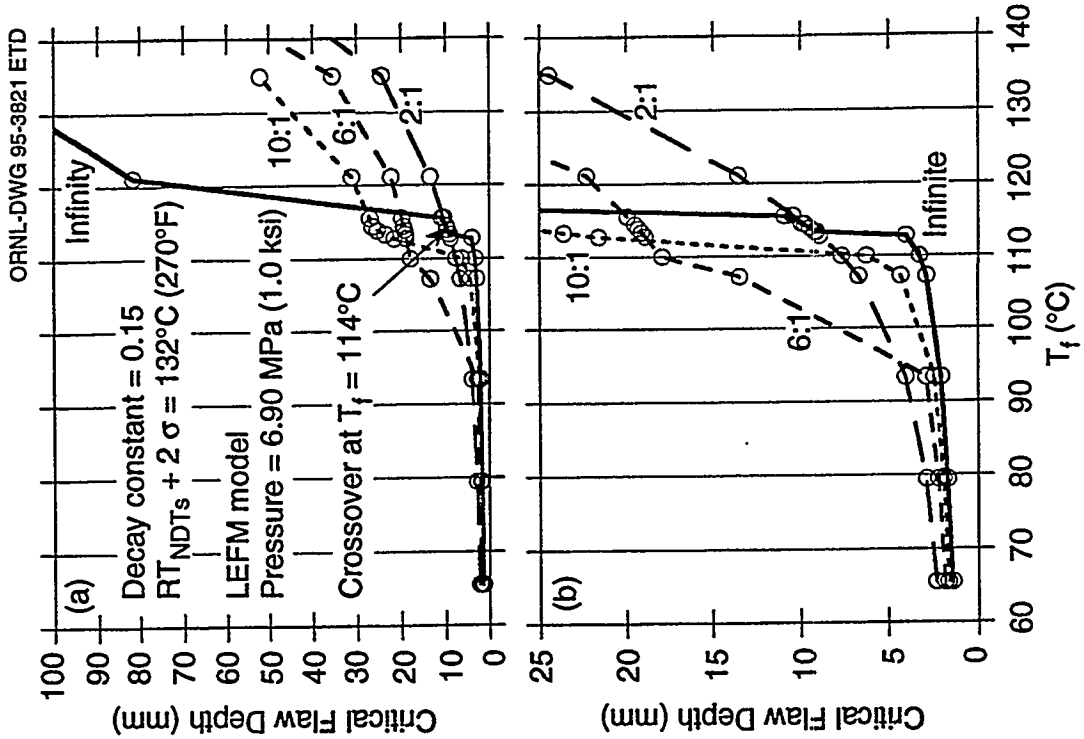

Figure 3.7 Critical flaw depths (scale 0–100 mm) vs T_f for four flaw configurations in RPV evaluated at PTS screening criteria; LEFM model with pressure p = 6.9 MPa

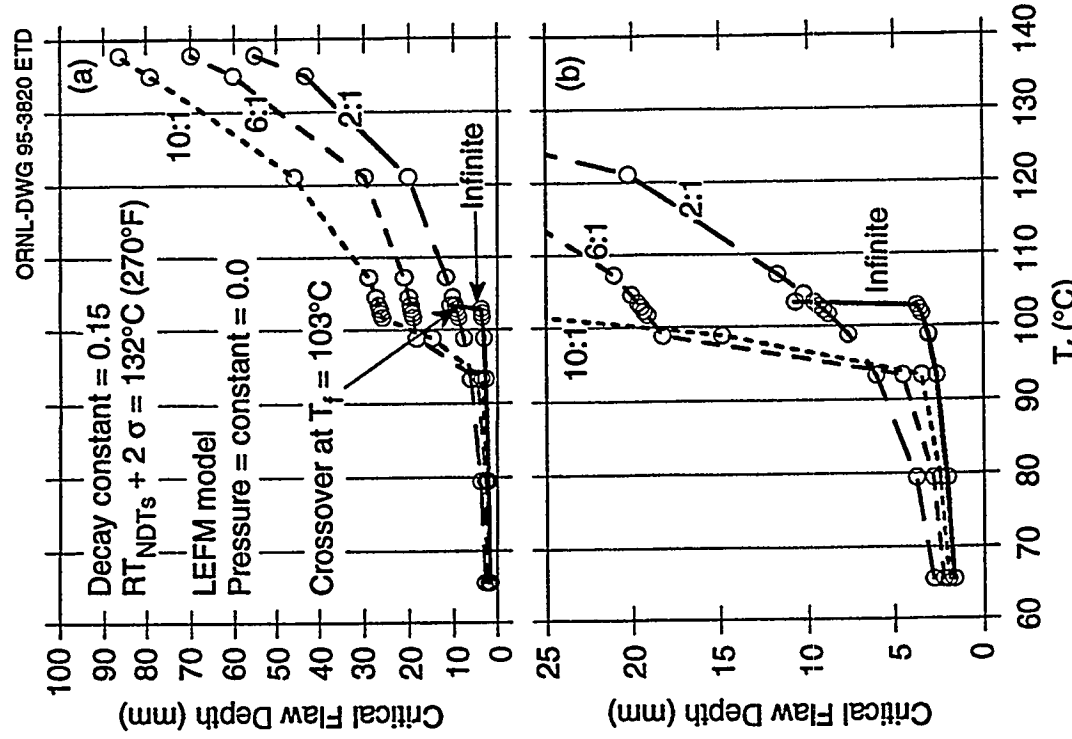

Figure 3.6 Critical flaw depths (scale 0–100 mm) vs T_f for four flaw configurations in RPV evaluated at PTS screening criteria; LEFM model with pressure p = 0

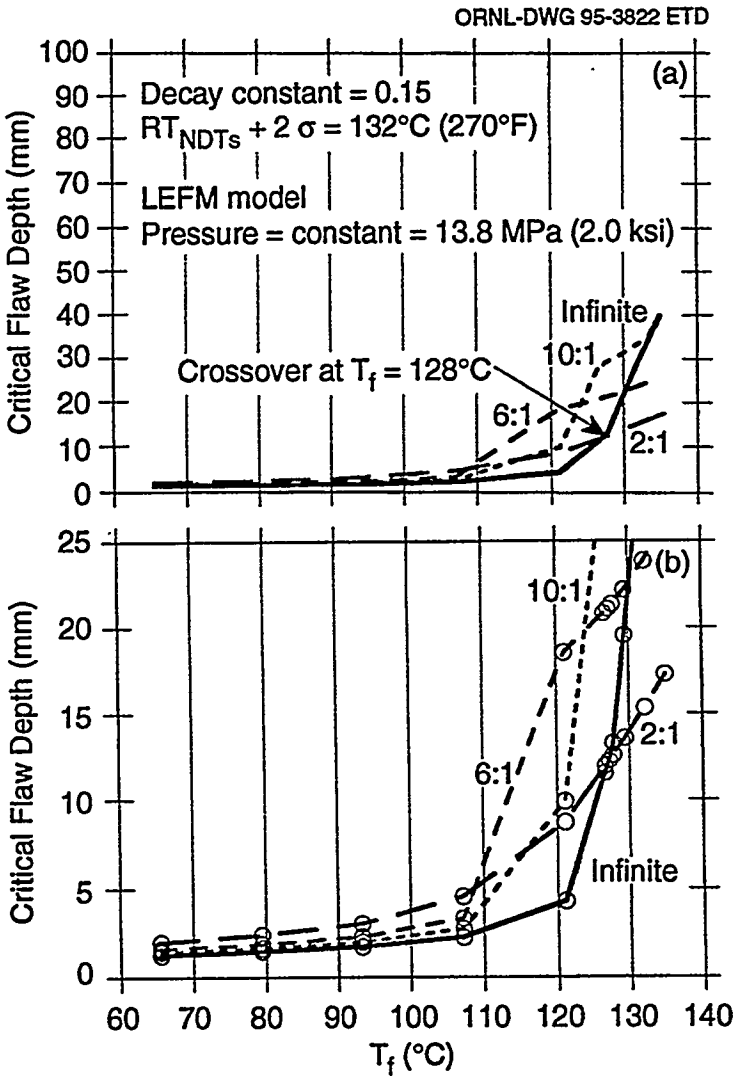

Figure 3.8 Critical flaw depths (scale 0–100 mm) vs T_f for four flaw configurations in RPV evaluated at PTS screening criteria; LEFM model with pressure p = 13.8 MPa

point increases with increasing internal pressure. Also, note that critical flaw depth is relatively less sensitive to flaw aspect ratio for the lower values of T_f considered in this study.

The K-ratios (defined as the ratio of applied K_I to the fracture toughness K_{Ic} at temperature T) computed for semicircular flaws (aspect ratio = 2) have a maximum at the intersection of the flaw with the inner surface for all transients used to generate Figs. 3.6–3.8. However, for flaws with aspect ratios of 6 and 10, the point of maximum K-ratio moves from the deepest point toward the surface for increasing values of T_f. This behavior of the point of maximum K-ratio provides an explanation for the relatively smooth curves generated for semicircular flaws and for the abrupt changes in critical flaw depth exhibited by curves for aspect ratios of 6 and 10.

The curves of critical flaw depth in Fig. 3.9 were constructed from Figs. 3.6–3.8 by selecting, for a given pressure and final coolant temperature, the minimum value of critical flaw depth computed for the four aspect ratios. The FAVOR analyses were repeated using Models II through IV from Table 3.2 to generate the results depicted in Figs. 3.10–3.12, corresponding to internal pressures p = 0, 6.9, and 13.8 MPa, respectively. Thus, the curves for Models II through IV also represent minimum values of critical flaw depth computed for the four aspect ratios. For the case p = 0, Fig. 3.10 shows the increase in critical flaw depth that follows when the assumptions from Table 3.2 concerning clad fracture toughness and yield stress are applied separately (i.e., Models II and III, respectively) and then in combination (i.e., Model IV). Also, Fig. 3.10 includes, for comparison, the critical flaw depth curve taken from Fig. 3.8 that corresponds to the base case of Model I and p = 0. Analogous results for constant internal

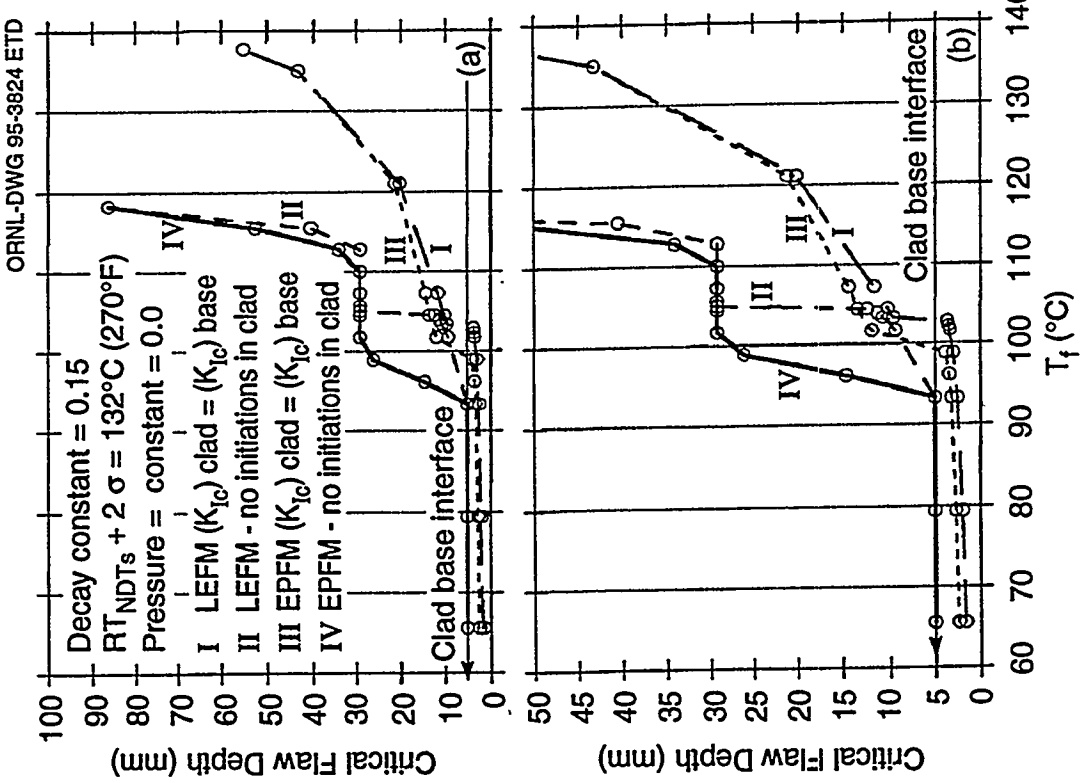

Figure 3.10 Critical flaw depths (scale 0–100 mm) vs T_f for four cladding models applied to RPV evaluated at PTS screening criteria; pressure = 0

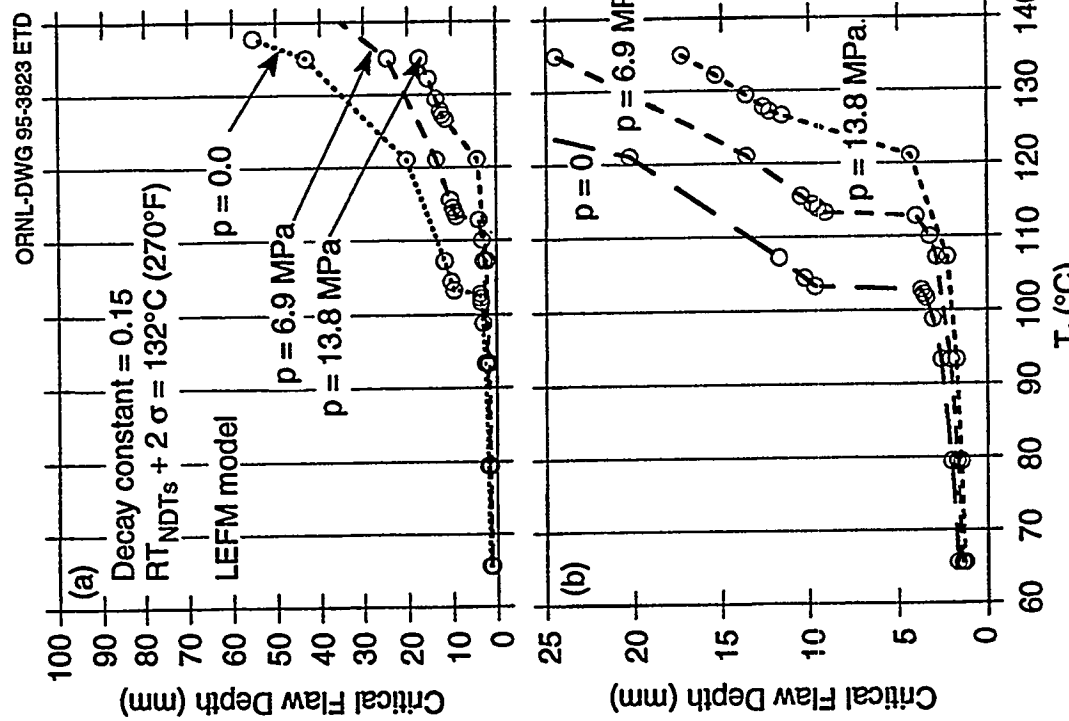

Figure 3.9 Minimum critical flaw depths (scale 0–100 mm) vs T_f and pressure for RPV evaluated at PTS screening criteria; LEFM model

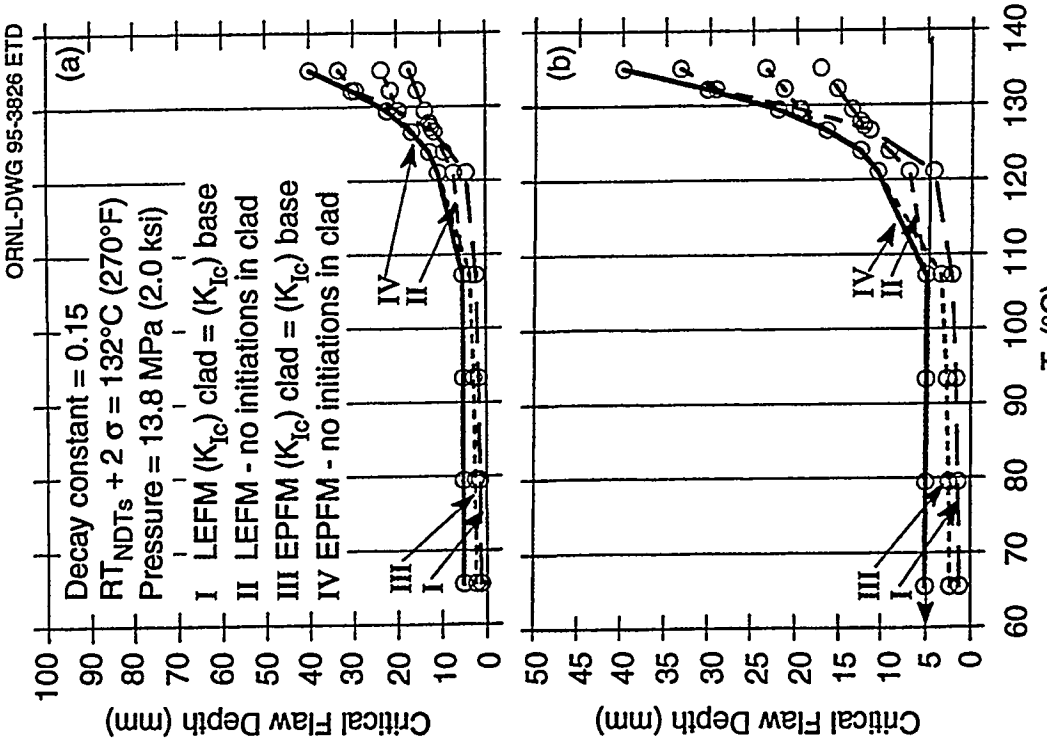

Figure 3.12 Critical flaw depths (scale 0–100 mm) vs T_f for four cladding models applied to RPV evaluated at PTS screening criteria; pressure = 13.8 MPa

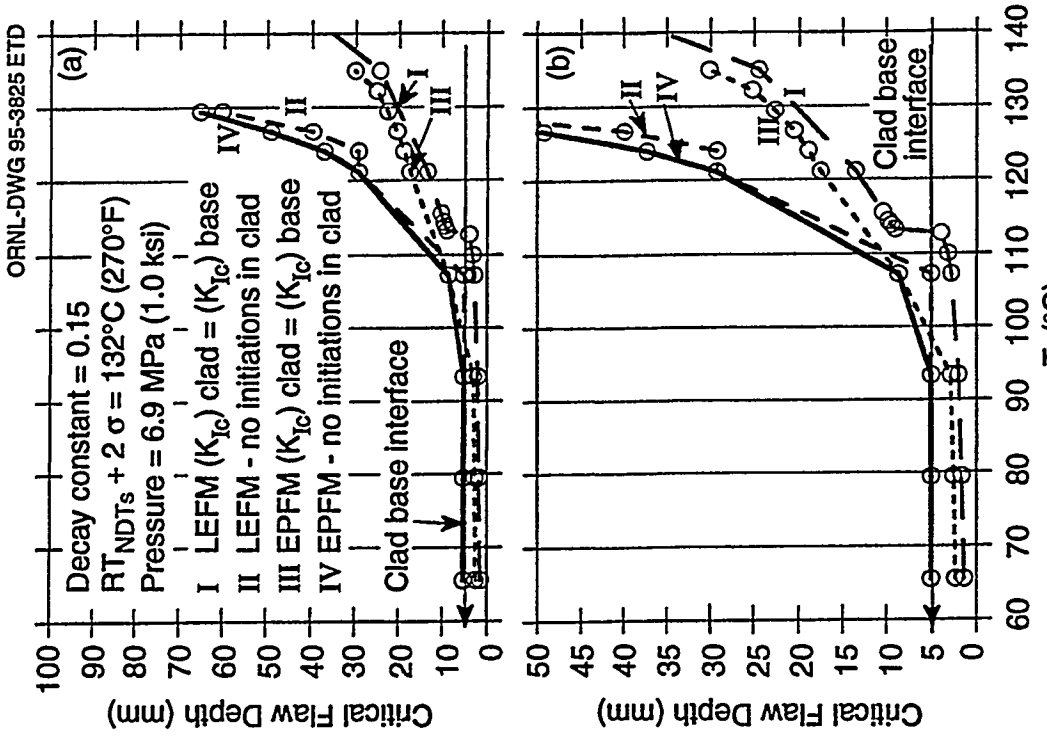

Figure 3.11 Critical flaw depths (scale 0–100 mm) vs T_f for four cladding models applied to RPV evaluated at PTS screening criteria; pressure = 6.9 MPa

pressures p = 6.9 and 13.8 MPa are given in Figs. 3.11 and 3.12, respectively. The results for Model III imply that the clad yielding assumption has a somewhat limited effect on the critical flaw depth curves for the range of pressures and final coolant temperatures considered in this study. Furthermore, effects of the cladding toughness assumption (see Model II) on critical flaw depth are more pronounced for lower pressures and for less severe thermal transients (i.e., higher values of final coolant temperature).

Results from the deterministic analyses showed that critical flaw depth and shape are strongly dependent on the severity of the thermal-shock transient. The 2-D flaws provided the minimum values of critical flaw depth for the more severe thermal transients (i.e., lower values of T_f considered herein). With increasing T_f (i.e., less severe thermal transients), a point is reached beyond which the results for semicircular flaws (aspect ratio = 2) provide the minimum critical flaw depth. When initiations are precluded in the cladding layer, predicted increases in critical flaw depth were more pronounced for lower pressures and for less severe thermal transients. The clad yielding assumption had less influence on critical flaw depth curves than the toughness assumption for the range of pressures and final coolant temperatures considered in this study.

3.2.3.4 Probabilistic Analyses

Changes in the conditional probability of initiation associated with changes in selected elements of clad RPV models for a set of PTS transients will be described in the next reporting period. These analyses will be performed using the PFM option incorporated into the FAVOR code.

3.3 Determination of Residual Stresses in Full-Thickness Clad Beams

(J. A. Keeney)

Welding can cause high tensile residual stresses during the fabrication of vessels from plates due to the temperature gradients produced during the process.[31] These stresses cause additional crack-tip loading that may be significant, especially for shallow cracks, and can be as high as the yield stress of the material. Because residual stresses can affect the performance of welded structures, and ultimately structural integrity assessments, it is important to understand the magnitude and distribution of residual stresses due to welding.

The HSST Program has been testing full-thickness clad beam specimens to quantify fracture toughness for shallow cracks in material for which metallurgical conditions are prototypic of those found in RPVs.[21] The beam specimens were fabricated from the SNUPPS shell segment that was available from a canceled pressurized-water reactor plant (the plant was canceled during construction, and the vessel was never in service). Based on standard procedures, the vessel underwent a postweld heat treatment at ~620°C (1150°F) after the cladding layer was applied. The SNUPPS material is A 533 B with a stainless steel clad overlay on the inner surface. The shell segment includes two circumferential welds and one longitudinal weld. The welds are submerged-arc welds with A 533 B class 1 filler metal. The plate material, clad overlay, and weldment are completely prototypic of a production-quality RPV. This section describes an analytical study that was carried out to estimate the residual stresses in the full-thickness clad beam specimens.

3.3.1 Details of Test Specimen

The full-thickness clad beam specimens were fabricated from the SNUPPS shell segment that has a nominal inner radius of 2210 mm (87 in.) and a thickness of 232 mm (9.125 in.). Because the initial series of three specimens was intended to investigate the fracture behavior of the longitudinal weld material, the test beams were cut in the circumferential direction of the shell. A longitudinal master blank with a length sufficient to fabricate three test beams was first flame-cut from the shell. The three required blanks were then saw-cut from the master blank and machined to final dimensions incorporating handling, load contact, and flaw details. A sketch of the specimen geometry is shown in Fig. 3.13.

The specimen was designed to be tested in three-point bending with a load span (S) of 1219.2 mm (48 in.). Flat, parallel load-contact points were machined on the top and bottom surfaces of the beam (see Fig. 3.13) to remove surface irregularities and to ensure uniform load application across the width of the beam. The flaw was machined in the beam using the wire electro-discharge machining (EDM) process and extended from the shell inner surface, that is, the clad surface, to predetermined depths into the beam. In the initial test series, one deep-flaw specimen (CB-1.1) and two shallow-flaw specimens (CB-1.2 and -1.3) were produced. Measurements of the EDM notch width were made with feeler gages prior to fatigue precracking and are listed in Table 3.3. The final dimensions for each clad beam specimen are shown in Table 3.4. Note that the flaw in each beam was machined to a different depth.

The transition temperature and tensile data were used to develop a consistent set of material properties, listed in Table 3.5, needed for the clad beam test data evaluation and the finite-element analyses. The full-thickness clad beam testing program is described in detail in Ref. 21.

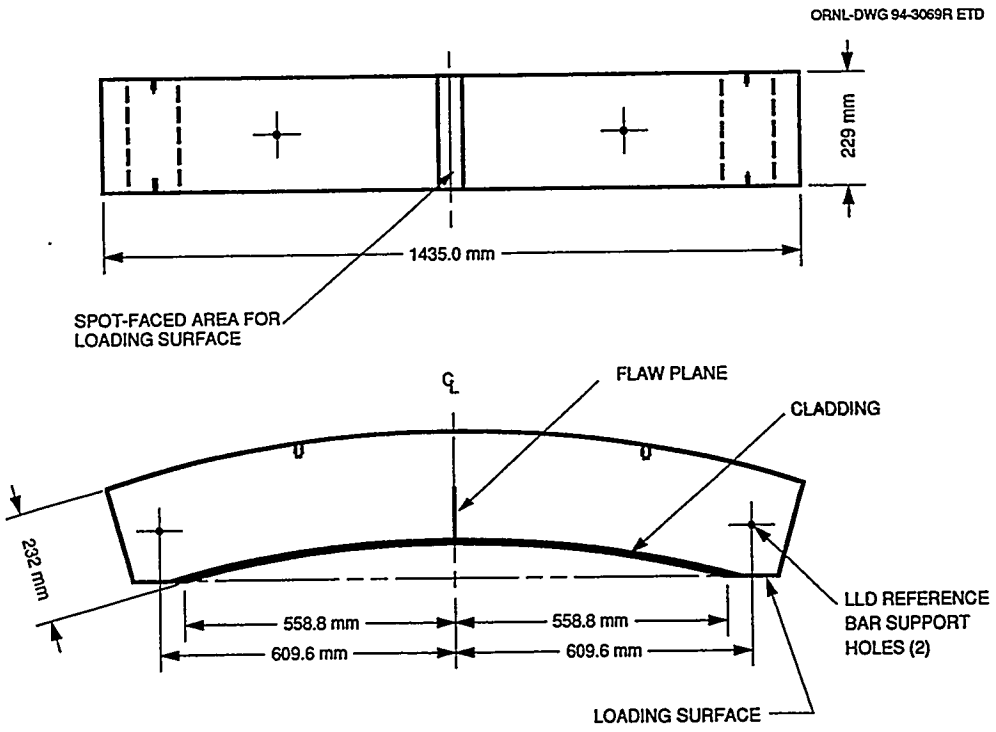

Figure 3.13 Sketch of full-thickness clad beam specimen

Table 3.3 EDM notch width measurements of full-thickness clad beam specimens

Distance from inner surface [mm (in.)]	EDM notch width [mm (in.)]		
	CB-1.1[a]	CB-1.2[b]	CB-1.3[b]
0.000 (0.0)	0.546 (0.0215)	0.033 (0.013)	0.033 (0.013)
3.800 (0.15)		0.030 (0.012)	
7.600 (0.30)		0.028 (0.011)	
10.20 (0.40)			0.030 (0.012)
20.30 (0.80)			0.028 (0.011)
38.10 (1.50)	0.470 (0.0185)		
63.50 (2.50)	0.445 (0.0175)		
88.90 (3.50)	0.406 (0.0160)		
114.3 (4.50)	0.406 (0.0160)		

[a]Average of front and back side measurements.
[b]Center measurements.

Table 3.4 Parameters defining specimen geometry of full-thickness clad beam specimens

	CB-1.1[a]	CB-1.2	CB-1.3
Load span (S), mm	1219.2	1219.2	1219.2
Thickness (B), mm	230.2	230.2	229.6
Width, (W), mm	225.7	224.3	224.3
Crack depth before fatigue precracking, mm	114.3	7.6	20.3
Crack depth, mm	117.5	10.8	23.7
Ratio, a/W	0.50	0.05	0.10

[a]Used as development beam.

3.3.2 Finite-Element Model

The 2-D plane-strain TE analyses were performed on the clad beam specimen depicted in Fig. 3.13 using the ABAQUS[32] finite-element program. A one-half section of the complete clad beam specimen illustrated in Fig. 3.13 is represented in the 2-D finite-element model of Fig. 3.14. The model of the clad beam specimen with a/W = 0.05 in Fig. 3.14 incorporates the curvature of the plate and the flat cut-out where the specimen is supported during loading. The model consists of 3712 nodes and 1155 eight-node isoparametric elements. The crack depth for each model is listed in Table 3.4 (prior to fatigue precracking). Material properties used for the analyses of the clad beam specimens were taken from Table 3.5 and from the multilinear true stress vs true plastic-strain curves given in Fig. 3.15.

The adequacy of using an elastic plane-strain model in the study was investigated by performing TE and

Table 3.5 Clad beam material properties

	Base metal	Weld metal	Cladding
Modulus of elasticity (E), MPa	200,000	200,000	152,000
Poisson's ratio (ν)	0.3	0.3	0.3
Density (ρ), kg/m^3	7861	7861	8027
Coefficient of thermal expansion (α), /°C	1.45×10^{-5}	1.45×10^{-5}	1.64×10^{-5}
Yield stress (σ_0), MPa (ksi)	440 (64)	599 (87)	367 (53)
Ultimate stress (σ_u), MPa (ksi)	660 (96)	704 (102)	659 (96)
RT_{NDT}, °C		–23	
NDT, °C		–50	

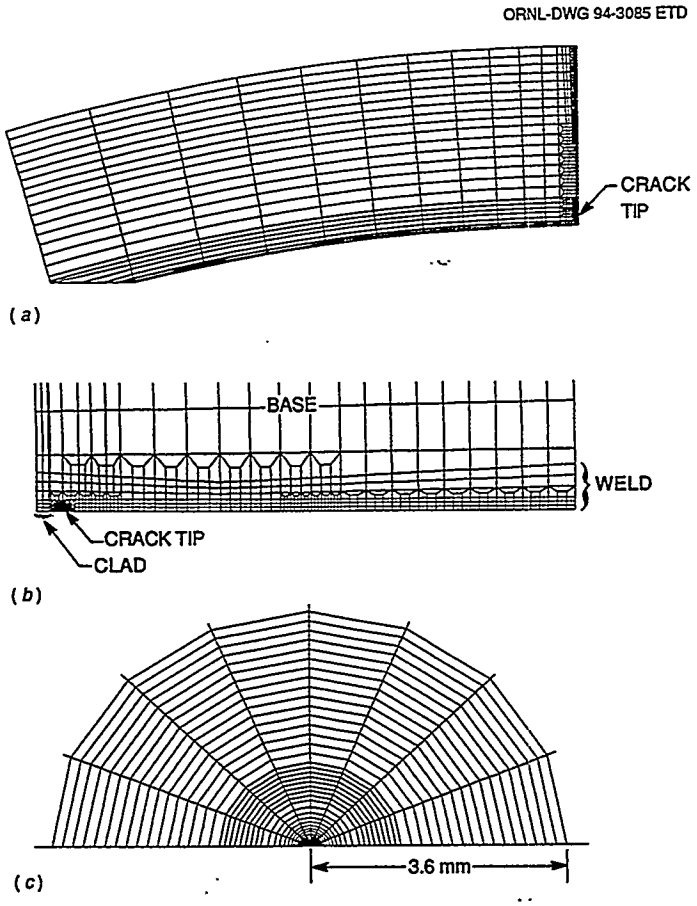

Figure 3.14 (*a*) **Finite-element mesh of clad beam specimen with a/W = 0.05,** (*b*) **crack-plane region, and** (*c*) **crack-tip region**

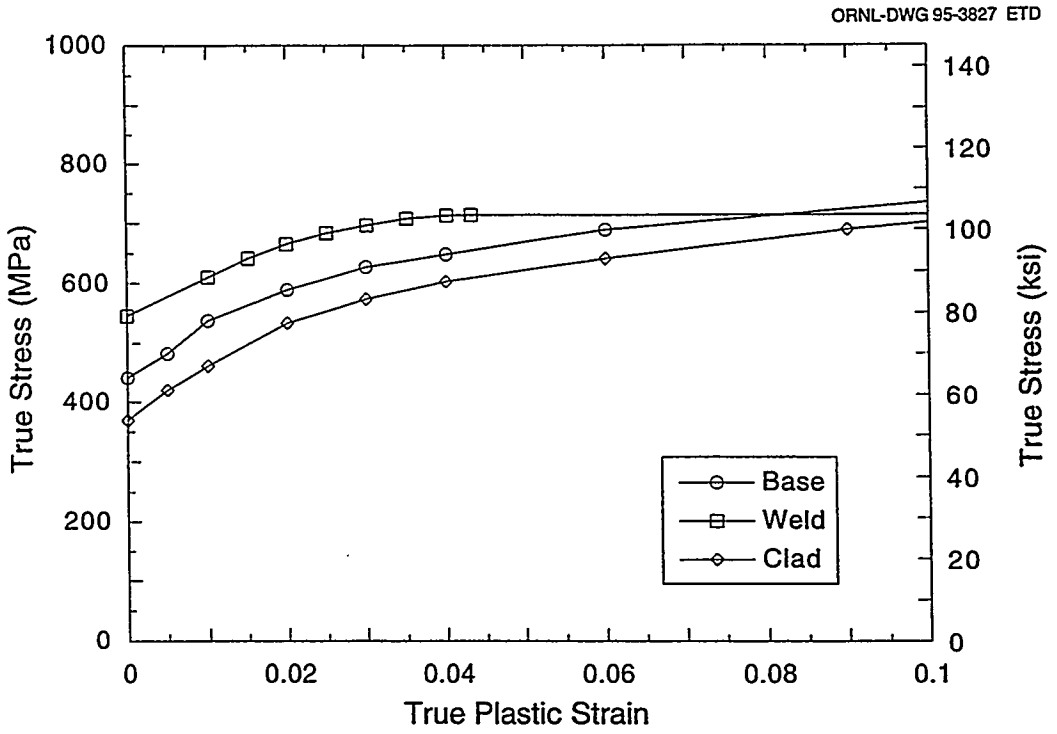

Figure 3.15 Material representation for clad beam

thermoelastic-plastic (TEP) 3-D analyses of a clad beam model without a notch. The results indicate the following:

1. 3-D analyses gave the same principal stress values using TE or TEP material models for analyses having a small or large ΔT [initial temperature set to 0°C (small ΔT) or the "stress-free" temperature (large ΔT)];
2. 2-D TE plane-strain analysis gave approximately the same in-plane stress value at the inner surface (~3% higher) as that from the 3-D TE analysis;
3. 2-D TEP plane-strain analysis techniques cannot be utilized if there is a large ΔT because it produces a large, physically unrealistic, out-of-plane stress component (σ_{zz}) and lowers the stress of interest (σ_{yy}) due to plasticity.

It was determined that the 2-D TE plane-strain model would be appropriate for this study.

3.3.3 Residual Stress Calculations

Residual stresses are generally tensile on the inside and outside surfaces of a vessel and compressive in the midwall. The stress profile is a self-equilibrating type and closely approximates a cosinusoidal shape through the vessel wall.[33] Figure 3.16, taken from Ref. 34, is an example of the approximate cosinusoidal shape of the residual stresses in an unclad welded plate. The plate material is A 533 B steel with a K bevel weld-groove geometry and thickness B = 45 mm (1.7 in.). The peak residual stress in Fig. 3.16 is ~62 MPa (9 ksi), which is similar to residual stress values [55 MPa (8 ksi)] from measurements by Combustion Engineering[33] for RPV geometries.

In the case of a single material with homogeneous properties, the postweld heat treatment of an RPV would generally relieve residual stresses. However, because of the difference in coefficients of expansion between the cladding and the base material, a residual stress pattern remains due to the cooling from the heat treatment temperature to room temperature. In an experimental study[35] to determine residual stresses in a bimaterial plate, a plate with cladding on both sides was stress relief annealed at 538°C and allowed to cool uniformly to room temperature. It was determined that the stresses in the cladding are tensile, while the stresses in the base material are compressive. In Fig. 3.17, the stresses are tensile in the cladding and increase in magnitude to a peak value of 379 MPa (55 ksi) at the weld fusion line, where the stresses become compressive in the base material. Another aspect of the study[35] was to determine the residual stresses in a 32-mm-thick specimen (cladding on one side) cut from the clad plate. Figure 3.18 shows that the stress distribution is similar to the left side of Fig. 3.17 for the full uncut plate, but the stresses for the 32-mm-thick specimen are much lower [peak stress value of 241 MPa (35 ksi)] than those for the full plate. In that case, stresses in the specimen were allowed to relax when the restraining effects of the plate were removed. Also shown in Fig. 3.18 are the base material stresses becoming

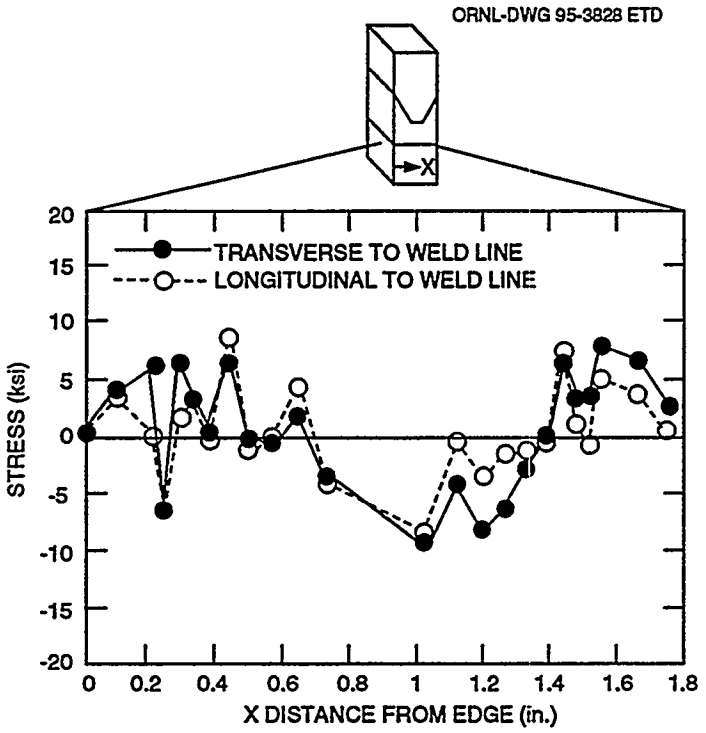

Figure 3.16 Comparison of transverse and longitudinal through-thickness residual stress distributions at back of K weld (*Source*: Ref. 39)

tensile at the outside surface. In both the specimens, the transverse and longitudinal stress distributions were essentially identical, because the width and length dimensions of the block are at least as large as the thickness dimension.

3.3.3.1 Thermal Gradient Method

The residual stresses were generated in the 2-D clad beam model by applying a fictitious temperature distribution through the thickness (B) of the beam in the form of a cosine function, shown in Fig. 3.19. The cosine function has the following form:

$$T = T_{amp} \cdot \cos\left[p \cdot (x/B)\right] \quad \left[p \cdot (x/B)\right] \leq 2\pi \ , \qquad (3.2)$$

and

$$T = -T_{amp} \quad \left[p \cdot (x/B)\right] > 2\pi \ ,$$

where T is the beam temperature, T_{amp} is the prescribed (temperature) amplitude of the cosine curve, p is a parameter that sets the period of the cosine function, and x is the distance through the beam. The initial ("stress-free") temperature was set to an arbitrary value of 0°C. The opening displacements of the notch slot were compared to the measured slot width (SW) values from Table 3.3 after the values were normalized [$SW_n = (SW - SW_d)/2$, where SW_n is the normalized slot width, SW_d is the slot width at the deepest point, and the value is divided by 2 for comparison with the 2-D model]. Good agreement was obtained between the measured and calculated displacements (shown in Fig. 3.20) for the deep notch and fair agreement for the two shallower notches, when the cosine function period (p) is set to 0.7375 and the amplitude (maximum temperature) to 14.76, 45.0, and 17.25°C for CB-1.1, -1.2, and -1.3, respectively. The period of the cosine function is less than B (not symmetric across the beam) because the beam material is not homogeneous.

When the same amplitude used in the analysis of CB-1.1 (14.76°C) was used in the analysis of CB-1.2 and -1.3, the opening displacement at the notch mouth was underpredicted by 200 and 15%, respectively. The percent error between the measured and calculated displacements increased as the notch depth decreased. The EDM notch width for CB-1.1 was measured with calipers and feeler gages at several locations along the notch and showed good agreement between the two methods of measurement. The notch widths for CB-1.2 and -1.3 were measured with feeler gages at three locations. The shallower the notch depth, the smaller the amount of deformation at the notch surface. At the lower limit of precision for the instruments (feeler gages) and with the procedures used to measure the notch width, the probable error increases as notch depth decreases, and the reliability of the measurements therefore decreases. The opening-mode (transverse) stresses, shown in Fig. 3.21, have peak values at the weld fusion line of 74, 239, and 86 MPa (11, 35, and 12 ksi) for CB-1.1, -1.2, and -1.3, respectively. The shapes of the stress

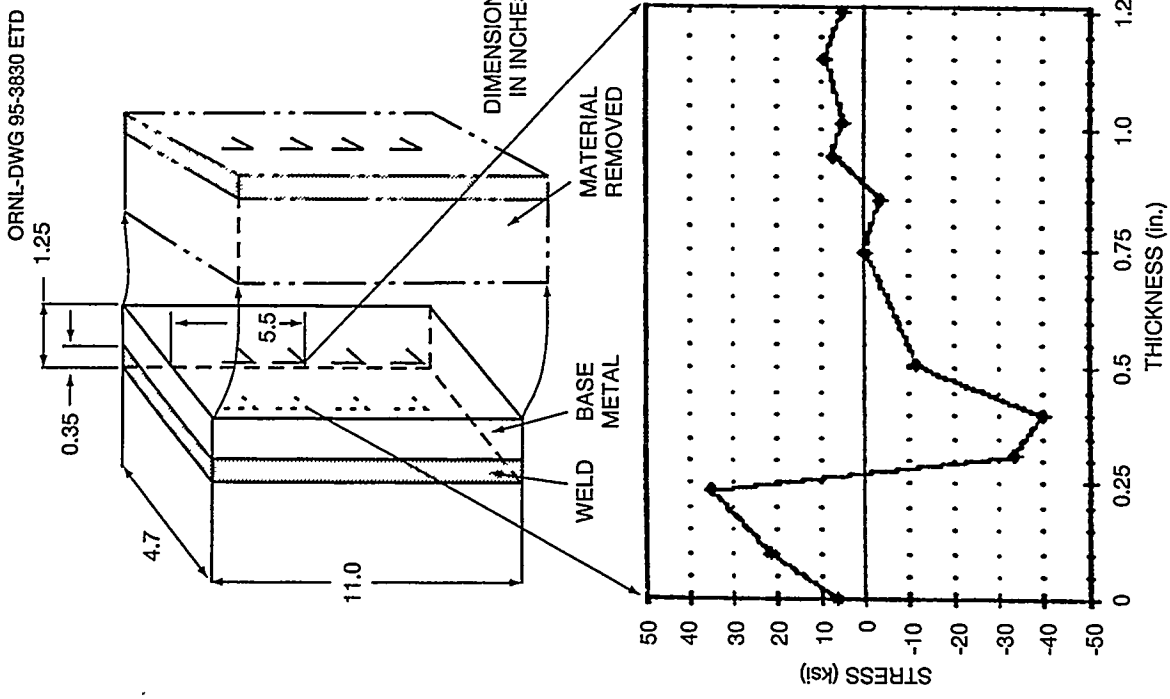

Figure 3.18 Transverse, through-thickness residual stresses in 32-mm-thick specimen with full cladding on one side measured at gage position 140 mm (5.5 in.) from edge (*Source*: Ref. 40)

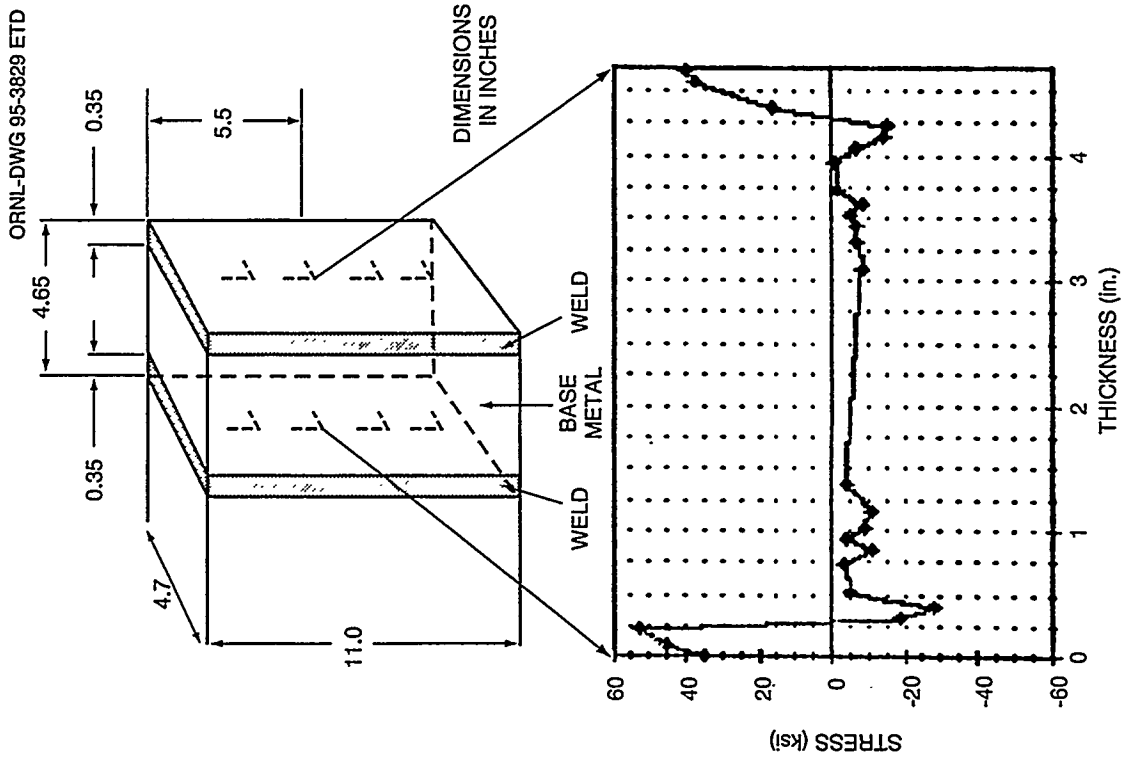

Figure 3.17 Transverse, through-thickness residual stresses in clad plate measured at gage position 140 mm (5.5 in.) from edge (*Source*: Ref. 40)

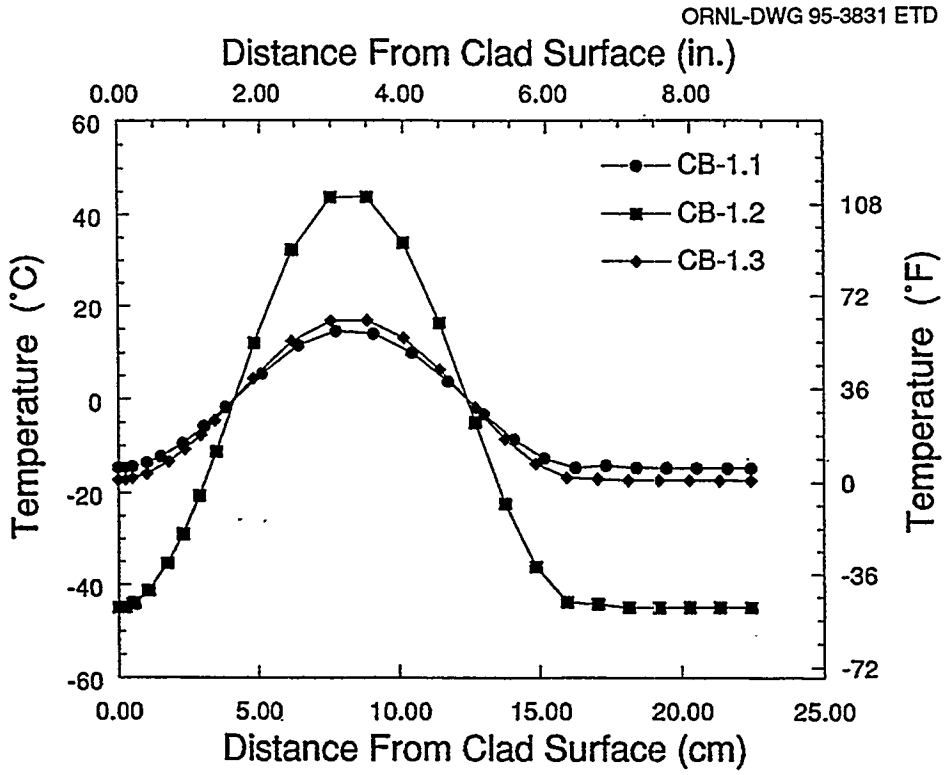

Figure 3.19 Temperature distribution through wall for clad beam specimens

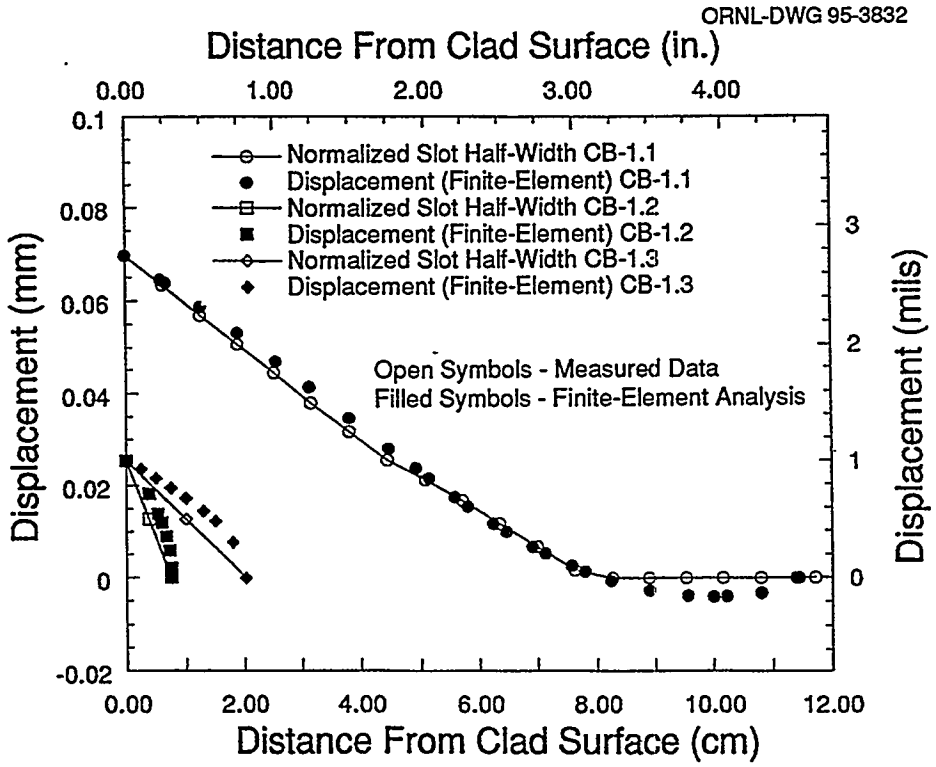

Figure 3.20 Notch-opening displacement for clad beam specimens

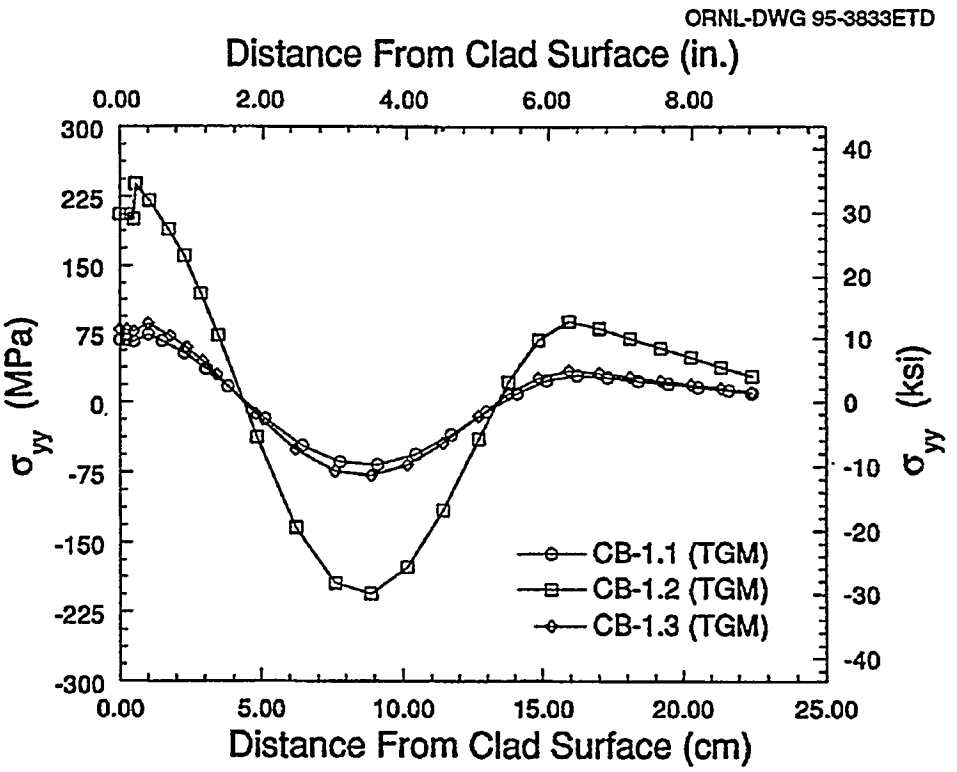

Figure 3.21 Comparison of opening-mode stress distributions for clad beam specimens calculated by thermal gradient method (TGM)

distributions compare well with what was observed in previous studies.[34,35] The peak stress values are below the yield stress values for the materials. The peak stress values for CB-1.1 and -1.3 compare well with the values reported in Refs. 33 and 34.

3.3.3.2 Fixed Displacement Method

Another method used in this study to determine the residual stresses in the clad beams is to apply fixed displacement boundary conditions (the measured notch openings) to the notch faces in the finite-element models and use elastic analysis techniques. A comparison of the opening-mode stress distributions for CB-1.1 using both methods [thermal gradient method (TGM) and fixed displacement method (FDM)] is shown in Fig. 3.22. The stresses calculated in the analyses using the FDM were reversed in sign so the comparison could be made (tension at the inner surface). There appears to be a good comparison between the two methods, except the FDM does not show a stress peak at the weld fusion line (no thermal effects). The peak stress values using the TGM and FDM are 74 and 87 MPa (11 and 13 ksi), respectively. The stress values are obtained at quarter-beam when the TGM is used, whereas the stress values using the FDM are taken from the notch plane (inner surface to the notch tip).

The FDM was also utilized in analyzing CB-1.3 (the CB-1.3 notch width measurements are thought to be more accurate than the measurements for CB-1.2). As a comparison, two analyses were performed: (1) linear notch opening (from measured data) and (2) curved notch opening (as calculated by ABAQUS using the TGM for CB-1.3). A comparison of the opening-mode stress distributions for CB-1.3 using the TGM and the FDM (linear and curved notch opening) are shown in Fig. 3.23. The peak stress values using the TGM, FDM (linear notch opening), and FDM (curved notch opening) are 86, 138, and 90 MPa (12, 20, and 13 ksi), respectively. And as a check to both methods, there is good agreement between the TGM and the FDM (curved notch opening). The two analyses using the FDM indicate that a small change in notch-opening shape results in a large change in the peak stress value at the inner surface, which highlights the importance of accurate notch-opening measurements for the shallow flaws.

3.3.3.3 Residual Stress Contributions

The measured slot openings in the clad beam specimens were the result of relaxing residual stresses from (1) clad-base material differential thermal expansion (DTE) and (2) residual stresses generated by the structural welding process that were not completely relaxed by the postweld

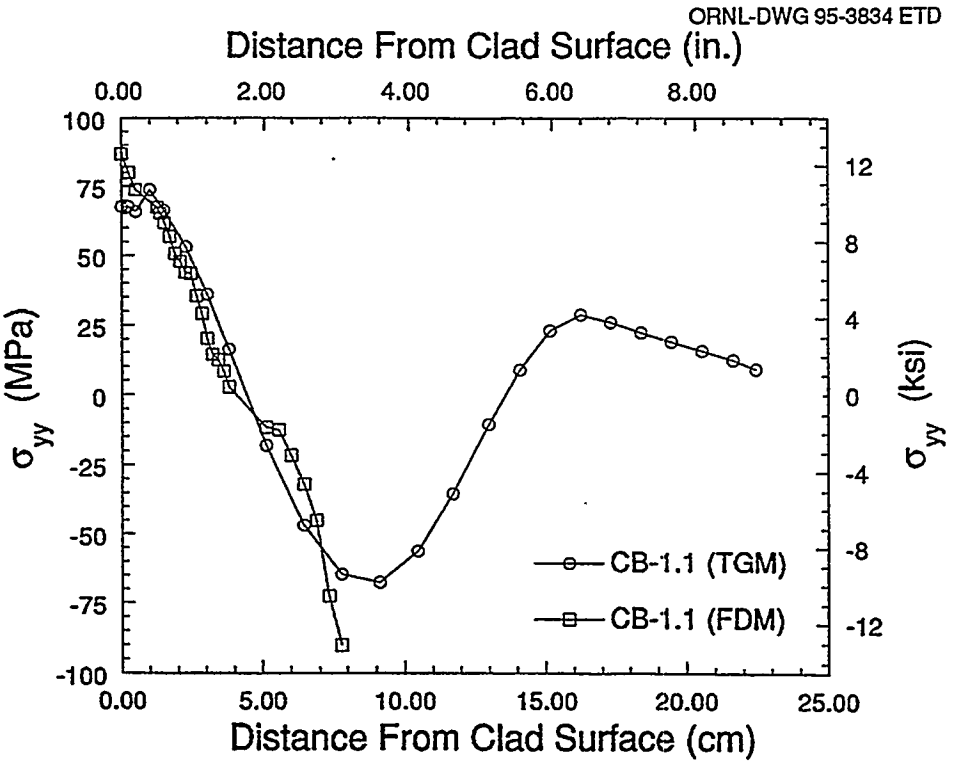

Figure 3.22 Comparison of opening-mode stress distributions for CB-1.1, calculated by TGM and FDM methods

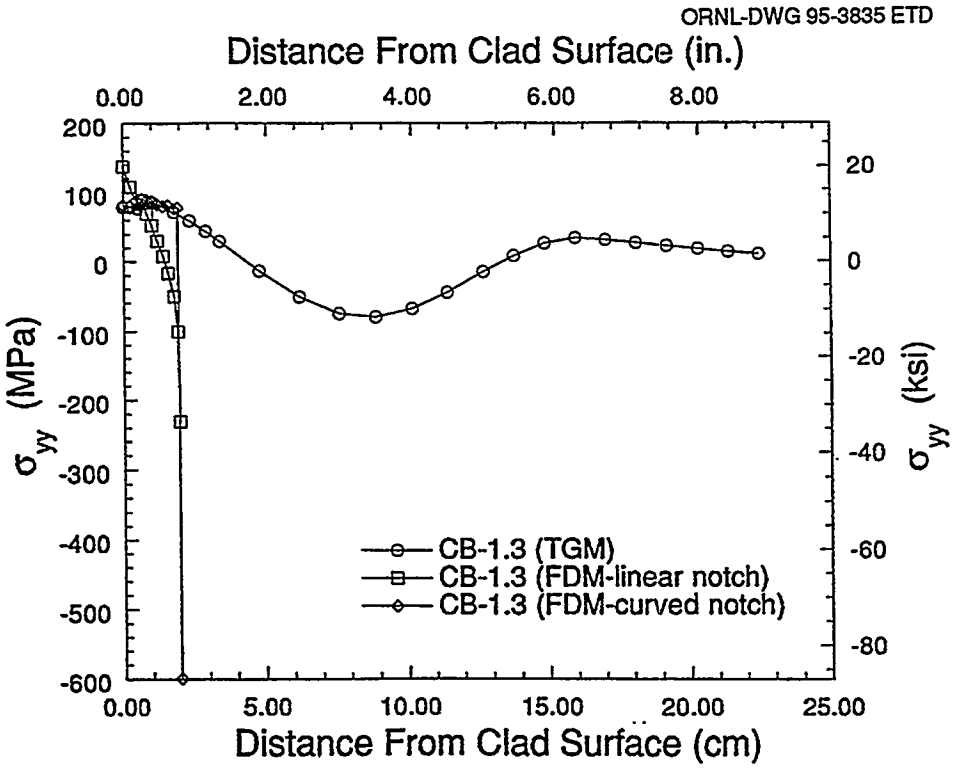

Figure 3.23 Comparison of opening-mode stress distributions for CB-1.3, calculated by TGM and FDM methods

heat treatment. A method used to estimate the effects of the welding process alone (item 2) was to cool the clad beam specimen uniformly from an assumed stress-free temperature of 315.6°C to room temperature (22°C). The opening displacement of the notch from the cooldown is due to the DTE of the two materials. The difference between the slot displacement from the cooldown and the total displacement is the contribution from the welding process. This method was utilized for CB-1.1 and -1.3 and resulted in the welding process contributing to 69 and 34% of the measured slot displacements, respectively.

Good agreement was obtained between the measured and calculated displacements for the deepest notch and fair agreement for the two shallow notches using the TGM. The period of the cosine function used in these calculations is less than B (not symmetric across the beam) because the beam material is not homogeneous (clad, weld, and base material). The percent error between the measured and calculated displacements increased as the notch depth decreased when the same cosine amplitude was used. At the lower limit of precision for the instruments (shallow notch widths), the measurement error increases and the reliability of the measurements decreases. Accurate notch-opening measurements are important because a small change in notch-opening shape results in a large change in the peak stress value. A method used to estimate the effects of the welding process alone on the amount of slot displacement resulted in a contribution of 69 and 34% of the measured slot displacements for CB-1.1 and -1.3, respectively.

There appears to be a good comparison between the calculated residual stress values using the TGM and the FDM for CB-1.1, except that the FDM does not show a stress peak at the weld fusion line (no thermal effects). The peak stress values using the TGM and FDM are 74 and 87 MPa (11 and 13 ksi), respectively. The residual stress values may be larger in the RPV shell segment from which the clad beam specimens were fabricated. A previous study[35] showed that the stress level in the specimen cut from the plate is lower than that in the plate prior to cutting (57% decrease in the peak stress value). In that case, stresses in the specimen were allowed to relax when the restraining effects of the plate were removed.

3.4 Full-Thickness Clad Beam Testing and Analysis (B. R. Bass, J. A. Keeney, and W. J. McAfee, ORNL; R. J. Fields and R. deWit, NIST)

Detailed finite-element analyses were performed at ORNL on the test data obtained from the fourth full-thickness clad beam specimen (CB-1.4). The CB-1.4 specimen was tested at the National Institute of Standards and Technology (NIST), Gaithersburg, Maryland, during August 1994.

3.4.1 Clad Beam Model

The 2-D finite-element model of the clad beam specimen (see Fig. 3.13) employed in these analyses is essentially the same as the model depicted Fig. 3.14. The model of the clad beam with a/W = 0.05 incorporates the curvature of the plate and the flat cut-out where the specimen is supported during loading. The model has a highly refined mesh in the crack-tip region [see Fig. 3.14(*c*)] to provide resolution of stress fields over the normalized distance $2 \le r\sigma_0/J \le 10$ in front of the crack; r is the distance from the crack tip, and σ_0 is the yield stress. Collapsed-prism elements arranged in a focused fan configuration at the crack tip are used to produce a 1/r strain singularity appropriate for inelastic analysis. Reduced integration (fewer sampling points) was used for all the elements except for the inner ring of elements at the crack tip in the shallow-crack models. The use of full integration for the innermost ring of elements helps in the convergence of the model at high loads.

Material properties used for posttest analyses of the clad beam specimen were taken from Table 3.5 and from the multilinear true stress vs true plastic-strain curves given in Fig. 3.15. The plane-strain analyses were carried out using an incremental elastic-plastic constitutive model and small-strain theory. Local crack-tip fields obtained from these analyses are used in the application of stress-based constraint characterization models.

3.4.2 Analysis Results

Results from the posttest analyses of test CB-1.4 are summarized in Figs. 3.24–3.29. Comparison of the measured and calculated P vs displacement responses provides a way to interpret the accuracy of the analysis results and to establish confidence in the calculated fracture-mechanics parameters. The calculated P vs LLD curves are compared with measured data from the test in Fig. 3.24. For comparison, results for tests CB-1.1, -1.2, and -1.3 are also included in Fig. 3.24. For the shallow-crack specimens, calculated LLD values at a given load were greater than measured values for the full range of loading. In contrast, comparisons of calculated and measured P vs CMOD in Fig. 3.25 show good agreement. The difficulties in analytically modeling the measured responses of P vs LLD and P vs CMOD simultaneously have been described in Ref. 21. For the analyses presented herein, emphasis was placed on modeling the P vs CMOD response accurately for use in determining fracture toughness.

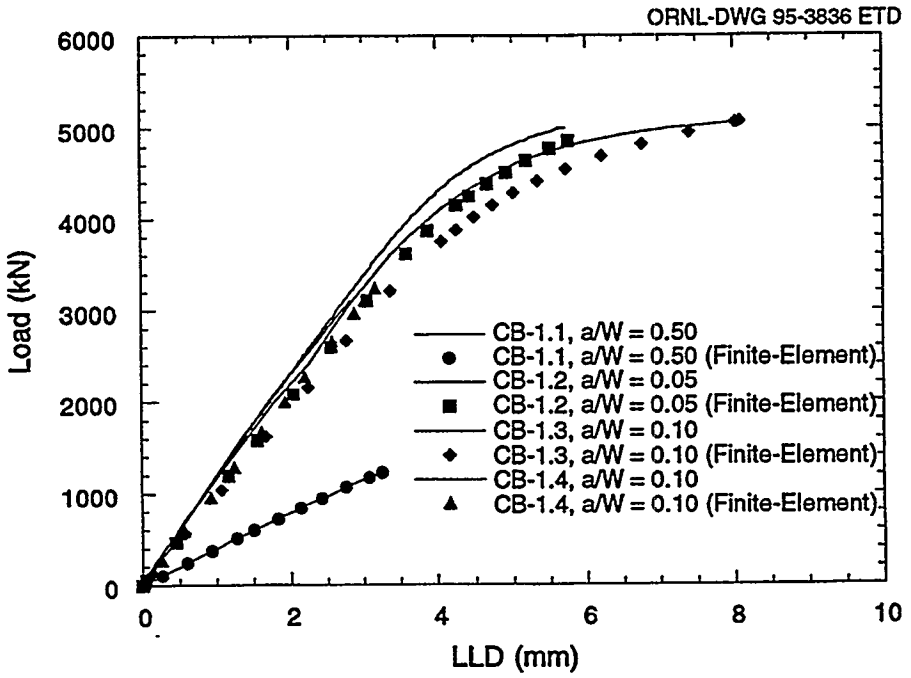

Figure 3.24 Comparison of calculated and measured LLD for full-thickness clad beam specimens

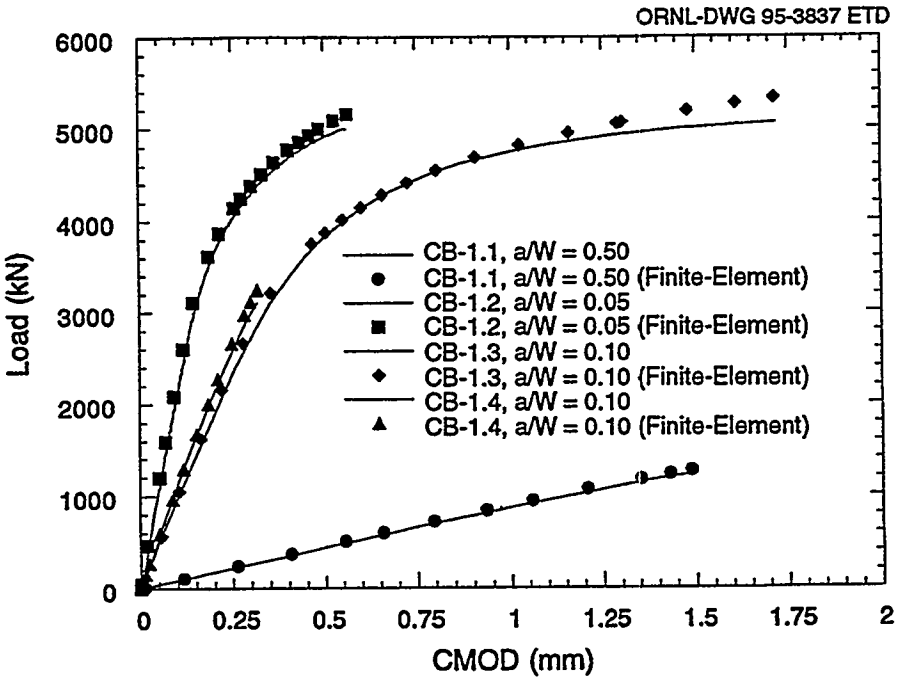

Figure 3.25 Comparison of calculated and measured CMODs for full-thickness clad beam specimens

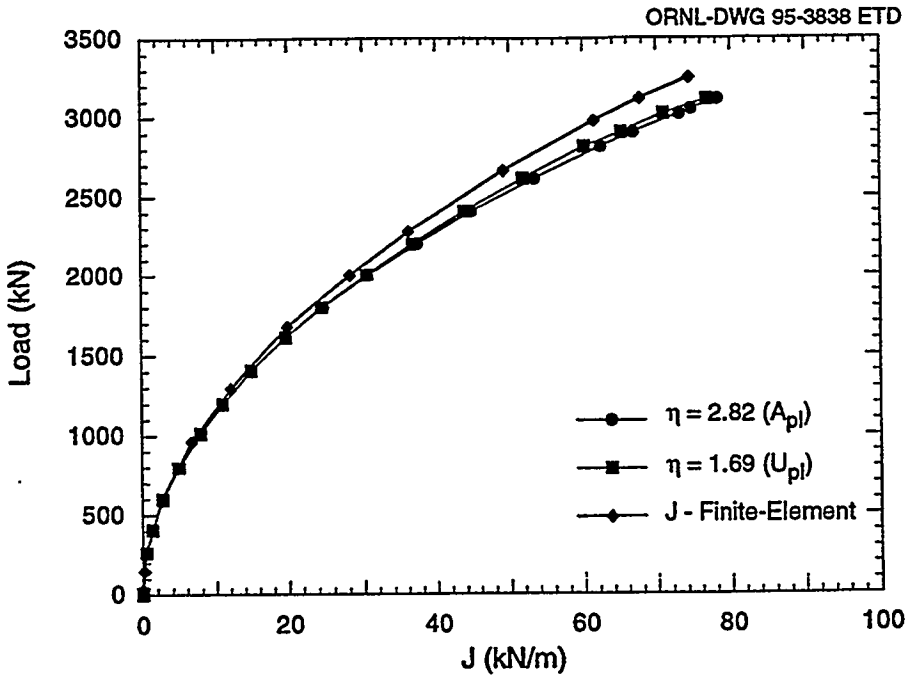

Figure 3.26 Comparison of calculated J values for clad beam specimen CB-1.4 (a/W = 0.10)

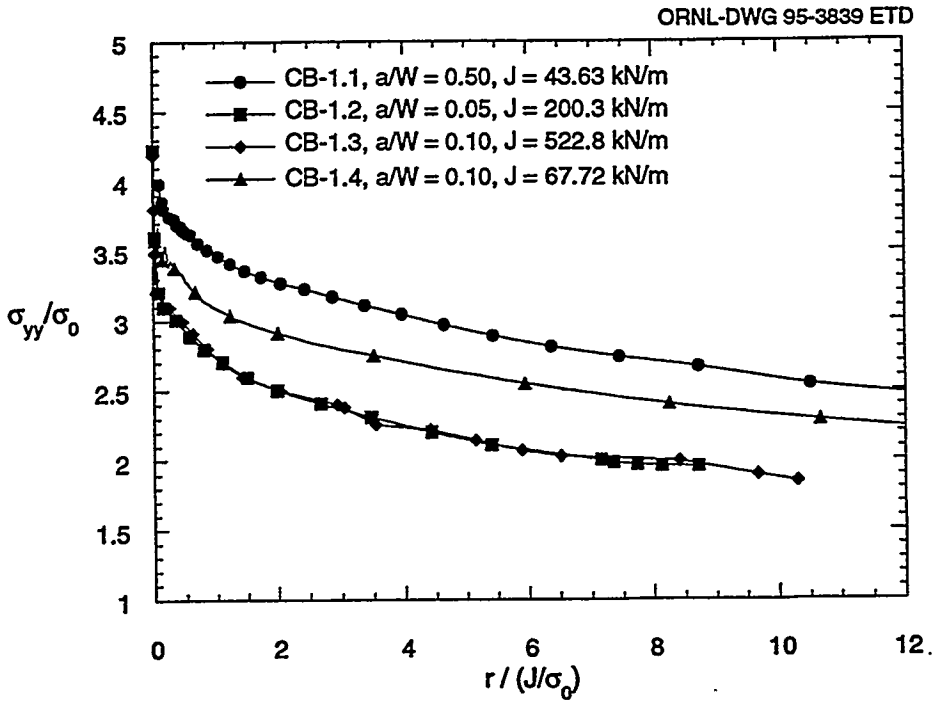

Figure 3.27 Distribution of normalized opening-mode stress for clad beam specimens as function of applied J at crack initiation

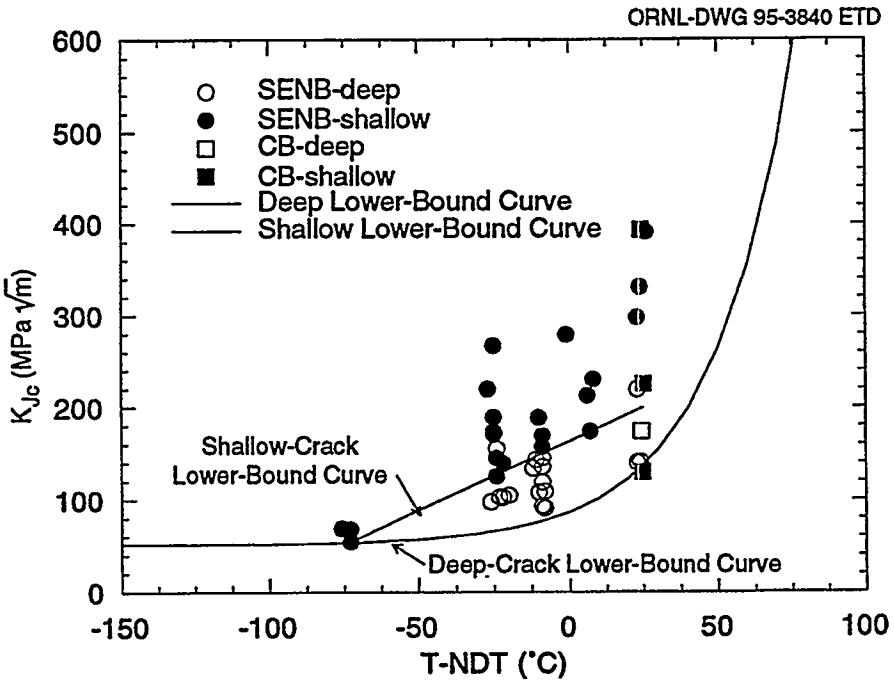

Figure 3.28 HSST fracture-toughness results as function of normalized temperature T – NDT

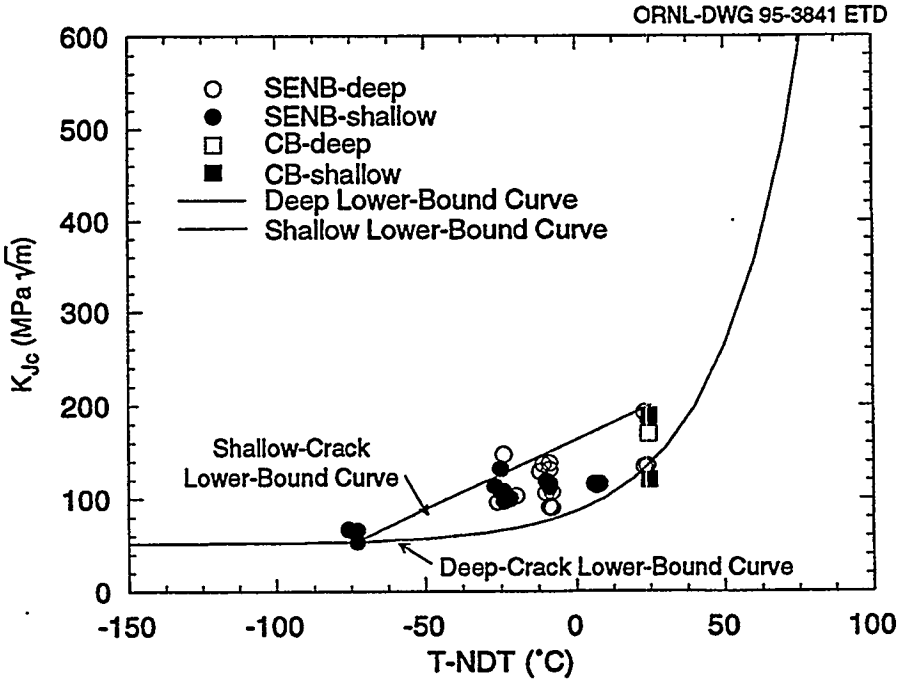

Figure 3.29 SSY toughness (K_o) results as function of normalized temperature

3.4.3 Toughness Estimation Techniques

For the clad beam tests, fracture toughness is estimated in terms of the critical J-integral and then converted into an elastic-plastic SIF, K_{Jc}. The two techniques used to determine the critical J are based on the "work" at the crack tip as measured by the area under the load-displacement (LLD or CMOD) curves. The methods require an η-factor, which relates work at the crack tip to the plastic portion of the crack-driving force. The first method of estimating J uses the P vs LLD test record as input for the toughness estimate. The J-integral is divided into elastic and plastic terms given by

$$J = J_{el} + J_{pl} , \qquad (3.3)$$

where

$$J_{pl} = \frac{\eta_{pl}^{\ell} U_{pl}}{Bb} , \qquad (3.4)$$

and U_{pl} is the plastic component of the area under the P vs LLD curve, B is specimen thickness, b is the remaining ligament (W-a), and η_{pl}^{ℓ} is the dimensionless constant relating the area term (U_{pl}) to J_{pl}. Finite-element analysis provides values of η_{pl}^{ℓ} as a function of U_{pl} for each loading and specimen configuration. Analysis is also required to determine the relationship between J_{el} and P. The U_{pl} value from the measured P vs LLD curve and the corresponding value of η_{pl}^{ℓ} for the CB-1.4 test at cleavage initiation are included in Table 3.6. The second technique for determining the critical J-integral uses the plastic component of the area under the P vs CMOD curve (A_{pl}) to

Table 3.6 Summary of results from the full-thickness clad beam testing program

	CB-1.1	CB-1.2	CB-1.3	CB-1.4
a/W	0.50	0.05	0.10	0.10
Temperature, °C	–25.5 ± 1.0	–25.0 ± 1.0	–25.0 ± 1.0	–25.3 ± 1.0
Stroke rate, mm/min	2.49	8.38	6.89	3.755
Time to failure, s	230	366	440	309
Failure conditions				
P, kN	1232.5	5002.3	5,060	3,114
LLD, mm	3.236	5.767	8.083	2.825
CMOD, mm	1.485	0.567	1.718	0.318
U_{pl}, kN-mm	135	6,427	16,879	93
A_{pl}, kN-mm	88	1,473	5,486	79
η-factors				
η_{pl}^{ℓ}	1.37	0.79	1.05	1.69
η_{pl}^{c}	2.26	4.16	4.08	2.82
Fracture toughness				
Elastic component				
J_{el}, kN/m	131.3	110.6	230.5	73.52
K_I, MPa$\sqrt{m}$	173.0	154.5	223.1	126.0
P vs CMOD				
J_{pl}, kN/m	8.1	124.7	486.0	4.69
Total J, kN/m	139.4	235.3	716.5	78.21
K_{Jc}, MPa$\sqrt{m}$	173.5	225.4	393.3	130.0
P vs LLD				
J_{pl}, kN/m	7.4	103.8	384.8	3.31
Total J, kN/m	138.7	214.4	615.3	76.83
K_{Jc}, MPa$\sqrt{m}$	173.1	215.2	364.5	128.8

calculate J_{pl}. The values of A_{pl} (from the measured P vs CMOD data) and η_{pl}^{c} for the test at initiation are also listed in Table 3.6.

In Fig. 3.26, values of J calculated for CB-1.4 from the two η-factor techniques are compared to J determined from finite-element analyses. These results showed good agreement among the three methods of calculating J.

3.4.4 Constraint Analyses

The J-Q methodology[36] was used to assess crack-tip stress triaxiality in the clad beam specimens. In these analyses, results for the deep-crack specimen (CB-1.1) at a J value of 43.63 kN/m [J_c = 139.4 kN/m (in Table 3.6)] are employed as an approximation to the SSY reference solution. Earlier analyses have shown that $Q \approx 0$ for the deep-crack specimens under these loading conditions. The opening-mode stresses ahead of the crack tip for the CB-1.4 specimen, shown in Fig. 3.27, exhibit an essentially uniform deviation from the SSY solution over a distance of $2 \le \tilde{r} \le 10$ (i.e., spatially uniform). From Fig. 3.27, the clad beam specimen has a Q value of about –0.36 at failure (for $\tilde{r} = 2$). This moderate loss of constraint in the CB-1.4 specimen is due primarily to the relatively lower failure load observed in the test.

3.4.5 Fracture-Toughness Scaling Model

The Dodds-Anderson (or D-A) scaling model[37] analyzes constraint conditions by utilizing the area (or volume for 3-D geometries) within principal stress contours to correlate toughness values from finite-body geometries with SSY conditions. The SSY state is then considered to yield fracture toughness results independent of specimen size or loading mode and is comparable to a specimen of infinite size. The scaling model has been successfully applied to fracture-toughness results exhibiting either a loss of in-plane constraint (i.e., shallow cracks) or out-of-plane constraint (i.e., thickness effects).[37] The scaling model assumes that the volume of critically stressed material surrounding the crack tip is the same in different specimens with different constraint conditions. As a result, the SSY critical fracture toughness can be determined in a high-constraint geometry and then applied to a low-constraint geometry or vice versa.

The D-A scaling model was used to investigate in-plane constraint loss in the clad beam test specimen. Application of the model was based on information available in the literature[38] that obviates additional crack-tip analysis. Fracture toughness data from the HSST clad beam and shallow-crack[22] programs are shown in Fig. 3.28 as a function of normalized temperature (T – NDT). A lower-bound curve to the uniaxial shallow-crack data is drawn as a straight line. Figure 3.28 indicates an increase in toughness and data scatter with decreased constraint.

The following criterion developed by Dodds and Anderson[37] determines dimensions in deep-crack ($a/W \ge 0.5$) specimens necessary for SSY:

$$a, b, B \ge 200\, J_c/\sigma_f \quad . \tag{3.5}$$

In Eq. (3.5), a is the crack depth, b is the remaining ligament, B is the specimen thickness, J_c is the cleavage J-integral toughness, and σ_f is the flow stress of the material. Specimens not meeting the criterion are expected to exhibit a toughness increase due to the loss of constraint. The ratio $a\sigma_f/J_c$ determined for each clad beam specimen is listed in Table 3.7. As expected, the ratio exceeds 200 for the deep-crack specimen and is considerably less than 200 for the shallow-crack specimens.

Table 3.7 Results of scaling model applied to clad beam data

HSST clad beam	a(mm)	K_{Jc} (MPa$\sqrt{m}$)	$a\sigma_f/J_c$	J_{FB}/J_o	K_o (MPa$\sqrt{m}$)
CB-1	117.5	174	499	1.04	170
CB-2	10.84	225	27	3.12	128
CB-3	23.69	393	20	4.35	189
CB-4	22.57	130	171	1.18	120

Using the D-A analysis results, Wallin[38] has quantified in-plane constraint loss by the following equation:

$$J_o \approx J_{FB} \Big/ \left\{1 + \left[A \cdot J_{FB}/(a \cdot \sigma_0)\right]^B\right\} \quad , \tag{3.6}$$

where

$A = 38.1 \cdot \ln(N/3.14),\ 5 \le N \le 50,$
$B = 1.27 + N/104.0,\ 5 \le N \le 50,$
J_o = SSY or reference value of J,
J_{FB} = value of J in the finite-body geometry,
N = hardening exponent.

It is recommended in Ref. 37 that the scaling model not be used in situations in which $J_{FB}/J_o > 4$. The SSY value (J_o) was computed from Eq. (3.6) for each clad beam specimen using N = 10, and the results are listed in Table 3.7 as J_{FB}/J_o and K_o. The K_o results for the HSST clad beam and shallow-crack SENB programs are shown in Fig. 3.29 as a

function of T – NDT. The K_0 results show no toughness increase associated with the shallow-crack specimens. The K_0 values evaluated for specimens that exhibited $J_{FB}/J_0 > 4$ do not represent the SSY toughness value and were not included in Fig. 3.29. The scaling model appears to be effective in adjusting the HSST test data to account for in-plane loss of constraint.

3.5 Drop-Weight Testing of SNUPPS Shell Material

Drop-weight testing was performed on base metal from the SNUPPS shell to determine NDT and, thus, set test conditions for the first base-metal full-thickness clad beam specimen (CB-2.1) being tested at NIST. Eight specimens were machined from a slab 280 × 230 × 25 mm (11 × 9 × 1 in.). The 280-mm length was oriented in the circumferential direction with respect to the vessel, with the 230- and 25-mm dimensions in the axial and thickness directions, respectively. The closest surface of the slab on which the crack-starter bead was placed was about 13 mm (0.5 in.) from the inside clad surface of the vessel. The flaw would tend to run in the L-T direction on the surface of the drop weight specimen. The latter surface on the specimen could be at a distance of 0.3 to 0.6 in. from the interface between the cladding and base. Thus, the surface could be in or very close to the HAZ of the clad layer. The location of the slab (and resulting drop-weight specimens) was selected to provide information on material at approximately the same depth in the beam as the flaws being tested. In addition, the specimens could be taken from a region with a high toughness gradient. Because this material has not been fully characterized, it was necessary to use some judgment on the starting test conditions for the drop-weight specimens. To provide guidance, a Rockwell-B hardness (HRB) traverse was performed on the shell base metal region of a segment of a ring forging-to-shell circumferential weld that was available. No gradient in hardness was apparent, with an average HRB of 89 to 90. The drop-weight NDT was determined to be –34.4°C (–30°F).

3.6 Fabrication of Clad Cruciform Test Specimens

Clad cruciform specimens will be fabricated from clad-weld-plate SNUPPS material taken from broken halves of uniaxial beams and from the remaining portion of the SNUPPS wall section at ORNL. Characterization data from the clad beam specimens revealed that the yield stress for the weld material at –25°C (i.e., 599 MPa) is 36% higher than that of the plate material. At room temperature, the yield stress for the weld material is 565 MPa (82 ksi). The yield stress properties of the weld material as a function of temperature can be represented by the relation

$$\sigma_0(\text{MPa}) = 390 + 51{,}650/(T + 273) \ , \qquad (3.7)$$

where T is the temperature in degrees Celsius. Original plans called for the clad cruciform specimens to be heat-treated to simulate appropriate properties (mechanical and fracture toughness) for the plate material near NDT. However, fabrication plans for the clad cruciforms have been altered to take advantage of these high yield-stress properties of the weld material. A section of the cruciform specimen containing the shallow flaw will be fabricated from weld material and tested in the "as-received" condition, that is, without any additional heat treatment of the test section. It is anticipated that satisfactory mechanical and toughness properties for the test material can be realized by an appropriate choice of the temperature for testing of the cruciform specimen.

3.7 Participation in Phase II of CSNI/FAG Project FALSIRE

[B. R. Bass, ORNL; and C. W. Schwartz, University of Maryland (UM)]

The HSST Program participated in Phase II of the FALSIRE Project by providing analytical solutions for three reference experiments used in the project. Project FALSIRE is sponsored by the Fracture Assessment Group (FAG) of the Committee on the Safety of Nuclear Installations (CSNI) Principal Working Group No. 3 (PWG-3). On behalf of the CSNI/FAG, ORNL and the Gesellschaft fur Anlagen-und Reaktorsicherheit (GRS), Köln, Germany, have responsibility for organizational arrangements related to Project FALSIRE. (The chairman of the CSNI/FAG is H. Schulz of GRS.) The CSNI/FAG was formed to evaluate fracture prediction capabilities currently used in safety assessments of nuclear components. Members are from laboratories and research organizations in Western Europe, Japan, and the United States. The CSNI/FAG completed Phase I of FALSIRE, which assessed various fracture methodologies through interpretive analyses of selected large-scale fracture experiments.[39] The six experiments, performed in Germany, Japan, United Kingdom, and the United States, were designed to examine various aspects of ductile crack growth in RPV steels under PTS loading.

3.7.1 Organization of FALSIRE II

It was proposed in Ref. 39 that a follow-on Phase II program (FALSIRE II) emphasize experiments that focus on behavior in the transition temperature region of

relatively shallow cracks subjected to combined thermal and mechanical loading. Investigations of crack extension in connection with clad surfaces should also be included. The action plan developed for FALSIRE II is summarized in Table 3.8. In September 1993, the Organizing Committee (OC) of the CSNI/FAG completed the preparation of comprehensive problem statements for a set of experiments proposed by testing organizations in France, Germany, Russia/Finland, United Kingdom, and the United States. The primary focus of the experiments (see Table 3.9) was on the behavior of relatively shallow cracks under PTS loading in the transition temperature region; effects of biaxial loading and effects of cladding on cleavage fracture were studied separately in two sets of experiments. The OC began distribution of these problem statements in November 1993 to analysts who had previously indicated a willingness to participate in FALSIRE II.

Table 3.8 Schedule of events for Phase II CSNI/FAG Project FALSIRE

November 1993	OC distributes problem statements and participant response form
February 1994	Participants submit response forms to OC
April 1994	OC distributes 1-page reminder concerning submission of structural analysis results from participants
May 1994	Participants submit summaries of structural analysis results to OC
May 1994	OC meets to review (1) progress in Phase II and (2) structural analysis results submitted by participants
June 1994	Participants submit summaries of fracture-mechanics assessment to OC
August 1994	OC completes development of evaluation programs FEDIT/FPLOT
October 1994	OC compiles analysis results submitted electronically by participating analysts
November 8–10, 1994	OC hosts Phase II FALSIRE Workshop for participating analysts in Atlanta, Georgia
March 1995	Participants submit additional data and analysis results to OC (action items)
May 1995	OC meets to review progress in preparation of final report and to discuss future work of CSNI/FAG
November 1995	OC submits draft final report for reviews
December 1995	OC completes final report
Spring 1996	OC submits final report to CSNI/PWG-3
Spring 1996	Publication of final reports—ORNL/NRC (NUREG); GRS/CSNI

Table 3.9 Large-scale reference fracture experiments proposed for FALSIRE II

Experiment	Organization	Testing country
Thick cylinder, thermal/centrifugal load (SC-4)	AEA Technology, Risley	United Kingdom
Thick cylinder, thermal/pressure load (PTS I/6)	Central Research Institute of Structural Mechanics (Prometey),[a]	Russia
	Technical Research Center of Finland (VTT)[b]	Finland
Clad beam, isothermal/uniaxial bend load (DD2/DSR3)	Electricité de France (EdF)	France
Thick cylinder, thermal/pressure/tension load (NKS-5)	MPA, Universität Stuttgart	Germany
Thick cylinder, thermal/pressure/tension load (NKS-5)	MPA, Universität Stuttgart	Germany
Cruciform beam, isothermal/biaxial bend load (BB-4)	ORNL	United States

[a]Organization performing test.
[b]Organization performing analysis.

Participants were requested to provide summaries of structural analysis results to the OC in April 1994. The submitted results were reviewed and assessed by the OC during scheduled May 1994 working sessions held at GRS. The primary purpose of this evaluation was to ensure that proper modeling of structural response was being achieved by analysts prior to performing fracture assessments of the reference experiments.

Documentation describing final results from fracture-mechanics assessments of the reference experiments was requested from the participants starting at the end of June 1994. Analysts were asked to transmit their results electronically to GRS, where a special-purpose computer program was developed to organize the analyses into a comparative data base. This data base also includes selected portions of the measured data generated in the six reference experiments. Summaries were generated from the data base for use in the FALSIRE II Workshop.

The FALSIRE II Workshop was held during November 8–10, 1994, at the Terrace Garden Hotel in Atlanta, Georgia. Over 30 participants representing 22 organizations from 12 countries took part in the workshop that focused on analyses of the reference fracture experiments. Final results for 45 analyses of the reference experiments were received by the OC from the participating analysts.

The OC opened the workshop by providing an overview of the objectives of the CSNI-FAG, the format used in the workshop program, and a summary of recent activities within FALSIRE II. Comparative summaries prepared from analyses of the reference experiments performed by participants were discussed in detail during the workshop. Also, for each reference experiment, a panel assembled from the group of participating analysts who contributed solutions to that experiment provided additional detailed information concerning the analyses. An extensive list of preliminary results, conclusions, and action items was compiled for each experiment as a result of these discussions. These preliminary results and conclusions were summarized in the official minutes of the workshop by the OC and sent to participants in mid-December 1994.

3.7.2 HSST Participation in FALSIRE II

The HSST Program provided analytical solutions for four of the FALSIRE II reference experiments given in Table 3.9:

- French clad beam experiments DD2 and DSR3 (J. A. Keeney, ORNL);
- ORNL biaxial cruciform beam experiment BB-4 (W. J. McAfee and J. W. Bryson, ORNL);
- AEA Technology spinning cylinder PTS experiment SC-4 (C. W. Schwartz, UM).

Analysis results for the clad beam experiments DD2 and DSR3 were reported in Ref. 40 and for the biaxial cruciform beam experiment BB-4 in Refs. 25–27. Results provided by the UM for the SC-4 spinning cylinder experiment are described in the following section.

3.7.3 Analysis of the SC-4 Spinning Cylinder Experiment (C. W. Schwartz, UM)

This section focuses on the UM analyses of the AEA Technology Fourth Spinning Cylinder Test (SC-4) as performed under Phase II of Project FALSIRE. The following subsections provide a review of the test configuration, the details of the analysis model and assumptions, the analysis results (in the context of similar results for SC-4 from the other FALSIRE II analysts), and a discussion of the results.

3.7.3.1 Test Configuration

The Spinning Cylinder Project at AEA Technology, Risley, focused on the investigation of fracture behavior of thick-walled test specimens under severe thermal-shock and simulated pressure loading conditions. A special test rig was constructed at Risley to produce the appropriate loading conditions. Pressure loading is simulated by rotating the cylinder about its own axis; the generated hoop stress distribution resembles that in a large-diameter pressurized vessel. Specimens can be heated to 350°C and rapidly cooled on the inside surface using a water spray system.

The SC-4 test was performed on a specimen extracted from a steel forging having the chemical composition of A 508 Class 3 steel. This material was given a nonstandard heat treatment to provide suitable mechanical properties for test purposes. The RT_{NDT} was reported as higher than 100°C.

A schematic of the SC-4 test specimen is depicted in Fig. 3.30. The specimen contained two semicircular defects at the inner surface. The defects were oriented in an axial plane, located halfway along the length of the cylinder and separated circumferentially by 135°. Both defects were fatigue precracked. Two sizes of defect (40- and 60-mm radii) were produced to maximize the likelihood of achieving the test objectives.

Twelve strain gages were positioned on the cylinder at selected locations. Also, thermocouples were installed to measure the cylinder temperature variations axially, circumferentially, and through-thickness. Cylinder speed was measured by an analog tachometer, with backup provided by electromagnetic and optical digital counters. On-line monitoring of crack growth was provided by the alternating current potential drop (ACPD) method developed for use on the quenched surface of the specimen.

The cylinder was initially thermally stabilized at a mean temperature of 305°C. The test was conducted at a low rotational speed of 530 rpm, and the thermal shock was generated by a 7°C (approximately) water spray cooling of the inner surface of the preheated cylinder. Crack-tip temperatures at the beginning of the test were consistent with upper-shelf fracture behavior. As the test progressed, the crack-tip temperatures at the near surface fell through the brittle/ductile transition regime.

Data collected during the test provided indications of crack growth at each end of the 40-mm defect. Subsequent destructive examination confirmed this result and revealed

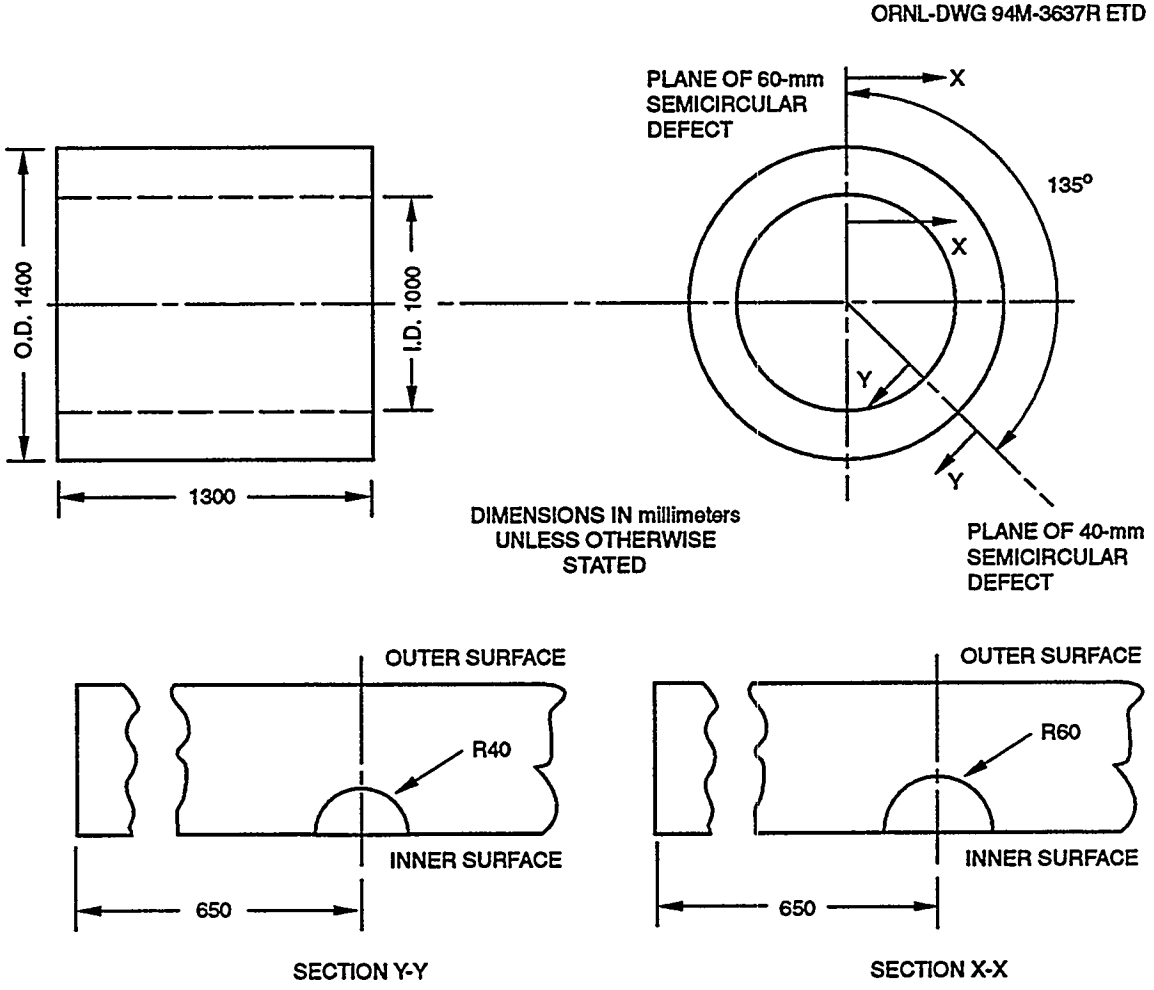

Figure 3.30 Specimen geometry for SC-4 experiment (*Source*: Ref. 27)

growth at the ends of the 60-mm defect that had not been detected using the ACPD method. As indicated in Fig. 3.31, the fracture surfaces were similar in several respects. First, the cracks grew in an axial direction, and no growth from the deepest point of either defect was observed. Second, the aspect ratios of the arrested cracks were similar at an ~5:1 length-to-depth ratio. Third, a thin (2- to 5-mm) ligament of material extended to, or very close to, the point of intersection of the crack with the inner surface of the cylinder. The presence of this ligament indicated that the cleavage initiation site was some distance below the surface. It also explained the failure of the ACPD method to detect growth of the 60-mm defect, which had the thicker ligament.

The locations of the cleavage initiation sites were established by postmortem examination of the fracture surfaces. These data have been used with the temperature data and the results of 3-D, elasto-plastic, finite-element analyses performed at Risley to evaluate the toughness under large-scale conditions. Additional information on these experimental and analytical results is available in Ref. 41.

3.7.3.2 Analysis Model

The geometry of the analysis model is based upon the SC-4 specimen geometry as given in the FALSIRE II problem statement. The specimen is a cylinder having an internal radius of 500 mm, a wall thickness of 200 mm, and an axial length of 1300 mm. The ends of the cylinder are modeled as stress-free boundaries without any rotational restraint.

The semicircular defects are located along axial planes on the inner surface of the cylinder at midheight. Two defects were tested in the SC-4 specimen, one having a radius of 40 mm and the other a radius of 60 mm. However, these defects are separated by sufficient distance in the circumferential direction that interactions between the defects are negligible for modeling purposes. Consequently, each defect was analyzed separately and independently in the UM study.

The finite-element mesh for the analysis model geometry is illustrated in Figs. 3.32 and 3.33. Because each defect was

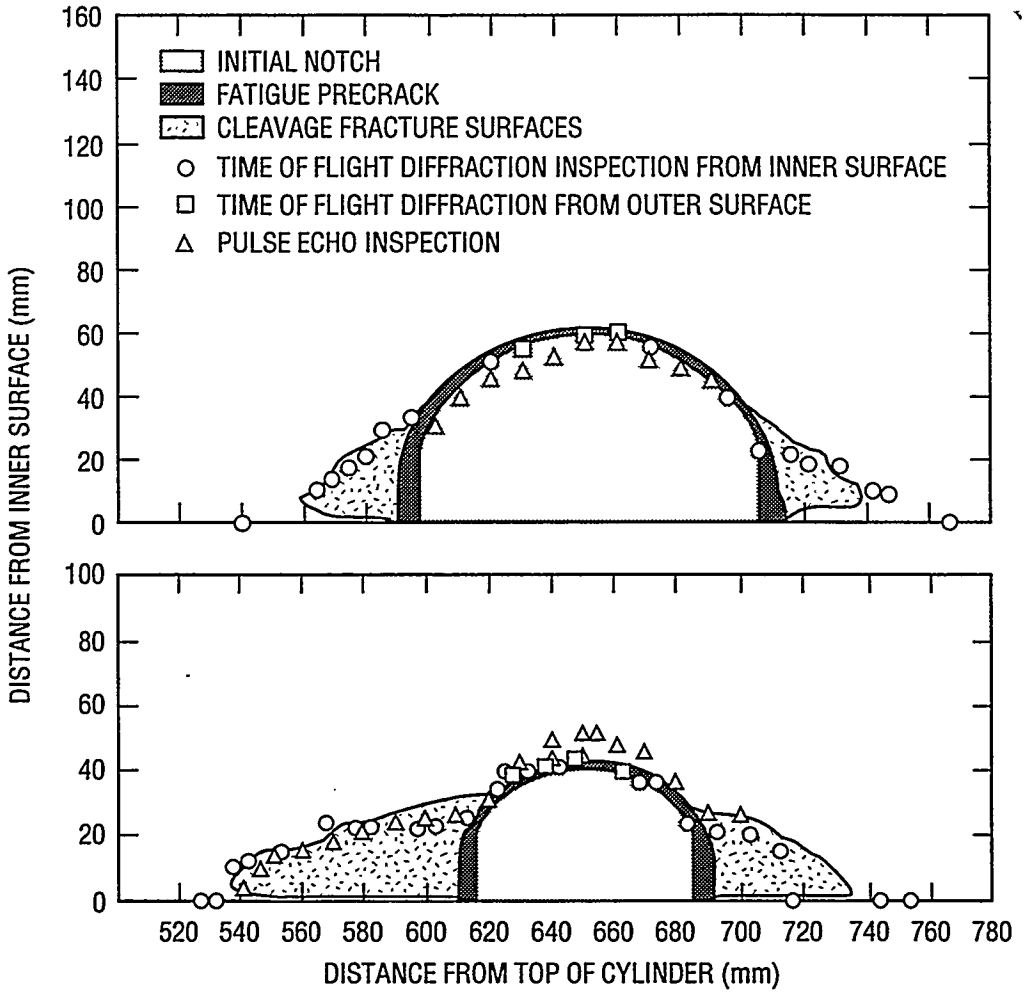

Figure 3.31 Comparison of fracture surfaces and ultrasonic profiles for two defects: (*a*) 60-mm crack depth and (*b*) 40-mm crack depth (*Source*: Ref. 27)

assumed to behave independently of the other and given the inherent symmetry of the problem, only one half-quadrant of the upper half of the cylinder was modeled in the analysis (i.e., 1/16th of the cylinder), and appropriate symmetry boundary conditions were applied to the cut faces of the specimen. The mesh consisted of 5780 nodes and 4608 8-node 3-D solid isoparametric elements (ABAQUS element type C3D8), producing a total of 16,473 degrees of freedom. Two variations of this mesh were analyzed, corresponding to the two defect radii of 40 and 60 mm. Element sizes along the crack front were ~8 to 10% of the crack depth (defect radius) and ~1.5 to 2.5% of the wall thickness.

Most material properties, including the mass density, thermal expansion coefficient, elastic moduli, and yield stress, were taken directly from the FALSIRE II problem statement. Temperature dependence of these properties was included where significant. The measured stress-strain data at various temperatures were fit to a power law Ramberg-Osgood deformation plasticity constitutive model:

$$\varepsilon/\varepsilon_0 = \sigma/\sigma_0 + \alpha(\sigma/\sigma_0)^n \quad . \tag{3.8}$$

Because the analyses were only to be performed up to the point of maximum J (i.e., no load reversals), the use of a deformation plasticity constitutive model is appropriate.

The values for the various material properties used in the analyses are summarized in Table 3.10. All properties except mass density were treated as temperature dependent. Property values were determined at temperatures of 20, 150, and 350°C and linearly interpolated or extrapolated to other temperatures as necessary.

A thermal analysis of the thermal-shock transient was not performed as part of the UM study. Instead, the measured

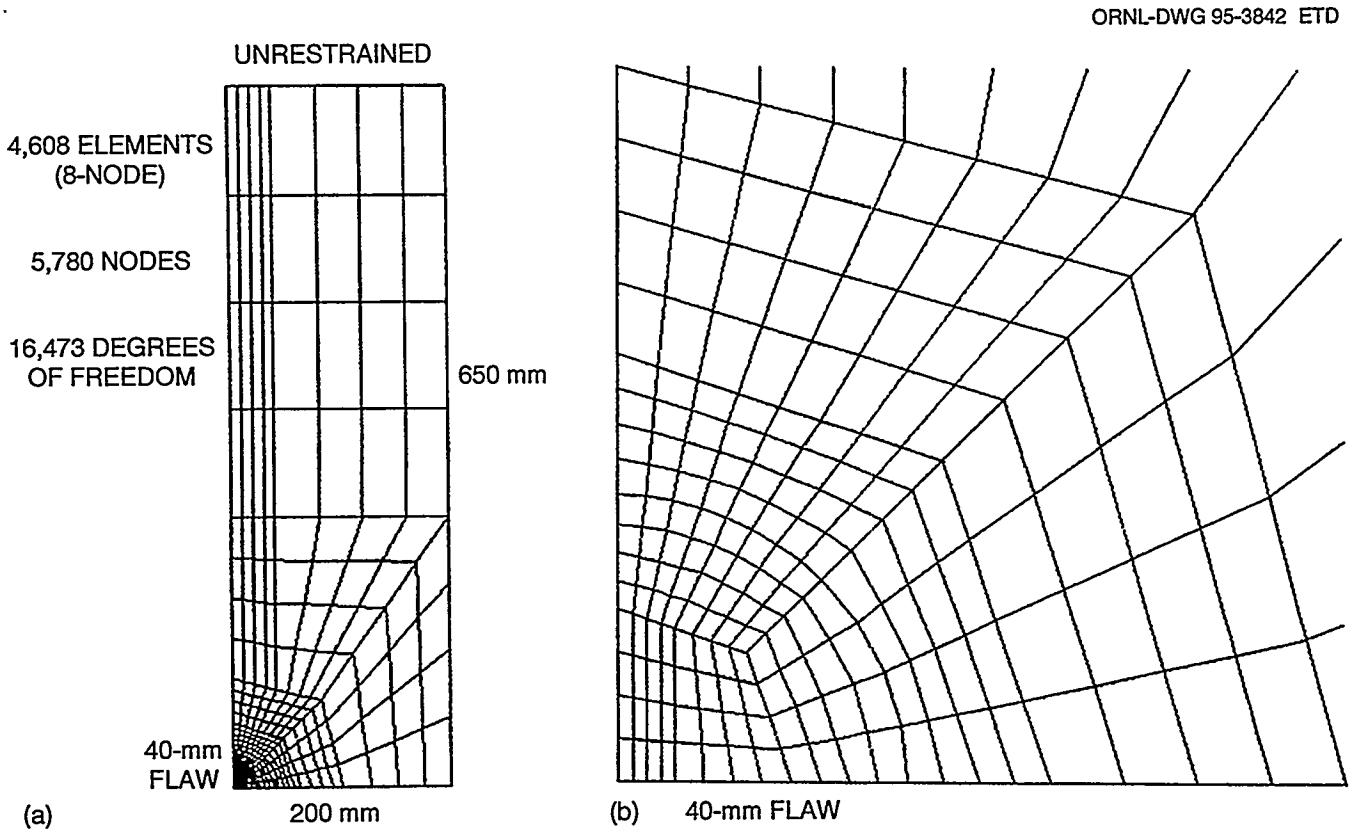

Figure 3.32 Axial view of finite element mesh for analysis model: (*a*) full axial section and (*b*) magnified view of crack-tip region

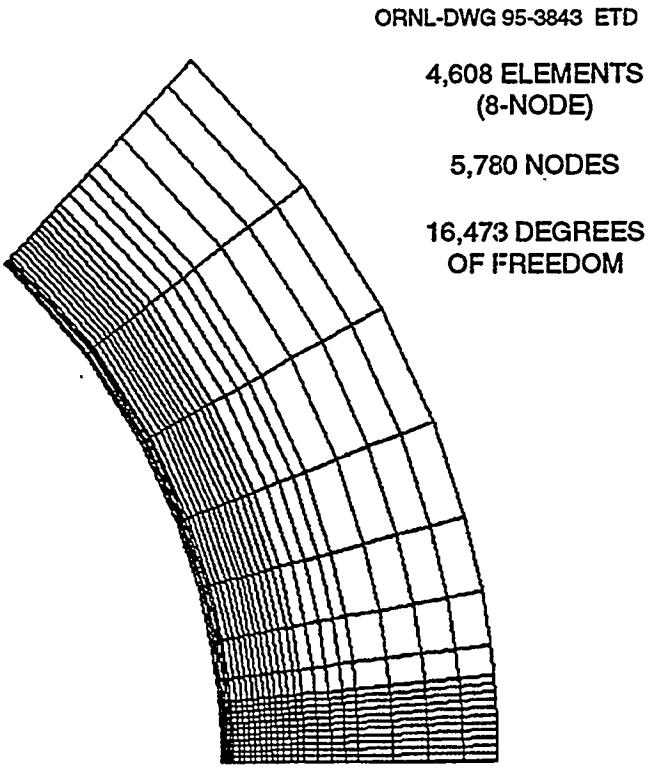

Figure 3.33 Diametral view of finite element mesh for analysis model

Table 3.10 Property values used in SC-4 analysis

Property	Temperature °C		
	20	150	350
ρ, kg/m^3	7787	7787	7787
$\alpha_{thermal}$, /°C	11.69×10^6	12.37×10^6	13.40×10^6
E, GPa	211.0	202.4	189.1
ν	0.28	0.28	0.28
σ_0, MPa	543.0	532.4	516.1
n	17.2	15.2	14.5
α	0.259	1.658	0.709

temperature responses recorded by the thermocouples during the test were used as input to the stress analysis. The measured temperature records during the test as determined from tabulated data provided in the problem statement are summarized in Fig. 3.34. A brief interruption in the cooling spray at ~200 s into the experiment caused a momentary minor temperature rise at the inner surface of the vessel, as indicated by the records for thermocouples T1–T6 in Fig. 3.34; this small detail in the actual thermal history was included in the analysis. The centrifugal mechanical loading from the 530-rpm rotation of the specimen was also included in the stress analysis, although this makes only a small contribution to the peak crack-driving force.

The thermal-shock transient was analyzed as a nonlinear transient thermal stress problem under small displacement and small strain assumptions. All mass inertia effects other than those from the cylinder rotation were neglected. Conditions at the crack tip were quantified using a domain integral J-integral formulation as implemented in ABAQUS (Version 5.3-1). Five J-integral contours were evaluated at nodes along the crack fronts.

3.7.3.3 Analysis Results

Because several other organizations also analyzed the SC-4 test as part of FALSIRE II, it is more useful and interesting to present the UM results in the context of those from the other analysts. Consequently, selected figures presented in this section are the comparative graphs prepared by J. Sievers of GRS for distribution and use at the FALSIRE II Workshop in November 1994. In each of these comparative graphs, the results from the various analysts are indicated by a legend code; those from the UM analyses are designated as "A_14."

3.7.3.3 Outer Surface Mechanical Strains

The predicted outer surface axial strains for the 40-mm defect analysis case are presented in Fig. 3.35 for gage G8 at the specimen midheight. The experimentally measured strain values have been added to these figures and are

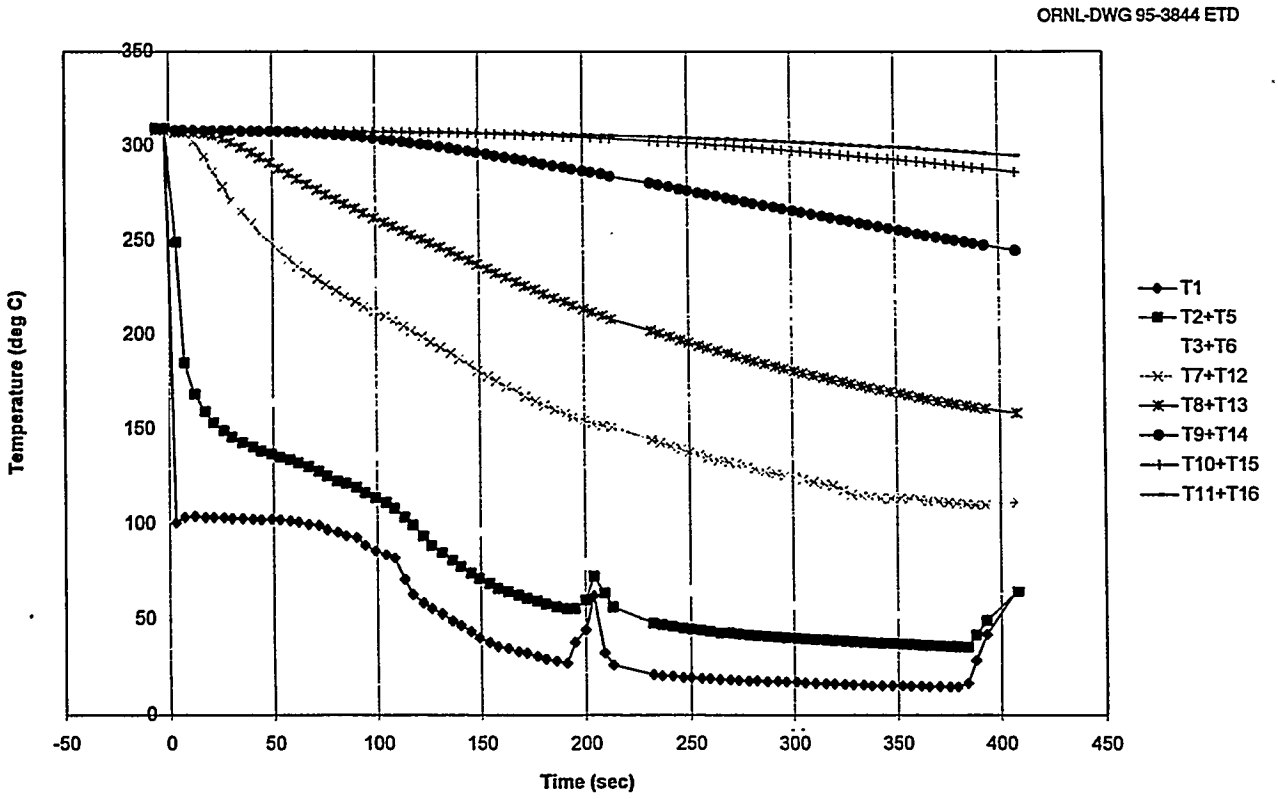

Figure 3.34 Summary of thermocouple records during SC-4 transient

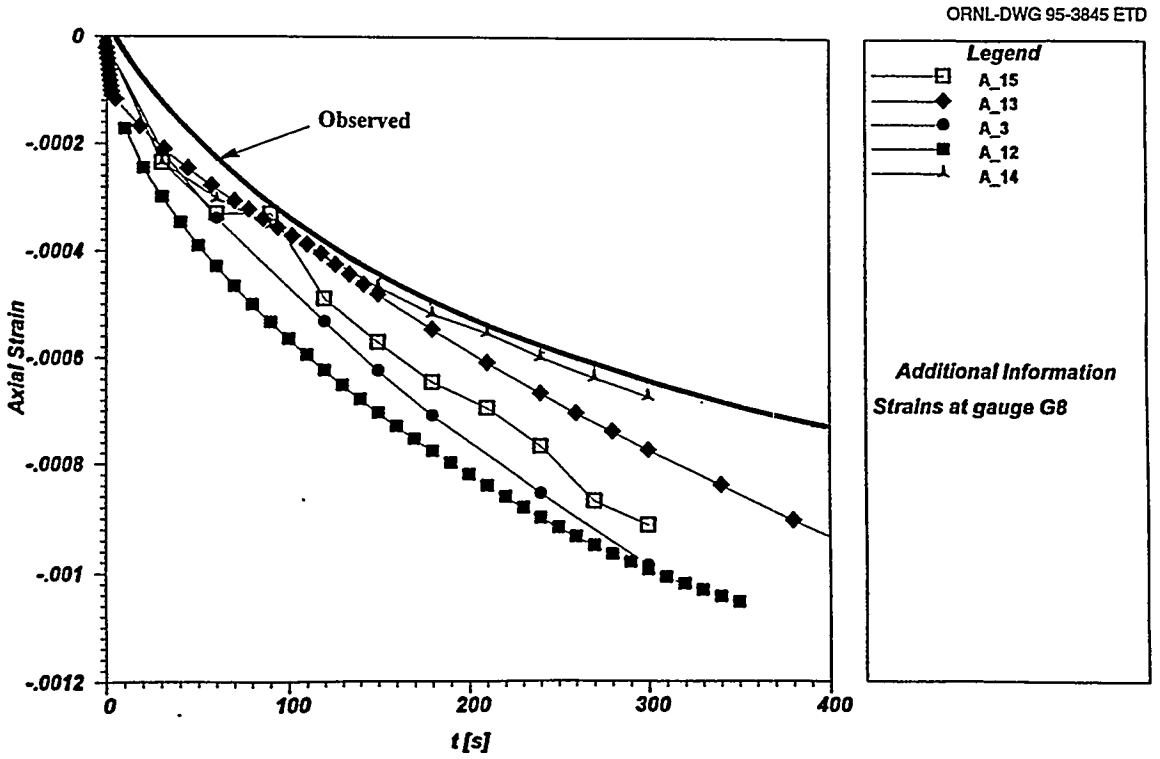

Figure 3.35 Predicted vs measured outer surface axial strains for gage G8 near specimen midheight (*Source*: B. R. Bass et al.*)

indicated by a solid heavy line. Results for the 60-mm defect are essentially the same as those for the 40-mm case, because the defects have negligible influence on the remote strains on the outer surface of the specimen.

In Fig. 3.35, the predicted outer surface axial strains and their deviation from the measured values is shown at the specimen midheight location. In this case, some of the predicted strains deviate from the measured values by up to 70%. The UM results (A_14) lie at the edge of the range of predictions.

The predicted, outer surface hoop strains for the 40-mm defect analysis case are presented in Fig. 3.36 for gage G5 at the specimen midheight. Again, the experimentally measured strain values have been added to the figure and are indicated by the solid heavy lines.

The scatter in the predicted outer surface hoop strains at the specimen midheight location (Fig. 3.36) is also quite small, but now the deviations of the predictions from the corresponding measured values are considerably larger. The maximum deviation of the predicted from the measured strains at 300 s is on the order of 250%. Again, this discrepancy is perplexing because the outer surface axial strain predictions at this location (Fig. 3.35) were quite good.

In evaluating the results in Figs. 3.35 through 3.36, two issues must be addressed: the variability among the various predictions and the deviations of the predictions from the measured values. The variability among the various predictions is reasonably small, particularly if certain outliers are eliminated with cause. The variability that remains is likely due to slight differences in material property values, meshing details, and strain computation techniques among the various analyses. The deviations of the predictions from the measured values are more difficult to explain, however, and in some cases these deviations are quite large (Fig. 3.36). All analyses slightly overpredict the outer surface axial strains at the specimen midheight (Fig. 3.35), and significantly overpredict the outer surface hoop strains at the specimen midheight (Fig. 3.36).

3.7.3.4 J-Integral Value vs Crack Front Angle

The computed J-integral values vs crack front angle are summarized in Figs. 3.37 for the 40-mm crack at 4 min into the thermal shock and in Figs. 3.38 for the 60-mm crack at 4 min (Note: The UM results—analysis A_14—were not included in J. Sievers' original version of these figures but have been added to the versions included here). Crack front angle is defined such that 0° corresponds to the

*B. R. Bass et al., Lockheed Martin Energy Research Corp., Oak Ridge Natl. Lab., "CSNI Project for Fracture Analyses of Large-Scale International Reference Experiments (FALSIRE II)," USNRC Report NUREG/CR-6460 (ORNL/TM-13207), to be published.

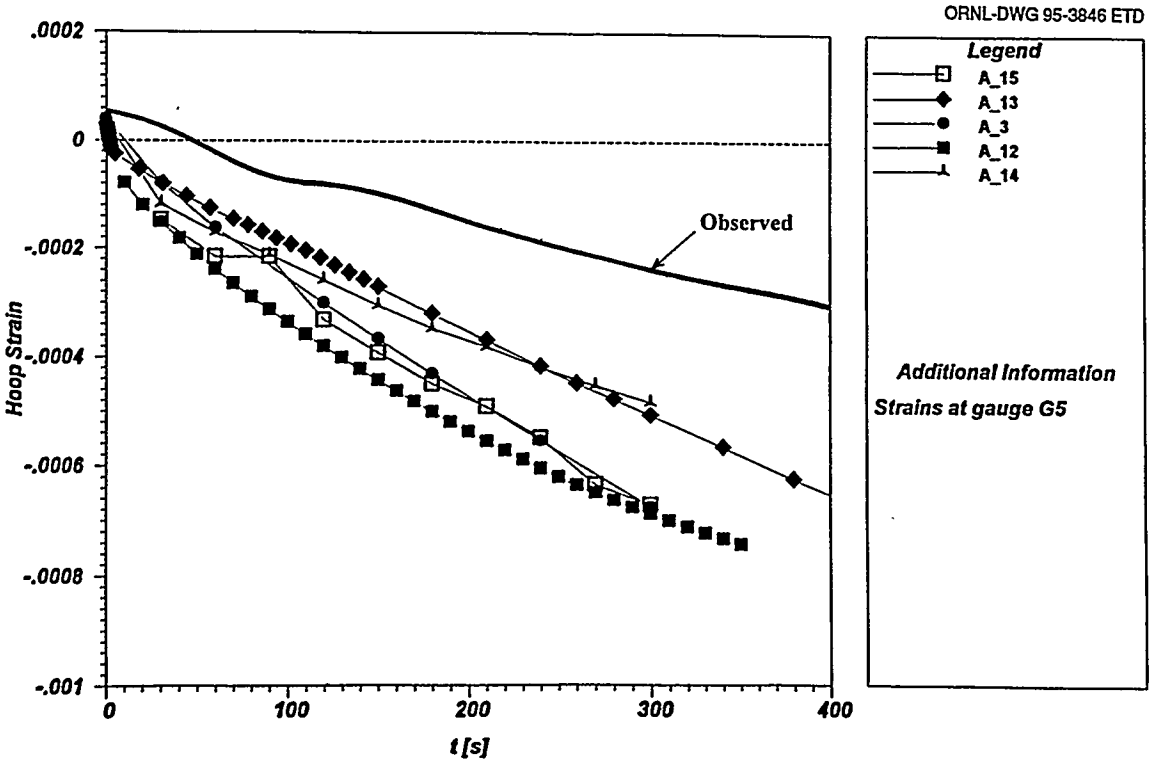

Figure 3.36 Predicted vs measured outer surface hoop strains for gage G5 near specimen midheight (*Source*: B. R. Bass et al.*)

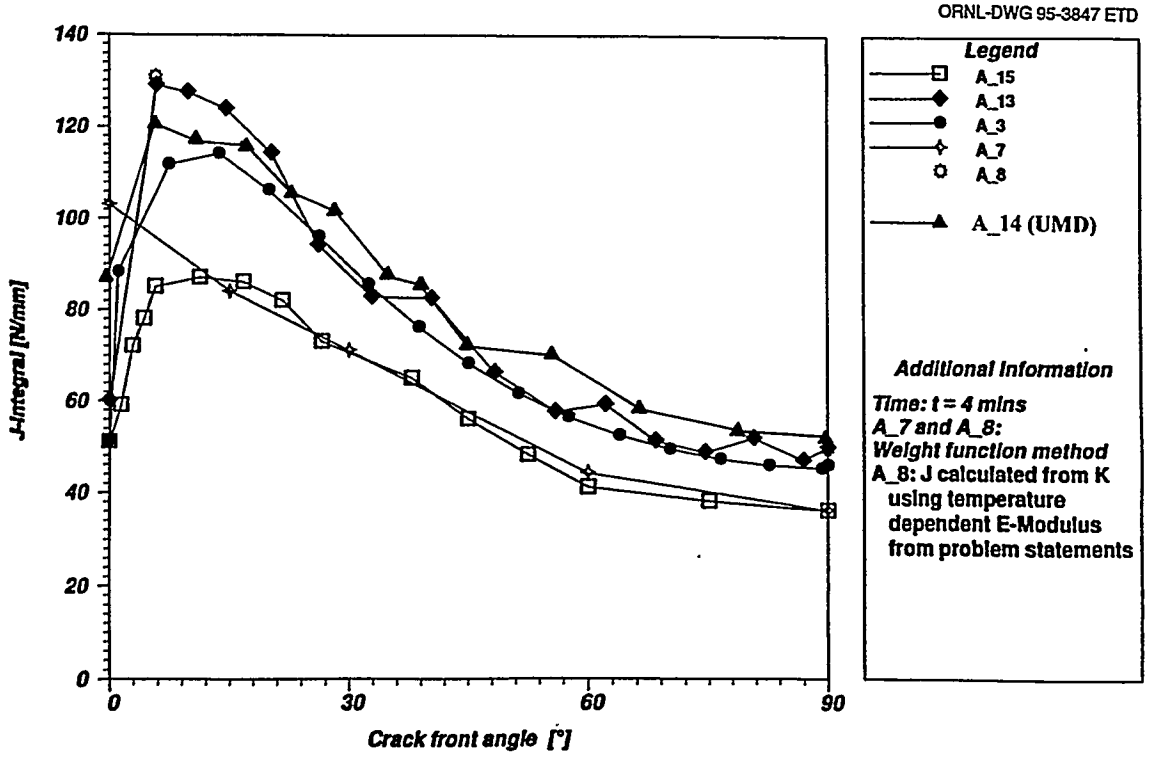

Figure 3.37 Predicted J-integral along crack front for 40 mm crack at 4 min into thermal transient (*Source*: B. R. Bass et al.*)

*B. R. Bass et al., Lockheed Martin Energy Research Corp., Oak Ridge Natl. Lab., "CSNI Project for Fracture Analyses of Large-Scale International Reference Experiments (FALSIRE II)," USNRC Report NUREG/CR-6460 (ORNL/TM-13207), to be published.

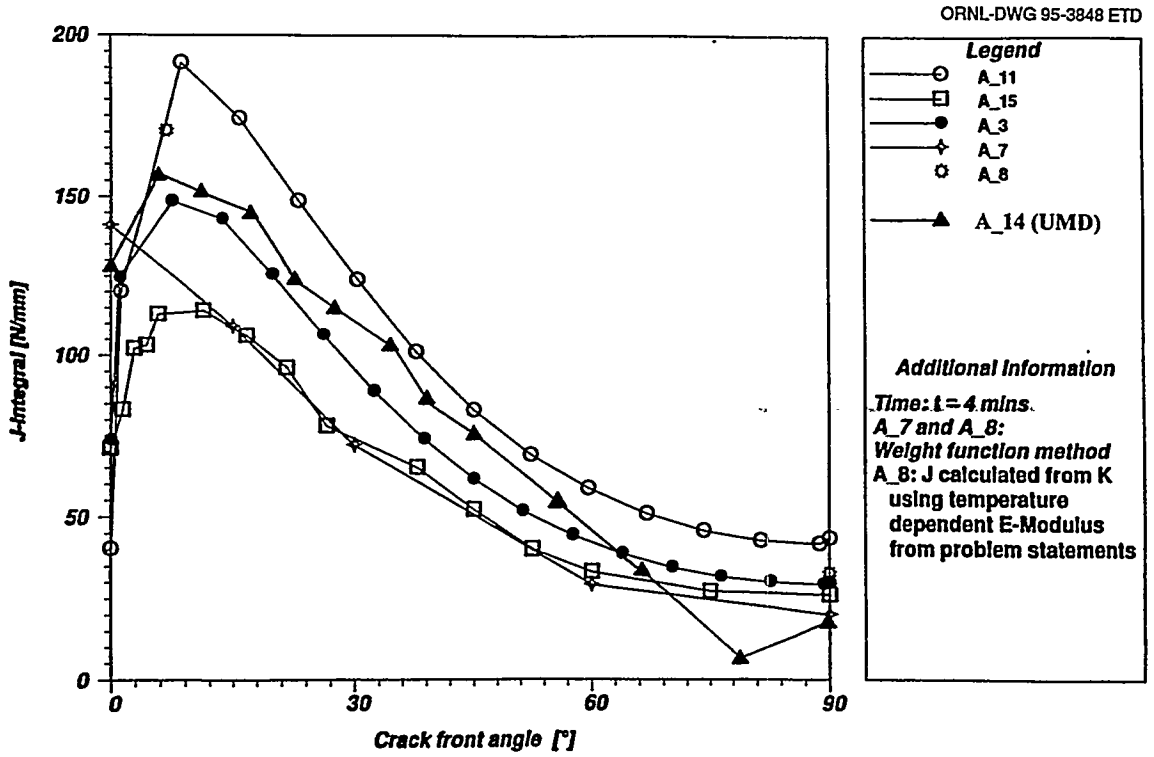

Figure 3.38 Predicted J-integral along crack front for 60 mm crack at 4 min into thermal transient (*Source*: B. R. Bass et al.*)

inner surface of the specimen and 90° corresponds to the deepest point. Several observations can be made from these figures: (1) the minimum J values occur at a crack front angle of 90° (i.e., at the deepest location of the crack); (2) the maximum J value occurs just beneath the surface of the specimen at a crack front angle between ~6 to 12°; (3) the UM results (A_14) generally lie near the upper end of the prediction scatter band, except for the 60-mm crack at the deep locations; (4) the scatter in the predictions is small at the deepest crack front locations; and (5) the scatter in both the magnitude and the precise location of the near-surface peak J value is quite large among the various analyses. One hypothesis for the large degree of scatter in the results for the near-surface location is the sensitivity of the predictions to slight differences in mesh configuration and other analysis details in this region where the thermal-shock gradients are the highest.

An implication of the results shown in Figs. 3.37–3.38 is that the prediction of crack initiation and advance for shallow surface defects under thermal-shock loading may be problematic. Intuitively, crack initiation and maximum advance should occur proximate to the near-surface location where J is the largest. However, the FALSIRE II predictions demonstrate the difficulty in predicting J accurately at this near-surface location. In addition, it is expected that loss-of-constraint effects will also be greatest at this near-surface location and that these effects will need to be included in the fracture evaluation. This loss-of-constraint issue will be examined in a subsequent section.

3.7.3.5 K_I vs Crack-Tip Temperature

The computed K_I values vs crack-tip temperature during the thermal shock event for the near-surface point of the 40-mm crack are summarized in Fig. 3.39. In most of the analyses, K_I is obtained from the computed J-integral histories. The crack-tip temperature is obtained from the measured temperature (or computed temperature, if a thermal analysis was performed) at the corresponding time value. As indicated in Fig. 3.39, all analyses predicted broadly similar K_I vs temperature trajectories, with the trends in the scatter mirroring those for the J-integral histories (i.e., smallest scatter for the deepest crack front location, greater scatter for the near-surface location). The UM predictions (A_14) lie at or near the upper bound the scatter bands for the 40-mm crack in Fig. 3.39.

Figure 3.40 summarizes the computed K_I vs crack-tip temperature histories for the deep and near-surface point of the 60-mm crack. The scatter in the predictions for the 60-mm crack case are larger than those for the 40-mm crack. The UM results (A_14) lie at or near the lower bound for the predictions for the 60-mm crack in Fig. 3.40.

*B. R. Bass et al., Lockheed Martin Energy Research Corp., Oak Ridge Natl. Lab., "CSNI Project for Fracture Analyses of Large-Scale International Reference Experiments (FALSIRE II)," USNRC Report NUREG/CR-6460 (ORNL/TM-13207), to be published.

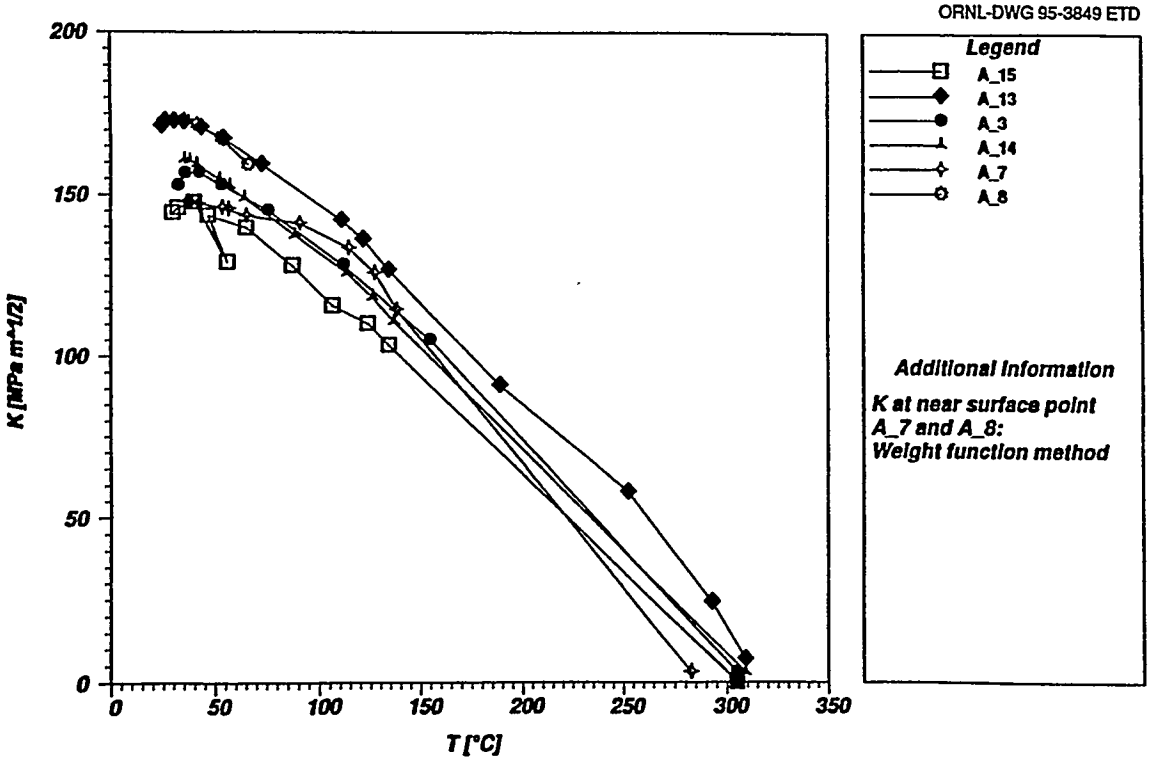

Figure 3.39 Stress-intensity factor and crack-tip temperature during SC-4 thermal transient at near-surface point of 40-mm crack (*Source*: B. R. Bass et al.*)

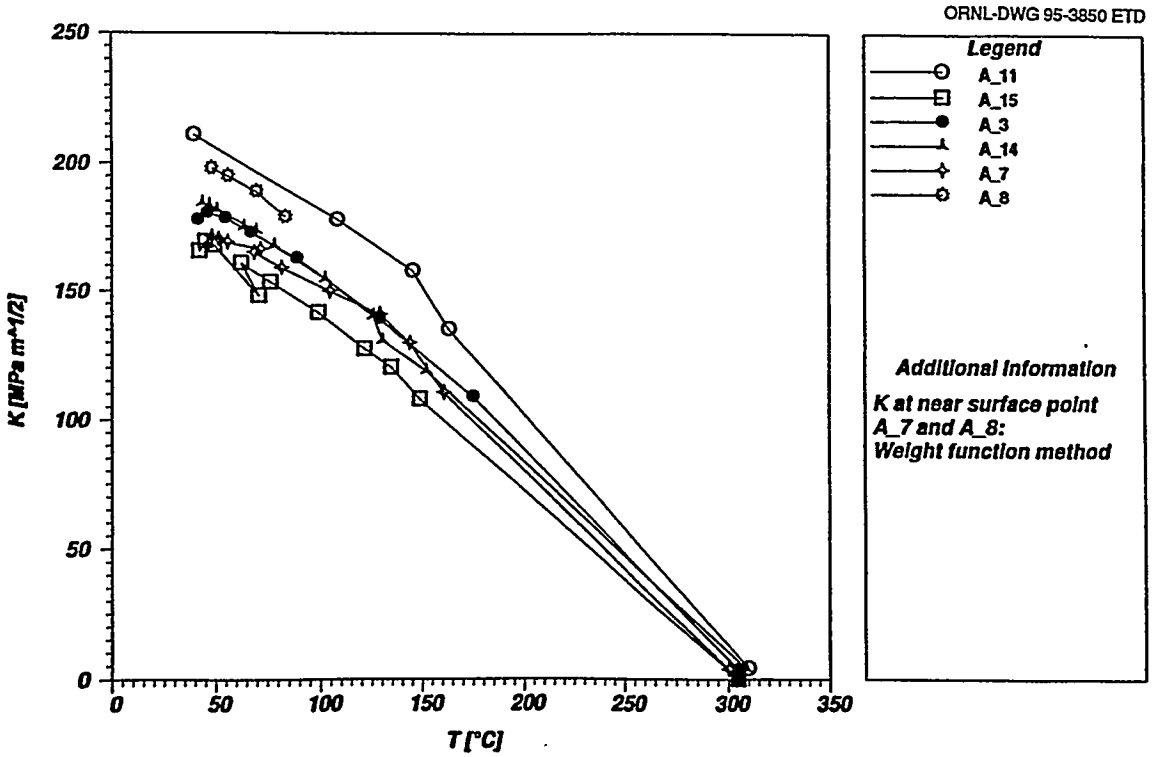

Figure 3.40 Stress-intensity factor and crack-tip temperature during SC-4 thermal transient at near-surface point of 60-mm crack (*Source*: B. R. Bass et al.*)

*B. R. Bass et al., Lockheed Martin Energy Research Corp., Oak Ridge Natl. Lab., "CSNI Project for Fracture Analyses of Large-Scale International Reference Experiments (FALSIRE II)," USNRC Report NUREG/CR-6460 (ORNL/TM-13207), to be published.

3.7.3.6 Crack Initiation and Advance

Crack initiation can be evaluated by superimposing the predicted K_I vs crack-tip temperature histories onto the material toughness K_J vs temperature plot provided as part of the FALSIRE II problem statement. The near-surface region will be critical for this evaluation, because it is in this region that the predicted K_I values are the highest and the crack-tip temperatures are the lowest; that is, the crack tip is the most heavily loaded and the most brittle. Based upon the UM analysis results, the critical near-surface locations (i.e., the locations having the highest J values) are at depths of 4 and 6 mm for the 40- and 60-mm defect cases, respectively.

Figure 3.41 presents the overlay of the UM-predicted K_I vs crack-tip temperature history onto the material toughness curve for the near-surface locations for both the 40- and 60-mm defect cases. Each data point for the predicted K_I vs crack-tip temperature curve represents the results from a particular step in the finite-element analysis, and the corresponding time value for each of these steps is indicated next to the data point. The measured material toughness data exhibit the usual data scatter. As a consequence, the time, K_I, and temperature values at initiation must be estimated as ranges. These ranges are given in Table 3.11.

Table 3.11 Predicted initiation times, crack-tip temperatures, and toughnesses for the SC-4 test

	40-mm Crack	60-mm Crack
Initiation time, s	115–140	120–150
Crack-tip temperature, °C	92–68	102–77
K_I, MPa$\sqrt{m}$	135–145	155–165

Data from the ACPD instrumentation in the SC-4 test indicated crack extension for the 40-mm flaw at 4 to 5 min into the test. The ACPD instrumentation indicated no extension for the 60-mm flaw, although significant crack growth was discovered during the postmortem fracture surface examination. The fracture surface evaluation also indicated cleavage initiation sites at ~6 to 8 mm and 9 to 12 mm deep in the 40- and 60-mm defect cases, respectively. These initiation depths are in fair agreement with the predicted critical values of 4 and 6 mm.

The observed initiation times for the 40-mm defect disagree with the predictions summarized in Table 3.11.

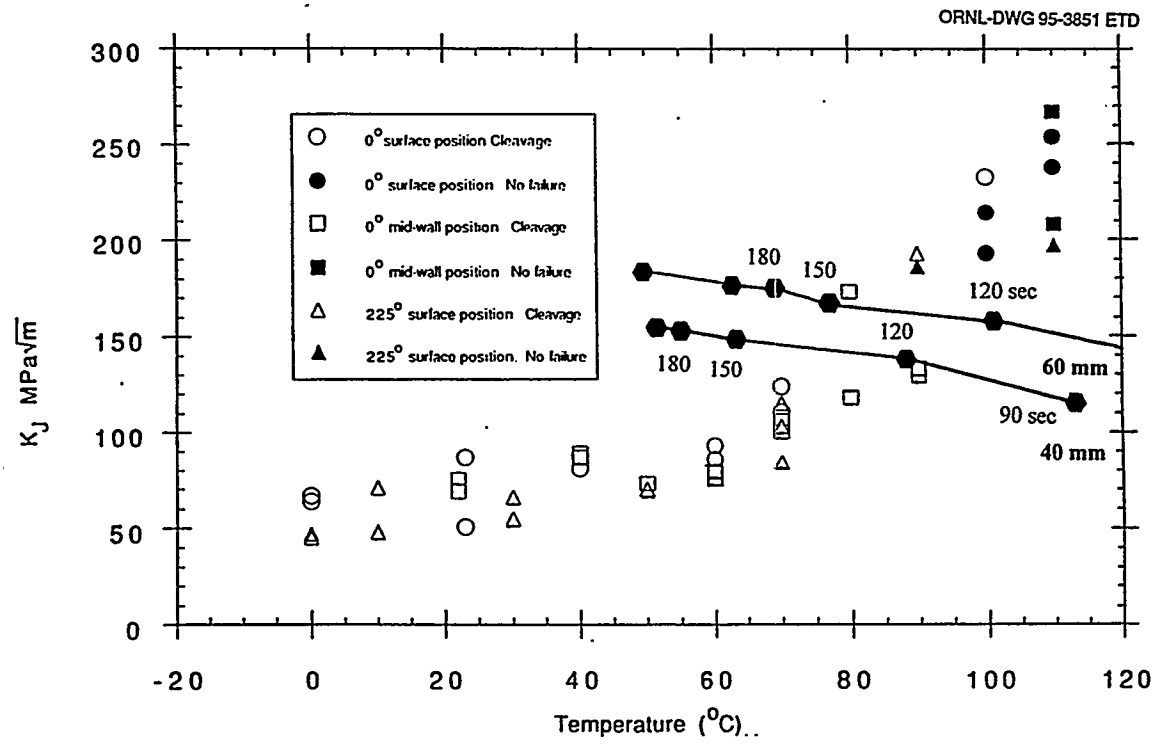

Figure 3.41 Predicted stress-intensity factor vs crack-tip temperature trajectory and measured material toughness for near-surface points of 40- and 60-mm cracks (adapted from FALSIRE II problem statement)

The analyses predicted crack initiation for the 40-mm flaw at between 115 and 140 s into the test. These values are significantly earlier than those observed (at least for the 40-mm flaw) during the experiment.

3.7.3.7 Discussion

The comparisons of the predictions with the actual measured response are not as good as hoped. The only measured response records available for comparison with the predictions are the strain gage histories. These primarily provide a record of the gross structural response of the overall specimen. The predictions are close to the measured values at some gage locations but far from the measurements at others. This suggests that either some fundamental modeling error was made by all analysts (because all of the predictions are in broad agreement) or there was some error in the instrumentation records.

At the specimen midheight, there are both significant axial and hoop stresses (the radial stresses remain zero, since the gage is on the outer surface). However, there appears to be an unexpected physical relationship between the measured axial and hoop strains. Consider, for example, the peak strains at 400 s. The measured axial compressive strain (Fig. 3.35) is ~0.0007, and the measured hoop compressive strain (Fig. 3.36) is ~0.0003. If these measured strains are substituted into Hooke's law (using the elastic properties in Table 3.10) and converted to stresses, the corresponding compressive axial stress is ~134 MPa, and the compressive hoop stress is ~97 MPa. These stresses contradict physical intuition in that one would expect the hoop stress in a thermal-shock experiment to have a higher magnitude than the axial stress, particularly given that the test cylinder is open and unrestrained at the ends. Repeating the same calculations using the predicted strain values of 0.00092 for the axial compression and 0.00066 for the hoop compression (based on representative results from analysis A_12) produces an axial compressive stress of ~147 MPa and a hoop compressive stress of ~173 MPa. These predicted stress values are more in line with physical expectations. Again, some questions are raised regarding the accuracy and internal consistency of the measured strain values.

Alternatively, the discrepancies between the predicted and measured strains could result from errors in the analyses. Of course, this explanation would imply that all of the FALSIRE II analysts made the same errors because their predictions are all broadly consistent and exhibit similar variances from the measurements. Incorrect treatment of the boundary conditions at the ends of the specimen is always a potential source of modeling errors. However, the boundary support conditions were considered with some care by the test designers. The bottom of the specimen hangs freely in the spinning cylinder rig, while the top of the specimen is suspended in a fixture expressly designed to eliminate any rotational restraint effects. The effectiveness of this fixture was demonstrated during the early spinning cylinder tests of full-length axial flaws, where no variations were observed in the crack extension along the flaw length. Analysis errors might also be attributable to temperature gradients along the length of the test specimen, for example, maximum cooling at the midheight and reduced cooling at the specimen ends. All of the analyses assume a uniform temperature distribution along the length. The temperature records appear to validate this assumption; however, a symmetric gradient about the specimen midheight would not be detected by the symmetrically located thermocouple arrays in the SC-4 test.

Only limited comparisons can be made between the predicted and measured fracture response in the SC-4 test. CMOD was not measured during the test, and J is an unmeasurable quantity. The time of crack initiation was observed during the test (at least for the 40-mm defect), as were the locations of the initiation sites, and these can be compared to the predictions. Crack advance was also determined from postmortem examination of the fracture surface, but the analyses were unable to make any corresponding predictions of crack advance because of limited material property data.

The ACPD instrumentation indicated an initiation time at ~4 to 5 min into the thermal shock (for the 40-mm defect). The postmortem fracture surface examination indicated that the initiation sites were located at depths of 6 to 8 mm and 9 to 12 mm beneath the inner surface for the 40- and 60-mm defects, respectively. The corresponding predicted initiation locations of 4 and 6 mm beneath the inner surface (UM analysis A_14) are in fair agreement with these observations. However, the initiation times of 115 to 150 s (Table 3.11) are considerably earlier than the observed initiation times. This difference in turn implies predicted crack initiation at higher crack-tip temperatures—and thus higher crack-driving forces—than observed in the test.

One partial explanation for the early predicted initiation is the neglect of loss-of-constraint effects in the region near the inner surface of the specimen. Constraint loss will tend to lower the "effective" crack-driving force, which in turn will delay the predicted initiation time. If constraint loss is considered, then it is clear that the predicted K_I values overlaid on the measured K_J material data in Fig. 3.41 are incompatible; the measured K_J values are from highly constrained compact tension specimens (i.e., K_J is an approximation to K_{Ic}), while the predicted K_I values represent lower constraint values from the actual test specimen.

Evaluation

Shih's Q-stress methodology[42] provides one approach for quantifying the constraint loss near the inner surface of the test specimen. Unfortunately, the element mesh in the UM analysis is insufficiently fine for extracting the Q value from the near-tip stress fields. However, analyses by Dodds et al.[43] for a surface-cracked plate that is broadly similar to the SC-4 flaw conditions can be used to develop an approximate value for Q for the SC-4 thermal-shock test. Figure 3.42 from Dodds et al.[43] presents the 3-D analysis results for Q as a function of load level $J_{local}/(a\sigma_o)$ at various locations along a semielliptical crack front for the cases of uniaxial and biaxial loading. Dodds et al.[43] assumed a power law deformation plasticity material model in their analyses, with material properties of $n = 10$, $\alpha = 1$, $E/\sigma_o = 500$, and crack geometry properties of $a/t = 0.25$ (crack depth ratio) and $2c/a = 6$ (crack aspect ratio). Corresponding values for the SC-4 test material and geometry are $n = 15$, $\alpha = 0.9$, $E/\sigma_o = 400$, $a/t = 0.2$ to 0.3, and $2c/a = 2$; these are reasonably similar to the Dodds et al.[43] values. The J_{local} values computed in the UM analysis for the peak of the SC-4 thermal transient are on the order of 100 to 150 N/mm, which correspond to a $J_{local}/(a\sigma_o)$ value of roughly 0.005. For this load level at near-surface locations (i.e., around 3° to 6° along the crack front), Fig. 3.42 indicates that Q ranges between –0.7 to –1.0 for the uniaxial tension case and between –0.4 and –0.7 for biaxial tension conditions. The stress conditions at the peak of the SC-4 thermal shock lie somewhere between uniaxial and biaxial tension, and probably closer to the biaxial case, suggesting that a Q value range of approximately –0.5 to –0.7 is a reasonably broad estimate for the SC-4 conditions at the peak of the thermal transient. This estimated Q value agrees in broad terms with the values predicted by other FALSIRE II analysts, as indicated in Fig. 3.43.

Unfortunately, the estimated Q value cannot be used to correct the prediction of crack initiation times because there are no test data for quantifying the J-Q material toughness locus for the SC-4 material. However, the constraint methodology proposed by Anderson and Dodds[44] can be employed as an alternative. The Anderson and Dodds approach relates J_{local} (termed $J_{Finite\ Body}$ or J_{FB} in their terminology) to the highly constrained J_o under SSY conditions by equating the areas enclosed within the near-tip critical principal stress contours. Dodds et al.[43] applied this methodology to their surface cracked plate analyses; the results from their calculations are presented in Fig. 3.44. In this figure, the line for $J_o = J_{FB}$ represents the case of no constraint loss; curves below this line correspond to increasing constraint loss where the "effective" or equivalent J_o for highly constrained conditions is less than the computed J_{FB} for the actual specimen conditions. To apply Fig. 3.44 to the SC-4 conditions, $J_{FB}/(a\sigma_o)$ is interpreted as being equal to $J_{local}/(a\sigma_o)$ in Shih's Q-stress methodology, that, as discussed previously, has a value of ~0.005 at the peak of the SC-4 response. A value of $J_{FB}/(a\sigma_o)$ equal to 0.005 for a crack front angle ϕ of 17° (the only value reported) under biaxial tension corresponds to a $J_o/(a\sigma_o)$ value of ~0.0025 in Fig. 3.44; in other words, the "effective" J value acting on the crack tip is ~50% lower than the computed J value as a consequence of constraint loss.

The J_o/J_{FB} ratio can be converted to K_o/K_{FB} (i.e., K_{Ic}/K_I) as follows:

$$K_o/K_{FB} = (J_o/J_{FB})^{1/2} \cdot \qquad (3.9)$$

The J_o/J_{FB} ratio of 0.5 for the SC-4 peak response corresponds to a K_o/K_{FB} ratio of ~0.7. Thus, the data in Fig. 3.44 can be used in a very approximate way to convert the computed K_I values from the UM predictive analyses to equivalent "effective" K_{Ic} values for superposition onto the material toughness data. The results from these manipulations are presented in Fig. 3.45. Again, each analysis data point represents results from a particular time step during the computations, and these time values are

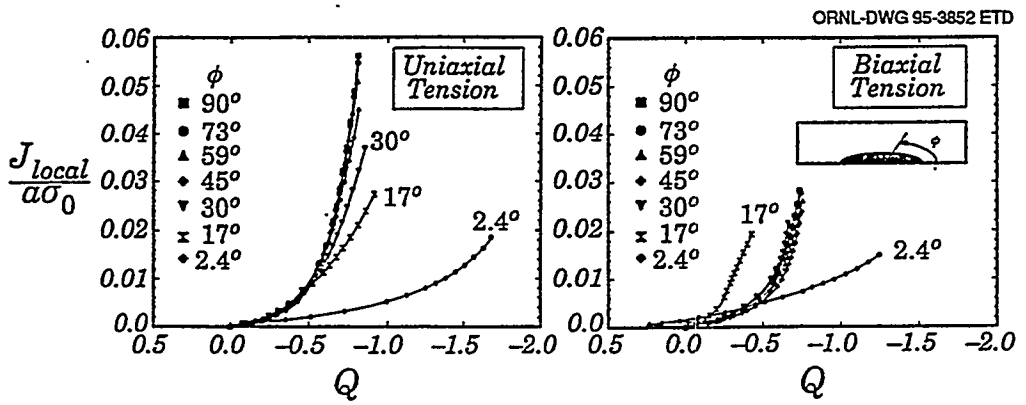

Figure 3.42 Evolution of stress triaxiality in surface-cracked plate with increasing local deformation, as measured by $J_{local}/(as_0)$ at different points along crack front (*Source*: Ref. 43)

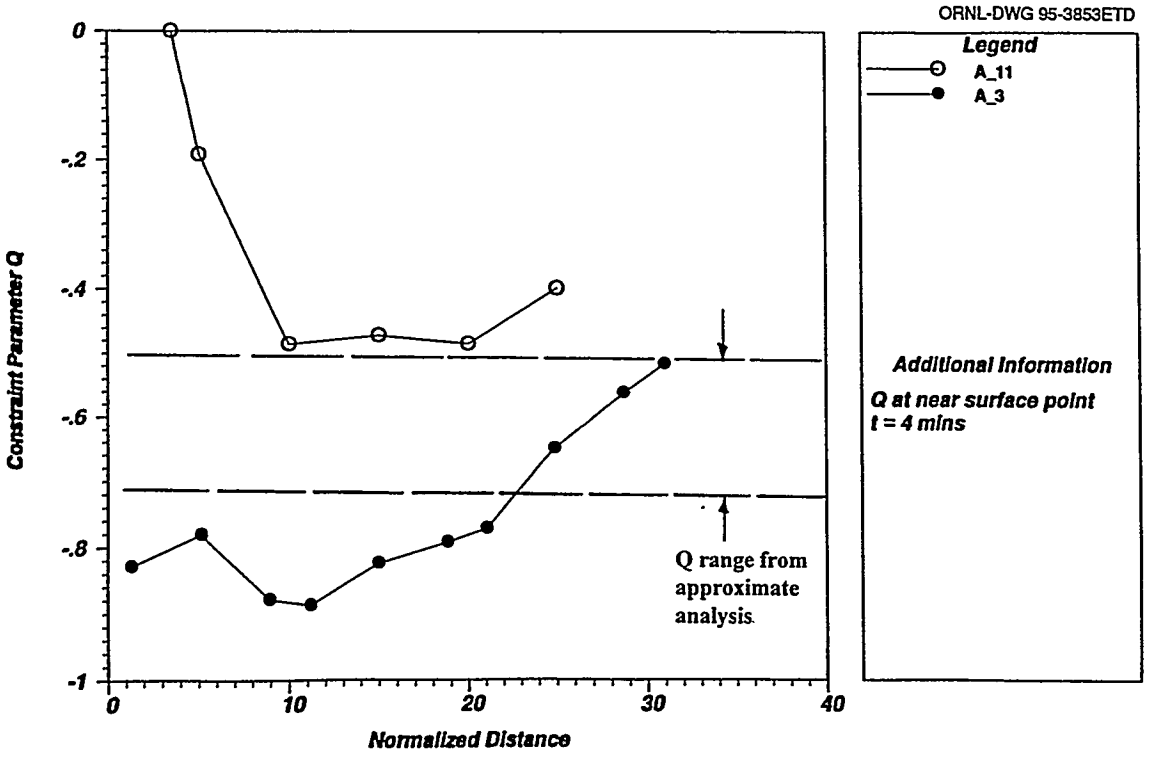

Figure 3.43 Predicted Q-stress values for 60-mm crack at 4 min into SC-4 thermal transient (*Source*: B. R. Bass et al.*)

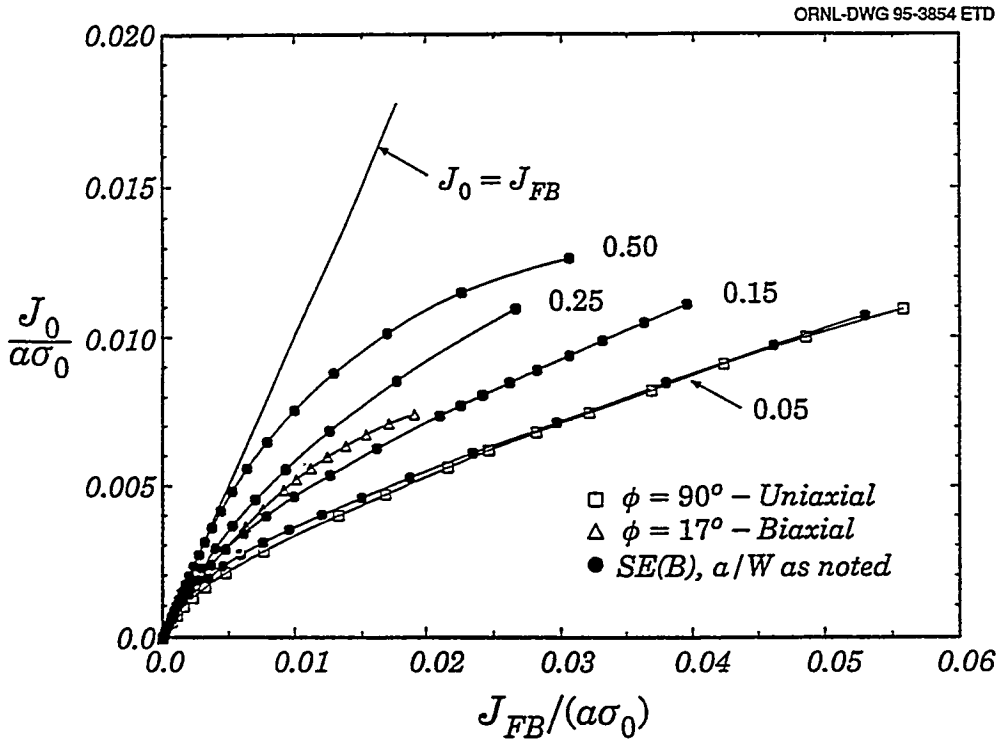

Figure 3.44 Application of the micromechanics methodology to relate actual driving force in structural configuration (J_{FB}) to equivalent driving force under highly constrained conditions (J_0) (*Source*: Ref. 43)

*B. R. Bass et al., Lockheed Martin Energy Research Corp., Oak Ridge Natl. Lab., "CSNI Project for Fracture Analyses of Large-Scale International Reference Experiments (FALSIRE II)," USNRC Report NUREG/CR-6460 (ORNL/TM-13207), to be published.

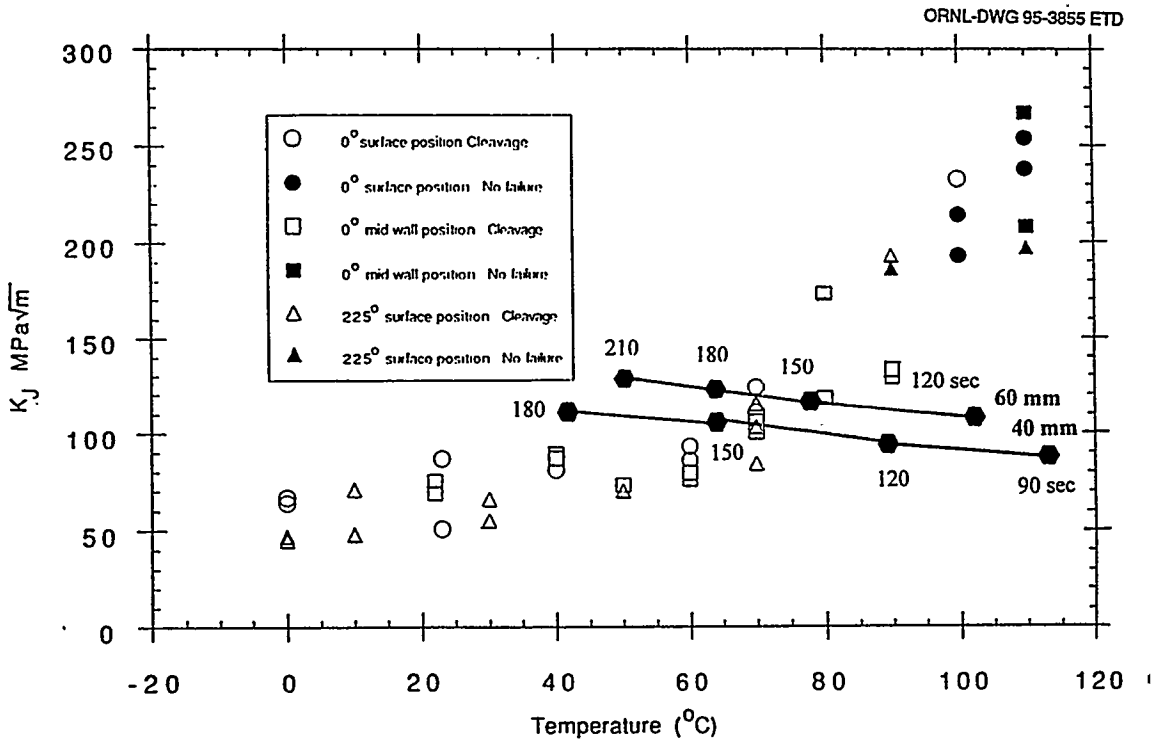

Figure 3.45 Predicted stress-intensity factor vs crack-tip temperature trajectory and measured material toughnesses for near-surface points of 40- and 60-mm cracks after correction for constraint loss effects (*Source*: Adapted from FALSIRE II problem statement)

noted next to each data point. The time, K_J, and temperature values at initiation must again be estimated as ranges because of the experimental scatter in the material toughness data; these ranges are given in Table 3.12. The net effect of the constraint correction is to lower the prediction curves in Fig. 3.45 as compared to the uncorrected curves shown previously in Fig. 3.41. The initiation time increases to between 140 and 200 s for the 40-mm defect, which is closer to but still short of the observed time of 240 to 300 s (4 to 5 min). Some of the remaining discrepancy may be due to an underestimate of the constraint loss effect; recall that the only biaxial tension results available in Fig. 3.44 are for $\phi = 17°$, which is deeper and more highly constrained than the predicted (and observed) crack initiation sites. Undoubtedly, some of the remaining discrepancy is also due to the very approximate nature of this constraint loss evaluation and to other factors unrelated to constraint loss.

Table 3.12 Predicted initiation times, crack-tip temperatures, and toughnesses after correction for constraint loss

	40-mm Crack	60-mm Crack
Initiation time, s	130–200	140–200
Crack-tip temperature, °C	78–46	84–60
K_J, MPa$\sqrt{m}$	110–120	115–130

3.7.3.8 Summary

The predictions for the SC-4 test made by UM and the other FALSIRE II analysts provide a reasonable approximation of the actual behavior observed during the test. The following specific observations are offered:

1. The UM analysis results are generally consistent with those from the other FALSIRE II analyses of the SC-4 test. The few significant discrepancies that do exist are explainable in reasonable terms.

2. The predicted gross structural response of the specimen (as quantified by strain histories remote from the crack tip) does not compare well with the actual measured response at all locations. In some instances, independent approximate evaluations of the strains cast some question on the integrity of the measured strain data. However, the discrepancies may also be due to modeling errors (e.g., boundary conditions at the ends of the specimen). This issue merits further investigation.

3. The UM analysis predicted crack initiation at near-surface locations reasonably near the actual initiation sites as determined from postmortem examination of the fracture plane. However, the analyses predict initiation times considerably earlier than those observed during the test. This also implies predicted crack initiation at higher crack-tip temperatures and higher K_I values than in the actual test.

4. Part of the discrepancy between predicted and observed initiation times may be due to constraint loss effects in the region near the inner surface of the specimen. Approximate analyses based on published results from Dodds et al.[43] suggest that the equivalent high constraint K_{Ic} value at the initiation sites may be only 70% of the low-constraint K_I values computed for the test specimen. Including these constraint loss effects increases the predicted initiation time and correspondingly decreases the predicted crack-tip temperatures and K_{Ic} values at initiation. However, computed initiation times are still short of observed initiation times.

References

1. W. Marshall, "An Assessment of the Integrity of PWR Pressure Vessels," Report by a Study Group, U. K. Atomic Energy Authority, Risley, October 1976.

2. W. Marshall, "An Assessment of the Integrity of PWR Pressure Vessels," Second Report by a Study Group, U. K. Atomic Energy Authority, Risley, March 1982.

3. U.S. Nuclear Regulatory Commission, Regulatory Guide 1.154, "Format and Content of Plant-Specific Pressurized Thermal Shock Safety Analysis Reports for Pressurized Water Reactors."*

4. R. D. Cheverton, J. W. Bryson, D. J. Alexander, and T. Slot, Martin Marietta Energy Systems, Inc., Oak Ridge Natl. Lab., "Thermal Shock Experiments TSE-7," USNRC Report NUREG/CR-4304 (ORNL/TM-6177), August 1985.†

5. R. D. Cheverton, Union Carbide Corp., Nucl. Div., Oak Ridge Natl. Lab., "Pressure Vessel Fracture Studies Pertaining to a PWR LOCA-ECC Thermal Shock: Experiments TSE-1 and TSE-2," USNRC Report ORNL/NUREG/TM-31, September 1976.†

6. R. D. Cheverton et al., Martin Marietta Energy Systems, Inc., Oak Ridge Natl. Lab., "Pressure Vessel Fracture Studies Pertaining to the PWR Thermal-Shock Issue: Experiments TSE-5, TSE-5A, and TSE-6," USNRC Report NUREG/CR-4249 (ORNL-6163), June 1985.†

7. T. J. Burns et al., Martin Marietta Energy Systems, Inc., Oak Ridge Natl. Lab., "Pressurized Thermal Shock Evaluation of the Oconee-1 Nuclear Power Plant," USNRC Report NUREG/CR-3770 (ORNL/TM-9176), May 1986.†

8. D. L. Selby et al., Martin Marietta Energy Systems, Inc., Oak Ridge Natl. Lab., "Pressurized Thermal Shock Evaluation of the Calvert Cliffs Unit 1 Nuclear Power Plant," USNRC Report NUREG/CR-4022 (ORNL/TM-9408), September 1985.†

9. D. L. Selby et al., Martin Marietta Energy Systems, Inc., Oak Ridge Natl. Lab., "Pressurized Thermal Shock Evaluation of the H. B. Robinson Unit 2 Nuclear Power Plant," USNRC Report NUREG/CR-4183 (ORNL/TM-9567), Vols. 1 and 2, September 1985.†

10. G. C. Robinson, J. G. Merkle, and R. W. Derby, Union Carbide Corp., Nucl. Div., Oak Ridge Natl. Lab., "Fracture Initiation Aspects of the Loss of Coolant Accident for Water Cooled Nuclear Reactor Pressure Vessels," HSSTP-TM-24, September 1973.†

11. R. D. Cheverton, S. K. Iskander, and D. G. Ball, "Review of Pressurized-Water-Reactor-Related Thermal Shock Studies," *Fracture Mechanics: Nineteenth Symposium, ASTM STP 969*, T. A. Cruse, Ed. (American Society for Testing Materials, Philadelphia, 1988), pp. 752–66.‡

12. R. D. Cheverton, J. W. Bryson, D. J. Alexander, and T. Slot, "Thermal Shock Experiments with Flawed Clad Cylinders," *Nucl. Eng. Des.* 124, 109–19 (1990).‡

13. J. Keeney-Walker, B. R. Bass, and W. E. Pennell, "Evaluation of the Effects of Irradiated Cladding on the Behavior of Shallow Flaws Subject to Pressurized-Thermal-Shock Loading," in *Proceedings of the 11th Conference on Structural Mechanics in Reactor Technology, August 18–22, 1991, Tokyo, Japan* (1991).

14. J. Keeney-Walker, J. G. Merkle, S. K. Iskander, and T. L. Dickson, Martin Marietta Energy Systems, Inc., Oak Ridge Natl. Lab., "Finite-Length Surface Crack Propagation in Clad Cylinders," USNRC Report NUREG/CR-5915 (ORNL/TM-12166), November 1992.†

15. D. K. Shum, J. W. Bryson, and J. G. Merkle, Martin Marietta Energy Systems, Inc., Oak Ridge Natl. Lab., "Potential Change in Flaw Geometry of an Initially

Shallow Finite-Length Surface Flaw During a Pressurized-Thermal-Shock Transient," USNRC Report NUREG/CR-5968 (ORNL/TM-12279), September 1993.†

16. F. M. Haggag, W. R. Corwin, and R. K. Nanstad, Martin Marietta Energy Systems, Inc., Oak Ridge Natl. Lab., "Irradiation Effects on Strength and Toughness of Three-Wire Series-Arc Stainless Steel Weld Overlay Cladding," USNRC Report NUREG/CR-5511 (ORNL/TM-11439), 1990.†

17. "Rules for Inservice Inspection of Nuclear Power Plant Components," Section XI, *American Society of Mechanical Engineers Boiler and Pressure Vessel Code*, American Society of Mechanical Engineers, New York, 1986.‡

18. R. D. Cheverton and D. G. Ball, Martin Marietta Energy Systems, Inc., Oak Ridge Natl. Lab, "OCA-P, A Deterministic and Probabilistic Fracture Mechanics Code for Applications to Pressure Vessels," USNRC Report NUREG/CR-3618 (ORNL-5991), May 1984.†

19. D. E. McCabe, "Fracture Evaluation of Surface Cracks Embedded in Reactor Vessel Cladding," USNRC Report NUREG/CR-4841 (MEA-2200), May 1987.†

20. D. E. McCabe, "Fracture Evaluation of Surface Cracks Embedded in Reactor Vessel Cladding," USNRC Report NUREG/CR-4841 (MEA-2329), May 1989.†

21 J. A. Keeney, B. R. Bass, W. J. McAfee, and S. K. Iskander, Martin Marietta Energy Systems, Inc., Oak Ridge Natl. Lab., "Preliminary Assessment of the Fracture Behavior of Weld Material in Full-Thickness Clad Beams," USNRC Report NUREG/CR-6228 (ORNL/TM-12735), October 1994.†

22. T. H. Theiss and D. K. M. Shum, Martin Marietta Energy Systems, Inc., Oak Ridge Natl. Lab., "Experimental and Analytical Investigation of the Shallow-Flaw Effect in Reactor Pressure Vessels," USNRC Report NUREG/CR-5886 (ORNL/TM-12115), July 1992.†

23. M. G. Dawes, "Significance of Locally Intensified Strain Aging to the Fracture Toughness of Welded Steel Structures," *Fracture Mechanics: 26th Volume, ASTM STP 1256*, W. G. Reuter, J. H. Underwood, and J. C. Newman, Jr., Eds. (American Society for Testing Materials, Philadelphia, 1995).‡

24. M. F. Kanninen and G. C. Chell, "An Assessment of the Importance of Vessel Cladding and Flaw Shape in the Analysis of Nuclear Reactor Pressure Vessel Integrity—A Report on an Experts' Workshop Meeting," co-organized by Electric Power Research Institute and U.S. Nuclear Regulatory Commission, May 1994.

25. T. J. Theiss et al., Martin Marietta Energy Systems, Inc., Oak Ridge Natl. Lab., "Initial Results of the Influence of Biaxial Loading on Fracture Toughness," USNRC Report NUREG/CR-6036 (ORNL/TM-12349) June 1993.†

26. B. R. Bass, J. W. Bryson, T. J. Theiss, and M. C. Rao, Martin Marietta Energy Systems, Inc., Oak Ridge Natl. Lab., "Biaxial Loading and Shallow Flaw Effects on Crack-Tip Constraint and Fracture Toughness," NUREG/CR-6132 (ORNL/TM-12498), January 1994.†

27. W. J. McAfee, B. R. Bass, J. W. Bryson, and W. E. Pennell, Martin Marietta Energy Systems, Inc., Oak Ridge Natl. Lab., "Biaxial Loading Effects on Fracture Toughness of Reactor Pressure Vessel Steels," USNRC Report NUREG/CR-6273 (ORNL/TM-12866), March 1995.†

28. Title 10, Code of Federal Regulations, Part 50, Sect. 50.61, "Fracture Toughness Requirements for Protection Against Pressurized Thermal Shock Events."‡

29. B. A. Bishop, "Benchmarking of Probabilistic Fracture Mechanics Analyses of Reactor Vessels Subjected to Pressurized Thermal Shock (PTS) Loading," EPRI Research Project 2975-5, March 1993.

30. T . L. Dickson, Martin Marietta Energy Systems, Inc., Oak Ridge Natl. Lab., "FAVOR: A Fracture Analysis Code for Nuclear Reactor Pressure Vessels," Release 9401, ORNL/NRC/LTR/94/1, February 1994.**

31. E. F. Rybicki and R. B. Stonesifer, "Computation of Residual Stresses Due to Multiple Welds in Piping Systems," *J. Pressure Vessel Technol.* 101, 149–54 (May 1979).‡

32. *ABAQUS Theory Manual*, Version 5–3, Hibbit, Karlson, and Sorensen, Inc., Providence, R.I., 1993.

33. Combustion Engineering Owners Group, Combustion Engineering Inc., "Low Temperature Overpressurization Transient Pressure-Temperature Limit For Determination of Low Temperature Overpressure Protection Setpoints," CEN-381-P, December 1988.

34. E. F. Rybicki and J. R. Shadley, Mechanical Engineering Department, The University of Tulsa, "Residual Stress Evaluation of a K-Bevel Weld," ORNL/NRC/LTR-90/27, October 31, 1990.**

35. E. F. Rybicki, J. R. Shadley, and A. S. Sandhu, The University of Tulsa, Mechanical Engineering Associates, Inc., "Experimental Evaluation of Residual Stresses in a Weld Clad Plate and Clad Test Specimens," USNRC Report NUREG/CR-4646 (MEA-2145), October 1986.†

36. N. P. O'Dowd and C. F. Shih, "Family of Crack-Tip Fields Characterized by a Triaxiality Parameter: Part I—Structure of Fields," *J. Mech. Phys. Solids* 39, 989–1015 (1991).‡

37. R. H. Dodds, T. L. Anderson, and M. T. Kirk, "A Framework to Correlate a/W Ratio Effects on Elastic-Plastic Fracture Toughness (J_c)," *Int. J. Fract.* 48, 1–22 (1991).‡

38. K. Wallin, "Statistical Aspects of Constraint with Emphasis on Testing and Analysis of Laboratory Specimens in the Transition Region," *Constraint Effect in Fracture, ASTM STP 1171*, E. M. Hackett, K. H. Schwalbe, and R. H. Dodds, Eds. (American Society for Testing and Materials, Philadelphia, 1993), pp. 264–88.‡

39. B. R. Bass et al., Martin Marietta Energy Systems, Inc., Oak Ridge National Lab., *CSNI Project for Fracture Analysis of Large-Scale International Reference Experiments (Project FALSIRE)*, USNRC Report NUREG/CR-5997 (ORNL/TM-12307), June 1993.†

40 J. A. Keeney, Martin Marietta Energy Systems, Inc., Oak Ridge Natl. Lab., "Cleavage Fracture Analyses of the French Clad Beam Experiments—DSR3 and DD2," ORNL/NRC/LTR-94/24, October 31, 1994.**

41. D. J. Lacey et al., "Spinning Cylinder Test 4: An Investigation of Transition Fracture Behavior for Surface Breaking Defects in Thick-Section Steel Specimens," AEA Technology Report AEA TRS 4098, June 1991.

42. N. P. O'Dowd and C. F. Shih, "Family of Crack-Tip Fields Characterized by a Triaxiality Parameter: Part II—Fracture Applications," *J. Mech. Phys. Solids* 40, 939–63 (1992).‡

43. R. H. Dodds, Jr., C. F. Shih, and T. L. Anderson, "Continuum and Micromechanics Treatment of Constraint in Fracture," USNRC Report NUREG/CR-5971 (UILU-ENG-92-2014; CDNSWC/SME-CR-19-92), July 1993.†

44. T. L. Anderson and R. H. Dodds, "Specimen Size Requirements for Fracture Toughness Testing in the Ductile-Brittle Transition Region," *J. Test. Eval.* 19, 123–34 (1991).‡

---

*Copies are available from U.S. Government Printing Office, Washington, D.C. 20402. ATTN: Regulatory Guide Account.

†Available for purchase from the National Technical Information Service, Springfield, VA 22161.

‡Available in public technical libraries.

**Available in NRC PDR for inspection and copying for a fee.

4 Ductile-to-Cleavage Fracture-Mode Conversion

J. A. Keeney

4.1 Introduction

The objective of Task 4 is to study the fracture process in the transition regime, where crack extension begins in a stable ductile tearing mode and then converts to a brittle cleavage mode after some amount of crack extension. The material failure by cleavage after ductile tearing can be regarded as a combined effect of a deterministic stable-tearing process (J-R curve) and a probabilistic cleavage process. This ductile-to-brittle mode conversion is associated with large scatter in fracture-toughness testing in the transition temperature regime. Understanding the fracture-mode conversion will permit a better prediction of actual crack extension in vessels and allow more realistic safety margins to be used in analyses.

During this report period, work continued on the characterization of precleavage tearing behavior and development of a fracture-mode conversion model to take into account any precleavage ductile tearing in fracture predictions.

4.2 Metallurgical Investigations (D. J. Alexander, M. C. Rao, and R. K. Nanstad)

The process of precleavage ductile tearing and mode conversion to cleavage is being investigated metallurgically using existing test results. The physical factors involved in this phenomenon have to be accounted for in the development of a fracture-mode conversion model. Also, different fractographic features are important depending on the model that is used (i.e., void and inclusion volume fraction for void formation and coalescence models). This investigation will (1) identify potential sources of fracture surfaces relevant to precleavage ductile tearing (i.e., ORNL); (2) secure the fracture surfaces that are from other sources besides ORNL; and (3) conduct examinations of the fracture surfaces. The initial metallurgical examination will (1) characterize the extent of crack-tip blunting prior to crack growth, (2) identify and characterize the microstructural features associated with microvoid formation and growth, (3) identify and characterize the microstructural features responsible for the mode conversion to cleavage, and (4) describe the relationship between the ductile crack morphology and the trigger points at mode conversion. The results from these investigations will be used in the development of the fracture-mode conversion model.

The first step of this project was to select a material and to measure the metallurgical features that might be involved in the fracture-mode conversion process. This would demonstrate the capabilities of the characterization facilities and provide an initial set of parameters that might be involved in any modeling of the material. These microstructural features would be incorporated in the appropriate constitutive equations and models used to analyze the mode conversion process. A letter report that describes the initial characterization of the first candidate material has been written.

The material selected for the initial characterization was the weld metal from the SNUPPS shell, which was taken from a canceled nuclear RPV. This material is being used to determine the effects of material inhomogeneities and fabrication procedures on the fracture toughness of prototypical material from an actual RPV. The submerged-arc weld was made with A 533 B class 1 filler metal in A 533 B base metal.[1] A stainless steel cladding was deposited on the inner surface of the vessel. Large bend bars complete with the cladding layer on the inner surface have been sectioned from the RPV. These specimens have been tested at the National Institute for Standards and Technology (NIST).[1] Some of these tests have shown significant stable tearing prior to final fracture that occurred by cleavage, making this material a suitable candidate. In addition, the inclusions expected in a weld metal should be spherical and well suited to automated image analysis techniques.

The SNUPPS bend bars tested at NIST included portions of the longitudinal weldment from the RPV. The only immediately available material from the welds in the RPV was in the form of broken Charpy specimens from the circumferential weld, which may not be identical to the longitudinal weld. However, the mechanical properties of the circumferential weld are similar to those of the longitudinal weld;[1] therefore, this material provides a convenient surrogate for these preliminary examinations. The Charpy specimens had been oriented across the circumferential weldment so that the fracture surface lay along the centerline of the weld (T-L orientation). One specimen was selected, and three sections were taken to reveal the microstructure. The inclusions present on the face parallel to the fracture surface (the "T" face) were examined by quantitative image analysis to characterize their size distribution and spacing.

The sample was examined in the as-polished condition on an SEM, equipped with a Robinson back-scattered electron (BSE) detector, an image analysis system, and an energy dispersive X-ray analysis system. Most of the imaging was done in the back-scattered mode with the SEM operating at an accelerating voltage of 20 kV. Image analysis was done at 4000X, a magnification chosen to achieve reasonable resolution while still being able to examine a large number of features (roughly 1000) over a reasonable number of viewing fields (80).

Selected results of the analysis are shown in Figs. 4.1 to 4.4. The average diameter, mean free path, and elongation ratio data show significant "tails," indicating non-Gaussian distributions. The lack of uniformity in particle spacing was apparent in the micrographs. The image analysis data indicate that significant errors may be introduced in modeling or analyses that assume a random distribution of particle size, shape, and spatial distribution.

This preliminary examination of a typical candidate material has raised several issues. One of these is the effect of the voltage at which the SEM is operated. The present data were gathered with the SEM operating at 20 kV. This voltage will result in the sampling of a volume of material that extends well below the specimen surface. This approach will reveal particles that are actually below the surface, which would not be visible in an optical examination. This, in turn, will give larger apparent volume fractions of particles than are actually present. One way to examine this effect is to repeat the measurements with a much lower operating voltage. At a low voltage only the very near surface features will be revealed. If the lower voltage results in a lower volume fraction of particles, a lower voltage will be necessary for the measurements.

Another check of a possible voltage effect is to compare the results from the SEM examination to those obtained by optical measurements. The optical measurements will have to be taken at much lower magnification, which will result in many more particles being sampled in each field of view. However, the lower magnification may not permit the smallest particles to be resolved. The fact that more particles will be present in each field of view will permit the optical comparison to be made in a short time.

The lower magnification used in the optical measurements will also ensure that the larger particles are measured. Initial examination of the as-polished microstructure suggests that some very large particles are present. The high magnification used in the SEM study may have resulted in missing these large particles. These large particles are likely to be the first particles to form voids in the fracture process, and so their characterization is critically important. The optical measurement will indicate whether these particles are being sampled. Should the optical and SEM examinations reveal significantly different particle distributions, a decision as to the suitability of each technique will have to be made.

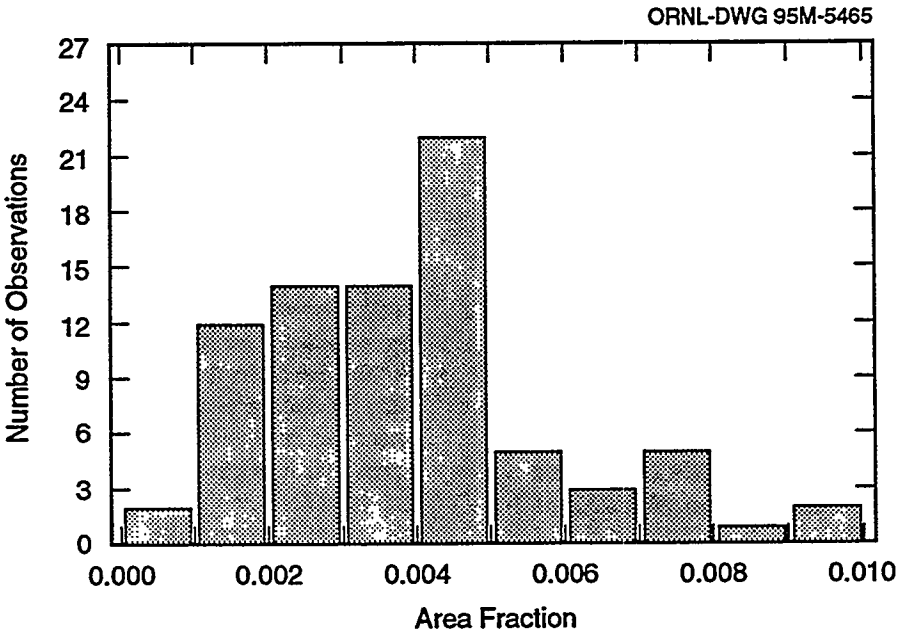

Figure 4.1 Histogram summarizing image analysis data, showing distribution of area fraction (equivalent to volume fraction) of features (inclusions) measured in 80 viewing fields sampled

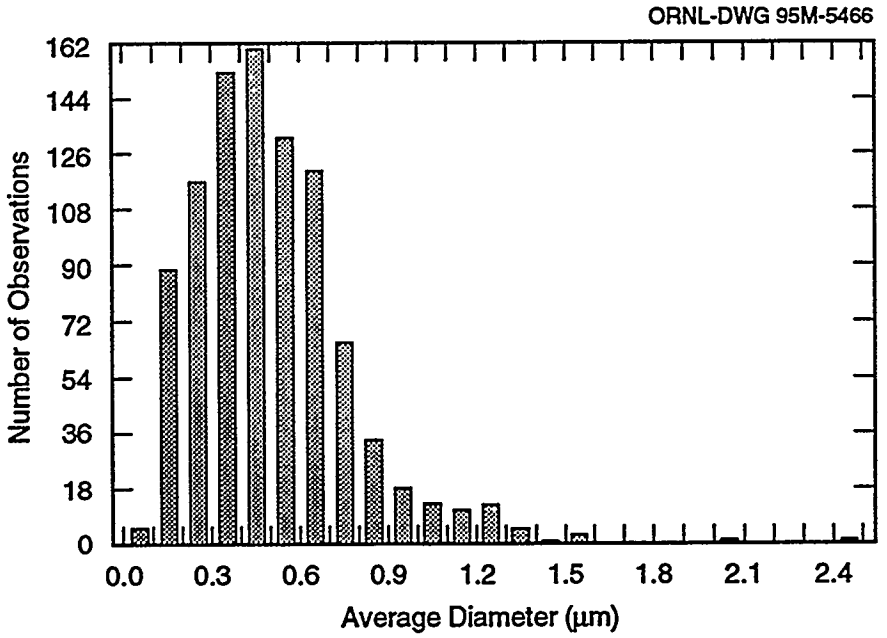

Figure 4.2 Histogram summarizing image analysis data, showing distribution of average diameters of 942 features (inclusions) measured

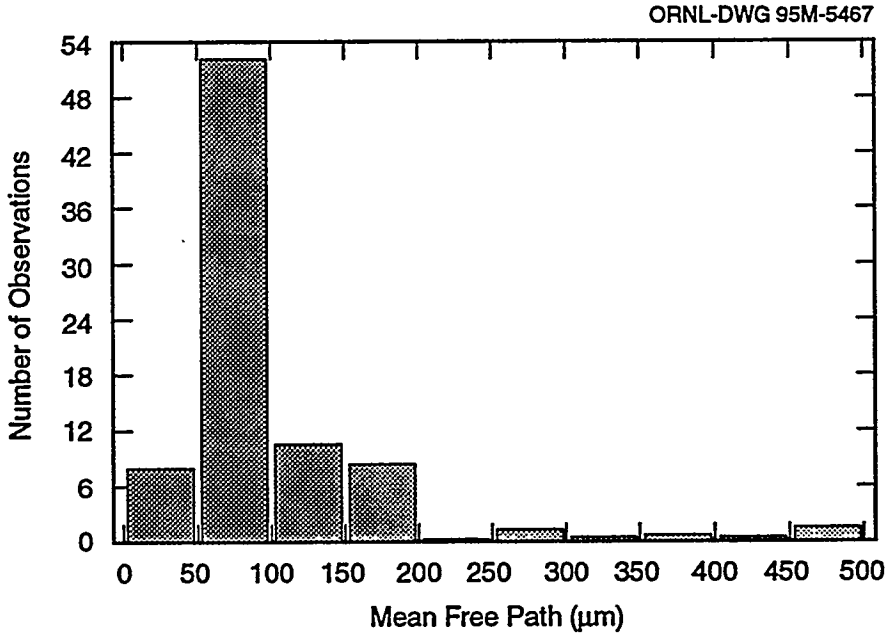

Figure 4.3 Histogram summarizing image analysis data, showing distribution of mean free path (average distance between particles) measured in 80 viewing fields sampled

Fractographic examination of the fracture surface will provide direct evidence of which particles are involved in the fracture process. Each dimple should have a particle associated with it, if the fracture process occurs by the classical mechanism of voids initiating at a particle in the matrix. This method should provide additional guidance as to which particles must be characterized for incorporation into the modeling effort. A decision must be made as to exactly which of the many parameters generated by the image analysis software provides useful information for the modeling effort.

It appears that an actual microstructure is much more complex than the simple "cartoon" view of a material that is often used in the development of models. To properly

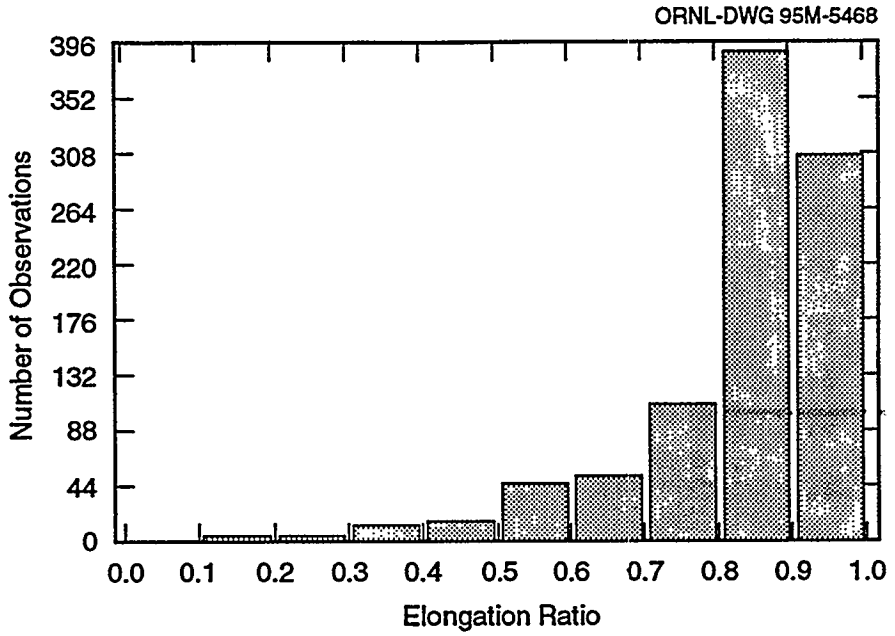

Figure 4.4 Histogram summarizing image analysis data, showing distribution of elongation ratio (a measure of particle sphericity) of 942 features (inclusions) measured

characterize a real material will demand significant time and effort and, thus, expense. These will almost certainly increase for a base metal material, which can be expected to have a lower volume fraction of particles that will not be as evenly distributed and as regularly shaped as the inclusions in a weld metal. This fact will again demand a further increase in the effort and expense necessary to properly characterize the microstructure.

4.3 Fracture-Mode Conversion Model Development (B. R. Bass and J. A. Keeney)

4.3.1 Fracture Models

The fracture prediction model being developed for the transition toughness region includes the effects of precleavage ductile tearing, as well as those due to large-scale yielding. The strategy employed within the HSST Program to develop and validate a fracture model for predicting mode conversion in the transition temperature region was described previously in Ref. 2. In that approach, five areas of investigation, which contribute to the overall objective of achieving a validated model, were defined.

1. Fracture- and Tearing-Toughness Data—Analyses of postulated PTS events in RPVs have demonstrated that the majority of predicted crack initiations originate from shallow-flaws located on the inner surface of the vessel. Fracture mechanics tests of SENB specimens,[3] coupled with detailed elastic-plastic finite-element analyses, have shown that shallow surfaced flaws exhibit an elevation of mean fracture toughness caused, in part, by effects of constraint relaxation at the crack tip.[3] A limited biaxial toughness data base developed at ORNL[4] from cruciform beam specimens provides evidence of a significant out-of-plane biaxial loading effect on the cleavage fracture toughness of shallow flaws. The shallow-flaw data obtained from SENB and cruciform specimens play an important role in the validation of models that characterize cleavage and ductile tearing processes.

2. Cleavage Initiation Model—A key element in the development of a fracture model describing mode conversion in the transition temperature region is a viable model of cleavage initiation for stationary cracks (i.e., no stable tearing). A validated model for cleavage fracture must successfully predict the effects of both uniaxial and biaxial loading on shallow-flaw fracture toughness in the transition region of RPV steels. Evaluations being conducted concurrently under Task 2 are focused on the selection of a validated model for initiation of cleavage fracture. The verification process for the selected cleavage model will (1) demonstrate the practicality of the model and (2) identify the parameter(s) controlling cleavage initiation.

3. Ductile Tearing Model—The ductile tearing model provides output data that represent essential input to the selected cleavage model for predicting fracture initiation. Functional requirements for candidate ductile tearing models include the following: (1) reproduce J_R-curve test data; (2) require only input data that are validated and readily available; and (3) provide output

that includes crack-tip radius and crack-plane plastic zone width as a function of crack growth. Initial evaluations will focus on constitutive formulations that describe progressive damage and material softening of the local crack-tip region. Should the local damage approach prove not to be viable, emphasis will shift to a model based on a parametric correlation of J_R-curve data with controlled changes in crack-tip constraint. These data will be obtained from cruciform specimen tests performed with varying biaxial load ratios. Output from these performance evaluations will be used to define the form of the ductile tearing-to-cleavage mode conversion model.

4. Fractography and Micromechanical Features—Determinations will be made concerning the availability of required data for the calibration and practical application of the ductile tearing models. This includes relevant information concerning distributions of void nucleating particles in RPV steels. Fractographic examinations will be conducted on fracture surfaces of test specimens for which ductile tearing preceded initiation of cleavage fracture. These examinations will provide essential data for performance evaluations of candidate ductile tearing models and final validation checks on the proposed fracture-mode conversion model.

5. Fracture-Mode Conversion Models—Performance assessments based on applications of the candidate cleavage and ductile tearing models to measured data from RPV steels will provide necessary input for defining the tearing-to-cleavage mode conversion model. The ORNL uniaxial and biaxial fracture-toughness data base provides essential input to this process. The candidate models will be evaluated to determine how the progression from crack-tip blunting to stable ductile tearing would affect predictions of mode conversion to cleavage for that particular correlation.

4.3.2 Ductile Tearing Model Development

In recent years, developments of models to quantify ductile tearing resistance in steels increasingly have emphasized the coupling of fracture processes on the microscale with conventional continuum approaches. Particular attention has been given to constitutive models that describe the evolution of local damage in front of the growing crack. The paper by Brocks et al.[5] provides an argument in favor of the continuum damage approach to modeling of the ductile tearing process. Constraint conditions influence triaxiality of the crack-tip stress fields, which impacts the extent of plastic flow around the crack tip. Higher stress triaxiality inhibits plastic flow, promotes void growth on the micromechanical level, and leads to increased damage in the fracture process zone. Constitutive equations have been formulated to describe the physical effects of constraint on void nucleation, growth and coalescence and, consequently, on tearing resistance. An advantage claimed for micromechanical models over conventional continuum models is that material parameters describing the tearing process can be transferred in a more general way among different specimen geometries. Typically, these parameters for the damage model are determined through a process that combines small-specimen testing and numerical modeling. Key issues giving rise to different analytical formulations for damage models include requirements to define characteristic length scales and constitutive equations incorporating material damage parameters.

4.3.2.1 Length Scales

The issue of characteristic length scales has been closely linked to mesh refinement in the crack-tip region. Predictions of local damage from constitutive models that include strain softening are strongly dependent upon mesh refinement near the crack tip. Shih and Xia[6] emphasize that crack initiation toughness and crack growth resistance are not influenced by element dimensions only when a length scale is introduced into the calculation. They also observe that void growth models utilizing a highly refined mesh of the crack-tip region must include a statistical treatment of voids or inclusions. Approaches of the latter type have been described by Pineau[7] and by Rousselier.[8]

In their review of prior developments, Shih and Xia[6] briefly summarize several approaches to modeling the fracture process and to introducing, either implicitly or explicitly, a characteristic length scale into the fracture calculations. The dilatant plasticity model of Gurson[9] was employed by Aoki et al.[10] and by Aravas and McMeeking[11] to study the behavior of long cylindrical holes ahead of a blunting crack tip. The distance between the crack tip and the void provided a length scale for fracture initiation. The Gurson formulation was used also by Becker et al.[12] to describe the growth of cracks along grain boundaries by void growth and coalescence. A characteristic length for the problem is derived from the grain boundary thickness. Tvergaard and Hutchinson[13] modeled the fracture process using a traction-separation law defined on the crack plane. The traction-separation law incorporates a characteristic length for the fracture problem. In studies performed by Needleman and Tvergaard,[14] the spacing between colonies of large void-nucleating inclusions served as the length scale for a fracture problem.

Brocks et al.[5] discussed the introduction of localization limiters into the constitutive model as one approach to the problem. In this technique, weight functions are introduced that limit the influence of neighboring points on the evolution of internal state variables at a material point. Several

methodologies of the latter type have been proposed,[15–18] all of which require the introduction of a new critical length material parameter. This length parameter defines the region of influence of the weight function and may be linked to microstructural features such as mean spacing between inclusions.

Alternative approaches that involve effectively an element averaging technique have been proposed in numerous studies, including those of Brocks et al.,[5] Klingbeil et al.,[19] Ruggieri and Dodds,* Xia and Shih,[20] and Shih and Xia.[6] Brocks et al.[5] calibrate the element size by numerically matching an experimental load vs displacement record for a cracked specimen. Xia and Shih,[20] Shih and Xia,[6] and Ruggieri and Dodds* propose a row of elements on the crack plane (designated as computational cells) of size D/2, where D is chosen to be representative of the mean spacing between voids. Void growth within the computational cell is governed by stress and strain fields averaged over that cell. The latter techniques for introducing a length scale into the calculation can be related to the French local approach embodied in the work of Rousselier[8] and Rousselier et al.,[21] as well as references included therein. The characteristic length in the Rousselier model may be compared with the previously referenced length scales such as D/2.

4.3.2.2 Constitutive Relations

Constitutive formulations that describe progressive damage and material softening of the local crack-tip region include the previously referenced Gurson model,[9] as well as those from Rousselier[8] and to Lemaitre.[22] Here, the Gurson theory will be emphasized because of an extensive body of technical literature supporting key features of the model. Relevant studies addressing numerical and experimental features include those by Aravas,[23] Tvergaard,[24] and Needleman, Tvergaard, and Hutchinson.[25] Applications by Brock et al.,[5] Shih and Xia,[6] Xia and Shih,[20] and Ruggieri and Dodds* will be reviewed below. Brock et al.[5] apply the Gurson model globally over the finite-element model, while the other studies confine the Gurson model to a slab-type region of height D at the crack plane.

4.3.2.2.1 Gurson Model

Papers by Brocks et al.,[5] Sun et al.,[26] and Klingbeil et al.[19] provide summaries of the Gurson formulation employed by IWM, Freiburg, and by BAM, Berlin, Germany, to model ductile tearing in engineering metals. The Gurson formulation comprises a yield condition, flow rule, definition of void volume fraction, criteria for void nucleation, and a rule for evolution of the void volume fraction. Microvoids nucleate at inclusions and second-phase particles by a process of debonding or cracking during plastic deformation. The ratio of the void volume to the whole volume of a unit cell is defined as the void volume fraction (f). The temporal evolution of f is governed by two terms that define void nucleation and growth rates,

$$\dot{f} = \dot{f}_{growth} + \dot{f}_{nucl} , \tag{4.1}$$

where the growth rate is given by

$$\dot{f}_{growth} = (1-f)\, D^{p}_{kk} , \tag{4.2}$$

and the initial condition by

$$f(t_0) = f_0 . \tag{4.3}$$

Here D_{ij} denotes components of the symmetric part of the spatial velocity gradient tensor and D^{p}_{ij} the plastic part thereof.

To describe the nucleation of voids, Brocks et al.[5] adopt the empirical formulation of Needleman and Rice,[27]

$$\dot{f}_{nucl} = A\,\dot{\sigma}_m + (B/3)\,\dot{\sigma}_{kk} , \tag{4.4}$$

where σ_{ij} is the macroscopic Cauchy stress. Brocks et al.[5] reference the formulation of Chu and Needleman[28] for the parameters A and B. These parameters have one form if void nucleation is driven by accumulated plastic strain (strain controlled) or another form if controlled by hydrostatic stress (stress controlled). (The reader is referred to Refs. 5 and 28 for details concerning the parameters A and B.)

In the material matrix undergoing plastic deformation, the nucleated microvoids experience shape changes and volumetric growth. Gurson[9] used a relationship that postulates that void growth rate depends exponentially on the stress triaxiality to describe plastic yielding of a matrix material containing voids. The constitutive relation employed to model an elastic-plastic solid containing voids is a form of the Gurson model that was modified by Tvergaard and Needleman[29–32] to improve accuracy of the model. The central feature of the modified Gurson model is the yield function given by

$$\Phi = \left(\frac{\sigma_e}{\sigma_0}\right)^2 + 2q_1 f \cosh\left(\frac{3}{2}\frac{q_2\sigma_m}{\sigma_0}\right) - \left(1+q_3 f^2\right) = 0 . \tag{4.5}$$

Here, σ_e is the macroscopic Mises effective stress, σ_m the macroscopic mean stress, σ_0 the current flow stress, f the

*C. Ruggieri and R. H. Dodds, "Numerical Modeling of Ductile Crack Growth for Porous Plastic Materials in 3-D Using Computational Cells," University of Illinois, to be published.

current void volume fraction, and q_1, q_2, q_3 are factors proposed by Tvergaard.[32] (Typical values for these factors are $q_1 = 1.25$, $q_2 = 1.0$, and $q_3 = q_1^2$.) A flow law relating the plastic strain rate to the stress rate is provided in various references (e.g., see Refs. 5 and 20). For the void-free condition given by $f = 0$, the Gurson model reduces to J_2 flow theory of plasticity.

A modified form of the void volume fraction (f^*) is employed to account for coalescence of voids, which occurs after a critical volume fraction (f_c) is reached:

$$f^* = \begin{cases} f & \text{for } f \le f_c \\ f_c + K(f - f_c) & \text{for } f > f_c \text{ with } K = \dfrac{f_u^* - f_c}{f_f - f_c} \end{cases} \quad (4.6)$$

The material loses stress-carrying capacity when the final void volume fraction (f_f) is reached and where f^* achieves its ultimate value f_u^*.

The modified Gurson formulation has been augmented with equations to account for strain rate and temperature dependence of the current yield stress.[33] Also, this model has been combined with an adiabatic heating model to incorporate the effects of temperature increase due to plastic work in dynamic fracture analyses.[34] Two groups of material parameters are required to characterize this model:

- parameters associated with classical rate-independent plasticity or strain-rate-dependent plasticity, which would include temperature effects, and
- parameters required for the modified Gurson model, that is, ε_n, f_n, s_n, f_0, f_c, f_f, and q_1, q_2, q_3.

Three parameters—ε_n, f_n, s_n—are required to model void nucleation [through Eq. (4.4)]. Other parameters—f_0, f_c, f_f—describe void growth, coalescence, and failure.

Strategies for evaluating the parameters in the modified Gurson model are discussed by Brocks et al.[5] While there may not be a generally accepted scheme for determining these parameters, load vs reduction of diameter curves from notched tensile bars appear to provide one avenue. Values for the parameters f_0, f_c, and f_f are determined by fitting various segments of the computationally determined load vs reduction in diameter curve with the experimental data. Note that the void volume fraction, f_0, was *not* determined from micrographs of the material. Tensile bars from a mild steel with notch radii of 4 and 10 mm were used to characterize parameters in the modified Gurson model as follows: $f_0 = 0.0025$, $f_c = 0.021$, and $f_f = 0.19$. A four-node linear displacement element with full integration and an edge length of 0.25 mm was used in the center of the tensile bar model. The remaining parameters describing void nucleation were taken from the paper of Needleman and Tvergaard.[31] This set of parameters characterizing the Gurson model was used to successfully predict J_R-curves from a range of specimen geometries subjected to static and dynamic loading conditions.

Sun et al.[26] performed a comparative study of the damage models based on the modified Gurson model and on the critical void growth model developed by Rice and Tracey[35] using the von Mises yield function. Damage parameters were investigated, and the local and global behavior of several specimen geometries were compared with experimental data. Both damage models were described as producing qualitatively consistent results with regard to the influence of stress triaxiality on void growth and on the early stages of material failure. Conclusions drawn from the study were that the Gurson model provided a more accurate simulation of material failure after the onset of void coalescence, while the critical crack growth model produced fewer numerical convergence problems in simulating large crack extension.

4.3.2.2.2 Slab-Type Gurson Model

Shih and Xia,[6] Xia and Shih,[20] and Ruggieri and Dodds* have idealized the void growth mechanism in a model which assumes that void growth and coalescence are confined to a narrow material layer of initial thickness D, which is centered about the macroscopic fracture plane (see Fig. 4.5). They justify this simplification on the basis that many metals that fail by void growth and coalescence exhibit a macroscopically planar fracture process zone of one or two void spacings in thickness. Ligaments between the voids experience intense plastic deformation. Voids that are outside this region are observed to display little or no growth. Within the fracture process zone layer of thickness D, the material response is described by a simplified form of the Gurson micromechanical model. Outside this layer, the material is assumed free of voids, and the response to deformation is described by classical J_2 flow theory of plasticity. The overall objective of this approach is to develop an engineering micromechanics model that embodies the essence of stress triaxiality on fracture toughness, while requiring only a few essential metallurgical parameters.

A further simplification of the Gurson model is introduced by neglecting the evolution equation for void nucleation, leaving only the void growth rate term in Eq. (4.1). (Some implications of void nucleation modeling for fracture

*C. Ruggieri and R. H. Dodds, "Numerical Modeling of Ductile Crack Growth for Porous Plastic Materials in 3-D Using Computational Cells," University of Illinois, to be published.

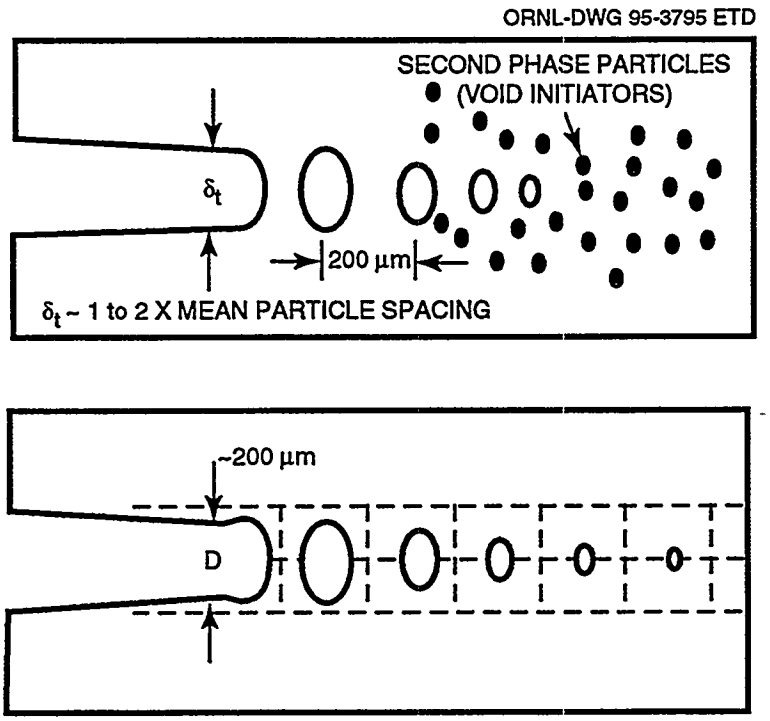

Figure 4.5 Ductile tearing by hole growth and coalescence is studied with computational tools including local damage models (Gurson) and highly refined (~100-mm) crack-tip meshes

predictions can be found in papers by Tvergaard and Hutchinson[13] and Needleman and Tvergaard.[31]) The parameters of the Gurson model remaining to be specified are the initial porosity f_0, the porosity at failure f_f, the explicit internal length scale D (which defines dimensions of the computational cells), and the number of finite elements to be defined over D (two to four elements are thought to be satisfactory). The important microstructural parameters are D and f_0, which can be taken as material parameters and estimated from metallurgical studies of the surfaces of fracture specimens. As an alternative, these parameters can be treated phenomenologically and selected to give the best fit to crack-growth data.

Shih and Xia[6] discretized the process zone with a single row of computational cells having dimensions D/2 by D/2. The Gurson cell is modeled using quadrilateral elements, each of which consists of four constant-strain triangular elements. Each cell contains a single void of initial volume fraction f_0, and growth of the void is governed by the stress and strain (computed from the Gurson model) averaged over that cell. Typically, the cell for which $f = 0.1$ is taken as the current position of the advancing crack tip. A damaged cell is rendered extinct using the element-vanishing technique of Tvergaard[36] when its volume fraction f exceeds a critical value f_f. When this failure condition is reached, the nodal forces computed from the remaining stresses in the now-extinct cell are released in N subsequent solution steps (N is typically 5 to 20).

Shih and Xia[6] employ the simplified Gurson material model (SGMM) in finite-element calculations to determine crack growth resistance curves for plane-strain mode-I crack growth under SSY conditions. Values of initial porosity (f_0) ranged from 0.001 to 0.03. Their calculations show that the stress peak and stress distribution in front of the crack tip are strongly affected by the initial porosity and length of the fracture process zone. For a low initial porosity, strong spatial gradients are computed for both the porosity and the normal stress ahead of the crack tip. These results are interpreted as being consistent with a single void interacting with the crack tip, the latter being a fracture mechanism previously studied by Rice and Johnson.[37] In the case of a higher initial porosity, results indicating less severe gradients in porosity and stress are interpreted as being consistent with multiple interacting voids.

These SGMM fields were shown to be different from those obtained from transient and steady state solutions for a growing crack that did not include damage and material softening in the calculations (such as Varias and Shih[38] and O'Dowd, Shih, and Dodds[39]). For low initial porosities, material softening was found to reduce the normal stress in the fracture process zone, but to cause an elevation immediately outside the process zone; the latter redistribution of stress was not found in Refs. 38 and 39. This result is cited as indicating a possible drawback for those analysis procedures that do not include material softening, such as node release techniques.

The SGMM was employed to compute J-resistance curves for deep- and shallow-crack bend bars previously tested by Joyce and Link.[40] Applications using damage parameters given by D/2 = 100 μm and $f_0 = 0.005$ ($f_f = 0.2$) successfully reproduced the experimentally measured J-Δa curves for both the shallow- and deep-crack bend bars.

Results from these calculations are used to address the competition between ductile tearing and unstable cleavage fracture in the transition temperature region. Their discussion focuses on the argument that the stress elevation caused by crack growth is one of several factors contributing to the transition to cleavage fracture after some amount of stable ductile crack growth. It is suggested that the SGMM can be used in combination with a statistical cleavage fracture model and a proper length scale to predict the transition to cleavage fracture after some amount of ductile tearing. A procedure is proposed for calibrating the parameters of such a combined ductile/cleavage computational model. A combined testing/analytical program would utilize high-constraint specimens (i.e., no ductile tearing) to determine parameters for the cleavage model, while low-constraint geometries would provide data incorporating substantial ductile tearing for calibration of D and f_0. The calibrated model would then be used to predict fracture behavior in a third geometry that exhibits some amount of precleavage tearing.

In a later study, Xia, Shih, and Hutchinson[41] select the two parameters, D and f_0, using a phenomenological approach; the parameters are adjusted to give the best fit for one set of experimental crack growth data for a specific material. In applications of the model to specific materials, it is recommended in Ref. 41 that the analyst first choose a subelement discretization scheme for the Gurson slab on the fracture plane. In the second step, D and f_0 are selected to best reproduce the experimental data for the material. The subelement discretization and parameters D, f_0 are then transferred to different specimen geometries of the same material. The latter technique was applied in Ref. 41 to model ductile crack growth in specimens of A 533 B and A710 steels, using as many as five different specimen geometries (i.e., three-point bend, compact tension, double-edge-notch tension strip, single-edge-notch tension strip, and center crack panel).

Ruggieri and Dodds* have incorporated the SGMM into the finite-element computer program WARP-3D,[42] which is under development at the University of Illinois. Descriptions of the WARP-3D program emphasize a solution strategy employing an implicit element-by-element, preconditioned conjugate-gradient algorithm. The computational scheme is implemented to execute in parallel/vector mode for the efficient solution of large-scale, 3-D finite-element models. The WARP-3D program is described as offering a range of nonlinear constitutive models (in addition to Gurson), a domain integral formulation for J-integral calculations, various procedures for crack growth modeling, and a global dynamic analysis capability.

Applications* of the WARP-3D model for ductile crack growth were described for an SSY model (with T = 0) and for a deeply notched SENB specimen (a/W = 0.6), based on properties typical of a moderate-strength pressure vessel steel.[42] The focus of these analyses was on the capabilities of the model to predict J-resistance curves for a range of initial void volume fraction values under both small- and large-scale yielding conditions. According to Ruggieri and Dodds,* crack growth by ductile tearing would be anticipated for relatively large initial porosity (e.g., $f_0 = 0.01$) because the high stresses necessary for cleavage initiation could not be achieved near the crack tip. As the porosity is lowered (e.g., to $f_0 = 0.001$), a transition to the cleavage mode is expected to be favored because the stresses ahead of the crack tip would be significantly higher and the high-stress region would extend over a larger region. Because the role of void nucleation is neglected in the SGMM, it is anticipated that the SGMM will perform better for materials characterized by larger initial porosities (such as low-to-moderate strength structural and pressure vessel steels).

The explicit length scale D was set at 0.2 mm, the critical volume fraction at $f_f = 0.2$, and values of f_0 ranged from 0.001 to 0.01, to allow comparisons of results with recent plane-strain analysis of Xia and Shih.[20] In Ruggieri and Dodds,* D and f_0 are regarded as computational parameters that are loosely coupled with specific metallurgical features of the material, such as mean spacing of particles. Mesh models used in the analyses employed 8-node, 3-D isoparametric elements incorporating a finite strain formulation. Plane-strain constraints were imposed on the 3-D elements to facilitate comparisons with results of Xia and Shih.[20]

Analysis results for an amount of crack growth equal to D in the SSY model indicate that near-tip stresses demonstrate an inverse dependence on initial porosity. Thus, a low initial value for the void volume fraction leads to higher stresses and to larger regions near the crack tip, which are subjected to higher tensile stresses. Before the onset of crack growth, stresses ahead of the tip are reduced in magnitude due to blunting of the crack tip. Crack growth restores the higher stresses and increases the distance ahead

*C. Ruggieri and R. H. Dodds, "Numerical Modeling of Ductile Crack Growth for Porous Plastic Materials in 3-D Using Computational Cells," University of Illinois, to be published.

of the crack tip over which the higher stresses occur. This feature of the stress fields associated with ductile tearing has implications for fracture-mode conversion in the transition temperature region. In particular, for materials with initially low void volume fraction, conversion to cleavage becomes more likely during the ductile crack growth process.

The model for the SENB specimen used to predict a J-Δa curve provided somewhat lower J-values than the experimental data. This result was attributed to the effects of using values for the computational parameters D, f_0 that were previously calibrated numerically by Xia and Shih[20] using a stiffer model.

4.3.2.3 Calibration of Gurson Model

In Task H.4, initial studies of ductile tearing models have focused on the Gurson-Tvergaard (G-T) dilatant plasticity model for void growth and an element extinction capability for modeling crack growth. These special features for modeling precleavage ductile tearing in pressure vessel steels are contained in the WARP-3D finite-element computer code[42] (described below). Using the G-T model, void nucleation and growth ahead of a stably tearing crack are incorporated into a finite-element model using computational cells with explicit length scales, as illustrated in Fig. 4.6. Two principal input parameters for the G-T model are the initial void volume fraction f_0 and the characteristic length D associated with the G-T crack plane elements. According to theory, these parameters are dependent only on the material and not on specimen geometry. To evaluate this model, Task 4 plans to generate ductile crack growth data from side-grooved compact tension (CT) specimens taken from the ORNL SNUPPS material. The parameters f_0 and D will be calibrated for the material through an iterative process involving finite-element analyses of these CT specimens (see Fig. 4.7). The calibrated parameters should provide analytical results in agreement with load vs CMOD and crack growth data from the CT specimens. Values of these parameters from the CT specimen analyses will then be transferred to large-scale structures (e.g., the full-thickness clad beams) to determine if they predict the observed response. (In preliminary studies, these parameters were set at $f_0 = 0.005$ and D = 200 μm.) Metallography may also provide some estimates of initial porosity and inclusion spacing in the weld, which could be compared with values assigned to parameters f_0 and D.

Recent analyses have verified the ductile crack growth capabilities for both plane-strain models and preliminary 3-D models, including side grooves. Parameters for the G-T model (initial porosity and cell size) were calibrated using an experimental R-curve for a deep-notch fracture specimen (e.g., a 1T-CT), and then predictions of the R-curve for a shallow-notch SE(B) specimen and tensile geometries were made. This approach has been remarkably successful in predicting constraint effects on R-curves. However, significant differences in the calibration parameters were found between plane-strain and 3-D analyses of the specimens. The initial porosity for the 3-D solutions must be on the order of 20% of the plane-strain value for the 3-D model to match the experimental R-curve (using properties for A 533 B). This effect is attributed to the maintenance of constraint levels to higher J-values in the 3-D models.

4.3.3 Computer Program Development (R. H. Dodds, Jr., University of Illinois)

During this report period, development and verification of the WARP-3D finite-element code[42] continued. Enhancement and verification of computer software to model ductile crack growth using the G-T model were completed. The WARP-3D software for 3-D nonlinear analyses of

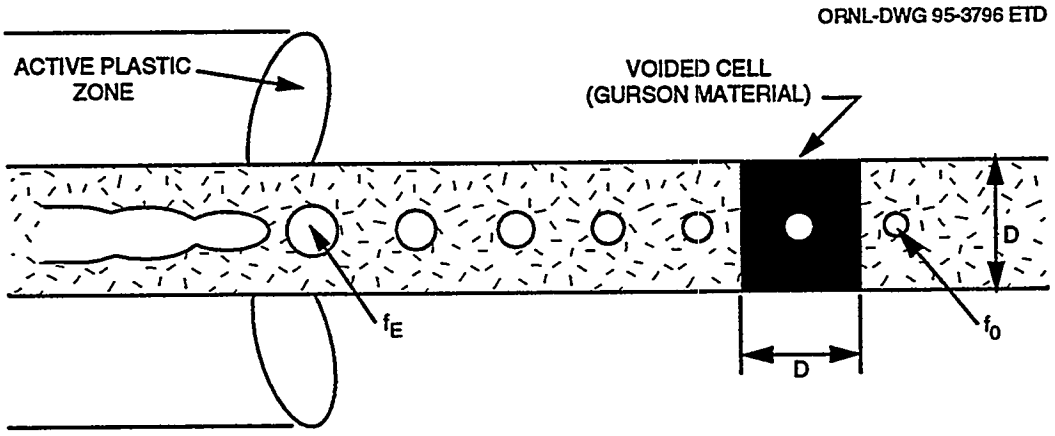

Figure 4.6 Two material damage parameters, initial slab height D and initial volume fraction f_0, selected to give best fit to experimental crack growth data

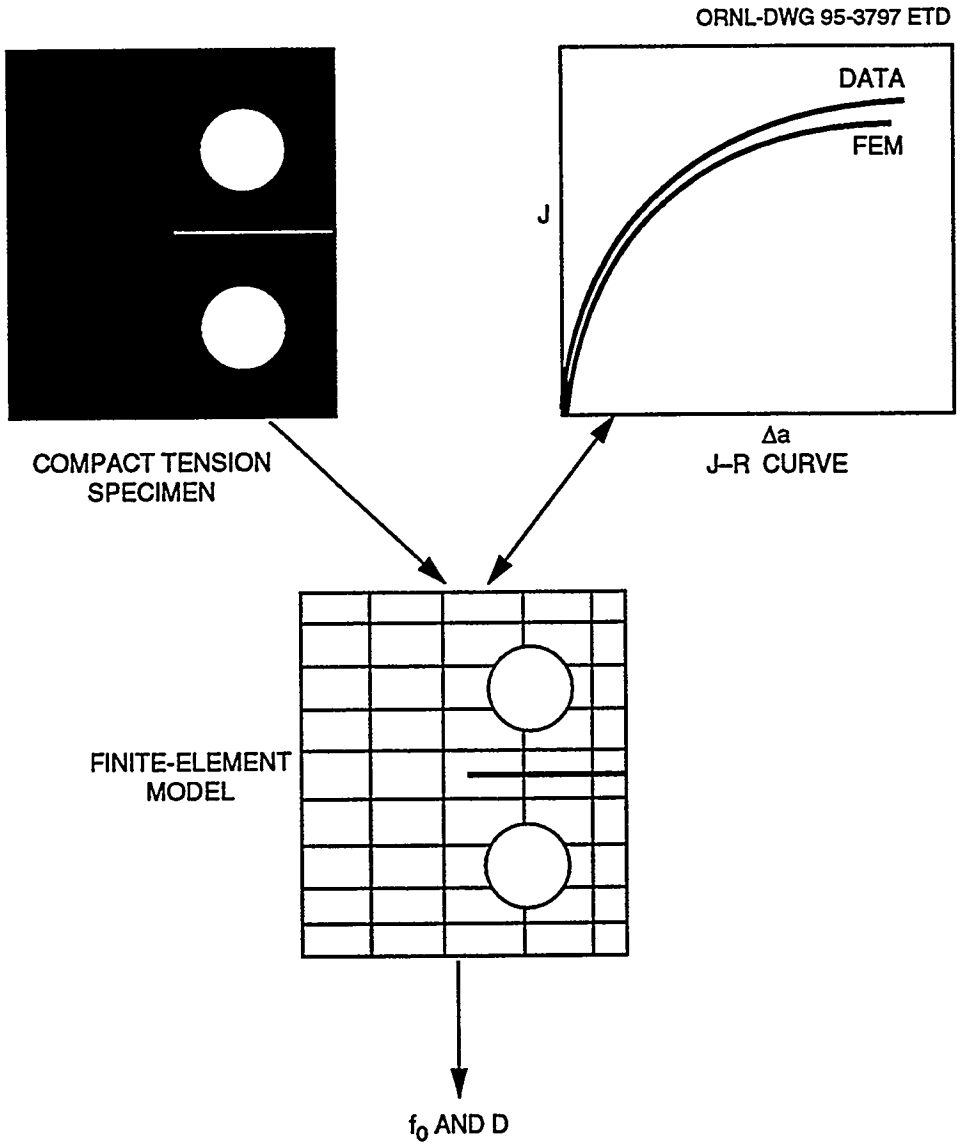

Figure 4.7 Small laboratory specimens used to calibrate Gurson model parameters f_0 and D

fracture-mechanics specimens and structural components has been successfully ported to the IBM RISC-6000 workstations. The unique features of this software include a G-T constitutive model to support ductile crack growth analyses using computational cell technology (described previously), a very efficient conjugate-gradient solver, domain integral evaluations, and static-impact loading.

Over the next few months, a discrete crack growth capability will be implemented in WARP-3D. A user-specified crack-tip opening angle (CTOA) will govern crack extension. Crack front tunneling in through-crack and surface crack models will be supported with this new capability.

References

1. J. A. Keeney, B. R. Bass, W. J. McAfee, and S. K. Iskander, Martin Marietta Energy Systems, Inc., Oak Ridge Natl. Lab., "Preliminary Assessment of the Fracture Behavior of Weld Material in Full-Thickness Clad Beams," USNRC Report NUREG/CR-6228 (ORNL/TM-12735), October 1994.*

2. W. E. Pennell, Martin Marietta Energy Systems, Inc., Oak Ridge Natl. Lab., "Heavy-Section Steel Technology Program Semiannual Progress Report for April–September 1994," USNRC Report NUREG/CR-4219 (ORNL/TM-9593/V11&N2), Vol. 11, No. 2, 1996.*

3. T. J. Theiss et al., Martin Marietta Energy Systems, Inc., Oak Ridge Natl. Lab., "Initial Results of the Influence of Biaxial Loading on Fracture Toughness," USNRC Report NUREG/CR-6132 (ORNL/TM-12498), January 1994.*

4. B. R. Bass, J. W. Bryson, T. J. Theiss, and M C. Rao, Martin Marietta Energy Systems, Inc., Oak Ridge Natl. Lab., "Biaxial Loading and Shallow-Flaw Effects on Crack-Tip Constraint and Fracture Toughness," USNRC Report NUREG/CR-6132 (ORNL/TM-12498), January 1994.*

5. W. Brocks, D. Klingbeil, G. Künecke, and D.-Z. Sun, "Application of the GURSON Model to Ductile Tearing Resistance," *Constraint Effects in Fracture: Theory and Application, ASTM STP 1244* (American Society for Testing and Materials, Philadelphia, 1994).†

6. C. F. Shih and L. Xia, "Modeling Crack Growth Resistance Using Computational Cells with Microstructurally-Based Length Scales," *Constraint Effects in Fracture: Theory and Application, ASTM STP 1244* (American Society for Testing and Materials, Philadelphia, 1994).†

7. A. Pineau, "Global and Local Approaches of Fracture—Transferability of Laboratory Test Results to Components," *Topics in Fracture and Fatigue*, A. S. Argon, Ed. (Springer-Verlag, New York, 1992), pp. 197–234.

8. G. Rousselier, "Ductile Fracture Models and Their Potential in Local Approach of Fracture," *Nucl. Eng. Des.* 105, 97–111 (1987).†

9. A. L. Gurson, "Continuum Theory of Ductile Rupture by Void Nucleation and Growth: Part I—Yield Criteria and Flow Rules for Porous Ductile Media," *J. Eng. Mater. Technol.* 99, 2–15 (1977).†

10. S. Aoki, K. Kishimoto, K. Takeya, and M. Sakata, "Effects of Mircovoids on Crack Blunting and Initiation in Ductile Materials," *Int. J. Fract.* 24, 267–78 (1984).†

11. N. Aravas and R. M. McMeeking, "Microvoid Growth and Failure in the Ligament between a Hole and a Blunt Crack Tip," *Int. J. Fract.* 24, 21–38 (1985).†

12. R. Becker et al., "An Analysis of Ductile Failure by Grain Boundary Void Growth," *Acta Metall.* 37, 99–120 (1988).†

13. V. Tvergaard and J. W. Hutchinson, "Effect of T-Stress on Mode I Crack Growth Resistance in a Ductile Solid," *J. Mech. Phys. Solids* 40, 1377–97 (1992).†

14. A. Needleman and V. Tvergaard, "An Analysis of Ductile Rupture Modes at a Crack Tip," *J. Mech. Phys. Solids* 35, 151–83 (1987).†

15. Z. Bazant and G. Pijaudier-Cabot, "Nonlocal Continuum Damage, Localization Instability and Convergence," *J. Appl. Mech.* 55, 163–82 (1988).†

16. A. Huerta and G. Pijaudier-Cabot, "Discretization Influence on the Regularization by Two Localization Limiters," *Int. J. Num. Meth. Eng.*, 65–72 (1992).†

17. G. Pijaudier-Cabot, A. Huerta, and L. Bode, "Nonlocal Continuum Damage and Adapted Solution Strategies in Computational Failure Mechanics," *New Advances in Computational Structural Mechanics*, 81–95 (1992).†

18. D.-Z. Sun and A. Hönig, "Significance of the Characteristic Length for Micromechanical Modeling of Ductile Fracture," *Proc. Third Int. Conf. on Localized Damage*, M. H. Aliabadi, A. Carpinteri, S. Kalisky, and D. J. Cartwright, Eds. (Computational Mechanics Publications, Southhampton, 1994), pp. 287–96.

19. D. Klingbeil, G, Künecke, and J. Schicker, "On the Application of Gurson's Model to Various Fracture Mechanics Specimens—Computational Analysis of Materials and Structural Components," CSAMI Course held in Sophia Antipolis, France, June 21–25, 1993.‡

20. L. Xia and C. F. Shih, "Ductile Crack Growth—I. A Numerical Study using Computational Cells with Microstructurally-Based Length Scales," *J. Mech. Phys. Solids* 43, 233–59 (1995).

21. G. Rousselier, J-C. Devaux, G. Mottet, and G. Devesa, "A Methodology for Ductile Fracture Analysis Based on Damage Mechanics: An Illustration of a Local Approach of Fracture," *Nonlinear Fracture*

Mechanics: Volume II—Elastic-Plastic Fracture, ASTM STP 995, J. D. Landes, A. Saxena, and J. G. Merkle, Eds. (American Society for Testing Materials, Philadelphia, 1989), pp. 332–54.†

22. J. Lemaitre, "A Continuous Damage Mechanics Model for Ductile Fracture," *J. Eng. Mater. Technol., Trans. ASME* 107, 83–89 (1985).†

23. N. Aravas, "On the Numerical Integration of a Class of Pressure-Dependent Plasticity Models," *Int. J. Numer. Methods Eng.* 24, 1395–1416 (1987).†

24. V. Tvergaard, "Material Failure by Void Growth to Coalescence," *Adv. Appl. Mech.* 27, 83–151 (1990).†

25. A. Needleman, V. Tvergaard, and J. W. Hutchinson, "Void Growth in Plastic Solids," *Topics in Fracture and Fatigue*, A. S. Argon, Ed. (Springer-Verlag, New York, 1992), pp. 145–78.

26. D.-Z. Sun, D. Siegele, B. Voss, and W. Schmitt, "Application of Local Damage Models to the Numerical Analysis of Ductile Rupture," *Fatigue Fract. Eng. Mater. Struct.* 12(3), 201–12 (1989).†

27. A. Needleman and J. R. Rice, "Limits to Ductility by Plastic Flow Localization," *Mechanics of Sheet Metal Forming*, D. P. Koistinen and N.-M. Wang, Eds. (Plenum Publishing Company, New York, 1978) pp. 237–65.

28. C. C. Chu and A. Needleman, "Void Nucleation Effects in Biaxially Stretched Sheets," *J. Eng. Mater. Technol.* 102, 249–56 (1980).†

29. V. Tvergaard and A. Needleman, "Analysis of the Cup-Cone Fracture in a Round Tensile Bar," *Acta Metall.* 32, 157–69 (1984).†

30. A. Needleman and V. Tvergaard, "An Analysis of Ductile Rupture in Notched Bars," *J. Mech. Phys. Solids* 32, 461–90 (1984).†

31. A. Needleman and V. Tvergaard, "An Analysis of Ductile Rupture Modes at a Crack Tip," *J. Mech. Phys. Solids* 35, 151–83 (1987).†

32. V. Tvergaard, "On Localization in Ductile Materials Containing Spherical Voids," *Int. J. Fract.* 18, 237–52 (1982).

33. J. Pan, M. Saje, and A. Needleman, "Localization of Deformation in Rate Sensitive Porous Plastic Solids," *Int. J. Fract.* 21, 261–78 (1983).†

34. A. Needleman and V. Tvergaard, "An Analysis of Dynamic Ductile Crack Growth in a Double Edge Cracked Specimen," *Int. J. Fract.* 49, 41–67 (1991).†

35. J. R. Rice and D. M. Tracey, "On the Ductile Enlargement of Voids in Triaxial Stress Fields," *J. Mech. Phys. Solids* 17, 201–17 (1969).†

36. V. Tvergaard, "Influence of Void Nucleation on Ductile Shear Fracture at a Free Surface," *J. Mech. Phys. Solids* 30, 399–425 (1982).†

37. J. R. Rice and M. A. Johnson, "The Role of Large Crack Tip Geometry Changes in Plane Strain Fracture," *Inelastic Behavior of Solids*, M. F. Kanninen, W. F. Adler, A. R. Rosenfeld, and R. I. Jaffee, Eds. (McGraw-Hill, New York, 1970), pp. 641–72.

38. A. G. Varias and C. F. Shih, "Quasi-Static Crack Advance under a Range of Constraints-Steady-State Fields Based on a Characteristic Length, *J. Mech. Phys. Solids* 41, 835–61 (1993).†

39. N. P. O'Dowd, C. F. Shih, and R. H. Dodds, "The Role of Geometry and Crack Growth on Constraint and Implications for Ductile/Brittle Fracture," in *Constraint Effects in Fracture: Theory and Applications, ASTM STP 1244*, M. Kirk and A. Bakker, Eds. (American Society for Testing and Materials, Philadelphia, 1994).

40. J. A. Joyce and R. E. Link, "Effects of Constraint on Upper Shelf Fracture Toughness," *Fract. Mech. 26, ASTM STP 1256,* W. G. Reuter, J. H. Underwood, and J. C. Newman, Jr., Eds. (American Society for Testing Materials, Philadelphia, 1994).†

41. L. Xia, C. F. Shih, and J. W. Hutchinson, "A Computational Approach to Ductile Crack Growth under Large

Scale Yielding Conditions," Mech-236, Division of Applied Sciences, Harvard University, Cambridge, Mass., June 1994.

42. K. C. Koppenhoefer et al., "WARP-3D: Dynamic Nonlinear Analysis of Solids using a Preconditioned Conjugate Gradient Software Architecture," UILU-ENG-94-2017, Department of Civil Engineering, University of Illinois at Urbana-Champaign, November 1994.

---

*Available for purchase from the National Technical Information Service, Springfield, VA 22161.
†Available in public technical libraries.
‡Available for purchase from sponsoring organization.

5 Fracture Analysis Methods Development and Applications

T. L. Dickson

5.1 PTS Applications: Development of Technical Bases and Methodologies for RG 1.154

The NRC plans to revise RG 1.154.[1] The objective is to publish a revised RG 1.154 that reflects the fracture technology developed in the last decade and lessons learned from the analysis of the Yankee Rowe nuclear plant.[2,3] Technical bases must be developed to support this revision. Specific aspects of the PTS problem that are being revisited include thermal-hydraulics, human factors, probabilistic risk assessment, and fracture-mechanics analyses. This effort involves interaction between personnel from Idaho National Engineering Laboratory (INEL) (thermal-hydraulics), Sandia [probabilistic risk assessment (PRA)], and Oak Ridge (fracture mechanics) national laboratories.

Currently, the NRC plan is to revise RG 1.154 according to a "two analysis" methods approach: (1) a best-estimate frequency of failure with specified flaw variables such as flaw density, flaw depths, and flaw lengths and (2) a more-detailed PRA with an uncertainty analysis that determines a "mean" frequency of vessel failure, using plant-specific flaw variables.

During this reporting period, there was continuing interaction with INEL and Sandia to develop a methodology for performing the "method 2" detailed PRA uncertainty analysis. This methodology requires that a specialized module of the FAVOR computer code be developed to generate data that will be used as input into a PRA uncertainty analysis. During this period, work was initiated on the development of the specialized version of the FAVOR computer code for performing PTS uncertainty analyses. The main feature of this specialized module is the requirement to include thermal-hydraulic variability in the analysis. This requirement necessitates that the code have the capability for simultaneously analyzing several transient definitions in a single analysis. The NRC has recently directed that this computer code should also have the capability to perform probabilistic fracture-mechanics (PFM) analyses for embedded flaws.

5.2 PTS Applications: Review of PTS Screening Criteria

In the early 1980s, extensive deterministic and PFM analyses were performed by NRC and others that led to the establishment of the PTS rule. The PTS rule specifies screening criteria in the form of limiting values of RT_{NDT}, which is a measure of the embrittlement of the RPV material due to neutron irradiation. The derivation of the PTS screening criteria is documented in SECY-82-465.[4] This document is quite comprehensive because it addresses all PTS considerations, including plant systems, thermal-hydraulics, and fracture mechanics.

The PTS screening criteria developed in SECY-82-465 were derived from both deterministic and probabilistic fracture considerations. During this reporting period, work was initiated on a letter report that has the objective to review and reconstruct in detail the fracture-mechanics methodologies, modeling assumptions, and fracture analyses results in SECY-82-465. This is a necessary prerequisite to revising the current PTS regulations. It is anticipated that this letter report, which will be entitled "Review of the PTS Screening Criteria," will be published during the next reporting period.

The OCA code[5] (developed at ORNL) was used to perform the deterministic analyses in SECY-82-465. The VISA code[6] (developed by the NRC and Pacific Northwest Laboratory) was used to perform the PFM analyses in SECY-82-465. All fracture analyses reconstructions done during this reporting period were performed using the FAVOR fracture analysis code.[7] The development of the FAVOR code is a continuing task in the HSST Program. FAVOR combines the best attributes of OCA and VISA into a single, validated, user-friendly, and well-documented RPV predictive fracture-mechanics computer code.

The methodology used to derive the PTS screening criteria from deterministic considerations was based on the determination of the critical value of RT_{NDT} at the vessel inner surface (designated as RT_{NDTs}) for infinite length flaws that penetrate 15% of the vessel wall thickness. Deterministic fracture analyses were performed for the eight most significant PTS events that actually occurred in the United States during 1970–1982. The methodology, modeling assumptions, and analyses results from which the PTS screening criteria were derived from deterministic considerations have been successfully reconstructed.

All of the deterministic fracture analyses from which the current PTS screening criteria were derived will be published in the previously mentioned letter report ("Review of the PTS Screening Criteria"). Here, as an example, the

results of a single deterministic analysis will be presented. Figure 5.1 illustrates the Three Mile Island PTS event. The critical value of RT_{NDTs} for an infinite-length axial flaw that penetrates 15% of the Three Mile Island RPV wall thickness is 210°F. Figure 5.2 illustrates the K_I and K_{Ic} time histories for the subject flaw, evaluated at the critical value of RT_{NDTs}. The subject flaw is predicted to initiate in cleavage fracture at a transient time of 330 min, at $K_I = K_{Ic} = 69$ ksi$\sqrt{\text{in.}}$

The methodology utilized in SEC-82-465 to derive PTS screening criteria from probabilistic considerations was to determine the value of RT_{NDTs} corresponding to a specified acceptance criterion. The NRC specified the acceptance criterion to be a maximum acceptable frequency of crack extension due to PTS of 5.0×10^{-6} per reactor year.

In SECY 82-465, the frequency of crack extension is specified to be the sum of the products of the transient frequencies of occurrence and the conditional probabilities of crack extension for the postulated PTS transients. Transient frequency of occurrence is expressed in PTS events per reactor year. The conditional probability of crack extension in an RPV is determined by performing a PFM analysis and is expressed as crack extensions per PTS event. The conditional probability of crack extension is conditional in the sense that the transient is assumed to occur. Therefore, the frequency of crack extension is expressed as the number of crack extensions per reactor year.

The PFM analyses were performed for postulated transient sequences obtained from the Westinghouse Owners Group. The transient groups were derived from the consideration of the various possible sequences following each of the initiating events such as steam line breaks, extended high-pressure injection (HPI), and steam generator tube ruptures. The total frequency of crack extension corresponding to the NRC-specified acceptance criterion of 5×10^{-6} per reactor year is almost exclusively due to the extended HPI transient. Therefore, to reconstruct the PFM analysis results from which the current PTS screening criteria were derived, it was necessary only to duplicate the results for the extended HPI PTS event. In SECY 82-465, the extended HPI PTS transient was characterized stylistically by $T_f = 125$°F, $\beta = 0.05$ min^{-1}, and a constant pressure of 2250 psi. The extended HPI PTS transient is illustrated in Fig. 5.3. This transient was determined to have an

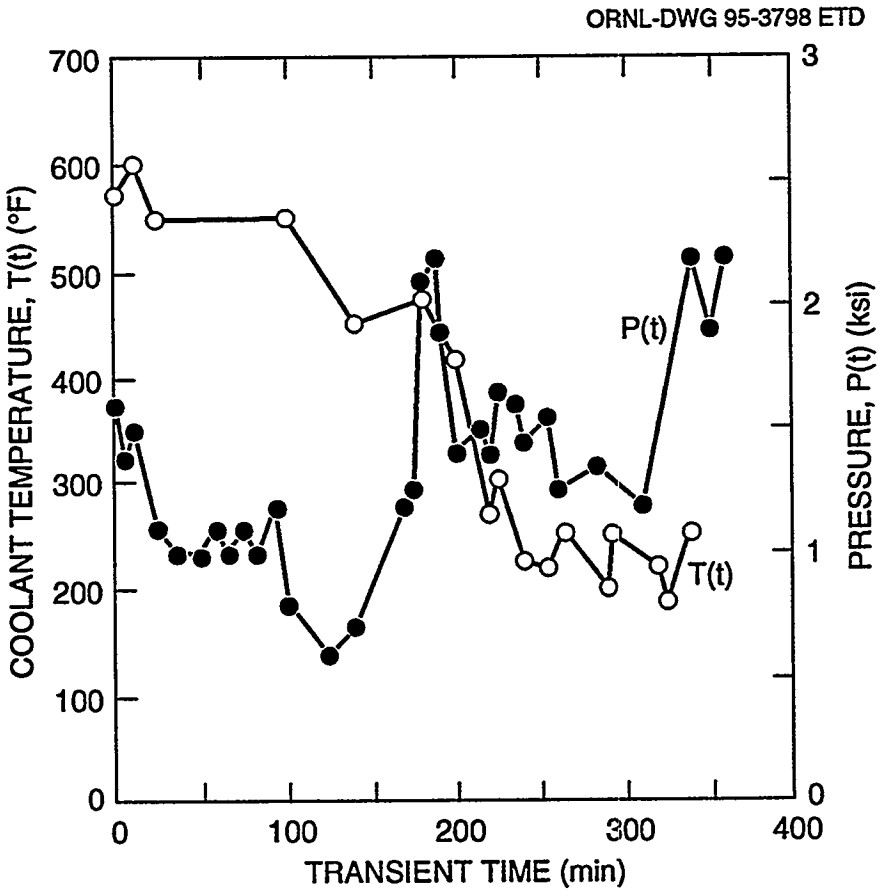

Figure 5.1 Three Mile Island PTS event

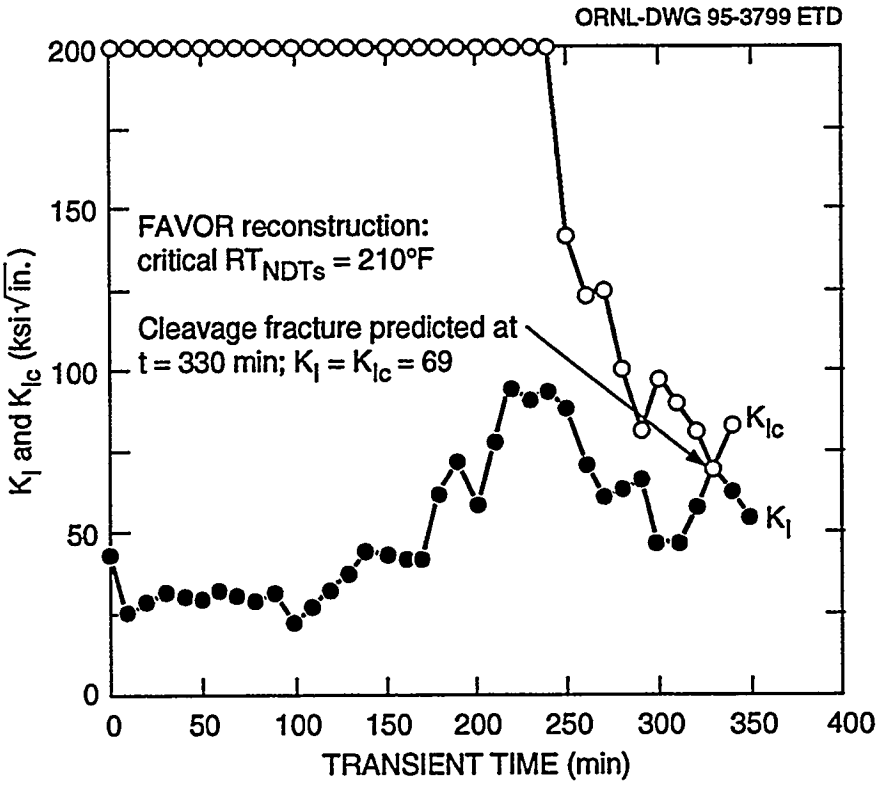

Figure 5.2 K_I and K_{Ic} time histories for 1.275-in.-deep infinite length axial flaw subjected to Three Mile Island PTS event

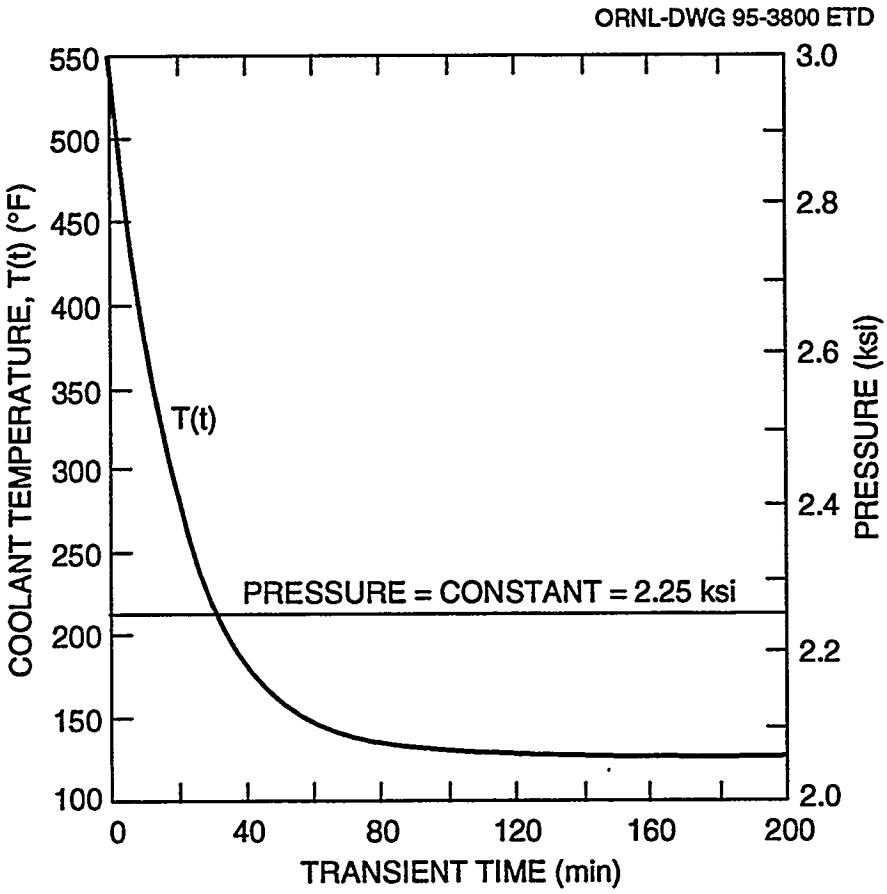

Figure 5.3 HPI expended transient—stylized characterization

frequency of occurrence of 1×10^{-4} PTS events per reactor year; therefore, the corresponding conditional probability of crack extension that would produce a frequency of crack extension of 5×10^{-6} is 5×10^{-2}.

The main requirement for reconstructing the PFM analysis results for the HPI PTS event was to define the PFM modeling assumptions, input data, and embrittlement and fracture toughness correlations. All of these details will be published in the letter report "Review of the PTS Screening Criteria." Regarding the PFM modeling assumptions, VISA and FAVOR have previously been compared and determined to use essentially the same modeling assumptions for calculating the conditional probability of crack extension.[2,8] The conditional probability of crack extension is sometimes referred to as the conditional probability of initiation. VISA and FAVOR have previously been benchmarked as calculating nearly identical solutions for the conditional probability of crack initiation when applied to a well-defined problem.[2,8]

The behavior of a flaw after initial initiation is sensitive to modeling assumptions regarding the through-wall variation of certain material properties. VISA and FAVOR use different modeling assumptions that have previously been identified as sometimes causing considerable discrepancies between their respective solutions for the conditional probability of failure, that is, probability of through-wall penetration.[2,8] Fortunately, all conditional probabilities reported in SECY 82-465 are for crack initiation only; therefore, it is known that the PFM modeling assumptions are essentially the same.

Figure 5.4 illustrates the PFM solutions from which the PTS screening criteria were derived, as generated by VISA and as reconstructed by FAVOR. As can be seen, the FAVOR PFM analyses results are almost identical to the solutions from which the current PTS screening criteria were derived. The value of RT_{NDTs} corresponding to a probability of crack extension of 5.0×10^{-2} is ~210°F. Adding a 2σ value (for the uncertainty associated with predicting RT_{NDTs}) of 60°F yields the PTS screening criterion of 270°F.

The FAVOR model will serve as a baseline model for future studies that will examine the impact of various fracture model variations on the PTS screening criteria.

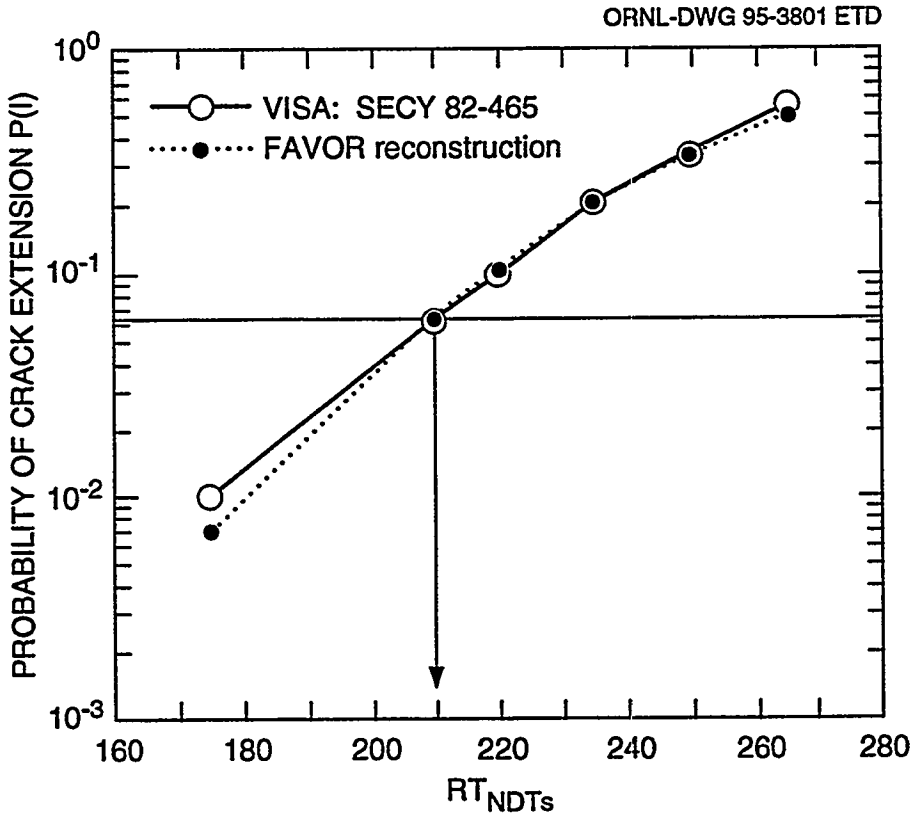

Figure 5.4 Benchmarking of VISA and FAVOR PFM analysis results for HPI PTS transient

5.3 NRC Support

Analyses were performed to investigate the equivalency of the margins specified in the acceptance criteria of ASME Sect. III, Appendix G (cleavage fracture) and the draft RG 1.161 (LUS ductile tearing). These analyses successfully assisted the NRC to resolve issues raised by the ACRS relating to the RG 1.161.

The method used to investigate the equivalency of margins was to calculate and compare the incipient pressure for cleavage and ductile fracture when a vessel is subjected to a thermal transient with a constant cooldown rate of 100°F/h, down to a minimum coolant temperature of 150°F. The incipient pressure is the maximum pressure at which the acceptance criterion is satisfied, using the appropriate factors of safety.

Figure 5.5 illustrates the results of these analyses, that is, the comparison of the incipient pressures calculated for cleavage and ductile fracture. The incipient pressure predicted for ductile fracture of Linde 80 weld material is shown to be higher than that predicted for cleavage fracture, thus demonstrating that the acceptance criterion for ductile fracture specified in RG 1.161 is equivalent to the acceptance criterion for cleavage fracture specified in ASME Sect. III, Appendix G.

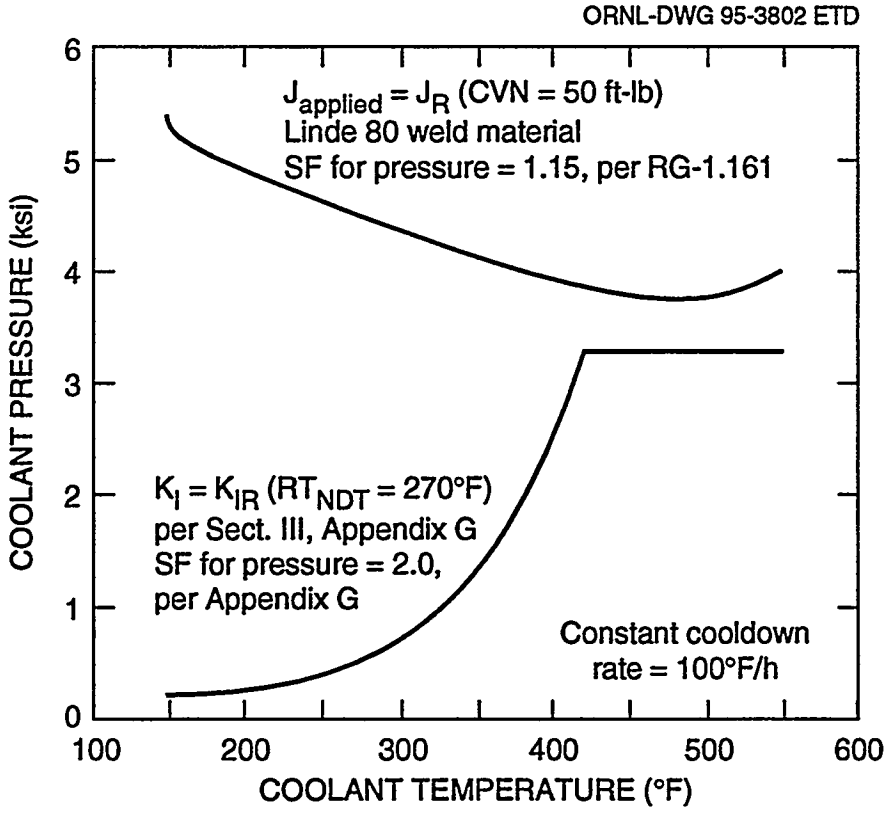

Figure 5.5 Comparison of P-T curves for ASME Sect. III, Appendix G, cleavage fracture analysis and RG-1.161 LUS ductile tearing analysis

References

1. U.S. Nuclear Regulatory Commission, RG 1.154, "Format and Content of Plant-Specific Pressurized Thermal Shock Safety Analysis Reports for Pressurized Water Reactors," 1987.*

2. T. L. Dickson and R. D. Cheverton, Martin Marietta Energy Systems, Inc., Oak Ridge Natl. Lab., "Review of Reactor Pressure Vessel Evaluation Report for Yankee Rowe Nuclear Power Station (YAEC No. 1735)," USNRC Report NUREG/CR-5799 (ORNL/TM-11982), Appendix D—ORNL Review of Probabilistic Fracture Mechanics, March 1992.†

3. T. L. Dickson et al., Martin Marietta Energy Systems, Inc., Oak Ridge Natl. Lab., "Pressurized Thermal Shock Probabilistic Fracture Mechanics Sensitivity

Analysis for Yankee Rowe Reactor Pressure Vessel," USNRC Report NUREG/CR-5782 (ORNL/TM-11945), August 1993.†

4. U.S. Nuclear Regulatory Policy Issue, "NRC Staff Evaluation of Pressurized Thermal Shock," SECY-82-465, November 1982.

5. R. D. Cheverton and D. G. Ball, Union Carbide Corp., Nucl. Div., Oak Ridge Natl. Lab., "OCA-P, A Deterministic and Probabilistic Fracture Mechanics Code for Application to Pressure Vessels," USNRC Report NUREG/CR-3618 (ORNL-5991), May 1984.†

6. F. A. Simonen et al., Pacific Northwest Lab., "VISA-II—A Computer Code for Predicting the Probability of Reactor Pressure Vessel Failure," USNRC Report NUREG/CR-4486 (PNL-5775), March 1986.†

7. T. L. Dickson, Martin Marietta Energy Systems, Inc., Oak Ridge Natl. Lab., "FAVOR: A Fracture Analysis Code for Nuclear Reactor Pressure Vessels, Release 9401," ORNL/NRC/LTR 94-1, February 1994.‡

8. B. A. Bishop, "Benchmarking of Probabilistic Fracture Analyses of Reactor Pressure Vessels Subjected to Pressurized Thermal Shock Loading," EPRI Research Project 2975-5, Electric Power Research Institute, March 1993.

---

*Copies are available from U.S. Government Printing Office, Washington, DC 20402. ATTN: Regulatory Guide Account.
†Available for purchase from the National Technical Information Service, Springfield, VA 22161.
‡Available in NRC PDR for inspection and copying for a fee.

6 Material Property Data and Test Methods

D. E. McCabe, R. K. Nanstad, and R. E. Link

Three NRC letter reports were prepared under this task during this reporting period. They are summarized below.

Presentation of Preliminary J-R Curve Fracture Toughness Data on Modified A 302 Grade B Steel, by D. E. McCabe, R. K. Nanstad, R. L. Swain, and E. T. Manneschmidt, ORNL/NRC/LTR-94/29, October 1994: This letter report presented both baseline material characterization data and fracture-mechanics-based J-R curve data. Seven heats of modified A 302 grade B steel and one early-vintage heat of A 533 grade B steel were tested. Test condition variables were test temperature [82, 204, and 288°C (180, 400, and 550°F)]; crack-plane orientation (longitudinal, transverse, and short transverse); and specimen size (1/2T, 1T, 2T, and 4T compacts). Single-value parameters that can be used to compare J-R curves are J_{Ic} at onset of ductile tearing and J after 1.5 mm (0.06 in.) of stable crack growth. These properties as well as tensile properties and CVN upper-shelf energies (USEs) are tabulated.

Table 6.1 illustrates a correlation between the CVN USE and the J-R curve development rate. Four CVN USE levels were selected that represent the range of values developed in these A 302 grade B materials. Values of J at 1.5 mm (0.06 in.) from R-curves of the matching materials are listed. It appears that there is a correlation. Figure 6.1 shows that the relationship between J-R curve and CVN USE does in fact exist, but the data scatter is wide enough that the correlation as an estimation scheme does not eliminate the need for direct J-R curve determinations. Table 6.1 also lists J at 1.5 mm (0.06 in.) of growth for A 533 grade B that was calculated using the Eason et al. multivariable modeling method.[1]

Assessment of Metallurgical Effects That Impact Pressure Vessel Safe Margin Issues, by D. E. McCabe, ORNL/NRC/LTR-94/26, October 1994: The objective of this work was to identify the outstanding issues that impact the low-temperature overpressurization (LTOP) transients. Currently, the factors of safety applied in analyses to set allowable temperature and pressure combinations during startup and shutdown operations reflect the uncertainty of the technical resources available in the early 1970s. At the same time, most operating reactors were relatively new, and the undamaged reactor vessels could operate under excessive imposed conservatism. However, the imposed safety margins are now severely hindering LTOP

Table 6.1 Comparison of J-R toughness values at 1.5-mm (0.06-in.) crack-growth point (theoretical for A 533 grade B vs experimental A 302 grade B)

USE [J (ft-lb)]	Test temperature [°C (°F)]	Multivariable model predictions for A 533 B base metal J-R [kJ/m^2 (in.-lb/in.^{2})]	Selected A 302 grade B test data, J-R at 1.5 mm (0.06 in.) Δa_p [kJ/m^2 (in.-lb/in.^{2})]			
			1/2T	1T	2T	4T
89 (65)	93 (180)	464 (2650)	236 (1350)	236 (1350)	236 (1350)	
	204 (400)	298 (1700)	184 (1050)			
	288 (550)	228 (1300)	140 (800)	148 (850)	131 (750)	
130 (95)	93 (180)	607 (3470)	385 (2200)	438 (2500)	508 (2900)	499 (2850)
	204 (400)	385 (2200)	236 (1350)	298 (1700)	341 (1950)	
	288 (550)	298 (1700)	192 (1100)	315 (1600)	324 (1850)	324 (1850)
171 (125)	93 (180)	718 (4100)	420 (2400)	560 (3200)	648 (3700)	455 (2600)
	204 (400)	472 (2700)	358 (2050)	315 (1800)	368 (2100)	
	288 (550)	385 (2200)	324 (1850)	298 (1700)	341 (1950)	
219 (160)	93 (180)	840 (4800)	674 (3850)	621 (3550)	612 (3500)	
	204 (400)	560 (3200)	525 (3000)	359 (2050)	455 (2600)	
	288 (550)	420 (2400)	306 (1750)	394 (2250)	464 (2650)	

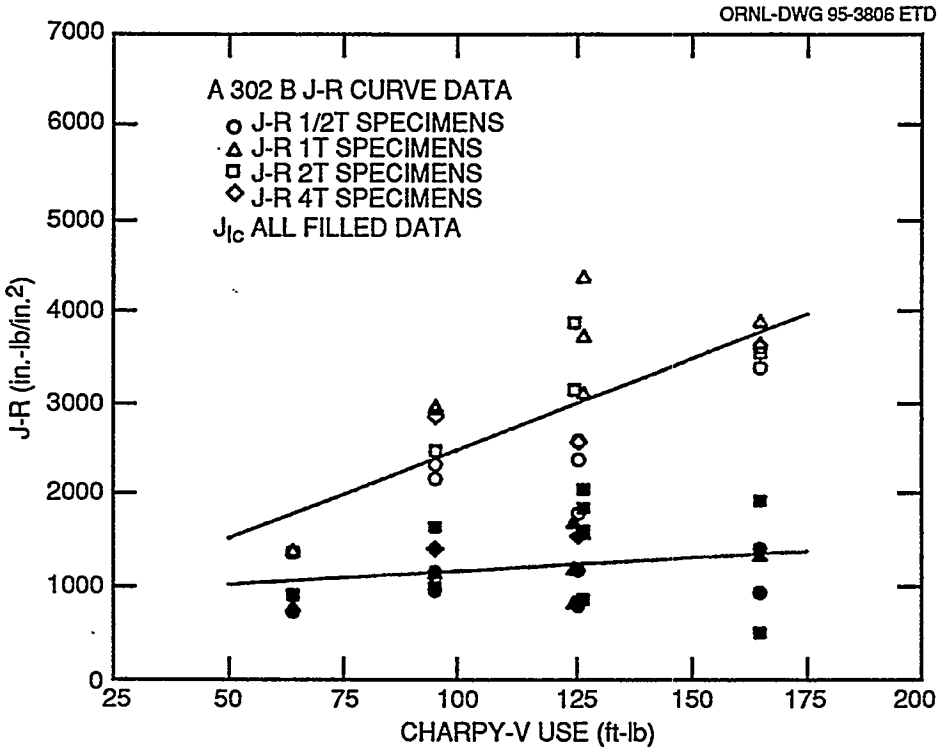

Figure 6.1 J-R and J_{Ic} toughness values at four selected values of Charpy USE. All specimen orientations were included. J-R values were determined at 1.5-mm crack extension.

operations in several operating reactors. The research activities discussed in this letter report have the potential for developing better LTOP pressure and temperature limits for aging operating units. The new information encompasses (1) the relevance of crack pop-in data, (2) the role of cladding as a cleavage crack initiation source, (3) the potential of warm prestress, and (4) new information on the margin between dynamic and static transition temperature curves.

With regard to item 1, the pop-in phenomenon occurs under two generic conditions. One condition involves weldments where cleavage cracks initiate in brittle low-toughness zones. These cracks arrest because of entering material of significantly higher fracture toughness. The other condition is in material that is essentially monolithic on a macroscale, but a running cleavage crack can be arrested for more subtle reasons. For a monolithic material that has low strain rate sensitivity (i.e., where the dynamic K_{IR} curve and the static K_{Ic} curve are relatively close), pop-in behavior will develop when the material is tested within the transition temperature range. This observation was made in the Heavy-Section Steel Irradiation Program Fifth Irradiation Series. Figure 6.2, taken from that work, shows how pop-in crack initiation tends to fit in with the K_{Jc} data of full cleavage instability, but pop-ins tend to cluster to the low end of the K_{Jc} data scatter band. The combination of the low initiation K_{Jc} and close proximity to the crack-arrest barrier (K_{IR} curve) combine to create the pop-in phenomenon. Often the arrested pop-in crack can sustain stability to a much higher K_{Jc} value, which suggests usable post-pop-in fracture toughness above the pop-in value. Some investigators argue that the highest value of K_{Jc} obtained, despite the pop-in, is the appropriate value to use. On the other hand, a structure with a large reserve of stored elastic strain energy might have no difficulty in driving virtually all crack initiations that occur within a characteristic pop-in temperature range.

Concerning item 2, crack initiation from the region of cladding layers, three publications were available that experimentally demonstrated the behavior of the composite clad/HAZ/base metal interface region. One involved research at Materials Engineering Associates,[2] and the other two involved work performed at ORNL.[3,4] All demonstrated that the cladding process does not adversely affect the transition temperature performance of the underlying base metal. In some cases, there can be marginal fracture toughness enhancement. When the three-wire clad layering process is performed, followed by a stress-relief anneal, the underlying HAZ material can have a lower transition temperature (higher fracture toughness) than the underlying A 533 grade B or A 508 class 2 base metal. The clad metal that contains typically 5 to 15% delta ferrite does not have the good crack-growth resistance of wrought austenitic stainless steels. The J-R curve at room

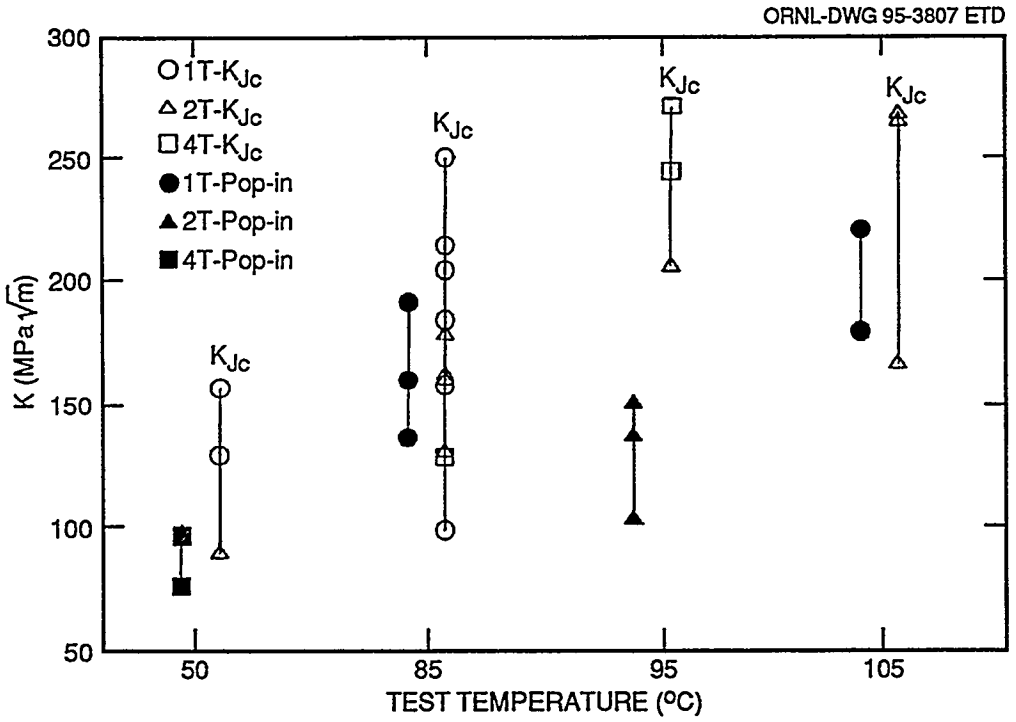

Figure 6.2 K_{Jc} at pop-in vs K_{Jc} at full cleavage for irradiated compact specimens from Fifth Irradiation Series

temperature is no better than that of a LUS pressure vessel steel. The crack-growth resistance against ductile tearing deteriorates at low test temperatures, contrary to the expected toughness increase that is a typical characteristic of austenitic stainless steels (see Fig. 6.3). A crack embedded in the clad layer will not introduce a running cleavage crack into the base plate. On the other hand, the low crack-growth resistance provides only a weak first line of defense, because the crack can grow at low crack drive to the HAZ. If it is assumed that the vessel has been given an adequate stress-relief anneal, the properties of the HAZ material will dominate the transition temperature performance of the composite region.

Regarding the third item, WPS is a phenomenon that has been identified as a potentially powerful characteristic by which the in-service fracture-toughness performance of a steel can exceed its expected performance established in laboratory tests on as-received material. Figure 6.4 shows how the transition temperature curve of an A 533 grade B pressure vessel steel is influenced by WPS cycles, by preloading at an upper-shelf temperature. The WPS initial load was up to the J_{Ic} level for the material. The two cycles to failure shown are (1) WPS load, P_{WPS}, partial unload to 2/3 P_{WPS} and sustain that load during cooldown to a lower-shelf temperature, followed by resumption of load to fracture (LCF); and (2) WPS load, completely unload, then cool to a lower-shelf temperature, then reload to fracture (LUCF). K_I instability at lower-shelf fracture toughness is elevated by a factor of 2 or more, depending on the proximity of the temperature for reload to that of the transition range of the virgin material. From a material standpoint, an initiative to incorporate WPS effects into LTOP operations is hampered by a lack of trust that the WPS phenomenon can be retained in materials that are exposed to damage mechanisms such as strain aging or neutron damage from in-service use. Experiments to dispel these doubts have yet to be made.

On item 4, static to dynamic margins, some effort has been initiated to reevaluate the test data that have been used to develop the ASME lower-bound K_{Ic} and K_{Ia} curves. These data were generated in the late 1960s when technology development was insufficient to know how fracture-mechanics test methods could be directly applied to structural materials. Plane-strain conditions were required to develop usable data, and only a crude statistical method was used, that is, drawing lower-bound curves on all qualified data that can be gathered. Material-specific toughness evaluations were applied to these lower-bound curves using reference temperatures that are derived from older empirical test methods. Correlations between fracture-mechanics methods and empirical methods tend to be questionable for many reasons. In recent years, the technology has improved to the point that correlations to empirical methods may no longer be required. Statistical methods have been developed that can handle the data scatter that is normally encountered in transition temperature tests, specimen size effects on fracture toughness can be modeled, and a more accurate methodology for establishing the transition curve

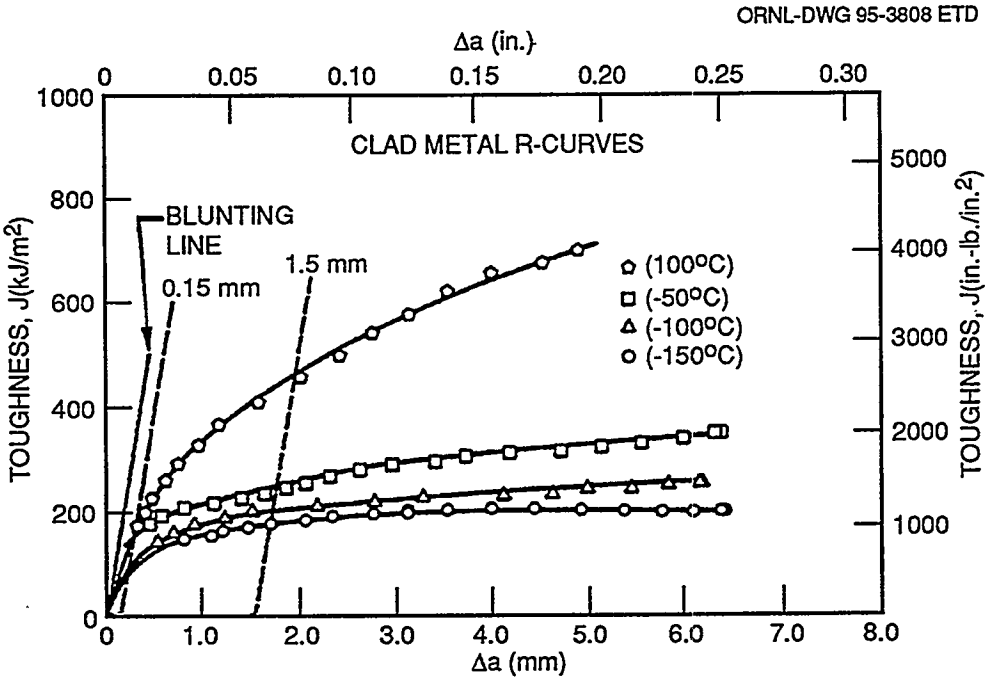

Figure 6.3 J-R curves for clad metal shown to be highly dependent on test temperature

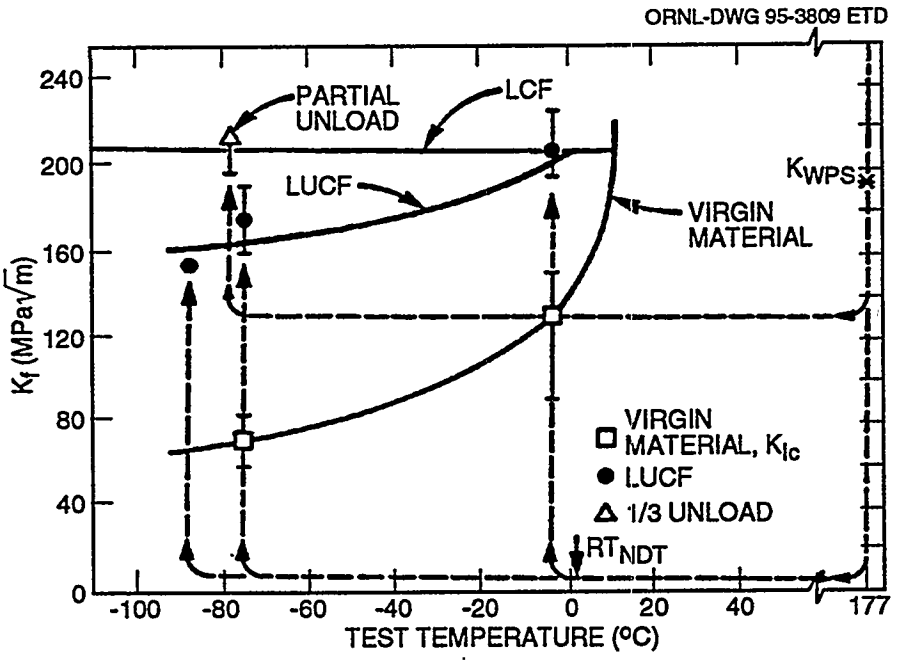

Figure 6.4 Material transition curves for K at fracture (K_f) representing baseline toughness transition and transition behavior as altered by LUCF and LCF WPS cycles

is available. An example is given here by revisiting the data used to establish the ASME lower-bound K_{Ic} curve (Fig. 6.5). In this case, all the data (not just the few lower-bound data) are used to establish a median curve fit to the data; this is called a master curve. Most ferritic steels can be characterized by this curve. The dashed line in Fig. 6.5 is a 5% tolerance bound, and this is easily established from the known standard deviation on the data. The dotted line represents the original ASME lower-bound curve used since the early 1970s. To make the comparison shown here,

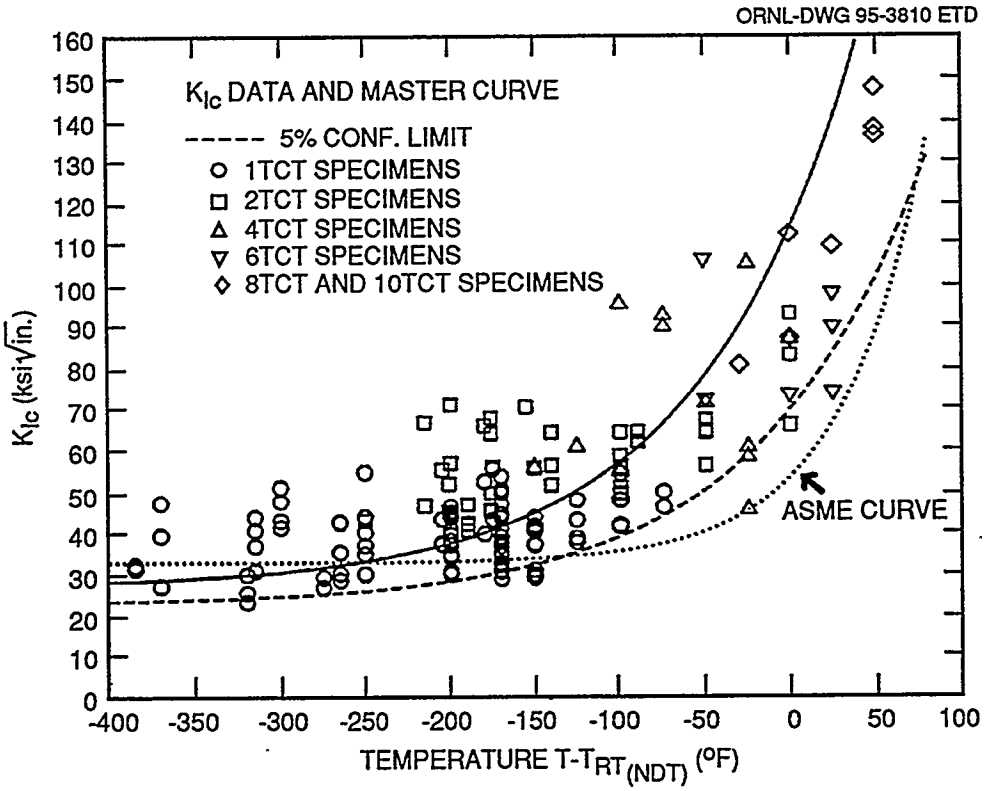

Figure 6.5 K_{Ic} plot showing data plus K_{Ic} lower-bound curve (dotted line) plus master curve (solid line) and 5% tolerance bound (dashed line) on master curve

the test temperature had to be defined as T – NDT to position on the master curve. Normally, the master curve is more material-specific, and test temperature alone is used to locate the toughness transition curve.

Another part of the item 4 issue was to revisit strain rate effects. Specifically, the accuracy of the temperature spread between the lower-bound K_{Ic} and K_{Ia} curves that appear in the ASME Code, Sect. XI, Appendix A, which show about a 35°C spread (Fig. 6.6). Only the K_{Ic} data were established by an ASTM consensus method of test. Crack-arrest data were developed by different laboratories prior to the availability of a standard test method. New crack-arrest data have been generated in laboratories that have used the recent ASTM guidelines of "Determining Plane-Strain Crack-Arrest Fracture Toughness, K_{Ia}, of Ferritic Steels," E 1221-88 (Figs. 6.7 and 6.8). These more recent tests indicate that the temperature offset of dynamic testing is on the order of 23 or 30°C, nominally a 10°C difference from that used in the ASME Code.

An NRC letter report, *Experimental Plan for Effects of Thermal Gradients on Fracture Toughness*, by D. E. McCabe (ORNL/NRC/LTR-94/43) was prepared and transmitted to the NRC Technical Monitor. This letter report documents the experimental plan developed for HSST Task H.6.2 for execution. The subject is the difference between J-R curves developed isothermally vs those developed nonisothermally. The reason for the proposed study is that the extent of ductile tearing observed in an intermediate pressure vessel test, PTSE-2A, had been underpredicted by about a factor of 2 in a finite-element simulation of the test.[5] The postulated reason for the error was that ductile-stable tearing of cracks under isothermal conditions differs from that of thermal gradient conditions. The experimental plan to prove this postulate was to obtain a remaining plate of the same material used in the vessel test and perform J-R curve tests in simulation of the thermal crack growth history of the test vessel. The plan cannot be carried out on the same time base, but the J vs temperature history can be reproduced in a furnace mounted on a test frame. A compact specimen that has a plan-view size of a 4T but with a thickness on the order of 25 mm (1 in.) can be heated through a known thermal history and simulated crack-growth history. Some preliminary work to demonstrate that constraint is adequately controlled in such specimens would have been an integral part of the experiment.

For the subtask on Dynamic Fracture Toughness, a section of HSST Plate 14 was identified for shipment to the Carderock Division, Naval Surface Warfare Center, Annapolis, Maryland, for their use in meeting the

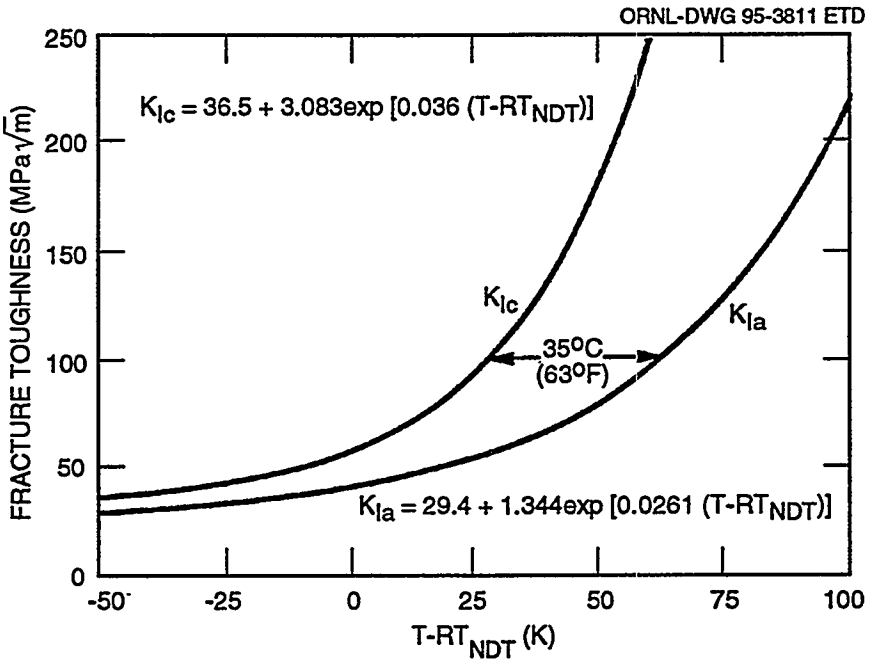

Figure 6.6 ASME Code K_{Ic} and K_{Ia} curves from Sect. XI, Appendix A, 1992

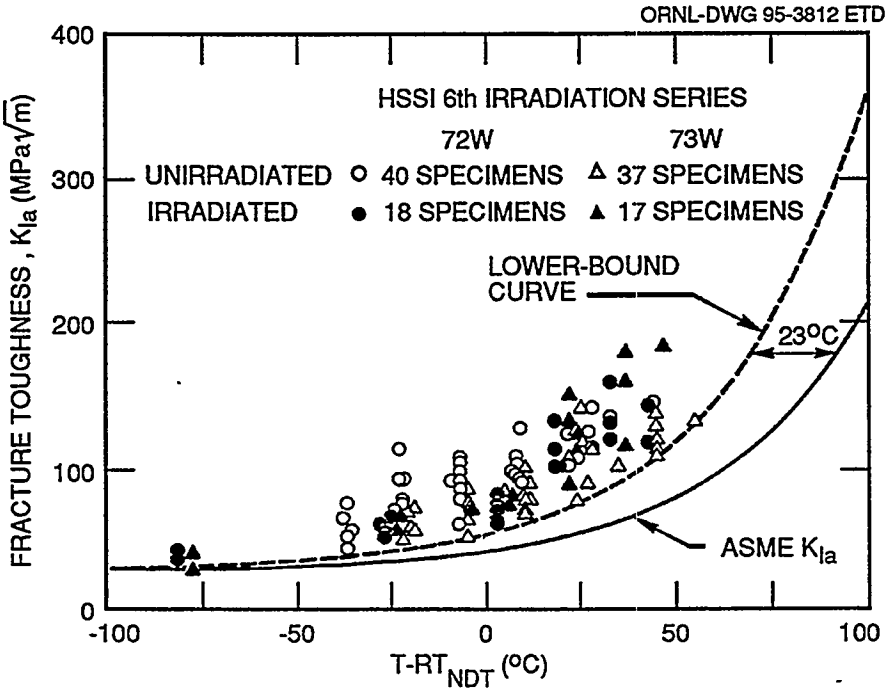

Figure 6.7 HSSI Fifth Irradiation Series K_{Ia} test data compared with ASME Code K_{IR} (K_{Ia}) curve

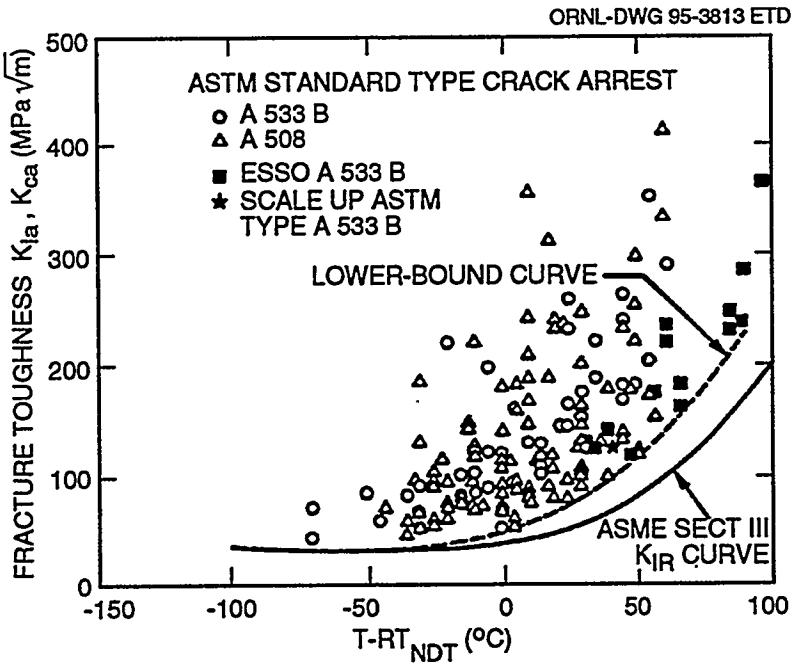

Figure 6.8 Base metal crack-arrest toughness data from Japanese (JAERI) round-robin tests, with dashed-line lower-bound fit added to show lack of agreement with ASME Code

provisions of their subcontract according to the HSST specification, "Dynamic Fracture Initiation Fracture Toughness Testing of a Reactor Pressure Vessel Steel." The specification included Charpy impact, tensile, drop-weight, and quasi-static fracture toughness testing for purposes of material characterization. A specimen fabrication plan for the characterization specimens as well as for the dynamic fracture toughness test specimens was completed, and special specimen grips were procured. Charpy impact specimens were tested in the T-L and L-T orientations, with no substantial differences observed in the preliminary comparison. An estimate of reference temperature, based on temperature at 50 ft-lb less 60°F is 7°F. Machining of 1T compact specimens was completed, and test temperatures of –81, –36, and 9°C (–114, –33, and 48°F) were selected, corresponding to $T_o - 45°C$, T_o, and $T_o + 45°C$. These test temperatures were selected based on the Charpy impact test results; the estimated value of T_o, the temperature at which the fracture toughness is 100 MPa$\sqrt{m}$, was based on the relation $T_o = T_{28J} - 18°C$. Preparations were under way for a readiness review anticipated for the latter part of May.

References

1. E. D. Eason, J. E. Wright, and E. E. Nelson, Modeling and Computing Services, "Modeling of Pressure Vessel and Piping J-R Data," USNRC Report NUREG/CR-5729 (MCS 910401), May 1991.*

2. D. E. McCabe, "Fracture Resistance of Irradiated Stainless Steel Clad Vessels," *Effects of Radiation on Materials: 14th International Symposium (Volume II), ASTM STP 1046*, N. H. Packan, R. E. Stoller, and A. S. Kumar, Eds. (American Society for Testing and Materials, Philadelphia, 1990), pp. 348–60.†

3. R. D. Cheverton, J. W. Bryson, D. J. Alexander, and T. Slot, "Thermal Shock Experiments with Flawed Clad Cylinders," *Nucl. Eng. Des.* 124, 109–19 (1990).†

4. S. K. Iskander et al., Martin Marietta Energy Systems, Inc., Oak Ridge Natl. Lab., "Experimental Results of Tests to Investigate Flaw Behavior of Mechanically Loaded Stainless Clad Plates," USNRC Report NUREG/CR-5785 (ORNL/TM-11950), April 1992.*

5. B. R. Bass, J. Keeney-Walker, R. H. Bryan, and G. C. Robinson, "Fracture Analysis of a Thick-Walled Pressure Vessel under Pressurized-Thermal-Shock Loading (PTSE-2)," pp. 3-131–3-178 in *Proceedings of the Seminar on Assessment of Fracture Prediction and Technology: Piping and Pressure Vessel, Nashville, Tennessee, June 18, 1990*, USNRC Report NUREG/CP-0037, February 1991.*

*Available for purchase from the National Technical Information Service, Springfield, VA 22161.

†Available in public technical libraries.

7 Integration of Results

J. G. Merkle

7.1 Estimation of Full-Constraint K_{Ic} Values from Three-Parameter Weibull Statistical Fits to Small-Specimen Fracture-Toughness Data

(J. G. Merkle and D. E. McCabe)

7.1.1 Background

The fracture toughness of most structural and pressure vessel steels is sufficiently high that laboratory specimens of reasonable size tend to yield before fracturing, when tested at service temperatures within the ductile-to-brittle transition regime.[1] Yielding before fracturing in plane-sided specimens tends to cause a loss of triaxial constraint near the crack tip and a consequent elevation of median fracture toughness with respect to values measurable with larger specimens.[2] In addition to elevated fracture-toughness values caused by loss of constraint, transition-range fracture-toughness data for ferritic steels are characterized by significant scatter, caused by the random variability of the distance in each specimen between the fatigue crack front and the microscopic physical feature that triggers unstable cleavage.[3,4] Because the probability that a trigger point is located close to the crack front increases with increasing crack-front length, the statistical nature of cleavage fracture also leads to a decrease in median fracture-toughness values with increasing specimen size. Thus, the cause of size effects in cleavage fracture toughness testing is somewhat ambiguous. Because even small flaws in actual structures may be located in stress fields and/or geometric configurations that promote high constraint, it is often not safe to assume that the toughness measured by a small plane-sided laboratory specimen is numerically equal to the governing fracture toughness for a flaw in the associated structure. Therefore, when analyzing fracture-toughness data obtained from relatively small specimens of ferritic steel tested in the transition regime, it may often be necessary both to account for the random variability of the data and to make a downward adjustment of the measured fracture-toughness values, or their statistical fitting parameters, to represent a condition of full triaxial constraint.

The development of methods to account for the statistical variability of the cleavage fracture-toughness values of steel has largely been based on the Weibull distribution,[5,6] for practical reasons. The probability density function does not extend below zero, the cumulative probability distribution has a closed-form equation, and simplified mechanistic models can be made to lead to the Weibull distribution.[7,8] Several physically based semiempirical methods have been developed for reducing the fracture-toughness values measured with small specimens to estimate the full-constraint values that would have been measured with larger specimens.[9] The Weibull statistical approach has become generally accepted for engineering application, for practical if not theoretical reasons. However, no method of constraint adjustment has become generally accepted, mainly because of a growing preference for theoretically based approaches and the absence of a theoretical approach proven applicable to 3-D nominal states of stress. Thus current efforts to develop an ASTM standard for transition-range fracture-toughness data evaluations are focused on the Weibull statistical representation of the data, leaving constraint adjustments to be added later after more research has been accomplished.

7.1.2 Development of an ASTM Test Method for Fracture Toughness in the Transition Regime

A draft test method for evaluating fracture-toughness data for ferritic steels in the transition temperature region has been developed by ASTM Task Group E08.08.03.* Review of this draft standard, by means of a subcommittee ballot, will begin during the summer of 1995. Because of the current disagreement concerning the treatment of specimen size effects, the present draft standard does not include a constraint adjustment by which K_{Ic} can be estimated. Thus, the statistical data fits produced by following the draft standard are representations of fracture toughness for a given specimen size, and these values will generally not correspond to a condition of full triaxial constraint in the upper transition range of temperature. This is true of the master curve appearing in the draft standard, which has the equation (in MPa$\sqrt{m}$):

$$K_{Jc}(med) = 30 + 70\exp\left[0.019(T - T_o)\right], \qquad (7.1)$$

and represents the variation with temperature of the median fracture-toughness values measured with a 1T CT specimen.

* ASTM Task Group E08.08.03, "Test Practice (Method) for Fracture Toughness in the Transition Range," Draft 10, Rev. 6-12-95, American Society for Testing and Materials, Philadelphia, 1995.

Integration

As explained in a technical basis document closely related to the draft standard,[10] statistical and constraint-based physical representations of specimen size effects do not lead to the same prediction of fracture toughness as a function of increasing specimen size. As shown by the solid curve in Fig. 7.1, taken from Ref. 10, the three-parameter Weibull size effect equation (in MPa$\sqrt{m}$):

$$K_{(med)x} = \left[K_{Jc(med)} - K_{min}\right]\left(\frac{B_o}{B_x}\right)^{1/4} + K_{min} \quad , \quad (7.2)$$

implies that the median fracture toughness value, $K_{(med)x}$, measured by a specimen of size B_x approaching infinity, approaches K_{min}. But K_{min}, which has a value of 20 MPa$\sqrt{m}$, is a temperature-independent numerical fitting parameter, without physical significance. On physical grounds, median fracture-toughness values as a function of increasing specimen size can reasonably be expected to reach a lower asymptotic value, and this value should correspond to K_{Ic}. Thus, there is practical motivation to seek a means for estimating K_{Ic} from Weibull statistical data fits. In doing so, it is well to keep in mind the need for directness and simplicity in standardized procedures, the successful experience with ASTM E399, and the desirability of consistency between the new transition range standard and ASTM E399.

7.1.3 Development of a Combined Statistical and Constraint-Based Analysis for Estimating K_{Ic}

As explained previously, the master curve, Eq. (7.1) represents a relation between $K_{Jc(med)}$ for a 1T specimen and normalized temperature, $T - T_o$. Because specimens tend to lose constraint with increasing temperature in the mid-transition range, Eq. (7.1) does not represent a full constraint toughness relation with temperature. However, an estimate of full constraint toughness can be obtained by combining the size effect condition expressed by Eq. (7.1) with a minimum size requirement to achieve a near-lower plateau for size independence. The result is a calculation of fracture toughness corresponding to the size of the smallest specimen that would give maximum achievable constraint. The ASTM E399 validity criterion is used in this case:

$$B = \alpha_o (K_{Ic}/\sigma_{YS})^2 \, , \quad (7.3)$$

where in ASTM E399, $\alpha_o = 2.5$. Equating B with B_x and K_{Ic} with $K_{Jc(x)}$ in Eq. (7.2) leads to the equation

$$\left(\frac{K_{Ic}}{K_{min}}\right)^{3/2} - \left(\frac{K_{Ic}}{K_{min}}\right)^{1/2} - G = 0 \, , \quad (7.4)$$

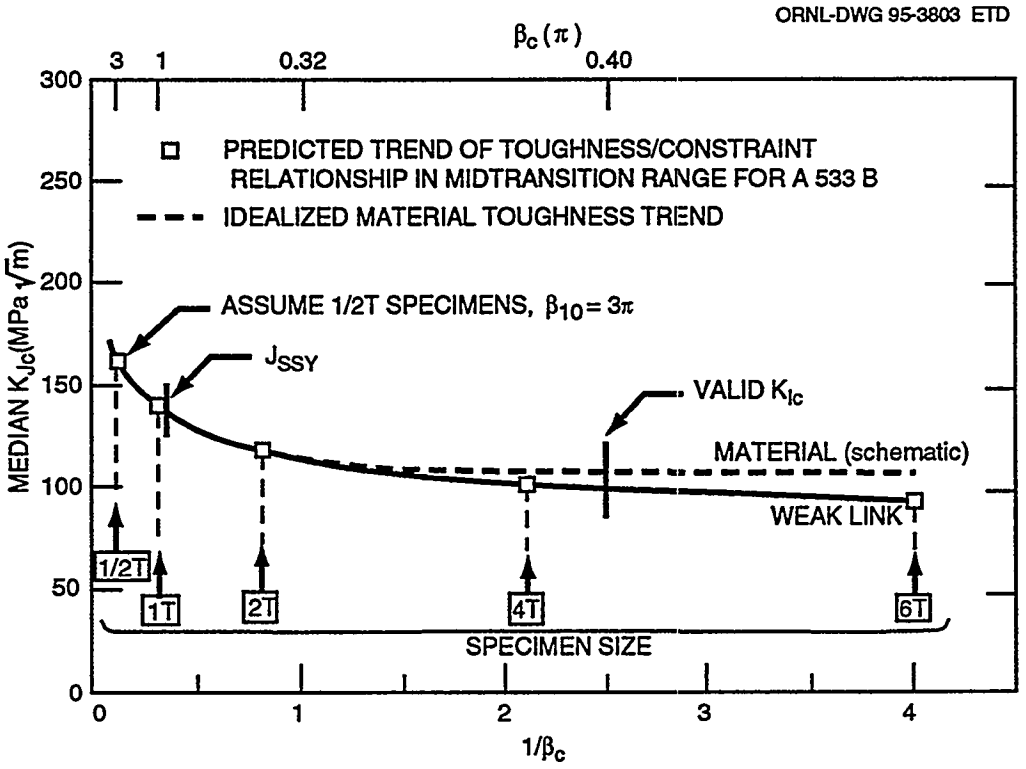

Figure 7.1 Material toughness decrease with increased size (schematic) and weakest-link predicted trend; J_{SSY} and E399 full constraint limits indicated

where

$$G = \left(\frac{K_{Jc(1T)}}{K_{min}} - 1\right)\left(\frac{\sqrt{B_{1T}/\alpha_o}}{K_{min}/\sigma_{YS}}\right)^{1/2} . \quad (7.5)$$

For $G > 2/\sqrt{27}$, which covers most practical cases, the value of K_{Ic} is calculated by applying the following equations:

$$M_1 = \frac{G}{2} + \sqrt{\left(\frac{G}{2}\right)^2 - \frac{1}{27}} , \quad (7.6)$$

$$M_2 = \frac{G}{2} - \sqrt{\left(\frac{G}{2}\right)^2 - \frac{1}{27}} , \quad (7.7)$$

$$y = M_1^{1/3} + M_2^{1/3} , \quad (7.8)$$

$$K_{Ic} = y^2 K_{min} . \quad (7.9)$$

The tolerance limit associated with the value of K_{Ic} calculated from Eq. (7.9) is the same as that associated with the value of $K_{Jc(1T)}$ used in Eq. (7.5) to calculate G.

Example calculations illustrate the application of the combined Weibull size effect–validity constraint criterion approach for estimating K_{Ic}. For example, at $(T - T_o) = 40°C$, the value of $K_{Jc(med)}$ for a 1T CT specimen, from Eq. (7.1), is 180 MPa$\sqrt{m}$. For a yield stress of 483 MPa and $\alpha_o = 2.5$, Eqs. (7.3)–(7.9) lead to an estimate of $K_{Ic} =$ 121 MPa$\sqrt{m}$, with the smallest specimen size capable of producing a valid measurement being $B_x = 158$ mm. Figure 7.2 shows results obtained by applying the method to various points on the master curve, represented by Eq. (7.1), and its 98% and 2% tolerance limit curves, based on a yield stress of 483 MPa and $\alpha_o = 2.5$. The reduction of values from the 2% tolerance limit curve is rather small compared to the other reductions.The directness and simplicity of the method developed means that a transition range standard can provide a direct estimate of K_{Ic}, if that is what the user needs. It also means that philosophical differences between the transition range standard and ASTM standard E399 are unnecessary and can be completely avoided. At the same time, different values of the size coefficient α_o in the expression $B \geq \alpha_o (K_{Ic}/\sigma_Y)^2$ can be used for different classes of material, if that can be justified experimentally. This augmentation of the conventional Weibull statistical analysis of small-specimen fracture-toughness data provides an easy way of dealing with the fact that the master curve of median fracture toughness

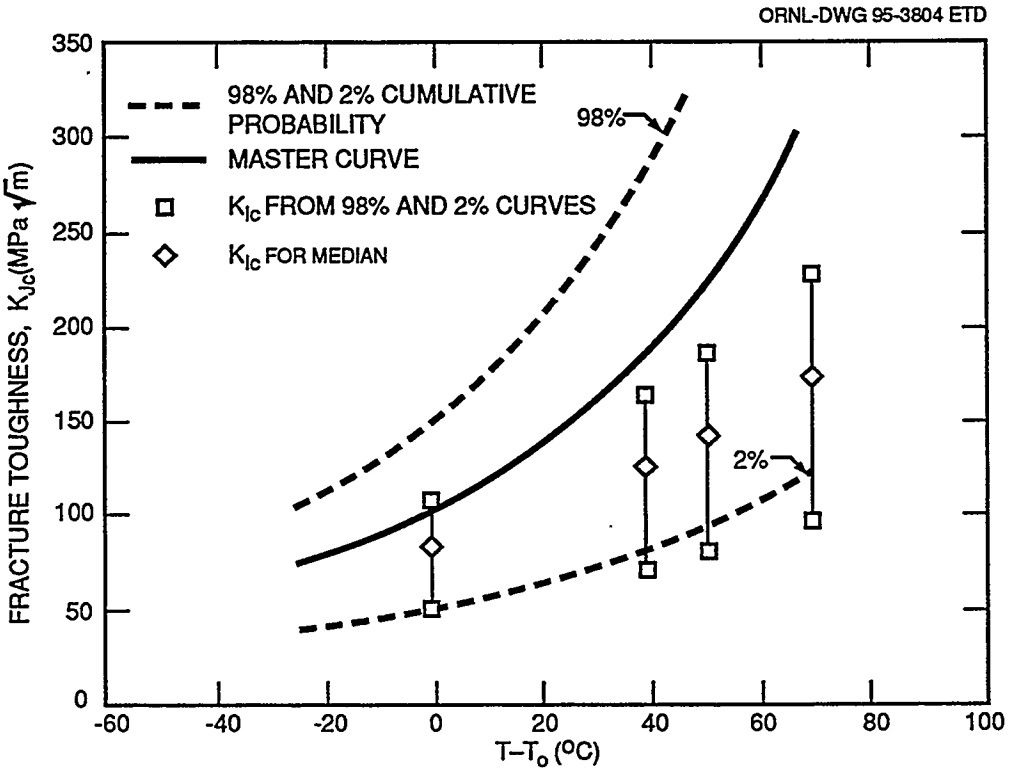

Figure 7.2 Results of applying combined Weibull size effect–validity constraint criterion to master curve and its 98% and 2% confidence limits, with $\sigma_{YS} = 483$ MPa and $\alpha_o = 2.5$

for a 1T specimen is not a curve of full-constraint fracture toughness, especially in the midtransition range. Further, there is no experimentally justified way of defining an effective specimen dimension governing triaxial constraint for a finite-length, part-through, surface flaw in a structure. Fortunately, the combined Weibull-E399 validity criterion approach, as described above, provides a convenient way of bypassing this possibly unsolvable problem. In the foregoing approach, the material yield stress is an important parameter. However, a precise description of material strain-hardening characteristics is not required, thereby avoiding dependence on either mathematical idealizations or frequently unavailable, experimentally exact, shapes of the stress-strain curve.

References

1. J. G. Merkle, "Patterns and Perspectives in Applied Fracture Mechanics," *Fracture Mechanics: 26th Volume, ASTM STP 1256*, W. G. Reuter, J. H. Underwood, and J. C. Newman, Jr. Eds. (American Society for Testing and Materials, Philadelphia, 1995).*

2. J. G. Merkle, Union Carbide Corp., Nucl. Div., Oak Ridge Natl. Lab., "An Examination of the Size Effects and Data Scatter Observed in Small-Specimen Cleavage Fracture Toughness Testing," USNRC Report NUREG/CR-3672, April 1984.†

3. J. Heerens, D. T. Read, A. Cornec, and K. H. Schwalbe, "Interpretation of Fracture Toughness in the Ductile-to-Brittle Transition Region by Fractographical Observations," *Defect Assessment in Components–Fundamentals and Applications*, ESIS/EGF9, J. G. Blauel and K. H. Schwalbe, Eds. (Mechanical Engineering Publications, London, 1991), pp. 659–78.

4. J. Watanabe et al., "Fracture Toughness in the Transition Region," *Eng. Fract. Mech.* 28(5/6), 589–600 (1987).

5. J. D. Landes and D. H. Shaffer, "Statistical Characterization of Fracture in the Transition Region," *Fracture Mechanics, Twelfth Conference, ASTM STP 700* (American Society for Testing and Materials, Philadelphia, 1980), pp. 368–82.

6. J. D. Landes and D. E. McCabe, "Effect of Section Size on Transition Temperature Behavior of Structural Steels," *Fracture Mechanics: Fifteenth Symposium, ASTM STP 833*, R. J. Sanford, Ed. (American Society for Testing and Materials, Philadelphia, 1984), pp. 378–92.

7. K. Wallin, "Statistical Modeling of Fracture in the Ductile-to-Brittle Transition Region," *Defect Assessment in Components–Fundamentals and Applications*, ESIS/EGF9, J. G. Blauel and K. H. Schwalbe, Eds. (Mechanical Engineering Publications, London, 1991), pp. 415–45.

8. T. L. Anderson and D. Stienstra, "A Model to Predict the Sources and Magnitude of Scatter in Toughness Data in the Transition Region," *J. Test. Eval.* 17(1), 46–53 (1989).*

9. D. E. McCabe, J. G. Merkle, and R. K. Nanstad, "A Perspective on Transition Temperature and K_{Jc} Data Characterization," *Fracture Mechanics–24th Volume, ASTM STP 1207*, J. D. Landes, D. E. McCabe, and J. A. M. Boulet, Eds. (American Society for Testing and Materials, Philadelphia, 1994), pp. 215–32.*

10. D. E. McCabe, U. Zerbst, and J. Heerens, *Development of Test Practice Requirements for a Standard Method on Fracture Toughness Testing in the Transition Range*, GKSS 93/E/81, GKSS-Forschungszentraum Geesthacht GmbH, Geesthacht, Germany, 1993.

*Available in public technical libraries.

†Available for purchase from the National Technical Information Service, Springfield, VA 22161.

CONVERSION FACTORS[a]

SI unit	English unit	Factor
mm	in.	0.0393701
cm	in.	0.393701
m	ft	3.28084
m/s	ft/s	3.28084
kN	lb_f	224.809
kPa	psi	0.145038
MPa	ksi	0.145038
$MPa \cdot \sqrt{m}$	$ksi \cdot \sqrt{in.}$	0.910048
J	ft•lb	0.737562
K	°F or °R	1.8
kJ/m^2	$in.\text{-}lb/in.^2$	5.71015
$W \cdot m^{-2} \cdot K^{-1}$	$Btu/h \cdot ft^2 \cdot °F$	0.176110
kg	lb	2.20462
kg/m^3	$lb/in.^3$	3.61273×10^{-5}
mm/N	$in./lb_f$	0.175127
$T(°F) = 1.8(°C) + 32$		

[a]Multiply SI quantity by given factor to obtain English quantity.

Prior Heavy-Section Steel Technology Program Publications

The work reported here was performed at Oak Ridge National Laboratory under the Heavy-Section Steel Technology (HSST) Program, W. E. Pennell, Program Manager. The program is sponsored by the Office of Nuclear Regulatory Research of the U.S. Nuclear Regulatory Commission (NRC). The technical monitor for NRC is S. N. M. Malik. Prior and future reports in this series are listed below.

1. S. Yukawa, General Electric Company, Schenectady, N.Y., *Evaluation of Periodic Proof Testing and Warm Prestressing Procedures for Nuclear Reactor Vessels*, HSSTP-TR-1, July 1, 1969.
2. L. W. Loechel, Martin Marietta Corporation, Denver, Colo., *The Effect of Testing Variables on the Transition Temperature in Steel*, MCR-69-189, November 20, 1969.
3. P. N. Randall, TRW Systems Group, Redondo Beach, Calif., *Gross Strain Measure of Fracture Toughness of Steels*, HSSTP-TR-3, November 1, 1969.
4. C. Visser, S. E. Gabrielse, and W. VanBuren, Westinghouse Electric Corporation, PWR Systems Division, Pittsburgh, Pa., *A Two-Dimensional Elastic-Plastic Analysis of Fracture Test Specimens*, WCAP-7368, October 1969.
5. T. R. Mager and F. O. Thomas, Westinghouse Electric Corporation, PWR Systems Division, Pittsburgh, Pa., *Evaluation* by *Linear Elastic Fracture Mechanics of Radiation Damage to Pressure Vessel Steels*, WCAP-7328 (Rev.), October 1969.
6. W. O. Shabbits, W. H. Pryle, and E. T. Wessel, Westinghouse Electric Corporation, PWR Systems Division, Pittsburgh, Pa., *Heavy-Section Fracture Toughness Properties of A533 Grade B Class 1 Steel Plate and Submerged Arc Weldment*, WCAP-7414, December 1969.
7. F. J. Loss, Naval Research Laboratory, Washington, D.C., *Dynamic Tear Test Investigations of the Fracture Toughness of Thick-Section Steel*, NRL-7056, May 14, 1970.
8. P. B. Crosley and E. J. Ripling, Materials Research Laboratory, Inc., Glenwood, Ill., *Crack Arrest Fracture Toughness of A533 Grade B Class 1 Pressure Vessel Steel*, HSSTP-TR-8, March 1970.
9. T. R. Mager, Westinghouse Electric Corporation, PWR Systems Division, Pittsburgh, Pa., *Post-Irradiation Testing* of *2T Compact Tension Specimens*, WCAP-7561, August 1970.
10. T. R. Mager, Westinghouse Electric Corporation, PWR Systems Division, Pittsburgh, Pa., *Fracture Toughness Characterization Study of A533, Grade B, Class 1 Steel*, WCAP-7578, October 1970.
11. T. R. Mager, Westinghouse Electric Corporation, PWR Systems Division, Pittsburgh, Pa., *Notch Preparation in Compact Tension Specimens*, WCAP-7579, November 1970.
12. N. Levy and P. V. Marcal, Brown University, Providence, R.I., *Three-Dimensional Elastic-Plastic Stress and Strain Analysis for Fracture Mechanics, Phase I: Simple Flawed Specimens*, HSSTP-TR-12, December 1970.
13. W. O. Shabbits, Westinghouse Electric Corporation, PWR Systems Division, Pittsburgh, Pa., *Dynamic Fracture Toughness Properties of Heavy Section A533 Grade B Class 1 Steel Plate*, WCAP-7623, December 1970.
14. P. N. Randall, TRW Systems Group, Redondo Beach, Calif., *Gross Strain Crack Tolerance of A 533-B Steel*, HSSTP-TR-14, May 1, 1971.
15. H. T. Corten and R. H. Sailors, University of Illinois, Urbana, Ill., *Relationship Between Material Fracture Toughness Using Fracture Mechanics and Transition Temperature Tests*, T&AM Report 346, August 1, 1971.
16. T. R. Mager and V. J. McLaughlin, Westinghouse Electric Corporation, PWR Systems Division, Pittsburgh, Pa., *The Effect of an Environment of High Temperature Primary Grade Nuclear Reactor Water on the Fatigue Crack Growth Characteristics of A533 Grade B Class 1 Plate and Weldment Material*, WCAP-7776, October 1971.
17. N. Levy and P. V. Marcal, Brown University, Providence, R.I., *Three-Dimensional Elastic-Plastic Stress and Strain Analysis for Fracture Mechanics, Phase II: Improved Modelling*, HSSTP-TR-17, November 1971.
18. S. C. Grigory, Southwest Research Institute, San Antonio, Tex., *Tests of 6-in.-Thick Flawed Tensile Specimens, First Technical Summary Report, Longitudinal Specimens Numbers 1 through 7*, HSSTP-TR-18, June 1972.
19. P. N. Randall, TRW Systems Group, Redondo Beach, Calif., *Effects of Strain Gradients on the Gross Strain Crack Tolerance of A533-B Steel*, HSSTP-TR-19, June 15, 1972.

Prior

20. S. C. Grigory, Southwest Research Institute, San Antonio, Tex., *Tests of 6-Inch-Thick Flawed Tensile Specimens, Second Technical Summary Report, Transverse Specimens Numbers 8 through 10, Welded Specimens Numbers 11 through 13*, HSSTP-TR-20, June 1972.

21. L. A. James and J. A. Williams, Hanford Engineering Development Laboratory, Richland, Wash., Heavy Section Steel Technology Program Technical Report No. 21, *The Effect of Temperature and Neutron Irradiation Upon the Fatigue-Crack Propagation Behavior of ASTM A533 Grade B, Class 1 Steel*, HEDL-TME 72-132, September 1972.

22. S. C. Grigory, Southwest Research Institute, San Antonio, Tex., *Tests of 6-Inch-Thick Flawed Tensile Specimens, Third Technical Summary Report, Longitudinal Specimens Numbers 14 through 16, Unflawed Specimen Number 17*, HSSTP-TR-22, October 1972.

23. S. C. Grigory, Southwest Research Institute, San Antonio, Tex., *Tests of 6-Inch-Thick Tensile Specimens, Fourth Technical Summary Report, Tests of 1-Inch-Thick Flawed Tensile Specimens for Size Effect Evaluation*, HSSTP-TR-23, June 1973.

24. S. P. Ying and S. C. Grigory, Southwest Research Institute, San Antonio, Tex., *Tests of 6-Inch-Thick Tensile Specimens, Fifth Technical Summary Report, Acoustic Emission Monitoring of One-Inch and Six-Inch-Thick Tensile Specimens*, HSSTP-TR-24, November 1972.

25. R. W. Derby, J. G. Merkle, G. C. Robinson, G. D. Whitman, and F. J. Witt, Oak Ridge Natl. Lab., Oak Ridge, Tenn., *Test of 6-Inch-Thick Pressure Vessels. Series 1: Intermediate Test Vessels V-1 and V-2*, ORNL-4895, February 1974.

26. W. J. Stelzman and R. G. Berggren, Oak Ridge Natl. Lab., Oak Ridge, Tenn., *Radiation Strengthening and Embrittlement in Heavy Section Steel Plates and Welds*, ORNL-4871, June 1973.

27. P. B. Crosley and E. J. Ripling, Materials Research Laboratory, Inc., Glenwood, Ill., *Crack Arrest in an Increasing K-Field*, HSSTP-TR-27, January 1973.

28. P. V. Marcal, P. M. Stuart, and R. S. Bettes, Brown University, Providence, R.I., *Elastic Plastic Behavior of a Longitudinal Semi-Elliptic Crack in a Thick Pressure Vessel*, HSSTP-TR-28, June 1973.

29. W. J. Stelzman, R. G. Berggren, and T. N. Jones, Oak Ridge Natl. Lab., Oak Ridge, Tenn., *ORNL Characterization of Heavy-Section Steel Technology Program Plates 01, 02 and 03*, USNRC Report NUREG/CR-4092 (ORNL/TM-9491), April 1985.

30. Canceled.

31. J. A. Williams, Hanford Engineering Development Laboratory, Richland, Wash., *The Irradiation and Temperature Dependence of Tensile and Fracture Properties of ASTM A533, Grade B, Class 1 Steel Plate and Weldment*, HEDL-TME 73-75, August 1973.

32. J. M. Steichen and J. A. Williams, Hanford Engineering Development Laboratory, Richland, Wash., *High Strain Rate Tensile Properties of Irradiated ASTM A533 Grade B Class 1 Pressure Vessel Steel*, July 1973.

33. P. C. Riccardella and J. L. Swedlow, Westinghouse Electric Corporation, Pittsburgh, Pa., *A Combined Analytical-Experimental Fracture Study of the Two Leading Theories of Elastic-Plastic Fracture (J-Integral and Equivalent Energy)*, WCAP-8224, October 1973.

34. R. J. Podlasek and R. J. Eiber, Battelle Columbus Laboratories, Columbus, Ohio, *Final Report on Investigation of Mode III Crack Extension in Reactor Piping*, December 14, 1973.

35. T. R. Mager, J. D. Landes, D. M. Moon, and V. J. McLaughlin, Westinghouse Electric Corporation, Pittsburgh, Pa., *Interim Report on the Effect of Low Frequencies on the Fatigue Crack Growth Characteristics of A533 Grade B Class 1 Plate in an Environment of High-Temperature Primary Grade Nuclear Reactor Water*, WCAP-8256, December 1973.

36. J. A. Williams, Hanford Engineering Development Laboratory, Richland, Wash., *The Irradiated Fracture Toughness of ASTM A533, Grade B, Class 1 Steel Measured with a Four-Inch-Thick Compact Tension Specimen*, HEDL-TME 75-10, January 1975.

37. R. H. Bryan, J. G. Merkle, M. N. Raftenberg, G. C. Robinson, and J. E. Smith, Oak Ridge Natl. Lab., Oak Ridge, Tenn., *Test of 6-Inch-Thick Pressure Vessels. Series 2: Intermediate Test Vessels V-3, V-4, and V-6*, ORNL-5059, November 1975.

38. T. R. Mager, S. E. Yanichko, and L. R. Singer, Westinghouse Electric Corporation, Pittsburgh, Pa., *Fracture Toughness Characterization of HSST Intermediate Pressure Vessel Material*, WCAP-8456, December 1974.

39. J. G. Merkle, G. D. Whitman, and R. H. Bryan, Oak Ridge Natl. Lab., Oak Ridge, Tenn., *An Evaluation* of *the HSST Program Intermediate Pressure Vessel Tests in Terms* of *Light-Water-Reactor Pressure Vessel Safety*, ORNL/TM-5090, November 1975.

40. J. C. Merkle, G. C. Robinson, P. P. Holz, J. E. Smith, and R. H. Bryan, Oak Ridge Natl. Lab., Oak Ridge, Tenn., *Test of 6-In.-Thick Pressure Vessels. Series 3: Intermediate Test Vessel V-7,* USNRC Report ORNL/NUREG-l, August 1976.

41. J. A. Davidson, L. J. Ceschini, R. P. Shogan, and G. V. Rao, Westinghouse Electric Corporation, Pittsburgh, Pa., *The Irradiated Dynamic Fracture Toughness of ASTM A533, Grade B, Class 1 Steel Plate and Submerged Arc Weldment,* WCAP-8775, October 1976.

42. R. D. Cheverton, Oak Ridge Natl. Lab., Oak Ridge, Tenn., *Pressure Vessel Fracture Studies Pertaining to a PWR LOCA-ECC Thermal Shock: Experiments TSE-1 and TSE-2,* USNRC Report ORNL/NUREG/TM-31, September 1976.

43. J. G. Merkle, G. C. Robinson, P. P. Holz, and J. E. Smith, Oak Ridge Natl. Lab., Oak Ridge, Tenn., *Test of 6-In.-Thick Pressure Vessels. Series 4: Intermediate Test Vessels V-5 and V-9 with Inside Nozzle Corner Cracks,* USNRC Report ORNL/NUREG-7, August 1977.

44. J. A. Williams, Hanford Engineering Development Laboratory, Richland, Wash., *The Ductile Fracture Toughness of Heavy Section Steel Plate,* USNRC Report NUREG/CR-0859, September 1979.

45. R. H. Bryan, T. M. Cate, P. P. Holz, T. A. King, J. G. Merkle, G. C. Robinson, G. C. Smith, J. E. Smith, and G. D. Whitman, Oak Ridge Natl. Lab., Oak Ridge, Tenn., *Test of 6-in.-Thick Pressure Vessels. Series 3: Intermediate Test Vessel V-7A Under Sustained Loading,* USNRC Report ORNL/NUREG-9, February 1978.

46. R. D. Cheverton and S. E. Bolt, Oak Ridge Natl. Lab., Oak Ridge, Tenn., *Pressure Vessel Fracture Studies Pertaining to a PWR LOCA-ECC Thermal Shock: Experiments TSE-3 and TSE-4 and Update of TSE-1 and TSE-2 Analysis,* USNRC Report ORNL/NUREG-22, December 1977.

47. D. A. Canonico, Oak Ridge Natl. Lab., Oak Ridge, Tenn., *Significance of Reheat Cracks to the Integrity of Pressure Vessels for Light-Water Reactors,* USNRC Report ORNL/NUREG-15, July 1977.

48. G. C. Smith and P. P. Holz, Oak Ridge Natl. Lab., Oak Ridge, Tenn., *Repair Weld Induced Residual Stresses in Thick-Walled Steel Pressure Vessels,* USNRC Report NUREG/CR-0093 (ORNL/NUREG/TM-153), June 1978.

49. P. P. Holz and S. W. Wismer, Oak Ridge Natl. Lab., Oak Ridge, Tenn., *Half-Bead (Temper) Repair Welding for HSST Vessels,* USNRC Report NUREG/CR-0113 (ORNL/NUREG/TM-177), June 1978.

50. G. C. Smith, P. P. Holz, and W. J. Stelzman, Oak Ridge Natl. Lab., Oak Ridge, Tenn., *Crack Extension and Arrest Tests of Axially Flawed Steel Model Pressure Vessels,* USNRC Report NUREG/CR-0126 (ORNL/NUREG/TM-196), October 1978.

51. R. H. Bryan, P. P. Holz, J. G. Merkle, G. C. Smith, J. E. Smith, and W. J. Stelzman, Oak Ridge Natl. Lab., Oak Ridge, Tenn., *Test of 6-in.-Thick Pressure Vessels. Series 3: Intermediate Test Vessel V-7B,* USNRC Report NUREG/CR-0309 (ORNL/NUREG-38), October 1978.

52. R. D. Cheverton, S. K. Iskander, and S. E. Bolt, Oak Ridge Natl. Lab., Oak Ridge, Tenn., *Applicability of LEFM to the Analysis of PWR Vessels Under LOCA-ECC Thermal Shock Conditions,* USNRC Report NUREG/CR-0107 (ORNL/NUREG-40), October 1978.

53. R. H. Bryan, D. A. Canonico, P. P. Holz, S. K. Iskander, J. G. Merkle, J. E. Smith, and W. J. Stelzman, Oak Ridge Natl. Lab., Oak Ridge, Tenn., *Test of 6-in.-Thick Pressure Vessels, Series 3: Intermediate Test Vessel V-8,* USNRC Report NUREG/CR-0675 (ORNL/NUREG-58), December 1979.

54. R. D. Cheverton and S. K. Iskander, Oak Ridge Natl. Lab., Oak Ridge, Tenn., *Application of Static and Dynamic Crack Arrest Theory to TSE-4,* USNRC Report NUREG/CR-0767 (ORNL/NUREG-57), June 1979.

55. J. A. Williams, Hanford Engineering Development Laboratory, Richland, Wash., *Tensile Properties of Irradiated and Unirradiated Welds of A533 Steel Plate and A508 Forgings,* USNRC Report NUREG/CR-1158 (ORNL/Sub/79-50917/2), July 1979.

56. K. W. Carlson and J. A. Williams, Hanford Engineering Development Laboratory, Richland, Wash., *The Effect of Crack Length and Side Grooves on the Ductile Fracture Toughness Properties of ASTM A533 Steel,* USNRC Report NUREG/CR-1171 (ORNL/Sub/79-50917/3), October 1979.

57. P. P. Holz, Oak Ridge Natl. Lab., Oak Ridge, Tenn., *Flaw Preparations for HSST Program Vessel Fracture Mechanics Testing: Mechanical-Cyclic Pumping and Electron-Beam Weld-Hydrogen Charge Cracking Schemes,* USNRC Report NUREG/CR-1274 (ORNL/NUREG/TM-369), May 1980.

58. S. K. Iskander, Computer Sciences Div., Union Carbide Corp. Nuclear Div., Oak Ridge, Tenn., *Two Finite Element Techniques for Computing Mode I*

Stress Intensity Factors in Two- or Three-Dimensional Problems, USNRC Report NUREG/CR-1499 (ORNL/NUREG/CSD/TM-14), February 1981.

59. P. B. Crosley and E. J. Ripling, Materials Research Laboratory, Glenwood, Ill., *Development of a Standard Test for Measuring K_{Ia} with a Modified Compact Specimen,* USNRC Report NUREG/CR-2294 (ORNL/Sub/81-7755/1), August 1981.

60. S. N. Atluri, B. R. Bass, J. W. Bryson, and K. Kathiresan, Computer Sciences Div., Oak Ridge Gaseous Diffusion Plant, Oak Ridge, Tenn., *NOZ-FLAW: A Finite Element Program for Direct Evaluation of Stress Intensity Factors for Pressure Vessel Nozzle-Corner Flaws,* USNRC Report NUREG/CR-1843 (ORNL/NUREG/CSD/TM-18), March 1981.

61. A. Shukla, W. L. Fourney, and G. R. Irwin, University of Maryland, College Park, Md., *Study of Energy Loss and Its Mechanisms in Homalite 100 During Crack Propagation and Arrest,* USNRC Report NUREG/CR-2150 (ORNL/Sub/79-7778/1), August 1981.

62. S. K. Iskander, R. D. Cheverton, and D. G. Ball, Oak Ridge Natl. Lab., Oak Ridge, Tenn., *OCA-I, A Code for Calculating the Behavior of Flaws on the Inner Surface of a Pressure Vessel Subjected to Temperature and Pressure Transients,* USNRC Report NUREG/CR-2113 (ORNL/NUREG-84), August 1981.

63. R. J. Sanford, R. Chona, W. L. Fourney, and G. R. Irwin, University of Maryland, College Park, Md., *A Photoelastic Study of the Influence of Non-Singular Stresses in Fracture Test Specimens,* USNRC Report NUREG/CR-2179 (ORNL/Sub/79-7778/2), August 1981.

64. B. R. Bass, S. N. Atluri, J. W. Bryson, and K. Kathiresan, Oak Ridge Natl. Lab., Oak Ridge, Tenn., *OR-FLAW: A Finite Element Program for Direct Evaluation of K-Factors for User-Defined Flaws in Plate, Cylinders, and Pressure-Vessel Nozzle Corners,* USNRC Report NUREG/CR-2494 (ORNL/CSD/TM-165), April 1982.

65. B. R. Bass and J. W. Bryson, Oak Ridge Natl. Lab., Oak Ridge Tenn., *ORMGEN-3D: A Finite Element Mesh Generator for 3-Dimensional Crack Geometries,* USNRC Report NUREG/CR-2997, Vol. 1 (ORNL/TM-8527/V1), December 1982.

66. B. R. Bass and J. W. Bryson, Oak Ridge Natl. Lab., Oak Ridge, Tenn., *ORVIRT: A Finite Element Program for Energy Release Rate Calculations for 2-Dimensional and 3-Dimensional Crack Models,* USNRC Report NUREG/CR-2997, Vol. 2 (ORNL/TM-8527/V2), February 1983.

67. R. D. Cheverton, S. K. Iskander, and D. G. Ball, Oak Ridge Natl. Lab., Oak Ridge, Tenn., *PWR Pressure Vessel Integrity During Overcooling Accidents: A Parametric Analysis,* USNRC Report NUREG/CR-2895 (ORNL/TM-7931), February 1983.

68. D. G. Ball, R. D. Cheverton, J. B. Drake, and S. K. Iskander, Oak Ridge Natl. Lab., Oak Ridge, Tenn., *OCA-II, A Code for Calculating Behavior of 2-D and 3-D Surface Flaws in a Pressure Vessel Subjected to Temperature and Pressure Transients,* USNRC Report NUREG/CR-3491 (ORNL-5934), February 1984.

69. A. Sauter, R. D. Cheverton, and S. K. Iskander, Oak Ridge Natl. Lab., Oak Ridge, Tenn., *Modification of OCA-I for Application to a Reactor Pressure Vessel with Cladding on the Inner Surface,* USNRC Report NUREG/CR-3155 (ORNL/TM-8649), May 1983.

70. R. D. Cheverton and D. G. Ball, Martin Marietta Energy Systems, Inc., Oak Ridge Natl. Lab., Oak Ridge, Tenn., *OCA-P, A Deterministic and Probabilistic Fracture-Mechanics Code for Application to Pressure Vessels,* USNRC Report NUREG/CR-3618 (ORNL-5991), May 1984.

71. J. G. Merkle, Martin Marietta Energy Systems, Inc., Oak Ridge Natl. Lab., Oak Ridge, Tenn., *An Examination of the Size Effects and Data Scatter Observed in Small Specimen Cleavage Fracture Toughness Testing,* USNRC Report NUREG/CR-3672 (ORNL/TM-9088), April 1984.

72. C. E. Pugh et al., Martin Marietta Energy Systems, Inc., Oak Ridge Natl. Lab., Oak Ridge, Tenn., *Heavy-Section Steel Technology Program—Five-Year Plan FY 1983–1987,* USNRC Report NUREG/CR-3595 (ORNL/TM-9008), April 1984.

73. D. G. Ball, B. R. Bass, J. W. Bryson, R. D. Cheverton, and J. B. Drake, Martin Marietta Energy Systems, Inc., Oak Ridge Natl. Lab., Oak Ridge, Tenn., *Stress Intensity Factor Influence Coefficients for Surface Flaws in Pressure Vessels,* USNRC Report NUREG/CR-3723 (ORNL/CSD/TM-216), February 1985.

74. W. R. Corwin, R. G. Berggren, and R. K. Nanstad, Martin Marietta Energy Systems, Inc., Oak Ridge Natl. Lab., Oak Ridge, Tenn., *Charpy Toughness and Tensile Properties of Neutron Irradiated Stainless Steel Submerged-Arc Weld Cladding Overlay,* USNRC Report NUREG/CR-3927 (ORNL/TM-9309), September 1984.

75. C. W. Schwartz, R. Chona, W. L. Fourney, and G. R. Irwin, University of Maryland, College Park, Md., *SAMCR: A Two-Dimensional Dynamic Finite Element Code for the Stress Analysis of Moving CRacks,* USNRC Report NUREG/CR-3891 (ORNL/Sub/79-7778/3), November 1984.

76. W. R. Corwin, G. C. Robinson, R. K. Nanstad, J. G. Merkle, R. G. Berggren, G. M. Goodwin, R. L. Swain, and T. D. Owings, Martin Marietta Energy Systems, Inc., Oak Ridge Natl. Lab., Oak Ridge, Tenn., *Effects of Stainless Steel Weld Overlay Cladding on the Structural Integrity of Flawed Steel Plates in Bending, Series 1,* USNRC Report NUREG/CR-4015 (ORNL/TM-9390), April 1985.

77. R. H. Bryan, B. R. Bass, S. E. Bolt, J. W. Bryson, D. P. Edmonds, R. W. McCulloch, J. G. Merkle, R. K. Nanstad, G. C. Robinson, K. R. Thoms, and G. D. Whitman, Martin Marietta Energy Systems, Inc., Oak Ridge Natl. Lab., Oak Ridge, Tenn., *Pressurized-Thermal-Shock Test of 6-in.-Thick Pressure Vessels. PTSE-1: Investigation of Warm Prestressing and Upper-Shelf Arrest,* USNRC Report NUREG/CR-4106 (ORNL-6135), April 1985.

78. R. D. Cheverton, D. G. Ball, S. E. Bolt, S. K. Iskander, and R. K. Nanstad, Martin Marietta Energy Systems, Inc., Oak Ridge Natl. Lab., Oak Ridge, Tenn., *Pressure Vessel Fracture Studies Pertaining to the PWR Thermal-Shock Issue: Experiments TSE-5, TSE-5A, and TSE-6,* USNRC Report NUREG/CR-4249 (ORNL-6163), June 1985.

79. R. D. Cheverton, D. G. Ball, S. E. Bolt, S. K. Iskander, and R. K. Nanstad, Martin Marietta Energy Systems, Inc., Oak Ridge Natl. Lab., Oak Ridge, Tenn., *Pressure Vessel Fracture Studies Pertaining to the PWR Thermal-Shock Issue: Experiment TSE-7,* USNRC Report NUREG/CR-4304 (ORNL-6177), August 1985.

80. R. H. Bryan, B. R. Bass, S. E. Bolt, J. W. Bryson, J. G. Merkle, R. K. Nanstad, and G. C. Robinson, Martin Marietta Energy Systems, Inc., Oak Ridge Natl. Lab., Oak Ridge, Tenn., *Test of 6-in.-Thick Pressure Vessels. Series 3: Intermediate Test Vessel V-8A—Tearing Behavior of Low Upper-Shelf Material,* USNRC Report NUREG/CR-4760 (ORNL-6187), May 1987.

81. R. D. Cheverton and D. G. Ball, Martin Marietta Energy Systems, Inc., Oak Ridge Natl. Lab., Oak Ridge, Tenn., *A Parametric Study of PWR Pressure Vessel Integrity During Overcooling Accidents, Considering Both 2-D and 3-D Flaws,* USNRC Report NUREG/CR-4325 (ORNL/TM-9682), August 1985.

82. E. C. Rodabaugh, E. C. Rodabaugh Associates, Inc., Hilliard, Ohio, *Comments on the Leak-Before-Break Concept for Nuclear Power Plant Piping Systems,* USNRC Report NUREG/CR-4305 (ORNL/Sub/82-22252/3), August 1985.

83. J. W. Bryson, Martin Marietta Energy Systems, Inc., Oak Ridge Natl. Lab., Oak Ridge, Tenn., *ORVIRT.PC: A 2-D Finite Element Fracture Analysis Program for a Microcomputer,* USNRC Report NUREG/CR-4367 (ORNL-6208), October 1985.

84. D. G. Ball and R. D. Cheverton, Martin Marietta Energy Systems, Inc., Oak Ridge Natl. Lab., Oak Ridge, Tenn., *Adaptation of OCA-P, A Probabilistic Fracture-Mechanics Code, to a Personal Computer,* USNRC Report NUREG/CR-4468 (ORNL/CSD/TM-233), January 1986.

85. J. W. Bryson and B. R. Bass, Martin Marietta Energy Systems, Inc., Oak Ridge Natl. Lab., Oak Ridge, Tenn., *ORMGEN.PC: A Microcomputer Program for Automatic Mesh Generation of 2-D Crack Geometries,* USNRC Report NUREG/CR-4475 (ORNL-6250), March 1986.

86. G. D. Whitman, Martin Marietta Energy Systems, Inc., Oak Ridge Natl. Lab., Oak Ridge, Tenn., *Historical Summary of the Heavy-Section Steel Technology Program and Some Related Activities in Light-Water Reactor Pressure Vessel Safety Research,* USNRC Report NUREG/CR-4489 (ORNL-6259), March 1986.

87. C. Inversini and J. W. Bryson, Martin Marietta Energy Systems, Inc., Oak Ridge Natl. Lab., Oak Ridge, Tenn., *ORPLOT PC: A Graphic Utility for ORMGEN.PC and ORVIRT.PC,* USNRC Report NUREG/CR-4633 (ORNL-6291), June 1986.

88. J. J. McGowan, R. K. Nanstad, and K. R. Thoms, Martin Marietta Energy Systems, Inc., Oak Ridge Natl. Lab., Oak Ridge, Tenn., *Characterization of Irradiated Current-Practice Welds and A533 Grade B Class 1 Plate for Nuclear Pressure Vessel Service,* USNRC Report NUREG/CR-4880 (ORNL/TM-10387), July 1988.

89. K. V. Cook and R. W. McClung, Martin Marietta Energy Systems, Inc., Oak Ridge Natl. Lab., Oak Ridge, Tenn., *Flaw Density Examinations of a Clad Boiling Water Reactor Pressure Vessel Segment,* USNRC Report NUREG/CR-4860 (ORNL/TM-10364), April 1987.

90. D. J. Naus, B. R. Bass, C. E. Pugh, R. K. Nanstad, J. G. Merkle, W. R. Corwin, and G. C. Robinson, Martin Marietta Energy Systems, Inc., Oak Ridge Natl. Lab., Oak Ridge, Tenn., *Crack-Arrest Behavior*

in SEN Wide Plates of Quenched and Tempered A 533 Grade B Steel Tested Under Nonisothermal Conditions, USNRC Report NUREG/CR-4930 (ORNL-6388), August 1987.

91. D. B. Barker, R. Chona, W. L. Fourney, and G. R. Irwin, University of Maryland, College Park, Md., *A Report on the Round Robin Program Conducted to Evaluate the Proposed ASTM Standard Test Method for Determining the Plane Strain Crack Arrest Fracture Toughness, K_{Ia},* of Ferritic Materials, USNRC Report NUREG/CR-4966 (ORNL/Sub/79-7778/4), January 1988.

92. W. H. Bamford, Westinghouse Electric Corporation, Pittsburgh, Pa., *A Summary of Environmentally Assisted Crack-Growth Studies Performed at Westinghouse Electric Corporation Under Funding from the Heavy-Section Steel Technology Program,* USNRC Report NUREG/CR-5020 (ORNL/Sub/82-21598/1), May 1988.

93. R. H. Bryan, B. R. Bass, S. E. Bolt, J. W. Bryson, W. R. Corwin, J. G. Merkle, R. K. Nanstad, and G. C. Robinson, Martin Marietta Energy Systems, Inc., Oak Ridge Natl. Lab., Oak Ridge, Tenn., *Pressurized-Thermal-Shock Test of 6-in.-Thick Pressure Vessels. PTSE-2: Investigation of Low Tearing Resistance and Warm Prestressing*, USNRC Report NUREG/CR-4888 (ORNL-6377), December 1987.

94. J. H. Giovanola and R. W. Klopp, SRI International, Menlo Park, Calif., *Viscoplastic Stress-Strain Characterization of A533B Class 1 Steel,* USNRC Report NUREG/CR-5066 (ORNL/Sub/87-SA193/1), September 1989.

95. L. F. Miller et al., Martin Marietta Energy Systems, Inc., Oak Ridge Natl. Lab., Oak Ridge, Tenn., *Neutron Exposure Parameters for the Metallurgical Test Specimens in the Fifth Heavy-Section Steel Technology Irradiation Series Capsules,* USNRC Report NUREG/CR-5019 (ORNL/TM-10582), March 1988.

96. Canceled.

97. D. J. Naus, J. Keeney-Walker, and B. R. Bass, Martin Marietta Energy Systems, Inc., Oak Ridge Natl. Lab., Oak Ridge, Tenn., *High-Temperature Crack-Arrest Behavior in 152-mm-Thick SEN Wide Plates of Quenched and Tempered A 533 Grade B Steel,* USNRC Report NUREG/CR-5330 (ORNL/TM-11083), April 1989.

98. K. V. Cook, R. A. Cunningham, Jr., and R. W. McClung, Martin Marietta Energy Systems, Inc., Oak Ridge Natl. Lab., Oak Ridge, Tenn., *Detection and Characterization of Indications in Segments of Reactor Pressure Vessels,* USNRC Report NUREG/CR-5322 (ORNL/TM-11072), August 1989.

99. R. D. Cheverton, W. E. Pennell, G. C. Robinson, and R. K. Nanstad, Martin Marietta Energy Systems, Inc., Oak Ridge Natl. Lab., Oak Ridge, Tenn., *Impact of Radiation Embrittlement on Integrity of Pressure Vessel Supports for Two PWR Plants,* NUREG/CR-5320 (ORNL/TM-10966), February 1989.

100. D. J. Naus, J. Keeney-Walker, B. R. Bass, S. K. Iskander, R. J. Fields, R. deWitt, and S. R. Low III, Martin Marietta Energy Systems, Inc., Oak Ridge Natl. Lab., Oak Ridge, Tenn., *SEN Wide-Plate Crack-Arrest Tests* Utilizing *A 533 Grade B Class 1 Material: WP-CE Test Series,* USNRC Report NUREG/CR-5408 (ORNL/TM-11269), November 1989.

101. D. J. Naus, J. Keeney-Walker, B. R. Bass, S. K. Iskander, R. J. Fields, R. deWitt, and S. R. Low III, Martin Marietta Energy Systems, Inc., Oak Ridge Natl. Lab., Oak Ridge, Tenn., *High Temperature Crack-Arrest Tests Using 152-mm-Thick SEN Wide Plates of Low Upper-Shelf Base Material: Tests WP-2.2 and WP-2.6,* USNRC Report NUREG/CR-5450 (ORNL/TM-11352), February 1990.

102. Canceled.

103. D. J. Naus, J. Keeney-Walker, B. R. Bass, G. C. Robinson, S. K. Iskander, D. J. Alexander, R. J. Fields, R. deWitt, S. R. Low, C. W. Schwartz, and I.-B. Johansson, Martin Marietta Energy Systems, Inc., Oak Ridge Natl. Lab., Oak Ridge, Tenn., *Crack-Arrest Behavior in SEN Wide Plates of Low Upper-Shelf Base Metal Tested Under Non-isothermal Conditions: WP-2 Series,* USNRC Report NUREG/CR-5451 (ORNL-6584), August 1990.

104. T. L. Dickson, R. D. Cheverton, and D. K. Shum, Martin Marietta Energy Systems, Inc., Oak Ridge Natl. Lab., Oak Ridge, Tenn., *Inclusion of Unstable Ductile Tearing and Extrapolated Crack-Arrest Toughness Data in PWR Vessel Integrity Assessment,* USNRC Report NUREG/CR-5473 (ORNL/TM-11450), May 1990.

105. T. J. Theiss, Martin Marietta Energy Systems, Inc., Oak Ridge Natl. Lab., Oak Ridge, Tenn., *Recommendations for the Shallow-Crack Fracture Toughness Testing Task Within the HSST Program,* USNRC Report NUREG/CR-5554 (ORNL/TM-11509), September 1990.

106. J. G. Merkle, Martin Marietta Energy Systems, Inc., Oak Ridge Natl. Lab., Oak Ridge, Tenn., *An*

Overview of the Low Upper Shelf Toughness Safety Margin Issue, USNRC Report NUREG/CR-5552 (ORNL/TM-11314), August 6, 1990.

107. D. K. M. Shum, J. G. Merkle, J. Keeney-Walker, and B. R. Bass, Martin Marietta Energy Systems, Inc., Oak Ridge Natl. Lab., Oak Ridge, Tenn., *Analytical Studies of Transverse Strain Effects on Fracture Toughness for Circumferentially Oriented Cracks*, USNRC Report NUREG/CR-5592 (ORNL/TM-11581), April 1991.

108. J. D. Landes, The University of Tennessee for Martin Marietta Energy Systems, Inc., Oak Ridge natl. Lab., Oak Ridge, Tenn., *Extrapolation of the J-R Curve for Predicting Reactor Vessel Integrity*, USNRC Report NUREG/CR-5650 (ORNL/Sub/89-99732/1), January 1992.

109. J. Keeney-Walker, B. R. Bass, and J. D. Landes, (The University of Tennessee), Martin Marietta Energy Systems, Inc., Oak Ridge Natl. Lab., Oak Ridge, Tenn., *An Investigation of Crack-Tip Stress-Field Criteria for Predicting Cleavage-Crack Initiation*, USNRC Report NUREG/CR-5651 (ORNL/TM-11692), September 1991.

110. G. R. Irwin, University of Maryland, for Martin Marietta Energy Systems, Inc., Oak Ridge Natl. Lab., Oak Ridge, Tenn., *Use of Thickness Reduction to Estimate Values of K*, USNRC Report NUREG/CR-5697 (ORNL/Sub/79-7778/5), November 1991.

111. P. Albrecht and X. Chen, University of Maryland for Martin Marietta Energy Systems, Inc., Oak Ridge Natl. Lab., Oak Ridge, Tenn., *Limit Pressure Analysis of PTSE-2 Vessel*, USNRC Report NUREG/CR-5698 (ORNL/Sub/79-7778/6) (to be published).

112. J. W. Dally, W. L. Fourney, and G. R. Irwin, University of Maryland for Martin Marietta Energy Systems, Inc., Oak Ridge Natl. Lab., Oak Ridge, Tenn., *Lower-Bound Initiation Toughness with a Modified-Charpy Specimen*, USNRC Report NUREG/CR-5703 (ORNL/Sub/79-7778/7), November 1991.

113. S. K. Iskander, G. C. Robinson, W. R. Corwin, B. C. Oland, D. J. Alexander, and K. V. Cook, Martin Marietta Energy Systems, Inc., Oak Ridge Natl. Lab., Oak Ridge, Tenn., *Experimental Results of Tests to Investigate Flaw Behavior of Mechanically Loaded Stainless Steel Clad Plates*, USNRC Report NUREG/CR-5785 (ORNL/TM-11950), April 1992.

114. S. T. Rolfe, University of Kansas for Martin Marietta Energy Systems, Inc., Oak Ridge Natl. Lab., Oak Ridge, Tenn., *Interpretive Report on the Application of Shallow-Flaw CTOD Test Data to the Structural Margin Assessment of Reactor Pressure Vessels with Flaws*, USNRC Report NUREG/CR-5767 (ORNL/Sub/90-SH640/1), November 1991.

115. D. E. McCabe, Martin Marietta Energy Systems, Inc., Oak Ridge Natl. Lab., Oak Ridge, Tenn., *Comparison of Weibull and β_{Ic} Analysis of Transition Range Fracture Toughness Data*, USNRC Report NUREG/CR-5788 (ORNL/TM-11959), January 1992.

116. R. D. Cheverton, T. L. Dickson, J. G. Merkle, and R. K. Nanstad, Martin Marietta Energy Systems, Inc., Oak Ridge Natl. Lab., Oak Ridge, Tenn., *Review of Reactor Pressure Vessel Evaluation Report for Yankee Rowe Nuclear Power Station (YAEC No. 1735)*, USNRC Report NUREG/CR-5799 (ORNL/TM-11982), March 1992.

117. T. L. Dickson, R. D. Cheverton, and J. W. Bryson, Martin Marietta Energy Systems, Inc., Oak Ridge Natl. Lab., Oak Ridge, Tenn., *Pressurized-Thermal-Shock Probabilistic Fracture Mechanics Sensitivity Analyses for Yankee Rowe Reactor Pressure Vessel*, USNRC Report NUREG/CR-5782 (ORNL/TM-11945), August 1993.

118. Canceled

119. J. W. Dally, G. R. Irwin, X-J. Zhang, and R. J. Bonenberger, University of Maryland for Martin Marietta Energy Systems, Inc., Oak Ridge Natl. Lab., Oak Ridge, Tenn., *The Influence of Precompression on the Lower-Bound Initiation Toughness of A 533 B Reactor Grade Steel*, USNRC Report NUREG/CR-5847 (ORNL/Sub/79-7778/8), May 1992.

120. Canceled

121. C. W. Schwartz, University of Maryland for Martin Marietta Energy Systems, Inc., Oak Ridge Natl. Lab., Oak Ridge, Tenn., *Crack Speed Relations Inferred from Large SEN Specimens of A 533 B Steel*, USNRC Report NUREG/CR-5861 (ORNL/Sub/79-7778/9), July 1994.

122. A. R. Rosenfield and C. W. Marschall, Battelle Columbus Division for Martin Marietta Energy Systems, Inc., Oak Ridge Natl. Lab., Oak Ridge, Tenn., *Fracture-Mechanics-Based Failure Analysis*, USNRC Report NUREG/CR-5860 (ORNL/Sub/82-17651/1), June 1992.

123. G. R. Irwin and X-J. Zhang, University of Maryland for Martin Marietta Energy Systems, Inc., Oak Ridge Natl. Lab., Oak Ridge, Tenn., *Gradient Study*

of a Large Weld Joining Two Forged A 508 Shells of the Midland Reactor Vessel, USNRC Report NUREG/CR-5867 (ORNL/Sub/79-7778/10), June 1992.

124. J. Keeney-Walker and B. R. Bass, Martin Marietta Energy Systems, Inc., Oak Ridge Natl. Lab., Oak Ridge, Tenn., *ORNOZL: A Finite-Element Mesh Generator for Nozzle-Cylinder Intersections Containing Inner-Corner Cracks*, USNRC Report NUREG/CR-5872 (ORNL/TM-11049), September 1992.

125. J. Keeney-Walker and B. R. Bass, Martin Marietta Energy Systems, Inc., Oak Ridge Natl. Lab., Oak Ridge, Tenn., *A Comparison of Analysis Methodologies for Predicting Cleavage Arrest of a Deep Crack in a Reactor Pressure Vessel Subjected to Pressurized-Thermal-Shock Loading Conditions*, USNRC Report NUREG/CR-5793 (ORNL/TM-11969), September 1992.

126. T. J. Theiss, D. K. M. Shum, and S. T. Rolfe (University of Kansas), Martin Marietta Energy Systems, Inc., Oak Ridge Natl. Lab., Oak Ridge, Tenn., *Experimental and Analytical Investigation of the Shallow-Flaw Effect in Reactor Pressure Vessels*, USNRC Report NUREG/CR-5886 (ORNL/TM-12115), July 1992.

127. B. R. Bass, D. K. M. Shum, and J. Keeney-Walker, Martin Marietta Energy Systems, Inc., Oak Ridge Natl. Lab., Oak Ridge, Tenn., *Constraint Effects on Fracture Toughness for Circumferentially Oriented Cracks in Reactor Pressure Vessels*, USNRC Report NUREG/CR-6008, (ORNL/TM-12131), August 1992.

128. R. E. Stoller, Martin Marietta Energy Systems, Inc., Oak Ridge Natl. Lab., Oak Ridge, Tenn., *Modeling the Influence of Irradiation Temperature and Displacement Rate on Radiation-Induced Hardening in Ferritic Steels*, USNRC Report NUREG/CR-5859 (ORNL/TM-12073), July 1992.

129. J. Keeney-Walker, J. G. Merkle, S. K. Iskander, and T. L. Dickson, Martin Marietta Energy Systems, Inc., Oak Ridge Natl. Lab., Oak Ridge, Tenn., *Recommendations for Thermal-Shock Testing of Clad Cylinders with Shallow Surface Cracks*, USNRC Report NUREG/CR-5915 (ORNL/TM-12166), November 1992.

130. W. E. Pennell, B. R. Bass, R. K. Nanstad, J. G. Merkle, T. L. Dickson, T. J. Theiss, J. Keeney-Walker, and D. K. Shum, *Heavy-Section Steel Technology Program Semiannual Progress Report for October 1991 through March 1992*, NUREG/CR-4219 (ORNL/TM-9593/V9&N1) June 30, 1992.

131. W. E. Pennell, Martin Marietta Energy Systems, Inc., Oak Ridge Natl. Lab., "Heavy-Section Steel Technology Program: Recent Developments in Crack Initiation and Arrest Research," *Nineteenth Water Reactor Safety Information Meeting*, NUREG/CP-0119, Vol. 1, pp. 29–51, October 1992.

132. W. E. Pennell, Martin Marietta Energy Systems, Inc., Oak Ridge Natl. Lab., "Aging Impact on the Safety and Operability of Nuclear Reactor Pressure Vessels," *Proceedings of the Aging Research Information Conference*, USNRC Conference Proceeding NUREG/CP-0122, Vol. 1, pp. 431–453, March 1992.

133. T. L. Dickson and F. A. Simonen, Martin Marietta Energy Systems, Inc., Oak Ridge Natl. Lab., "The Application of Probabilistic Fracture Analysis to Residual Life Evaluation of Embrittled Reactor Vessels," *Proceedings of the Aging Research Information Conference*, USNRC Conference Proceeding NUREG/CP-0122, Vol. 1, pp. 454-467, March 1992.

134. R. K. Nanstad, F. M. Haggag, D. E. McCabe, S. K. Iskander, K. O. Bowman, and B. H. Menke, Martin Marietta Energy Systems, Inc., Oak Ridge Natl. Lab., *Irradiation Effects on Fracture Toughness of Two High-Copper Submerged-Arc Welds, HSSI Series 5*, USNRC Report NUREG/CR-5913, Vol. 1 (ORNL/TM-12156/V1) October 1992.

135. D. E. McCabe, Martin Marietta Energy Systems, Inc., Oak Ridge Natl. Lab., *Evaluation of Crack Pop-ins and the Determination of Their Relevance to Design Consideration*, USNRC Report NUREG/CR-5952 (ORNL/TM-12247), February 1993.

136. Canceled

137. R. K. Nanstad, D. E. McCabe, R. L. Swain, and M. K. Miller, Martin Marietta Energy Systems, Inc., Oak Ridge Natl. Lab., *Chemical Composition and RT_{NDT} Determinations for Midland Weld WF-70*, USNRC Report NUREG/CR-5914 (ORNL-6740) December 1992.

138. T. J. Theiss, B. R. Bass, J. W. Bryson, W. J. McAfee , R. K. Nanstad, W. E. Pennell, and M. C. Rao, Martin Marietta Energy Systems, Inc., Oak Ridge Natl. Lab., *Initial Results of the Influence of Biaxial Loading on Fracture Toughness*, USNRC Report NUREG/CR-6036 (ORNL/TM-12349), June 1993.

139. D. K. Shum, J. W. Bryson, and J. G. Merkle, Martin Marietta Energy Systems, Inc., Oak Ridge Natl. Lab., *Potential Change in Flaw Geometry of an Initially Shallow Finite-Length Surface Flaw During a Pressurized Thermal Shock Transient*, NUREG/CR-5968 (ORNL/TM-12279), September 1993.

140. T. L. Dickson, Martin Marietta Energy Systems, Inc., Oak Ridge Natl. Lab., *Generic Analyses for Evaluation of Low Charpy Upper-Shelf Energy Effects on Safety Margins Against Fracture of Reactor Pressure Vessel Materials,* USNRC Report NUREG/CR-6023 (ORNL/TM-12340), July 1993.

141. C. W. Schwartz, Department of Civil Engineering, University of Maryland, *Crack-Speed Relations Inferred from Large Single-Edge-Notched Specimens of A 533 B Steel,* NUREG/CR-5861 (ORNL/Sub/79-7778/9), July 1994.

142. B. R. Bass, J. W. Bryson, W. J. McAfee, T. J. Theiss, and M. C. Rao, Martin Marietta Energy Systems, Inc., Oak Ridge Natl. Lab., *Biaxial Loading and Shallow-Flaw Effects on Crack-Tip Constraint and Fracture Toughness,* NUREG/CR-6132 (ORNL/TM-12498), January 1994.

143. Canceled.

144. Canceled.

145. Canceled.

146. Canceled.

147. Robert H. Dodds, Constraint Effects on Fracture Initiation Loads in HSST Wide-Plate Tests, NUREG/CR-6259 (ORNL/TM-12796), July 1994.

148. J. A. Keeney, B. R. Bass, W. J. McAfee, and S. K. Islander, *Preliminary Assessment of the Fracture Behavior of Weld Material in Full-Thickness Clad Beams,* USNRC Report NUREG/CR-6228 (ORNL/TM-12735), October 1994.

149. W. J. McAfee, B. R. Bass, J. W. Bryson, and W. E. Pennell, *Biaxial Loading Effects on Fracture Toughness of Reactor Pressure Vessel Steel,* USNRC Report NUREG/CR-6273 (ORNL/TM-12866), November 1994.

150. G. R. Irwin and X. J. Zhang, *Cleavage Behaviors in Nuclear Vessel Steels,* USNRC Report NUREG/CR-6262 (ORNL/Sub/79-7778/11), November 1994.

NUREG/CR-4219
ORNL/TM-9593/V12&N1
Vol. 12, No. 1
Dist. Category RF

Internal Distribution

1. D. J. Alexander
2. B. R. Bass
3. J. W. Bryson
4. W. G. Craddick
5. W. R. Corwin
6. T. L. Dickson
7. R. G. Gilliland
8. W. F. Jackson
9. S. K. Iskander
10. J. A. Keeney
11. W. J. McAfee
12. D. E. McCabe
13. J. G. Merkle
14. R. K. Nanstad
15. D. J. Naus
16–19. W. E. Pennell
20. C. E. Pugh
21. C. C. Southmayd
22. ORNL Patent Office
23. Central Research Library
24. Document Reference Section
25. Laboratory Records
26. Laboratory Records (RC)

External Distribution

27. R. D. Thompson, Office of Administration, Divison of Contracts and Properties, U.S. Nuclear Regulatory Commission, Mailstop T17/G-21, Washington, DC 20555-0001
28. J. Strosnider, Division of Engineering, NRR, U.S. Nuclear Regulatory Commission, Mailstop O7-D4, Washington, DC 20555-0001
29. E. M. Hackett, Materials and Chemical Engineering Branch, Mailstop O7-D4, U.S. Nuclear Regulatory Commission, Washington, DC 20555-0001
30–32. S. N. M. Malik, EMMEB/DET/RES, U.S. Nuclear Regulatory Commission, Washington, DC 20555-0001
33. M. E. Mayfield, EMMEB/DET/RES, U.S. Nuclear Regulatory Commission, Washington, DC 20555-0001
34. G. C. Millman, Division of Engineering, U.S. Nuclear Regulatory Commission, Washington, DC 20555-0001
35. M. Vassilaros, EMMEB/DET/RES, Mailstop T10-E10, U.S. Nuclear Regulatory Commission, Washington, DC 20555-0001
36. J. W. Dally, Department of Mechanical Engineering, University of Maryland, College Park, Maryland 20742
37. G. R. Irwin, Department of Mechanical Engineering, University of Maryland, College Park, Maryland 20742
38. L. James, Westinghouse Bettis Lab., P.O. Box 79, ZAP 13A, 814 Pittsburgh McKeesport Blvd., West Mifflin, Pennslyvania 15122
39. C. F. Shih, Box D, Division of Engineering, Brown University, Providence, Rhode Island 02912
40. R. Dodds, 3140 Newmark Laboratory, 205 North Matthews, Urbana, Illinois 61801
41. R. Fields, National Inst. of Standards and Technology, Bldg. 223, B144, Gaithersburg, Maryland 20899
42. W. L. Fourney, Department of Mechanical Engineering, University of Maryland, College Park, Maryland 20742
43. J. D. Landes, The University of Tennessee, Knoxville, Tennessee 37996-2030
44. S. T. Rolfe, The University of Kansas, Lawrence, Kansas 66045-2235
45. A. R. Rosenfield, Battelle Columbus Division, Columbus, Ohio 43201
46. C. W. Schwartz, Department of Civil Engineering, University of Maryland, College Park, Maryland 20742
47. E. T. Wessel, 312 Wolverine, Haines City, Florida 33844
48. R. L. Tregoning, Code-614, NSWC-CD, 3A Leggett Circle, Annapolis, Maryland 21402-5067
49. Office of Assistant Manager for Energy Research and Development, DOE–ORO, Oak Ridge, Tennessee 37831
50–51. Office of Scientific and Technical Information, P.O. Box 62, Oak Ridge, Tennessee 37831

NRC FORM 335 (2-89) NRCM 1102, 3201, 3202

U.S. NUCLEAR REGULATORY COMMISSION

BIBLIOGRAPHIC DATA SHEET

(See instructions on the reverse)

1. REPORT NUMBER (Assigned by NRC, Add Vol., Supp., Rev., and Addendum Numbers, if any.)
NUREG/CR-4219
ORNL/TM-9593/V12&N1
Vol. 12 No. 1

2. TITLE AND SUBTITLE
Heavy-Section Steel Technology Program
Semiannual Progress Report for October 1994 - March 1995

3. DATE REPORT PUBLISHED
MONTH: July
YEAR: 1996

4. FIN OR GRANT NUMBER
B0119

5. AUTHOR(S)
W. E. Pennell

6. TYPE OF REPORT
Technical

7. PERIOD COVERED (Inclusive Dates)
10/94 - 3/95

8. PERFORMING ORGANIZATION – NAME AND ADDRESS (If NRC, provide Division, Office or Region, U.S. Nuclear Regulatory Commission, and mailing address; if contractor, provide name and mailing address.)

Oak Ridge National Laboratory
Oak Ridge, TN 37831-6285

9. SPONSORING ORGANIZATION – NAME AND ADDRESS (If NRC, type "Same as above"; if contractor, provide NRC Division, Office or Region, U.S. Nuclear Regulatory Commission, and mailing address.)

Division of Engineering Technology
Office of Nuclear Regulatory Research
U.S. Nuclear Regulatory Commission
Washington, DC 20555-0001

10. SUPPLEMENTARY NOTES
S. N. M. Malik, NRC Project Manager

11. ABSTRACT (200 words or less)

The Heavy-Section Steel Technology (HSST) Program is conducted for the U.S. Nuclear Regulatory Commission (NRC) by Oak Ridge National Laboratory (ORNL). The program focus is on the development and validation of technology for the assessment of fracture-prevention margins in commercial nuclear reactor pressure vessels. The HSST Program is organized in seven tasks: (1) program management, (2) constraint effects analytical development and validation, (3) evaluation of cladding effects, (4) ductile to cleavage fracture mode conversion, (5) fracture analysis methods development and applications, (6) material property data and test methods, and (7) integration of results into a state-of-the-art methodology. The program tasks have been structured to place emphasis on the resolution fracture issues with near-term licensing significance. Resources to execute the research tasks are drawn from ORNL with subcontract support from universities and other research laboratories. Close contact is maintained with the sister Heavy-Section Steel Irradiation Program at ORNL with related research programs both in the United States and abroad. This report provides an overview of principal developments in each of the seven program tasks from October 1994 - March 1995.

12. KEY WORDS/DESCRIPTORS (List words or phrases that will assist researchers in locating the report.)

Heavy-Section Steel Technology (HSST), assessment, fracture prevention, semiannual progress report

13. AVAILABILITY STATEMENT
unlimited

14. SECURITY CLASSIFICATION
(This Page) unclassified
(This Report) unclassified

15. NUMBER OF PAGES

16. PRICE

Federal Recycling Program